FREIE UNIVERSITÄT BERLIN

Novel Non–Equilibrium Dynamics in Superconductors: Induced Superconductivity and Higgs Modes

im Fachbereich Physik
der Freien Universität Berlin
eingereichte

DISSERTATION

von

NIKOLAJ BITTNER

Berlin, Mai 2016

1. Gutachter (Betreuer):	Prof. Dr. Dirk Manske
2. Gutachter:	Prof. Felix von Oppen, PhD

Tag der Einreichung:	25. Mai 2016
Tag der Disputation:	2. November 2016

MAX–PLANCK–INSTITUT
FÜR FESTKÖRPERFORSCHUNG

FREIE UNIVERSITÄT BERLIN

"What I cannot create, I do not understand"

R. P. Feynman

"Through hardships to the stars"
(per aspera ad astra)

Seneca

Abstract

This thesis reports on theoretical investigations of the ultrafast nonequilibrium dynamics in superconductors. In particular, two nonequilibrium scenarios are modeled by combining several analytical and numerical methods: transient superconducting phase transition and collective excitations of a superconducting condensate.

In the first part of the thesis the possibility to induce singlet superconducting correlations far from equilibrium is explored by applying time–dependent Lanczos algorithm to the one–dimensional extended Hubbard model. Here, the system is driven into a nonequilibrium state by (i) interaction quench and (ii) quench by pulse. In both cases the buildup of the superconducting correlations is studied in view of several correlation functions. Moreover, a transient Meissner effect, which reflects fingerprints of the induced superconductivity, is observed in calculations of the important for experiments time–dependent optical conductivity. In addition, the differences between nonequilibrium dynamics of the extended Hubbard model initiated by interaction quench and by pulse quench are discussed in detail.

The second part is devoted to the excitation of collective modes in a superconductor out of equilibrium. First of all, focus is given to the properties of collective modes close to equilibrium conditions, where a linearized response can be expected. Within the framework of the (Nambu-) matrix kinetic theory in the clean limit a comprehensive gauge–invariant description of the collective modes associated with phase fluctuations of the order parameter is analytically formulated for the generalized case of two–band superconducting systems. Particular emphasis is on the application to the recently discovered noncentrosymmetric superconductors. A detailed analysis of the collective modes includes specification of the gauge mode (common to all superconductors) and the Leggett mode (collective fluctuations of the interband phase difference), and investigation of their subtle interplay in view of validity of the charge conservation law and the participation in the Anderson-Higgs mechanism. Further, the nonequilibrium excitation of the superconducting gaps for the case of two–band superconductors with singlet pairing correlations is investigated in a view of optical pump–probe experiments. For this purpose a semi–numerical method based on the density–matrix theory is formulated. In this case additional amplitude (Higgs) modes were identified, which allow to directly detect the properties of the superconducting condensates as a function of time. Moreover, a new interplay between the phase (Leggett) and amplitude (Higgs) modes is studied in detail. In particular it was found that the nonadiabatic excitation process leads to strong coupling between both modes. Finally, based on calculations of the time–dependent optical conductivity the prediction is made that the coupled Higgs and Leggett modes can be clearly visible in the pump–probe absorption spectra.

Zusammenfassung

In der vorliegenden Arbeit werden Resultate zu theoretischen Untersuchungen der ultraschnellen Nichtgleichgewichtsdynamik in Supraleitern vorgestellt. Insbesondere werden zwei Nichgleichgewichtssituationen mit Hilfe von verschiedenen analytischen und numerischen Methoden simuliert: ein transienter Phasenübergang in einen supraleitenden Zustand und kollektive Anregungen eines supraleitenden Kondensats.

Im ersten Teil dieser Arbeit wird die Möglichkeit der Entstehung supraleitender Spin–Singulett–Korrelationen in einem eindimensionalen erweiterten Hubbard–Modell weit vom Gleichgewicht unter Verwendung eines zeitabhängigen Lanczos–Algorithmus erforscht. Das System wird dabei mit Hilfe (i) eines Wechselwirkungs–Quenches und (ii) eines starken Pulses in einen Nichtgleichgewichtszustand gebracht. In beiden Fällen wird die Entstehung supraleitender Korrelationen im Hinblick auf verschiedene Korrelationsfunktionen untersucht. Außerdem wird eine für Experimente wichtige zeitabhängige optische Leitfähigkeit berechnet, bei der ein transienter Meissner–Effekt als Charakteristikum eines induzierten supraleitenden Zustandes beobachtet werden kann. Anschließend wird der Unterschied in den Nichtgleichgewichtsdynamiken eines erweiterten Hubbard–Modells hervorgerufen vom Wechselwirkungs–Quench und vom starken Puls im Detail diskutiert.

Der zweite Teil dieser Arbeit beschäftigt sich mit den Anregungen kollektiver Moden in Supraleitern weit weg vom Gleichgewicht. Zunächst werden die Eigenschaften kollektiver Moden im Fall der linearen Antwort eines Supraleiters unter den Bedingungen untersucht, die dem Gleichgewicht nahekommen. Dabei wird eine umfassende eichungsinvariante Beschreibung der Phasenfluktuationen des Ordnungsparameters und der damit assoziierten kollektiven Moden für den allgemeinen Fall der Zweiband–Supraleiter unter Verwendung der Nambu–Matrix–Kinetischen Theorie im reinen Grenzfall analytisch formuliert. Insbesondere wird die Anwendung auf die nicht–zentrosymmetrischen Supraleiter diskutiert. Es folgt dann eine detaillierte Analyse dieser kollektiven Moden, die eine Beschreibung der Eichmode (tritt in allen Supraleitern auf) und der Leggett Mode (kollektive Fluktuation in der Interbandphasendifferenz) und auch Untersuchungen des subtilen Zusammenspiels beider Moden im Hinblick auf die Teilchenzahlerhaltung und den Anderson–Higgs–Mechanismus beinhaltet. In Bezug auf optische pump–probe Experimente werden anschließend die Nichtgleichgewichtsanregungen von supraleitenden Energielücken im Fall der Zweiband–Supraleiter mit Spin–Singulett–Paarung untersucht. Für diesen Zweck wird eine halbnumerische Methode basierend auf der Dichtematrixtheorie formuliert. In diesem Fall können zusätzliche Amplitudenmoden (Higgs) identifiziert werden, die ermöglichen die Eigenschaften supraleitender Kondensate als Funktion der Zeit zu messen. Außerdem wird ein neues Zusammenspiel zwischen der Phasen–(Leggett–) und der Amplitudenmoden (Higgs) im Detail analysiert. Insbesondere wird gezeigt, dass ein nichtadiabatischer Anregungsprozess zu einer starken Kopplung beider Moden führt. Schließlich wird anhand der zeitaufgelösten Berechnungen der optischen Leitfähigkeit vorausgesagt, dass die gekoppelten Higgs- und Leggett–Moden in optischen pump–probe Spektren klar zu beobachten sind.

Contents

Terminology and Abbreviation

Symbol		Description
T_c	....	Transition temperature
THz	....	Terahertz
FWHM	....	Full width at half maximum
(A)SOC	....	(Antisymmetric) Spin orbit coupling
NCS	....	Noncentrosymmetric superconductors
MKT	....	Matrix kinetic theory
RPA	....	Random phase approximation
DMF	....	Density matrix formalism
EHM	....	Extended Hubbard model
ED	....	Exact diagonalization
CDW	....	Charge density wave
SDW	....	Spin density wave
SC	....	Superconductivity
PS	....	Phase separation
DoS	....	Density of states
$N(0)$	....	DoS on the Fermi level with one spin projection
N_F	....	DoS on the Fermi level ($N_\mathrm{F} = 2N(0)$)
$\mathbf{k}$	....	vectors are written in the **bold** face
E_F	....	Fermi energy
$\mathbf{v}_\mathrm{F}$	....	Fermi velocity
$\mathbf{k}_\mathrm{F}$	....	Fermi wave vector
FS	....	Fermi surface
$\langle \ldots \rangle_{\mathrm{F}S}$	....	Averaging over the Fermi surface

$\boldsymbol{\tau}_0$	....	2×2 identity matrix
$\boldsymbol{\tau}_j$	....	Pauli matrices, $j = \{1, 2, 3\}$
$\hbar$	....	Planck's constant ($\hbar = 6.58211928(15) \cdot 10^{-16}$eVs)
k_B	....	Boltzmann's constant ($k_\mathrm{B} = 1.3806488 \cdot 10^{-23}$J/K)

Chapter 1

Introduction and Motivation

In this chapter we introduce the experimental time–resolved methods and different theoretical approaches to study dynamics in superconductors driven far away from equilibrium. We begin with the general aspects and possible unresolved questions in physics of superconductivity. Further, after presenting of the basic ideas of the nonequilibrium pump–probe technique, we discuss its recent success in investigation of the ultrafast phenomena in solids, like electron and phonon dynamics or transient phase transitions. In addition, we give a careful overview of the known theoretical approaches and motivate the choice of theoretical methods for this work. Finally, the thesis overview will be presented.

1.1. Superconductors: from zero resistivity to Higgs mode

Since its discovery in 1911 by Heike Kamerlingh Onnes, superconductivity continues to keep solid state researchers on their toes and surprises consistently with the abundance of fascinating and complex physical phenomena. Owing to analogies in the description to the Lorentz invariant theories, superconductors even offer a playground for studying different processes, which are similar to that from the high energy physics. In both cases the symmetry–breaking phase transitions play an important role. In fact, according to the BCS [1] theory [1] the electrons in a conventional superconductor build pairs by cooling below its critical temperature T_c and appear in a collective ground state. The Cooper pair formation is responsible for the effect of zero resistivity in superconductors and leads to an important perfect diamagnetism, which is also known, as Meissner–Ochsenfeld effect. This superconducting transition can be understood in terms of a two–component order parameter $\Delta = |\Delta| e^{i\varphi}$ with an amplitude $|\Delta|$ and a phase φ. Hereby, its free energy $\mathcal{F}$ in the ground state as a function of Δ changes its shape from the paraboloid to a Mexican hat potential (shown in Fig. 1.1) revealing a new energy minimum for the system. This process is connected with the breaking of the $U(1)$ symmetry and has analogies in the electroweak theory in the high energy physics.

---

[1] named after J. Bardeen, L. Cooper, and J. R. Schrieffer

The breaking of the continuous symmetry has far–reaching consequences. For instance, it is well–known [2, 3] that this process leads to appearance of collective excitations. The free energy in a symmetry–broken phase is invariant with respect to the phase variation of the order parameter. Hence, its phase fluctuation corresponds to a massless boson, which was described in Refs. [4–6] and commonly referred as the Nambu–Goldsone mode [2]. While in the electroweak theory this boson yields a massless excitation, in case of superconductors it leads to fluctuation of the charge density, as was recognized by P.W. Anderson in 1958 [6, 7]. As a consequence of the long–range Coulomb interaction between the electrons, the Anderson–Bogoliubov boson gets a mass and is shifted to the plasma mode of higher energy. This process is generally known as the Anderson–Higgs mechanism [6, 8].

In 1964 P.W. Higgs predicted [8] the existence of another massive mode by using similar formalism, which is connected with the small amplitude fluctuations of the order parameter and was named after him. In the unified electroweak theory the interaction with this Higgs mode leads to the mass of W- and Z-bosons. In analogy, the amplitude fluctuation of the order parameter in a superconductor is responsible for the Meissner–Ochsenfeld–Effect, since this mode lends the photons as exchange particles of the magnetic field a "mass" and by this means expel them from the superconductor.

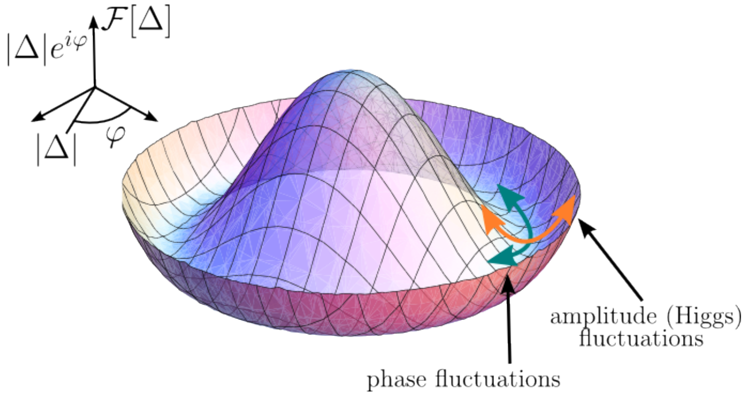

Figure 1.1: Illustration of the effective free–energy landscape $\mathcal{F}[\Delta]$ for a single band superconductor. The amplitude (Higgs) mode and phase (Anderson–Bogoliubov) mode are shown with the orange and blue arrows, respectively.

Although the experimental possibilities of the solid state physics are more flexible and do not require high energies, the observation of the amplitude Higgs mode in superconductors is still a quite challenging task. The reason is that this mode has neither charge nor dipole moment and can not be captured by the optical experiments. Moreover, the energy of the Higgs mode lies at 2Δ and therefore is not detectable with Raman measurements. Some indirect methods to excite the Higgs mode are, however, possible. At present there are only two known measurements [9–11], where the Higgs mode was observed under some special conditions. First experiment deals with the 2H–NbSe$_2$ material, where the charge

---

[2] in case of superconductors this mode is also known as Anderson–Bogoliubov mode

density wave (CDW) order and superconductivity can coexist below the superconducting critical temperature T_c=7.1K. In this case the CDW may couple to the superconducting condensate, which results in the excitation of the amplitude (Higgs) mode as indicated in Refs. [12, 13]. The measurements of the Raman susceptibility for 2H-NbSe$_2$ at different temperatures verifies this process and shows the transfer of the spectral weight from the CDW mode to the Higgs mode below T_c, which is shown in Fig. 1.2 (a).

An alternative experiment was accomplished on NbN films with different grades of disorder [11]. In this case an effect similar to that of the Raman experiment can be expected (see Fig. 1.2 (b)). In fact, with increased disorder in NbN films the critical temperature T_c and accordingly energy gap Δ_t gets smaller in this material. This was confirmed by the tunneling conductance measurements. An additional measurements of the real part of the dynamical conductivity $\sigma_1(\omega)$ versus frequency (energy) below T_c indicates qualitatively similar behavior. However, the comparison of the measured data $\sigma_1(\omega)$ with the calculated

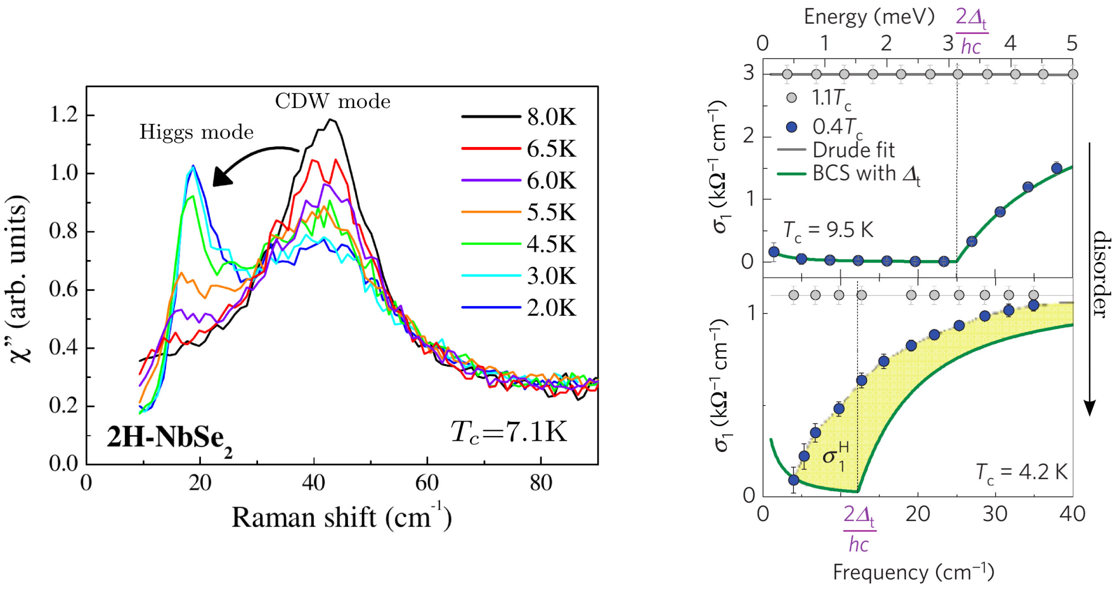

(a) Higgs mode in 2H-NbSe$_2$. Coupling to CDW **(b) Higgs mode in disordered NbN**

Figure 1.2: Experimental observation of Higgs mode in different superconducting materials. (a) Measurements of the Raman susceptibility for 2H-NbSe$_2$ at different temperatures. The preexisting charge density wave (CDW) couples to the superconducting condensate and the transfer of the spectral weight from the CDW mode to the Higgs mode below T_c=7.1K is observed. Figure is adapted from Ref. [10]. (b) Real part of the dynamical conductivity $\sigma_1(\omega)$ versus frequency (energy) measured above (gray dots) and below T_c (blue dots) for NbN film with different grades of disorder. A comparison of the measured data $\sigma_1(\omega)$ with the calculated curve (green line) based on the results from an additional tunneling experiment reveals a significant difference in their behavior in the case of the highly disorder material (yellow region). This indicates excitation of the Higgs mode. Figure is adapted from Ref. [11].

curve based on the corresponding tunneling results shows a significant difference in their behavior for the case of the disordered material and indicates excitation of the Higgs mode.

A detection of the Higgs mode in an experiment for all types of superconductors is an important piece of puzzle for our present understanding of the superconductivity. Indeed, order parameter in unconventional superconductors, like d–wave, has a lower grade of symmetry in contrast to the BCS type of superconductors and depends on the momentum $\mathbf{k}$. As a result, several Higgs modes reflecting gap symmetry can be expected in this case [14]. Also for exotic types of superconducting systems the studies of the collective modes may give an important information about its gap structure. For instance, in case of the not so long ago discovered noncentrosymmetric superconductors [15], where, due to the absence of the inversion center in its crystal structure, a superposition of both spin–singlet and spin–triplet contributions to the superconducting gaps is possible [16–18], the triplet–to–singlet ratio to the superconducting gap is still unknown.

A direct excitation of the Higgs mode may be achieved by the time–resolved spectroscopy, which uses ultrashort light pulses to drive a condensed matter system into a nonequilbrium state. With this technique one is able to access the intrinsic processes of the condensed matter on their fundamental time scale. And, what is more important, a system driven far away from equilibrium may reveal some novel properties, which are not reachable under normal thermodynamic conditions. This time–resolved spectroscopy will be introduced in the next section.

1.2. Time–resolved technique: Relevant experiments and theoretical methods

The pioneer in a field of the time–resolved measurements is believed to be a photographer Eadweard Muybridge, who invented photographic studies of motion and worked on motion–picture projection. In 1878 he was able to take images of a galloping horse for the first time by using several photo cameras with a relatively short exposure time. With this method he clearly put an end to the debate whether there is a moment in time when all four hooves of a horse are off the ground.

The work of Muybridge makes it clear that in order to capture an event which appears on a fast timescale and therefore is hidden to the naked eye one need a measuring instrument with a good time resolution. For instance, in conventional photo cameras the time resolution is regulated by a mechanical device called shutter, which in turn determines the exposure time. In this case, by adjusting the shutter speed one may get a series of sharp images of an object in motion, if the changes are negligibly small during the whole exposure period. Otherwise, the object on the image gets blurred. A combination of all taken images gives a reconstructed motion of the object. While modern cameras with a high speed shutter and an exposure time of some milliseconds can even resolve the motion of a flying bullet, the investigations of the dynamics in a solid state system on the atomic scale requires much better time resolution.

The invention of ultrashort pulsed laser systems in 80's opened new perspectives for studying the fundamental problems in condensed matter physics, chemistry and biology. In fact, only after developing femtosecond laser pulses one was able to investigate molecular motions and to analyze the transition states in the chemical reactions [19]. This pioneering work was rewarded in 1999 by the Nobel price in Chemistry. Now, the advances in laser technique enable to apply laser pulses with typical duration time lying in between some femtoseconds (10^{-15}s) and attoseconds (10^{-18}s) [3]. Hence, it is possible to resolve the dynamics of electrons and atoms in a solid state system in real time [20, 21]. Despite the complexity of the laser equipment, the basic concept of this type of measurements, which are generally known as the time–resolved spectroscopy, differs little from the high speed photography initiated by Muybridge. Here, instead of a photo camera one typically uses two laser pulses. The first strong ("pump") pulse induces dynamics in a solid state system by driving it far away from equilibrium. Then, the second weak one ("probe pulse") makes the "snapshots" of the nonequilibrium state and plays in this case a role similar to a photo camera. Hereby, the changes in the intensity of the laser pulse act as a camera shutter and its duration time determines the time resolution. Finally, by tuning the time delay Δt between pump and probe pulses and simultaneously studying transmitted light one is able to reconstruct the temporal evolution of the solid state system. The common experimental techniques include time resolved measurements of transmissivity, reflectivity or optical conductivity versus absorption frequency. Also angle–resolved photoemission spectroscopy with an additional time dependence [4] is possible [22].

Depending on the measuring conditions one is able to access different degrees of freedom in a solid state system. The relevant nonequilibrium experiments can be divided into several different categories [23, 24]. In the following we will discuss two of them with particular emphasis on application to studies of superconductors.

1.2.1. Non–Equilibrium spectroscopy

Into the first category fall experiments where the focus is given to relaxation processes in a solid state system. In this case a material is quenched by a light pulse on the ultrafast timescale, which at the same time acts quite softly to reduce temperature effects. The range of applications of this nonequilbrium technique varies from studies of relaxation dynamics in manganites [25], charge density wave insulators [26] and manipulation of spin dynamics in antiferromagnets [27] to disentangling different degrees of freedom in semiconductors [23].

Beginning with the pioneering work from the year 2005 on $Bi_2Sr_2CaCu_2O_{8+\delta}$ compound [28], where, for the first time, the dynamics of Cooper pair formation was studied by using ultrashort near–infrared optical pulses, the nonequlibrium pump–probe spectroscopy became an essential part in investigation of superconductors as well [29–39]. In particular, early nonequilbribum experiments already include studies of relaxation dynamics of the hot incoherent quasiparticles and the corresponding recovery of the superconducting conden-

---

[3] the pulses with the duration time shorter than 10^{-12}s are generally called *ultrafast*

[4] which is also known, as tr-ARPES

sate [29,31,32]. This way, it became possible to get access to important information about the electron–lattice interaction. Furthermore, by developing the measuring technique one was able to disentangle the electronic and phononic contributions to the superconducting glue by their different temporal evolution [33]. This type of measurements opened new way for investigations of electron–boson coupling in unconventional superconductors. Also, time–dependent Raman experiments with coherent phonon generation [30,37] could shed some light on the mechanism responsible for superconductivity. However, in all these cases a direct probe of the superconducting order parameter was not possible, since the experiments were done with near–visible or mid–infrared ultrashort pulses. In other words, the photoexcited hot electrons with energies of several eV generate large amounts of phonons, which break Cooper pairs in the superconducting condensate. Thus, a coherent excitation of the superconducting gap can not be observed [32,34]. A necessary prerequisite for these studies are, however, photon energies of the order of the superconducting gap, which are typically lying in the terahertz (THz) frequency range. In this case a laser pulse should directly modify the superconducting Mexican hat potential of the free energy (see Fig. 1.1) as a function of time in such a way that the amplitude (Higgs) oscillations around its minimum, reflecting the properties of the order parameter (see section 1.1), can occur.

The excitation of Higgs mode in superconductors in nonequilibrium represents a large effort not only from the experiment side, but also from the theory side. The first attempts to describe the condensate dynamics in superconductors use time-dependent methods based on the phenomenological approaches, like time–dependent Ginzburg–Landau theory [40,41], Boltzmann equation [41,42] or Rothwarf and Taylor model [43]. Some others describe a nonequilibrium distribution of quasiparticles in terms of an effective temperature T^* [44,45] or of a new chemical potential μ^* [45,46]. Because of the limited application range [5], these methods do not capture the important coherent excitation of the quasiparticles on a very short time range. A possible numerical solution was proposed in Refs. [47,48], where the nonequilibrium dynamics in a superconductor is described in the mean–field BCS approximation by using the extended density matrix formalism (DMF) [49]. In contrast to the common models, where the nonequilibrium situation is modeled by a quench and an analytical solution is possible [50–54], this technique enables to include a direct interaction between the fast varying electromagnetic field and the superconducting condensate. Moreover, the DMF method was used to describe the resonant generation of coherent phonons in superconductors [55], which is important for time–dependent Raman studies. This effect was further used in Refs. [56,57] to show that by tuning the intensity of the pump pulse one can bring the oscillations of the order parameter into resonance with the coherent phonons. In this way one can amplify the signal from superconducting oscillations in an experiment. Finally, some attempts towards nonequilibrium dynamics in unconventional superconductors based on DMF were reported in Refs. [58,59]. It should be also mentioned that other different aspects of the nonequilbrium behavior in a superconductor were studied by using alternative theories [60–66].

---

[5] for example, limitations to the temperature region close to the critical temperature T_c, or to the time scales, which are much larger than the typical changes of the order parameter

Since a detection of Higgs mode oscillations in a superconductor is essential for studying properties of the superconducting gap (see section 1.1), in this thesis we wish to give a comprehensive investigation of the possibility for a direct excitation of this and other collective modes in different types of superconducting systems. For this purpose we use density matrix formalism, which represents a very powerful tool not only for analytical studies of the superconductors under the close to equilibrium conditions, but also can be easily implemented and extended for nonequilibrium numerical calculations.

1.2.2. Optical control of matter

A solid state system driven far away from equilibrium may reveal some other interesting phenomena, like transient phase transitions. Indeed, a controlled switching between different phases of matter on the ultrafast timescale can be achieved by an intense pumping of the solid state system with ultrashort laser pulses [67, 68]. In the last years this type of nonequilbrium experiments has built a new research frontier of modern solid state physics and can be therefore allocated in the second category. Beginning with the investigations of the insulator to metal [68–73] or insulator to charge density wave (CDW) state transitions [74–76], as results of photodoping, where the system is driven into highly excited states and the effects of correlations may, however, get lost, the novel studies turned to the experiments with phase control by coherent manipulation of particular phonon mode [67, 77–80]. The latter type of measurements with the selective vibrational excitation enables to get a direct access into the dynamics of the electronic ground state of the system. This has become possible due to the development of pulsed technique to terahertz (THz) regime with lower photon energy compared to photodoping and even opened perspectives for controlled transient superconducting transitions, which attracted a high interest from both theoretical [81–87] and experimental [78, 80, 88–92] point of view. Since the possibility to induce superconductivity is of particular interest for this work, the progress in this field will be discussed in some details below.

Over already 100 years the condensed matter physicists try to find a root to enhance the critical temperature T_c of a superconductor and bring it closer to the room temperature mark. Therefore, in the pioneering optical control experiments on superconductors the preference was given to the high temperature cuprate compounds $La_{1.8-x}Eu_{0.2}Sr_xCuO_4$ (LESCO) [78, 93] and $YBa_2Cu_3O_{6+\delta}$ (YBCO) [80, 88], since they already have a quite high T_c. In both cases the intense light pulse at THz frequency has been tuned to a selected vibrational mode of the solid state system. In this way one was able to manipulate the position of the oxygen octahedra and consequently the electronic properties of the materials. In case of the LESCO compound [78] the measurements were done at $x = 1/8$, where the superconductivity is almost suppressed due to the emergence of competing spin and charge order (static stripe state) in the copper–oxygen plans. In contrast, in the $La_{2-x}Sr_xCuO_4$ (LSCO) compound without europium (Eu) the "striped order" is not so pronounced and its T_c is much higher (see Fig. 1.3 (a)). A measurement of reflectivity for $LESCO_{1/8}$ above its critical temperature after pumping at time delay $\tau = 5$ps showed appearance of a plasma edge at 60cm^{-1} (see Fig. 1.3 (b)). Since this effect reminiscent of

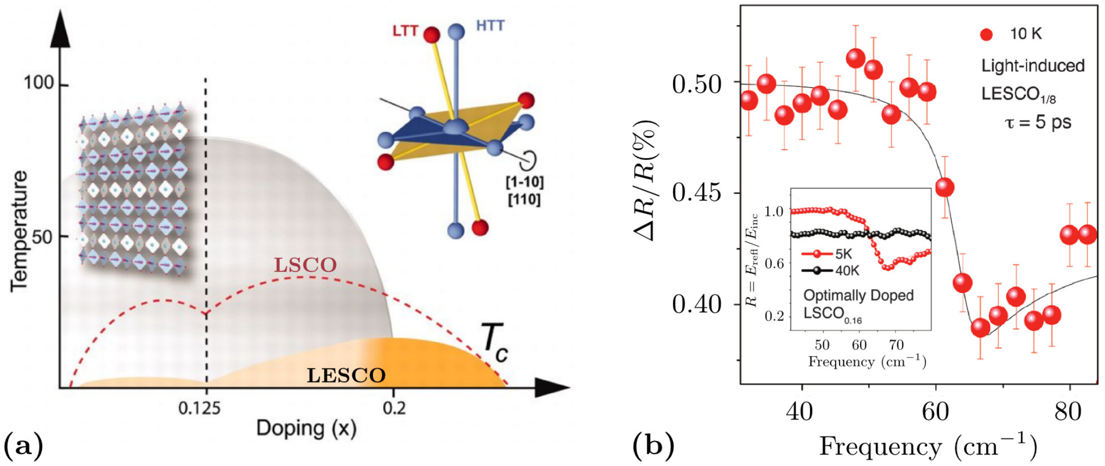

Figure 1.3: Light–induced superconductivity, as a result of melting the competing order. (a) Schematic phase diagram for $La_{1.8-x}Eu_{0.2}Sr_xCuO_4$ (LESCO) in equilibrium with the superconducting dome (yellow region). At the investigated 1/8 doping a striped order of charges and spins appears in copper–oxygen planes (left inset), which is associated with a low temperature tetragonal (LTT) distortion of the oxygen octahedrals (right inset), and results in suppression of superconductivity. For comparison, the superconducting dome for $La_{2-x}Sr_xCuO_4$ (LSCO) with less pronounced LTT structural modulation is shown by the red dashed curve. (b) Measurement of the normalized reflectivity for $\text{LESCO}_{1/8}$ above T_c after optical excitation with time delay $\tau = 5$ps. The plasma edge at 60 cm^{-1} indicates a superconducting transition. For comparison, results of the equilibrium measurements for LSCO above and below T_c are shown in the inset. Figures are adapted from Ref. [78].

Josephson plasma resonance can be seen at the same frequency as in optically measured LSCO below T_c in equilibrium (see inset in Fig. 1.3 (b)), this property reflects a possible fingerprint of the superconducting state [6]. Hence, one may conclude that an optical pump pulse induces a melting of the competing "striped order" in $\text{LESCO}_{1/8}$, which recovers on a larger timescale than superconducting correlation and, as a result a "regeneration" of the superconductivity can be observed. Similar behavior was also found in recent optical experiments with stripe ordered $La_{2-x}Ba_xCuO_4$ [91, 94].

In case of the bilayered YBCO compound with the conducting CuO_2 planes the effects of competing order may not be crucial in nonequilibrium since its superconducting dome in equilibrium is quite robust. However, the optical experiments with YBCO at different doping and different temperatures above T_c showed enhanced coherent transport along the axis perpendicular to the copper–oxygen plane [80, 88]. Hereby, the optical pump pulse was tuned to address the c–axis infrared–active (B_{1u}) mode, which basically modulates the displacement of the apical oxygen along the c–axis (see Fig. 1.4(a)). The measurements of transient c–axis optical properties of YBCO reveal, at all measured temperatures, a plasma

---

[6] Moreover, an additional measurement of optical conductivity reported in Ref. [93] indicates a transient superconducting state as well.

edge in reflectivity spectra and an approximate $1/\omega$ divergence at low frequencies ω in the imaginary part of optical conductivity (see Fig. 1.4(b)), indicating coherent transport along the c–axis. These results opened plenty of discussions about the nature of this transient phenomenon and whether or not one deals in this case with the possibly induced superconductivity [95,96]. A possible interpretation was given in Refs. [81,89,90] by using an *ab initio* density function theory calculation. It was found that a nonlinear coupling of the laser pulse to an infrared–active phonon mode in the YBCO compound causes displacement of the apical oxygen along the c–axis and induces simultaneously changes in the electronic structure. As a result a transient increase of the interlayer superconducting coupling was proposed. Also a phenomenological study of the electron–phonon coupling in nonequilibrium supports this idea [84]. Some alternative theories propose suppression of phase fluctuations [82, 83], as well as melting of the competing charge density wave order [85,86], which may give an additional contribution to the enhanced superconductivity.

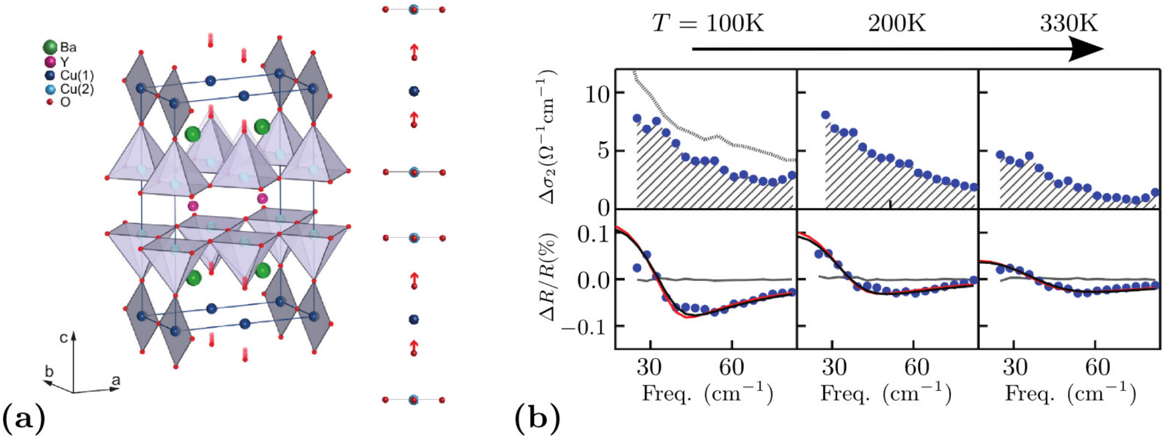

Figure 1.4: Light–induced coherent transport along the c–axis in $YBa_2Cu_3O_{6+\delta}$ (YBCO). (a) Schematic illustration of the structural modulations in a bilayered YBCO compound caused by optical pump pulse. Light pulse addresses the infrared–active B_1u mode which modulates the displacement of apical oxygen along the c–axis. (b) Changes in imaginary part of the optical conductivity (upper panels) and in reflectivity (lower panels) were measured at different temperatures T above T_c after optical excitation with time delay $\Delta t = 0.8$ps are shown with blue dots. Equilibrium measurements below T_c are indicated by gray dots. Figures are adapted from Ref. [92].

To summarize experimental results with cuprates one may say that the controlled phase transition into a superconducting–like state can be achieved in these layered materials by the resonant phonon excitation. However, the reasonable question would be whether the underlying physics is special in this case. In this thesis we wish to give a proof–of–principles and investigate the possibility to induce singlet superconducting correlations in nonequilibrium. For this purpose we analyze a one dimensional Hubbard model by using a time–dependent exact diagonalization technique based on the *Lanczos algorithm*. This method represents a very powerful tool in the cases when one needs to obtain properties of the ground state and some low–energy states of a system very fast and reliably. Furthermore, application of the Lanczos algorithm at every moment in time enables to exactly follow the changes induced in a solid state system by an external perturbation. It should be noted that a similar question was also addressed recently from the experimental point of view [92]. The results of experimental investigations of a conventional s–wave superconductor K_3C_{60} in nonequlibrium will be discussed in chapter 4 and compared qualitatively with our numerically simulated data.

1.3. Thesis overview

This thesis deals with two different time–resolved studies of a superconducting system in nonequilibrium, and is organized as follows:

In **Part I** the possibility to induce singlet superconducting correlations in the one dimensional extended Hubbard model (EHM) far from equilibrium is investigated. We start in Chap. 2 by discussing equilibrium properties of an electron system on a lattice described by EHM. In particular, we introduce several correlation functions to identify different phases in the model. Further, in Chap. 3, we generalize the extended Hubbard model to a nonequilibrium case and consider two possible nonequilibrium scenarios: (i) interaction quench and (ii) quench by pulse. For studying the temporal evolution of the electron system the time–dependent Lanzcos method is introduced. Additionally, we consider optical response of a solid state system in a linear response approximation and in the pump–probe experiment. Finally, in Chap. 4, the results of the time–dependent calculations after the interaction quench and quench by pulse for an electron system on a lattice of 10 sites are presented and discussed.

Part II is devoted to the collective modes in a superconductor out of equilibrium. First, in Chap. 5, we introduce two different classes of the multiband superconducting systems: ordinary two–band superconductors with s–wave pairing and noncentrosymmetric superconductors. Then, in Chap. 6, we formulate (Nambu-) matrix kinetic theory in the clean limit at zero temperature. Employing this approach we investigate analytically, within the linear response approximation, the collective modes in noncentrosymmetric superconductors, which are associated with phase fluctuations of the order parameter. In addition, we derive an expression for the gauge and Leggett mode in these materials. Chap. 7 deals with the extension of the density matrix theory to the nonequilibrium case. Here, a semi–numerical method is formulated in application to the two–band superconductors with the singlet pairing correlations. Finally, in Chap. 8, we present the results of our study of the collective excitations in MgB_2–like superconductors in nonequilibrium.

Part I

Optical control and induced superconductivity

Chapter 2

Extended Hubbard model in equilibrium

The physical properties of a solid state system are determined by the underlying interactions between its different degrees of freedom. In fact, strong Coulomb repulsion between electrons on a lattice may lead to a Mott isolator state with a spin–density wave (SDW) order. On the other hand, an additional attractive interaction mediated, e.g. by phonons in conventional BCS systems, results under certain circumstances in the occurrence of the superconducting correlations. Thus, the interplay between the dominant interactions in a system gives rise to a variety of the distinct stable phases. In turn, a possibility to control the strength of interactions and, consequently, the properties of a material is an important and challenging task in the solid state physics. A promising technique to realize such controlled phase transitions is the pump–probe method, where one uses a pump pulse excitation of high intensity in order to drive the system out of equilibrium [67, 71]. This way an energy landscape of the system can be changed and a crossover to a new phase might appear. With a development of pulsed technique to terahertz regime, where photon energy is almost of the order of the superconducting gap, controlled transient transitions into a superconducting state became possible [78, 80, 88–92]. As discussed in introduction this phenomenon was observed mostly in layered cuprate materials.

A good opportunity for studying controlled phase transitions from both experimental and theoretical point of view represents a one dimensional (1D) solid state system, where the strong correlations between its different degrees of freedom play an important role. Therefore, in this part of thesis we investigate the properties of the 1D strongly correlated electron system driven out of equilibrium by a strong pump excitation. We simulate the solid state system by using the extended Hubbard model and study its temporal evolution within the time–dependent Lanczos algorithm. Hereby, we consider two different nonequilibrium scenarios arised by (i) an interaction quench and by (ii) including a laser pulse into the Hamiltonian. Particular emphasis is on the possibility to induce singlet superconducting correlations in the extended Hubbard model.

2.1. The Extended Fermionic Hubbard model

Let us start with a discussion of a 1D electron system in equilibrium. The simplest "toy"–model to describe the interacting electrons on a lattice represents the extended Hubbard model (EHM) [97–99], which in one dimension given by the Hamiltonian:

$$\hat{H}_{\text{EHM}} = \underbrace{-t_h \sum_{\langle i,j\rangle\sigma} \left(\hat{c}^{\dagger}_{i,\sigma}\hat{c}_{j,\sigma} + \text{H.c.}\right)}_{\text{kinetic term ("hopping")}} + \underbrace{U\sum_{i} \hat{n}_{i\uparrow}\hat{n}_{i\downarrow}}_{\substack{\text{"on-site"}\\ \text{interaction}}} + \underbrace{V\sum_{\langle i,j\rangle} \hat{n}_i\hat{n}_j}_{\substack{\text{nearest neighbor}\\ \text{interaction}}} \tag{2.1}$$

with t_h being the nearest neighbor hopping constant, and U and V describing the strength of the on–site and nearest neighbor interaction, respectively. The operator $\hat{c}^{\dagger}_{i,\sigma}$ (or $\hat{c}_{i,\sigma}$) creates (or annihilates) one electron with spin $\sigma =\uparrow,\downarrow$ at a site i. Further, the occupation number operator is given by $\hat{n}_i = \hat{n}_{i\uparrow} + \hat{n}_{i\downarrow}$ with $\hat{n}_{i\sigma} = \hat{c}^{\dagger}_{i,\sigma}\hat{c}_{i,\sigma}$.

For our studies we consider the model with a half–filling at zero temperature, which is well–known in the literature [98–101] and can even be solved analytically for some parameter regions. Thus, a comparison of the results with previous equilibrium studies is possible. Despite its simplicity, EHM reveals several different phases due to the strong quantum fluctuations. Roughly speaking, a variation of the parameters U, V and t_h leads to various types of correlations, which dominates the ground state of the system. This give rise to different distributions of the electrons on a lattice. The results of previous theoretical studies [98–101] can be summarized in a diagram form presented in Fig. 2.1. Here, one observes for repulsive nearest neighbor interaction $V > 0$ appearance of the spin- (SDW) and charge–density–wave (CDW) phases, which are separated by the phase transition boundary at $U = 2V$. In case of the CDW phase the electrons build pairs on the

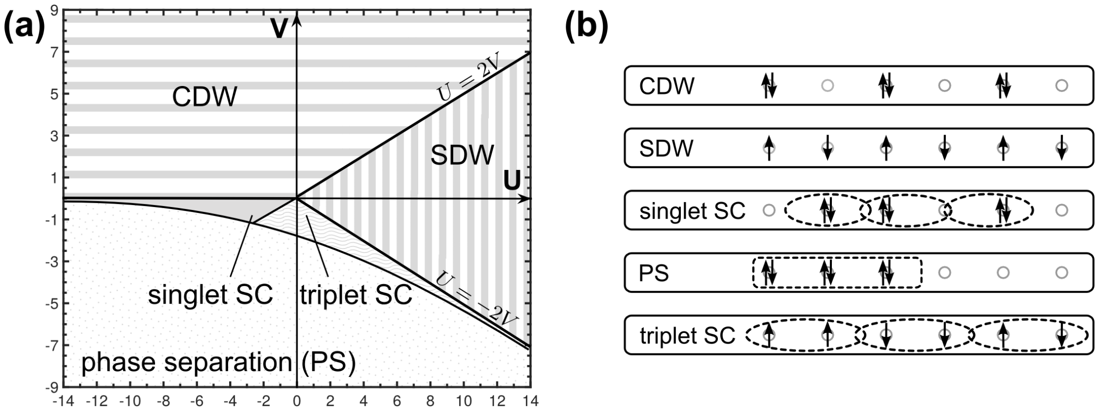

Figure 2.1: (a) Illustration of the equilibrium phase diagram (T=0) for the 1D extended Hubbard model at half filling with U and V being the strength of the on–site and nearest neighbor interaction from Eq. (2.1), respectively. Different phases are indicated on the diagram by different shaded regions. (b) Schematic representation of the phases from (a) showing a spatial distribution of the electrons on a 1D lattice.

lattice with an alternating order of double occupied and empty sites (see Fig. 2.1(b)). On the other hand, an alternating order of the unpaired electrons with different spin directions dominates in the SDW region. Besides the already mentioned phases, in case of $V < 0$ (attractive) the states with the dominant superconducting correlations (singlet and triplet) can be found in the proximity to a phase separation (PS) area, where the electron pairs build a cluster on one end of the lattice (see Fig. 2.1(b)). The superconducting singlet and triplet phases are characterized by paired electrons on a site and between neighbored sites, respectively. These pairs are homogeneously distributed over the lattice.

2.2. Exact diagonalization technique

An established method for obtaining relevant physical properties [1] of a finite–size system with strongly correlated electrons represents the *Lanczos based* exact diagonalization (ED) method [102, 103]. This numerical technique is generally used for diagonalizing sparse matrices and requires only the storage of the non–zero matrix elements in the computer memory. Therefore, ED algorithm provides results fast and reliable. In following we discuss some important principles of the method in application to EHM. In particular, it will be used in section 2.3 to reproduce a part of the phase diagram in Fig. 2.1.

2.2.1. Basis set for the Hubbard Hamiltonian

Let us start with the construction of a Hamiltonian matrix for the Hubbard model defined in Eq. (2.1) with a given interaction U, V and hopping t_h parameters. This matrix can be built from the orthonormal basis vectors, where each vector in the basis represents a unique configuration of the electrons on the lattice. For the N–sites model it is convenient to define the basis elements in the following way:

$$|i\rangle = \prod_{m=1}^{N_{e\uparrow}} \hat{c}^{\dagger}_{m\uparrow} \prod_{n=1}^{N_{e\downarrow}} \hat{c}^{\dagger}_{n\downarrow} \, |VS\rangle \tag{2.2}$$

with $N_{e\uparrow}$ and $N_{e\downarrow}$ being the number of up and down electrons, respectively. $|VS\rangle$ represents the vacuum state. Here, we separate electrons in groups according to their spin direction and sort them afterwards by the lattice index. The positive effect of this ordering is that there are no additional phase factors, which otherwise can appear due to the next neighbor hopping. Another advantage is that the Hilbert subspaces for up and down electrons can be considered separately. This simplifies the computation of numerical problem enormously.

Now, in order to translate the basis vectors introduced in Eq. (2.2) into the computer language we use the bit patterns. In this case, each electron on a lattice site corresponds to "1" and its absence is "0". For illustration we present in Table 2.1 the basis vectors for 2–site Hubbard model with one up–spin and one down–spin electrons. Hence, the electron system introduced in Eq. (2.1) is now modeled by the bit operations.

---

[1] for example, ground state energy, correlation or response functions

no.	basis vector	configuration	bit pattern
$\mid 0\rangle$	$\hat{c}^\dagger_{1\uparrow}\hat{c}^\dagger_{1\downarrow}\,\lvert VS\rangle$	$(0,\uparrow)\times(0,\downarrow)$	01×01
$\mid 1\rangle$	$\hat{c}^\dagger_{1\uparrow}\hat{c}^\dagger_{2\downarrow}\,\lvert VS\rangle$	$(0,\uparrow)\times(\downarrow,0)$	01×10
$\mid 2\rangle$	$\hat{c}^\dagger_{2\uparrow}\hat{c}^\dagger_{1\downarrow}\,\lvert VS\rangle$	$(\uparrow,0)\times(0,\downarrow)$	10×01
$\mid 3\rangle$	$\hat{c}^\dagger_{2\uparrow}\hat{c}^\dagger_{2\downarrow}\,\lvert VS\rangle$	$(\uparrow,0)\times(\downarrow,0)$	10×10

Table 2.1: Basis vectors for 2–site lattice with one up–spin and one down–spin electron. For simplicity, the electron position on the lattice together with the corresponding bit pattern is presented separately in the Hilbert subspace of each electron.

2.2.2. Lanczos algorithm

For obtaining the ground state of the strongly correlated electron system we apply Lanczos algorithm [102] and diagonalize the previously computed Hubbard Hamilton matrix $\hat{H}_{\mathrm{EHM}}$. The basic idea of this numerical method consists in the recursive construction of a real symmetric tridiagonal matrix T from the (hermitian) matrix $\hat{H}$ of the size $N\times N$. Hereby, one performs the unitary transformation by using the matrix U of the following form:

$$U = (\lvert u_1\rangle\,,\lvert u_2\rangle\ldots\lvert u_N\rangle)$$

Here, $\lvert u_i\rangle\,,\ i=1\ldots N$ denotes orthonormal vectors with N components, so that

$$U^\dagger\hat{H}U = T\ ,\quad U^\dagger U = I\ . \tag{2.3}$$

In this case, the matrix T should take the form:

$$T = \begin{pmatrix} a_1 & b_2 & & \cdots & 0 \\ b_2 & a_2 & b_3 & & \vdots \\ & \ddots & \ddots & \ddots & \\ \vdots & & & a_{N-1} & b_N \\ 0 & \cdots & & b_N & a_N \end{pmatrix}$$

The elements of this matrix can be calculated from Eq. (2.3) and obey the following recursive relations:

$$\begin{cases} \hat{H}\,\lvert u_1\rangle &= a_1\,\lvert u_1\rangle + b_2\,\lvert u_2\rangle \\ \hat{H}\,\lvert u_i\rangle &= b_i\,\lvert u_{i-1}\rangle + a_i\,\lvert u_i\rangle + b_{i+1}\,\lvert u_{i+1}\rangle\,, \quad \text{if } 2\le i\le N-1 \\ \hat{H}\,\lvert u_N\rangle &= b_N\,\lvert u_{N-1}\rangle + a_N\,\lvert u_N\rangle \end{cases} \tag{2.4}$$

In practice, one does not need to calculate all matrix elements of T in order to obtain the ground state together with some low–energy states of the strongly correlated electron system. A good convergence can be realized already for the matrix size $M \times M$ with $M < N$.

A numerical implementation of this Lanczos algorithm is quite straightforward and consists of the following steps: First, we construct a normalized initial vector

$$|u_1\rangle = \sum_{i=1}^{N} \alpha_i \, |i\rangle \tag{2.5}$$

with the randomly chosen coefficients α_i. It should be noted that the results of the matrix diagonalization do not depend on the exact form of this vector. Then, by applying the Hamilton matrix on the initial vector we can define a new one $|v_1\rangle \equiv \hat{H}\,|u_1\rangle$. Its scalar product with $|u_1\rangle$ leads to the first element of the matrix T:

$$\langle u_1 \, |v_1\rangle = \langle u_1| \, \hat{H} \, |u_1\rangle = a_1$$

Further, we repeat this procedure $M-1$ times and calculate the remaining contributions to the tridiagonal matrix:

$$\begin{cases} |\omega_i\rangle & \equiv \quad |v_i\rangle - a_i\,|u_i\rangle \\ b_{i+1} & = \quad \sqrt{\langle \omega_i \, |\omega_i\rangle} \\ |u_{i+1}\rangle & = \quad |\omega_i\rangle / b_{i+1} \\ |v_i\rangle & = \quad \hat{H}\,|u_{i+1}\rangle - b_{i+1}\,|u_i\rangle \\ a_{i+1} & = \quad \langle u_i \, |v_i\rangle \end{cases}$$

The tridiagonal matrix T is subsequently diagonalized by using the standard numerical routines from the MKL package [2]. Thus, the resulting eigenvalues represent the approximate eigenvalues $\tilde{\mathrm{E}}_i$ with $i = 0 \dots M-1$ of the hermitian matrix $\hat{H}$. The ground state energy and a few excited states (and also upper part of the spectrum) converge rapidly to the exact eigenvalues of the Hamiltonian $\hat{H}$. For our numerical calculations $M = 40$ iterations give us sufficiently good results.

Finally, by knowing the eigenvector $|x_0\rangle$ and corresponding eigenvalue $\tilde{\mathrm{E}}_0$ of the lowest state of the matrix T, one can construct the ground state wave vector in the following way:

$$|GS\rangle = \sum_{i=1}^{M} [\,|x_0\rangle]_i \, |u_i\rangle \tag{2.6}$$

with $[\,|x_0\rangle]_i$ being the i-th component of the vector $|x_0\rangle$.

---

[2] Math Kernel Library

2.3. Phases identification

Based on the knowledge of the ground state vector $\mid GS\rangle$, we can calculate the relevant physical quantities of a strongly correlated electron system. Thus, we consider the correlation functions in order to characterize its different phases. Unless specifically mentioned, these functions are calculated for a 10–sites lattice model with periodic boundary conditions. The energy is measured in units of hopping constant t_h. In following we discuss the behavior of the several correlation functions, which we will use for the identification of the important for this thesis CDW, SDW, and singlet superconducting phases.

2.3.1. Density–density correlation function

The signatures of the charge density wave phase can be captured by the density–density correlation function, which for each lattice distance j reads:

$$C(j) \equiv \frac{1}{L}\sum_{l=0}^{L-1} \langle GS|\hat{n}_{l+j}\hat{n}_l|GS\rangle = \frac{1}{L}\sum_{l=0}^{L-1} \langle GS|\left(\hat{n}_{l+j\uparrow}+\hat{n}_{l+j\downarrow}\right)\left(\hat{n}_{l\uparrow}+\hat{n}_{l\downarrow}\right)|GS\rangle \tag{2.7}$$

with L being the size of the one dimensional lattice. Indeed, depending on the electron configuration of a strongly correlated system this function reveals different behavior. For illustration we calculate $C(j)$ for several parameter values U, V of the lattice model, which according to section 2.1 should correspond to CDW, SDW, and singlet superconducting phases. As can be seen from the results shown in Fig. 2.2, only for the CDW phase we observe characteristic "zigzag" structure, which indicates alternating order of the electron

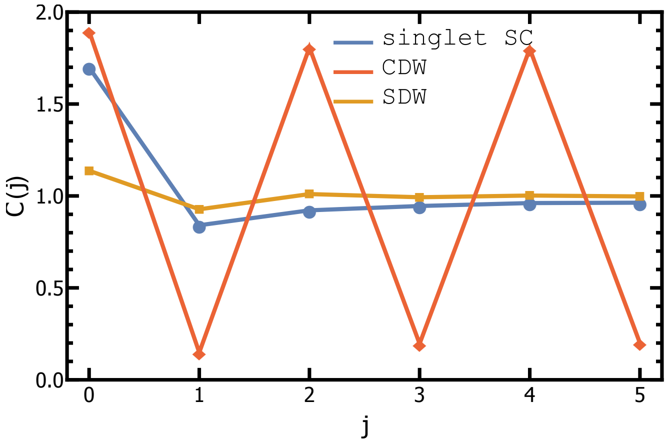

Figure 2.2: Density–density correlation function versus lattice distance j calculated for various phases of the extended Hubbard model. The calculations are done exemplary in the ground state of singlet superconducting phase with the interaction parameters $U = -3,\ V = -0.5$ (blue solid line), CDW with $U = 10,\ V = 5.5$ (red solid line), and SDW with $U = 10,\ V = 4.5$ (yellow solid line).

density with mostly double occupied and empty sites. In contrast, the correlation function $C(j)$ in the SDW and singlet superconducting phases shows for $j > 0$ an approximately constant behavior. In addition, we find that the self–correlations at $j = 0$ are stronger in the superconducting phase than in SDW due to existing electron pairs.

2.3.2. On–site correlation function

To characterize the states of the strongly correlated system with the dominant singlet superconducting correlations, we introduce an on–site correlation function $P_1(j)$ of the following form:

$$P_1(j) = \frac{1}{L}\sum_{l=0}^{L-1}\left\langle GS\left|\hat{c}^{\dagger}_{l+j\downarrow}\hat{c}^{\dagger}_{l+j\uparrow}\hat{c}_{l\uparrow}\hat{c}_{l\downarrow}\right|GS\right\rangle \tag{2.8}$$

with j being the lattice distance. This function gives an information about the on–site pairing correlations between electron pairs on lattice. Moreover, the self–correlation with $j = 0$ represents the double occupation function for a single lattice site. In order to illustrate the behavior of the on–site correlation function we calculate it for the same parameter values of the lattice model, as discussed in section 2.3.1. The results are presented in Fig. 2.3.

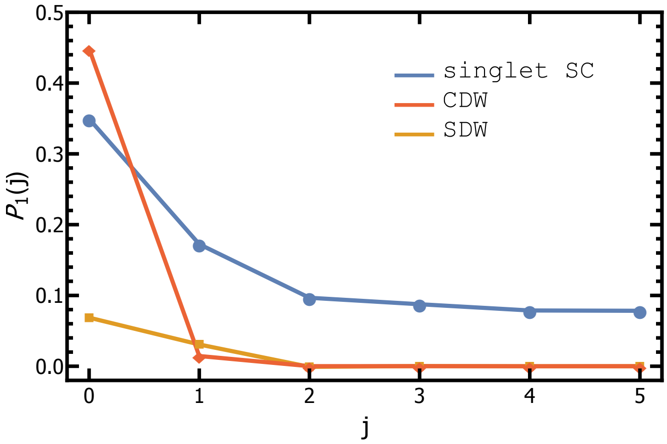

Figure 2.3: On–site correlation function versus lattice distance j calculated for various phases of the extended Hubbard model. The calculations are done with the same parameter values as discussed in connection with Fig. 2.2.

In our simulations we observe that the on–site correlation function $P_1(j)$ takes the finite values for each lattice distance j only in the singlet superconducting state. This indicates appearance of the superconducting correlations. Moreover, the on–site correlation function shows in this case slow algebraic decay with the lattice distance j. Physically this means that the electron pairs are homogeneously distributed over the one–dimensional lattice. It should be noted that since in a CDW state the number of electron pairs can be the same as in a singlet SC state, the double occupancy $P_1(0)$ show in this case for both phases similar result. Thus, $P_1(0)$ only is not enough to distinguish between CDW and SC phases.

2.3.3. Maxwell construction

It is well–known [101,104] that in the region with negative U and V the superconductivity exist in the proximity to a phase separation area (see Fig. 2.1 (a))). A phase separation state is also characterized by paired electrons, which occupy, however, only one part of the lattice (build a cluster, which is schematically shown in Fig. 2.1 (b)) and leave the other part unoccupied. This structure is also reflected in the behavior of the on–site correlation function $P_1(j)$. For demonstration we show in Fig. 2.4 the result of calculation of $P_1(j)$, where we choose following values for the interaction parameters of the system: $U = -3$ and $V = -1$. As one can see, the on–site correlation function show first strong decrease with increasing lattice distance j indicating absence of the superconducting correlation and then after $j = 3$ (corresponds to a midpoint of the lattice) it increases again. In other words, the superconducting correlations are observed only on one half of the lattice.

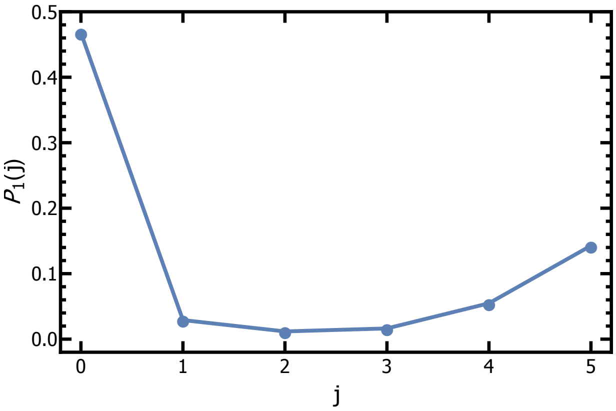

Figure 2.4: On–site correlation function versus lattice distance j calculated for the extended Hubbard model of 10 sites and parameters $U = -3, V = -1$.

Since in this thesis we are interested in the "pure" singlet superconducting correlations, we need to distinguish between a phase separation and a singlet superconducting state. In this sense we should precisely determine a phase boundary between both phases. For this purpose we use in addition to calculations of $P_1(j)$ the so–called Maxwell construction method [104]. This method implies the calculations of the ground state energy per site as a function of the electron density. By fixing the values of U and changing the values of V we are able to scan the phase diagram in the broad parameter region. The result of calculations for a 14 sites lattice [3] are shown in Figs. 2.5 (a) and (b), where we variate V and fix on–site interaction parameter values at $U = -4$ and $U = -2$, respectively. As one can see in the figures, the behavior of energy as function of electron density n changes from the convex to concave by crossing the phase separation boundary. This can be explained as follows: In the phase separated region, where one has a phase with low electron density on one part of the lattice and a phase with high electron density on the other, the energy

---

[3] here we choose 14 instead of 10–site model in order to obtain the transition boundary more precisely.

function should exhibit a linear behavior in the thermodynamic limit, i.e. an additional adding of an electron pair changes only the size of these two phases. Hence, the boundary between phase separation area and superconducting phase can be exactly obtained.

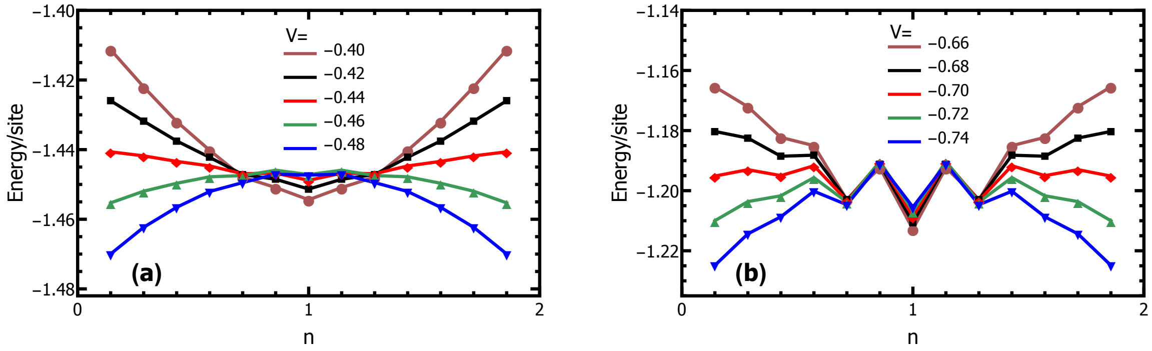

Figure 2.5: Maxwell constructions. Energy per lattice site as a function of electron density n calculated for the extended Hubbard model with fixed (a) $U = -4$ and (b) $U = -2$. The calculations at different parameter values V are give by color code. Here, we choose a lattice with 14 sites.

Now, in Fig. 2.6 we plot the results of Maxwell constructions for a wide parameter region with attractive $U < 0$ and $V < 0$. Here, the phase boundary between phase separation area and superconducting phase is shown by purple dashed line. In addition, we perform calculations of $P_1(j)$ according to section 2.3.2 for different combinations of U and V. The states with pronounced singlet superconducting correlations we indicate in Fig. 2.6 by blue

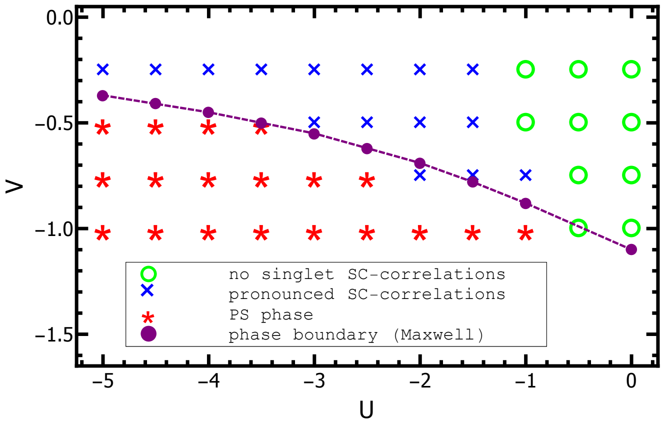

Figure 2.6: Phase diagram for negative U and V. From results of calculation of $P_1(j)$ function we identify phases with pronounced singlet superconducting (SC) correlations (shown with blue "x") and phase separation (PS) states (shown with red "*"). The results, where $P_1(j)$ drops to zero, are shown with green open circles. The phase boundary between superconducting phase and phase separation region is obtained from Maxwell constructions and indicated in the figure by the dashed purple line.

"x". The cases, where $P_1(j)$ drops to zero, we mark in this phase diagram by green open circles. Finally, the states with phase separation behavior are shown in Fig. 2.6 by red "*". It is important to note that the qualitative comparison of our numerically obtained results with the predictions from previous theoretical studies (which are schematically shown in Fig. 2.1) reveals a very good agreement.

Chapter 3

Generalization of the extended Hubbard model to nonequilibrium

Strong perturbation of an electron system on the ultrafast time scale may lead to the transient phase transitions. This can be realized in a special type of the time–resolved experiments, so–called optical control: By using an intense pump pulse the system is driven far away from equilibrium, where a crossover to a new phase may occur. This nonequilibrium state is then studied by applying a probe pulse with tunable time delay.

In this chapter we present a method for numerical simulation the nonequlibrium dynamics in an extended Hubbard model with strongly correlated electrons. The first part is devoted to a generalization of the Hamiltonian from section 2.1 to the case with the time–dependence. In particular, we focus on two types of the pump excitation in the model: interaction quench and quench by pulse. The second part deals with the computation of nonequlibrium correlation and response functions. Particular emphasis is on the time–dependent optical conductivity calculated after probing excitation. All functions will be used for analysis of the numerical data in Chap. 4.

3.1. Non–Equilibrium scenarios for EHM

Starting from the ground state of the equilibrium extended Hubbard Hamiltonian $\hat{H}_{\text{EHM}}$, which properties we have discussed in the previous chapter, we then perform a perturbation of the system at some moment in time $t = t_0$ by the pump excitation and drive it out of equilibrium in two different ways: (i) by interaction quench and (ii) by pulse quench. Hence, the corresponding nonequilibrium Hamiltonian $\hat{H}(t)$ is time dependent and takes the following form:

$$\hat{H}(t) = \hat{H}_{\text{EHM}} + \Theta(t - t_0)\hat{H}'(t) \tag{3.1}$$

with $\hat{H}'$ being the perturbation term, which describes the interaction between the pump excitation and the electrons in the system.

3.1.1. Interaction quench

Let us first discuss the case of interaction quench, where one deals with a quite simple and popular type [105] of a quantum quench protocol: One abruptly changes the interaction parameters of the extended Hubbard Hamiltonian in Eq. (2.1) at a fix moment in time, i.e.

$$U_{\text{quench}}(t) = \begin{cases} U & \text{for } t \leq t_0 \\ U' & \text{for } t > t_0 \end{cases} \quad \text{and/or} \quad V_{\text{quench}}(t) = \begin{cases} V & \text{for } t \leq t_0 \\ V' & \text{for } t > t_0 \end{cases} \tag{3.2}$$

Thus, the perturbation term in Eq. (3.1) takes in this case the following form:

$$\hat{H}' = (U' - U) \sum_i \hat{n}_{i\uparrow}\hat{n}_{i\downarrow} + (V' - V) \sum_{\langle i,j \rangle} \hat{n}_i \hat{n}_j \tag{3.3}$$

All in all, the strongly correlated electron system evolves for $t > 0$ under perturbed Hamiltonian $\hat{H}(t)$ with the changed interaction part. That way the system is driven out far from equilibrium. This type of quenching was recently realized in experiments on 1D organic molecules [67].

3.1.2. Pulse quench by means of Peierls substitution

Another situation can be realized by considering excitation of an electron system with a strong pump pulse. Here, we describe the pump pulse by a spatially uniform, but time–dependent vector potential $A(t)$ of the following form:

$$A(t) = A_0 e^{-t^2/2\tau^2} \cos(\omega_{\text{pump}} t) \tag{3.4}$$

where A_0 is the amplitude of the field, which takes its maximum value at $t = 0$, ω_{pump} gives the frequency of the pulse, and τ denotes the full width at half maximum ($FWHM$) of the pulse. The vector potential $A(t)$ is considered in a temporal or Wayl gauge, where

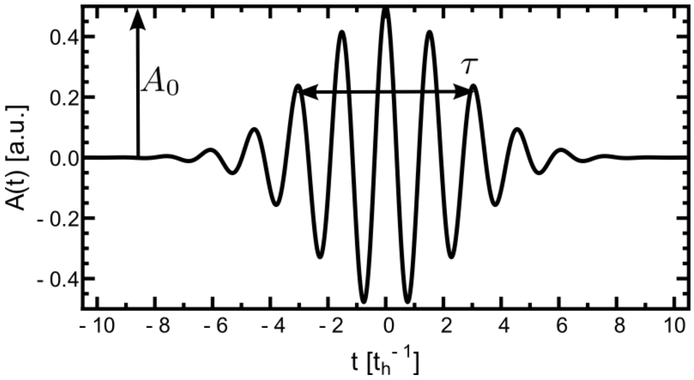

Figure 3.1: Illustration of a single pump pulse. The corresponding vector potential $A(t)$ has parameters: $A_0 = 0.5$, $\tau = 2.5$, and $\omega_{\text{pump}} = 4.1$

the scalar potential $\Phi(t)$ is chosen to be zero. For illustration we show in Fig. 3.1 the form of $A(t)$ for arbitrary parameter values. It should also be mentioned, that due to the finite broadening τ the pulse shows a Gaussian–like shape.

Now, to include pump pulse into the extended Hubbard model, we use an attempt based on the Peierls substitution. In this case the light field is incorporated into the kinetic part of the Hamiltonian (2.1) and the hopping constant gets the so–called Peierls phase, i.e.

$$t_{h,\text{pulse}}(t) = \begin{cases} t_h & \text{for } t \leq t_0 \\ t_h e^{iA(t)} & \text{for } t > t_0 \end{cases} \tag{3.5}$$

Hence, the perturbation part in Eq. (3.1) reads:

$$\hat{H}'(t) = -(t_h e^{iA(t)} - t_h) \sum_{\langle i,j\rangle,\sigma} \left(\hat{c}^{\dagger}_{i,\sigma} \hat{c}_{j,\sigma} + H.c. \right) \tag{3.6}$$

3.2. Time–dependent exact diagonalization

Generally speaking, the temporal evolution of the interacting electron system can be described by the Schrödinger equation:

$$i\frac{\partial}{\partial t} \left|\psi(t)\right\rangle = \hat{H}(t) \left|\psi(t)\right\rangle \tag{3.7}$$

with the time–dependent Hamiltonian $\hat{H}(t)$ defined in the previous section. In order to solve this equation we apply the time–dependent exact diagonalization. This technique is based on the idea of the stepwise approximation of the wave function $|\psi(t)\rangle$ by using Lanczos algorithm (shown in section 2.2.2) in time intervals δt. At each time step $t + \delta t$ the Lanczos method generates a tridiagonal matrix with the eigenvectors $|\phi_l\rangle$ and corresponding eigenvalues ϵ_l. These results are subsequently used for the approximation of the time–dependent wave function, which finally takes the following form:

$$\left|\psi(t + \delta t)\right\rangle \approx e^{-i\hat{H}(t)\delta t} \left|\psi(t)\right\rangle \approx \sum_{l=1}^{M} e^{-i\epsilon_l \delta t} \left|\phi_l\right\rangle \left\langle \phi_l \mid \psi(t)\right\rangle \tag{3.8}$$

A general structure of this algorithm is shown in Fig. 3.2. Thus, by knowing the wave function at each time step we can calculate the temporal evolution of both correlation and response functions. The most promising sensitive probes for studying nonequilibrium dynamics in the strong interacting electron systems are momentum distribution function together with its jump at the Fermi surface, time–dependent correlation function, and optical conductivity. For all our numerical calculations we employ periodic boundary conditions and use $M = 40$ iterations for the Lanczos method. The time interval is set to $\delta t = 0.01$. Further, we set the hopping constant $t_h = 1$ and measure energy and time in units t_h and t_h^{-1}, respectively.

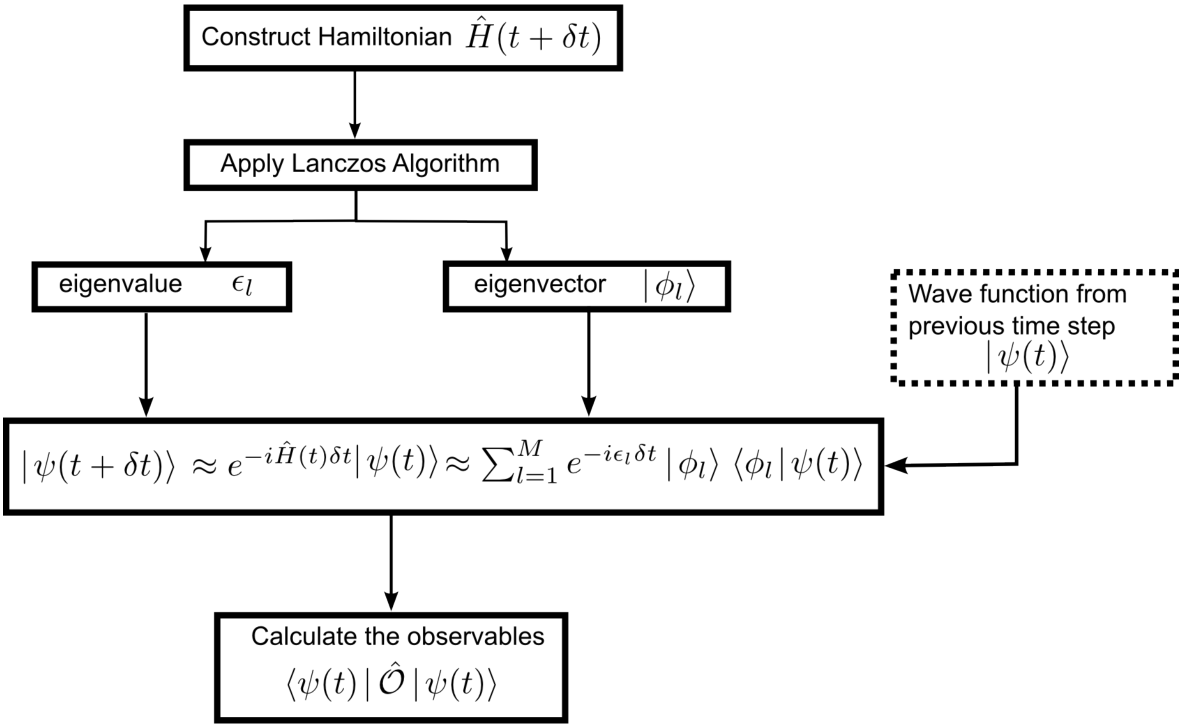

Figure 3.2: Workflow for the time–dependent Lanczos algorithm

3.3. Nonequlibrium momentum distribution function

Beside the correlation functions[1], a sensitive quantity for studying the dynamics of an electronic system represents the momentum distribution function $n_k(t)$, as discussed in Ref. [106]. In the momentum space of a 1D system this observable can be defined, as follows:

$$n_k(t) = \sum_{\sigma} \left\langle \psi(t) \left| \hat{c}^{\dagger}_{k\sigma} \hat{c}_{k\sigma} \right| \psi(t) \right\rangle \tag{3.9}$$

with $k = |\mathbf{k}| = 2\pi n/N$, $n = \{1 \dots N\}$ being the momentum in one dimension and N denoting the total number of sites in the lattice. However, for the numerical calculations it is useful to transform operators $\hat{c}^{(\dagger)}_{k\sigma}$ into the real space. Thus, we make a Fourier transformation [107]

$$\hat{c}^{\dagger}_{k\sigma} = \frac{1}{\sqrt{N}} \sum_{j=1}^{N} e^{ikj} \hat{c}^{\dagger}_{j\sigma} \quad ; \quad \hat{c}_{k\sigma} = \frac{1}{\sqrt{N}} \sum_{j=1}^{N} e^{-ikj} \hat{c}_{j\sigma} \ ,$$

which leads to the following form of the momentum distribution function:

$$n_k(t) = \frac{1}{N} \sum_{j,l,\sigma} \left\langle \psi(t) \left| e^{ik(l-j)} \hat{c}^{\dagger}_{l\sigma} \hat{c}_{j\sigma} \right| \psi(t) \right\rangle \tag{3.10}$$

---

[1] which were introduced in section 2.3

This function is quite sensitive to the changes in interaction part of the strongly correlated electron model. This is illustrated in Fig. 3.3.

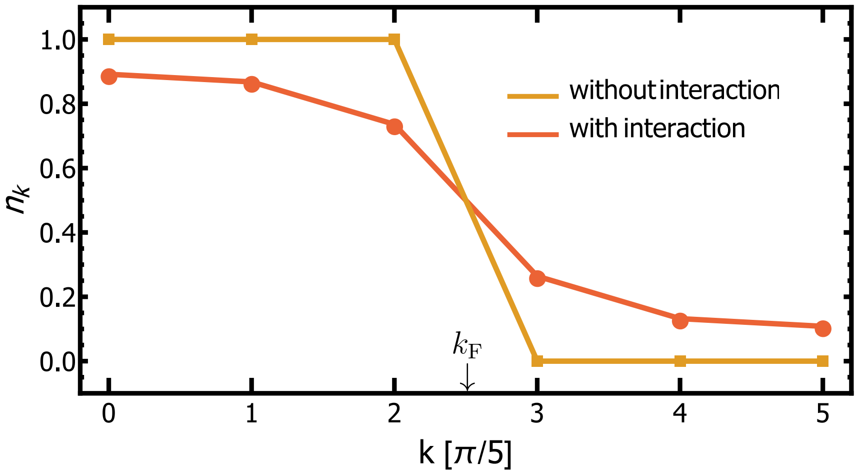

Figure 3.3: Illustration of the momentum distribution function in equilibrium (T=0) for non– (orange solid line) and interacting (red solid line) electron system.

In the noninteracting system one finds, as expected, stepwise momentum distribution for the electrons. However, due to the finite size effects, one observes large transition region around k_F. With increased interaction part the form of the momentum distribution function is changed and the jump Δn_k at the Fermi surface is reduced. Thus, Δn_k can be also used for probing the dynamics in the electron system. Therefore, we define the jump in the momentum distribution function for different time values t, as follows:

$$\Delta n_k(t) = \lim_{k \to k_F^-} n_k(t) - \lim_{k \to k_F^+} n_k(t) \qquad (3.11)$$

3.4. Time–dependent optical conductivity

Now, we discuss the response of an interacting electron system on an external perturbation. Especially, we focus on the optical experiments with measurements of the optical conductivity. In this type of experiment the electromagnetic field induces changes in the system at some point in time t' and the response of the system is measured later at $t > t'$.

3.4.1. Linear response approximation. Kubo–formalism

Let us restrict our consideration for a moment to the linear response, where we assume that the response signal of the system is directly proportional to the intensity of the external electromagnetic distortion. In this case the optical conductivity $\sigma(t)$ plays the role of the response function and connects the applied time–dependent electric field $E(t)$ with the induced electric current density $\Delta j(t)$ in the system in the following way:

$$\Delta j(t) = \int_{\infty}^{\infty} dt' \sigma(t-t') E(t') \tag{3.12}$$

In general, optical conductivity is a complex function $\sigma(t) = \sigma_1(t) + i\sigma_2(t)$, where we introduce the notation $\mathrm{Re}\sigma(t) \equiv \sigma_1(t)$ and $\mathrm{Im}\sigma(t) \equiv \sigma_2(t)$. For calculation $\sigma(t)$ we use a method, which is based on a well–known Kubo formula [108,109]. We start with the initial unperturbed system at $t \to -\infty$, which is described by the Hamiltonian:

$$\hat{H}_{\mathrm{EHM}} = \sum_n \epsilon_n \left|\psi_n\right\rangle \left\langle\psi_n\right| \tag{3.13}$$

with the eigenvectors $|\psi_n\rangle$ and energy eigenvalues ϵ_n. Its initial steady state is given by the density operator

$$\rho_0 = \sum_n p_n \left|\psi_n\right\rangle \left\langle\psi_n\right| \tag{3.14}$$

with p_n being the probabilities. Now, we perturb the system by the electromagnetic field. For this purpose, we include into the Hamiltonian (3.13) an additional term H', which represents the interaction of the system with the field. It is convenient to consider the time development of the system in the interaction representation, where H' is treated as a small perturbation. Thus, the temporal evolution of the system is given by the density operator of the following form:

$$\rho = S(t,-\infty)\rho_0 S^{\dagger}(t,-\infty) \tag{3.15}$$

with the time–ordered propagator

$$S(t,-\infty) = \mathbf{T} \exp\left[-i \int_{-\infty}^{t} dt' H'(t')\right] . \tag{3.16}$$

Here, we use the time ordering operator $\mathbf{T}$ and the definition

$$H'(t') = e^{iH_{\mathrm{EHM}}t'} H' e^{-iH_{\mathrm{EHM}}t'} . \tag{3.17}$$

The current density $\Delta j(t)$ induced in the system after perturbation is then given by difference between expectation values of the operator $j(t)$ at time t and in the initial state:

$$\Delta j(t) = \mathrm{tr}[j(t)\rho] - \mathrm{tr}[j(-\infty)\rho_0] \tag{3.18}$$

It should be noted that we use here the interaction representation of the current density operator $\hat{j}$, which reads:

$$j(t) = e^{iH_{\mathrm{EHM}}t}\, \hat{j}\, e^{-iH_{\mathrm{EHM}}t} \tag{3.19}$$

with

$$\hat{\jmath} = it_h \sum_{j,\sigma} \left(\hat{c}^{\dagger}_{j+1,\sigma} \hat{c}_{j,\sigma} - H.c. \right) \ . \tag{3.20}$$

Since there is no current in the initial steady state, we can neglect the second term in Eq. (3.18). Further, the first term can be divided in two parts $j(t) = j^{(1)}(t) + j^{(2)}(t)$. The expectation value $\left\langle j^{(1)}(t) \right\rangle = \mathrm{tr}\left(j^{(1)}(t)\rho \right)$ gives the diamagnetic part of the current density

$$\left\langle j^{(1)}(t) \right\rangle = -\frac{ne^2}{mc} A(t) = \frac{ine^2}{m\omega} E(t) \tag{3.21}$$

and leads to delta peak in the optical conductivity of superconductors. The second part can be calculated as follows:

$$\left\langle j^{(2)}(t) \right\rangle = \mathrm{tr}\left[j^{(2)}(t)\rho \right] = \mathrm{tr}\left[S^{\dagger}(t,-\infty) j^{(2)}(t) S(t,-\infty)\rho_0 \right] \tag{3.22}$$

Now, we can make use of the linear response approximation and insert in Eq. (3.22) the time–ordered propagator from Eq. (3.16) in the first order of $H'(t)$. After some algebra we arrive at:

$$\left\langle j^{(2)}(t) \right\rangle = -i \int_{-\infty}^{t} dt' \mathrm{tr}\left(\left[j^{(2)}(t), H'(t') \right] \rho_0 \right) \tag{3.23}$$

Finally, with the exact form of the perturbation Hamiltonian H' we get the Kubo–formula for the current density:

$$\left\langle j^{(2)}(t) \right\rangle = \frac{1}{\omega} \int_{-\infty}^{t} dt' \mathrm{tr}\left(\left[j^{(2)}(t), j^{(2)}(t') \right] \rho_0 \right) E(t') \tag{3.24}$$

The combination of Eqs. (3.24) and (3.21) leads to the result

$$\Delta j(t) = \frac{ine^2}{m\omega} E(t) + \frac{1}{\omega} \int_{-\infty}^{\infty} dt' \mathrm{tr}\left(\theta(t-t') \left[j^{(2)}(t-t'), j^{(2)}(0) \right] \rho_0 \right) E(t') \ , \tag{3.25}$$

where we have used a substitution $t - t' \to t$ in the integral. The comparison of Eq. (3.25) with Eq (3.12) gives the expression for the optical conductivity $\sigma(t)$. However, in the experiments one measures optical conductivity as a function of frequency. Therefore, it is convenient to consider its Fourier transformed form:

$$\sigma(\omega) = \frac{ine^2}{m\omega} \delta(\omega) + \frac{1}{\omega} \int_{-\infty}^{\infty} dt' e^{i\omega(t-t')} \mathrm{tr}\left(\theta(t-t') \left[j^{(2)}(t-t'), j^{(2)}(0) \right] \rho_0 \right) \tag{3.26}$$

Let us now discuss the expression (3.26) in some details. First, it is important to note that it has the time translational invariant form. In other words, it depends only on the time difference $t - t'$. Further, the formula (3.26) for optical conductivity can be rewritten in terms of the current–current correlation function χ_{jj}:

$$\sigma(\omega) = \frac{i}{\omega}\left[\frac{ne^2}{m}\delta(\omega) + \chi_{jj}(\omega)\right] \tag{3.27}$$

with

$$\chi_{jj}(\omega) = -i\int\limits_{-\infty}^{\infty} dse^{i\omega s}\mathrm{tr}\left(\theta(s)\left[j^{(2)}(s), j^{(2)}(0)\right]\rho_0\right) \ . \tag{3.28}$$

The imaginary part of $\chi_{jj}(\omega)$ is connected with the real part of the optical conductivity $\sigma_1(\omega)$ by

$$\sigma_1(\omega) = -\frac{1}{\omega}\lim_{\eta\to 0+}\mathrm{Im}\chi_{jj}(\omega + i\eta) \tag{3.29}$$

and gives the spectral representation of the current density operator

$$-\,\mathrm{Im}\chi_{jj}(\omega) = \frac{1}{L}\sum_n |\left\langle n|\hat{j}|0\right\rangle|^2\delta\left(\omega - \left(\epsilon_n - \epsilon_0\right)/\hbar\right) \tag{3.30}$$

with $|n\rangle$ being the n-th state with the energy ϵ_n. Here, we have introduced an artificial Lorentzian broadening η. According to symmetry arguments the spectral function $\mathrm{Im}\chi_{jj}(\omega)$ captures only odd–parity excited states of the system. The even–parity states can be found from the spectral representation of the stress tensor operator $\hat{\tau}$:

$$-\,\mathrm{Im}\chi_{\tau\tau}(\omega) = \frac{1}{L}\sum_n |\left\langle n|\hat{\tau}|0\right\rangle|^2\delta\left(\omega - \left(\epsilon_n - \epsilon_0\right)/\hbar\right) \tag{3.31}$$

with

$$\hat{\tau} = t_h\sum_{j,\sigma}\left(\hat{c}^\dagger_{j+1,\sigma}\hat{c}_{j,\sigma} + H.c.\right) \ . \tag{3.32}$$

The stress tensor operator $\hat{\tau}$ is equivalent to the kinetic part of the Hamiltonian $\hat{H}_{\mathrm{EHM}}$.

The spectral representation of both correlation functions $\chi_{jj}(\omega)$ and $\chi_{\tau\tau}(\omega)$ can be computed numerically by using Lanczos method, which was discussed in section 2.2.2. For this purpose we prepare instead of an arbitrary initial vector a vector of the form:

$$|u_1\rangle = \hat{\mathcal{O}}\,|GS\rangle\,/\sqrt{C} \tag{3.33}$$

with an operator $\hat{\mathcal{O}}$ under consideration, i.e.$\hat{\mathcal{O}} = \hat{j}$ or $\hat{\tau}$. The quantity $C = \left\langle GS|\hat{\mathcal{O}}^\dagger\hat{\mathcal{O}}|GS\right\rangle$ represents a normalization constant. After applying the Lanczos algorithm and the subsequent diagonalization of the $M \times M$ tridiagonal matrix T we can obtain the low–energy spectral representation of the corresponding correlation function, which is approximately given by:

$$I(\omega) \approx C\frac{1}{L}\sum_{n=0}^{M-1} |\left\langle x_n|u_1\right\rangle|^2\delta\left(\omega - \left(\tilde{\epsilon}_n - \epsilon_0\right)/\hbar\right) \tag{3.34}$$

Due to the discrete energy states of the finite–size system, we introduce an artificial Lorentzian broadening with a width $\eta = 0.1$ into the delta function. For illustration of the low energy excitation spectra for electron system of 10–sites we present in Fig. 3.4 the calculated spectral representations of the stress tensor (yellow solid line) and current (blue solid line) operator. Here, we chose the parameters for the interaction part of the Hamiltonian to be $U = -4$, $V = 0.25$. The electron configuration on the lattice corresponds to the CDW phase.

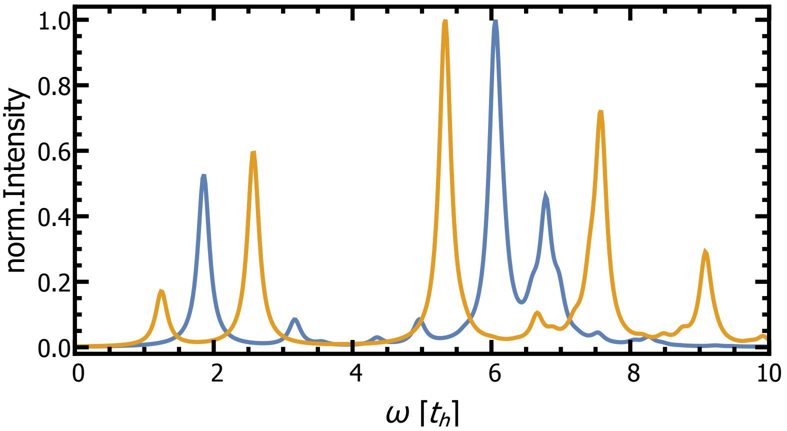

Figure 3.4: The calculated excitation spectrum for the finite–size system with interaction parameter values $U = -4$, $V = 0.25$ corresponding to CDW phase configuration. The spectral representation of the current–current and stress tensor correlation functions are shown by the blue and yellow solid lines, respectively.

3.4.2. Pump–probe conductivity

Inspired by the recent optical control experiments [80,92], we want now to calculate the optical pump–probe conductivity. In this type of experiment the system is driven out far from equilibrium by the first (pump) excitation and the optical properties are measured with the second (probing) excitation. Here, we assume the probe excitation to be very short in time and much weaker, than the pump perturbation. Thus, it should be possible to use previously discussed linear response approximation with respect to the probing field in calculations of the optical conductivity. It is important to note that the time translation symmetry does not preserved generally in nonequilibrium, since the initial nonequilibrium state is time–dependent. Therefore, one needs to calculate a two–time optical pump–probe conductivity $\sigma(\Delta t, t)$, which now additionally depends on the time difference Δt between the pump and probe excitation of the interacting electron system.

One opportunity is to use a generalization [110] of the Kubo formula from Eq. (3.27) to the nonequilbirium case:

$$\sigma_1(\Delta t, \omega) = \frac{1}{\omega L} \mathrm{Im} \int\limits_0^{t_m} ds \left(i e^{i(\omega + i\eta)s} \left\langle \psi(\Delta t) \mid \left[j^I(\Delta t + s), j^I(\Delta t) \right] \mid \psi(\Delta t) \right\rangle \right) \tag{3.35}$$

where $\sigma_1(\Delta t,\omega)$ is the real part of the Fourier transformed optical conductivity with respect to time t:

$$\sigma(\Delta t,\omega) = \int_0^{t_m} ds\sigma(\Delta t, s+\Delta t)e^{i(\omega+i\eta)s} \tag{3.36}$$

Here, t_m is the window width for the Fourier transformation. The current density operator $j^I(t)$ in Eq. (3.35) is given in the interaction representation

$$j^I(t) = U^\dagger(t,t')\hat{j}U^\dagger(t,t') \tag{3.37}$$

with $U(t,t')$ being the time evolution operator without probing excitation.

We will use, however, another approach, which was proposed in Refs. [76, 111] and can be easier implemented numerically. For this purpose we use the time–dependent Lanczos algorithm in order to find the temporal evolution of the wave function, which describes the interacting electron system in nonequilibrium. Based on its knowledge, we obtain first the time–dependent current density after only pump excitation:

$$j_\mathrm{p}(t) = \left\langle \psi(t)|\hat{j}|\psi(t)\right\rangle \tag{3.38}$$

with the current density operator $\hat{j}$ defined in Eq. (3.20). Then, we repeat this procedure one more time and calculate the total current density $j_\mathrm{tot}(\Delta t,t)$ after an additional probing excitation. The difference in both results gives the current density $j_\mathrm{pr}(\Delta t,t)$ induced by the probe excitation, i.e. $j_\mathrm{pr}(\Delta t,t) = j_\mathrm{tot}(\Delta t,t) - j_\mathrm{p}(t)$. Finally, the pump–probe optical conductivity is calculated from the Fourier transformation of $j_\mathrm{pr}(\Delta t,t)$ and the probe excitation $A_\mathrm{pr}(\Delta t,t)$ with respect to t:

$$\sigma(\Delta t,\omega) = \frac{j_\mathrm{pr}(\Delta t,\omega)}{i(\omega+i\eta)LA_\mathrm{pr}(\Delta t,\omega)} \tag{3.39}$$

with η being a small positive number. The parameter η is artificially added to $\sigma(\Delta t,\omega)$ and determines the broadening of the spectral lines, which is necessary for obtaining the spectral weight of the energy peaks.

Chapter 4

Results of simulations for EHM in nonequilibrium

In this chapter we discuss the results of the time–resolved simulations for an extended Hubbard model in nonequilibrium. The numerical computations are based on the time–dependent exact diagonalization algorithm from section 3.2. The first part of this chapter is devoted to the nonequilibrium processes initiated by an interaction quench. In particular, we consider quenches within CDW phase and from CDW into a singlet superconducting state, which are schematically shown by path (1) and (2) in Fig. 4.1, respectively. In the later case the buildup of the superconducting correlations is studied in view of several correlation functions. Also the behavior of the time–dependent optical conductivity is discussed. The second part of this chapter deals with a quench by pulse (path (3) in Fig. 4.1). Particular emphasis is on the possibility to induce superconductivity in this case, which is analyzed by using different correlation and response functions.

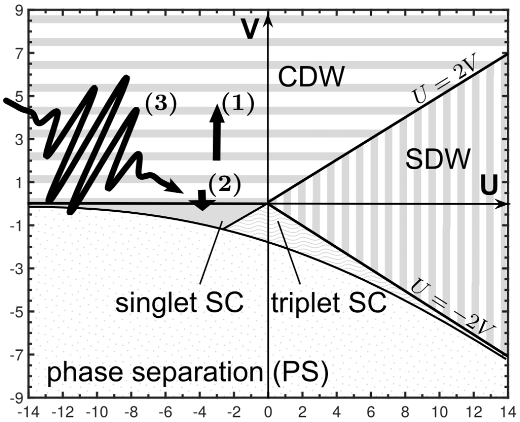

Figure 4.1: Schematic illustration of different quantum quench protocols on the phase diagram for EHM. The arrows (1) and (2) indicate interaction quenches within CDW phase and from CDW into a singlet superconducting phase, respectively. A pump pulse excitation is illustrated by the curve (3).

4.1. Interaction quench within a single phase

In the presented section we discuss an interaction quench, which is indicated by path (1) in Fig. 4.1. In this case, the initial U, V and the final U', V' values of the interaction parameters in the Hamiltonian are located within the same phase. For simplicity we prepare the strongly correlated electronic system at the initial time $t_0 = 0$ in the equilibrium ground state of the CDW phase. In this case the electrons on the lattice build an alternating order of double occupied and empty sites. The qualitative results, however, do not depend on the particular phase under consideration. The initial interaction parameters are chosen to be $U = -3$, $V = 2$. Further, immediately after $t = 0$ we change the nearest neighbor interaction part to $V' = 5$ and the system develops for $t > 0$ with the new Hamiltonian.

Using the time–dependent Lanczos method discussed in section 3.2 we obtain the temporal evolution of the wave function $|\psi(t)\rangle$. Based on this knowledge, we calculate all characteristic functions of interest. Let us start with the discussion of the density–density correlation function $C(j,t)$. The results of calculations are presented in Fig. 4.2, from which we can draw some important conclusions. First, we find that immediately after the interaction quench the correlation function $C(j,t)$ at each lattice site j start to oscillate with time (see Fig. 4.2(a)). Moreover, the frequency of these oscillations[1] is independent of j, which in turn means that the interaction quench affect the whole electron system and leads to its coherent oscillations. Now, by plotting the correlation function $C(j,t)$ versus j for different moments in time (see Fig. 4.2(b)) we recognize the characteristic for CDW phase "zigzag" structure, which qualitative form remains unaffected by the interaction quench. However, the intensity of this structure changes with time. Similar behavior was also observed by quenching from different initial states within the CDW phase.

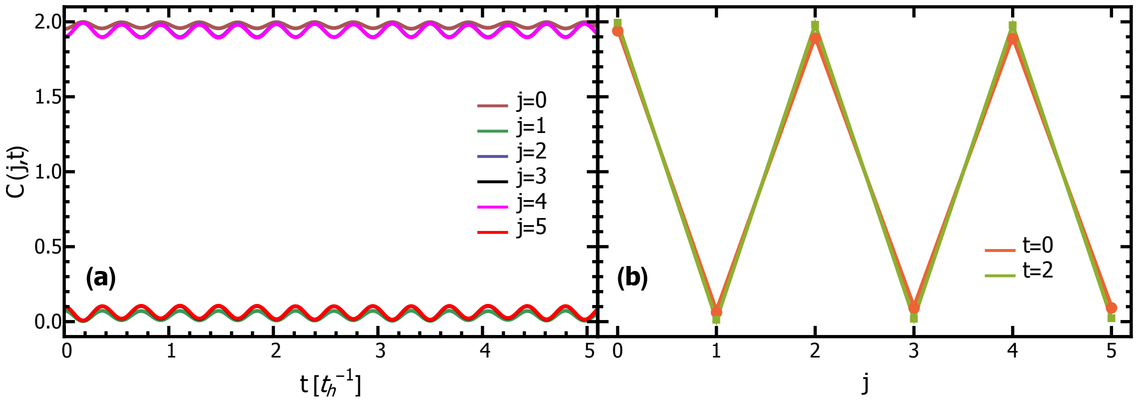

Figure 4.2: Density–density correlation function $C(j,t)$ calculated for an interaction quench within the CDW phase (path (1) in Fig. 4.1). The initial and final interaction parameters of the Hamiltonian are chosen to be $U = -3$, $V = 2$ and $U' = -3$, $V' = 5$, respectively. (a) Temporal evolution of $C(j,t)$ obtained for each lattice site j. (b) "Snapshots" of $C(j,t)$ at different moments in time shown as a function of j.

---

[1] the corresponding Fourier spectrum is discussed in connection with Fig. 4.3(b)

Finally, we find that the oscillations of the density–density correlation function $C(j,t)$ manifest itself in the dynamics of the momentum distribution function n_k. For illustration we plot the difference of n_k at the Fermi level as a function of time. The result for $\Delta n_k(t)$ is shown in Fig. 4.3(a). Thus, it is reasonable to assume that the wave function, describing the strongly correlated electron system in nonequilibrium, is not an eigenstate of the initial system in equilibrium. For further investigations we perform the Fourier transformation of the oscillations in Δn_k. The result is presented in Fig. 4.3(b) by the black solid line. We find that the oscillations correspond to a pronounced single peak at around $\omega = 17$ in the Fourier spectrum. Further, we calculate the low excitation states of the unperturbed electron system for both initial $U = -3$, $V = 2$ and final $U' = -3$, $V' = 5$ parameter values of the interaction part. The corresponding excitation spectra are shown in Fig. 4.3(b) by the green and red regions, respectively. The comparison of these spectra with the Fourier transformation of the nonequilibrium oscillations in Δn_k reveals that the single peak at $\omega = 17$ from the Fourier spectrum corresponds to the excited state of the CDW phase with the interaction parameter values $U' = -3$, $V' = 5$.

All in all, we can conclude that the interaction quench changes strongly the low energy states of the initial system and leads to the nonadiabatical temporal evolution of the wave function $|\psi(t)\rangle$. In other words, $|\psi(t)\rangle$ is not a "pure" eigenstate of the perturbed system (also do not appear as its ground state) and show oscillation between its excited states.

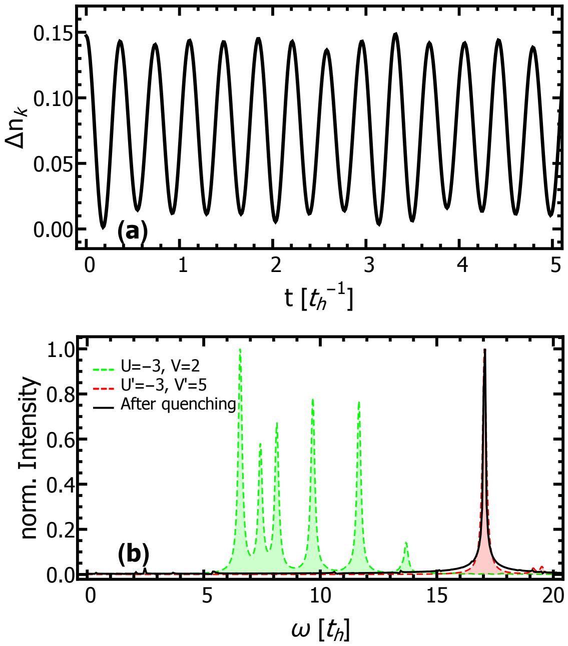

Figure 4.3: (a) Jump of the momentum distribution function Δn_k calculated after interaction quench. Here, we use same parameters, as in Fig. 4.2. (b) Fourier transformation of Δn_k from (a) shown by the black solid line. The green and red region correspond to the excitation spectrum of the electronic system with initial $U = -3$, $V = 2$ and final $U' = -3$, $V' = 5$ parameter values of the interaction part, respectively.

4.2. Induced singlet superconducting correlations by an interaction quench

Now, we examine the possibility to induce phase transition by an interaction quench. Especially, we are interested in the transitions into a superconducting state with singlet pairing correlations. For our investigations we use similar approach as discussed before (see section 4.1). First, we prepare the system at $t = 0$ in equilibrium ground state of the CDW phase with $U = -4$, $V = 0.25$. Then, immediately after $t = 0$ the nearest neighbor interaction parameter V is switched into the superconducting region with $V' = -0.25$ (see path (2) in Fig. 4.1). Finally, using time–dependent Lanczos method we evaluate the dynamics of the electron system and construct its corresponding wave function $|\psi(t)\rangle$.

4.2.1. Enhancement of the superconducting correlations

Using $|\psi(t)\rangle$ we calculate first the density–density correlation function $C(j,t)$ and singlet superconducting correlation function $P_1(j,t)$ in order to investigate the nonequlibrium dynamics of CDW and superconducting correlations resulted after interaction quench, respectively. In Fig. 4.4 we present the corresponding results obtained for different moments in time. Let us focus on the behavior of the density–density correlation function $C(j,t)$ shown in Fig. 4.4(a). While in the initial CDW state this correlation function exhibits characteristic for this phase "zigzag" structure, after quenching one observes a strong suppression of the charge density wave order. In fact, the value of $C(j,t)$ in nonequilibrium for $j > 1$ remains approximately constant. At the same time, the singlet superconducting correlation function $P_1(j,t)$ shows an enhancement of the superconducting correlations af-

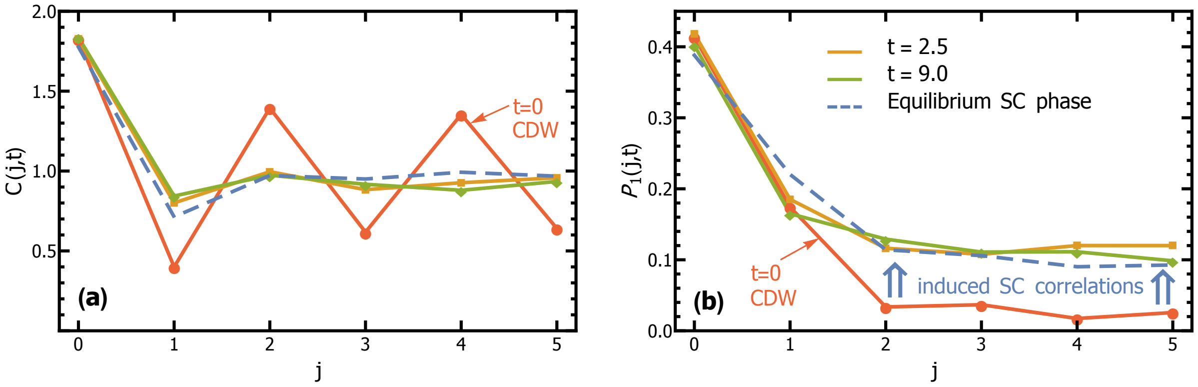

Figure 4.4: (a) Density–density $C(j,t)$ and (b) singlet superconducting $P_1(j,t)$ correlation functions versus lattice site j calculated for an interaction quench at several moments in time t. The initial and final interaction parameters of the Hamiltonian are chosen to be $U = -4$, $V = 0.25$ and $U' = -4$, $V' = -0.25$, respectively. For comparison, the corresponding correlation functions calculated for equilibrium singlet superconducting state with $U' = -4$, $V' = -0.25$ are shown with blue dashed lines.

ter interaction quench. This is demonstrated in Fig. 4.4(b). A direct comparison of the nonequilibrium results for $P_1(j,t)$ with its equilibrium counterpart in ground state of the singlet superconducting phase ($U' = -4$, $V' = -0.25$) reveals a good agreement in their behavior. Thus, we can argue that we observe the fingerprints of the induced superconducting state with the singlet pairing correlations.

Next reasonable questions would be how fast the superconducting correlations can be build after an interaction quench and how long the system can stay in this state. Also it is interesting to know, whether the initial CDW state is completely destroyed in nonequilibrium. In order to answer these questions we plot in Fig. 4.5 the temporal evolution of the numerically obtained singlet superconducting correlation function $P_1(j,t)$ for each lattice distance j. We found that immediately after the interaction quench the correlation function $P_1(j,t)$ for fixed values of j starts to oscillate. Interestingly, the magnitude of these oscillations depends strongly on the lattice distance j. For instance, the correlation function $P_1(j,t)$ at $j = 0$, which reflects the behavior of the double occupancy function (see section 2.3.2), shows oscillations around the initial value with a small magnitude. Physically this behavior might be interpreted as a redistribution of the electron pairs on the lattice initially prepared in the CDW phase, which was initiated by the interaction quench. Further, in the correlation function $P_1(j,t)$ with $j > 1$, which describe the buildup of the superconducting correlations, we found slow oscillations with almost similar strong magnitude. Therefore, the strong coherent enhancement of $P_1(j,t)$ with $j > 1$ appears in quite broad regions of time.

For deeper understanding of the nonequilibrium processes after quenching we need to perform Fourier transformation of the oscillation in the singlet pairing correlation function $P_1(j,t)$. However, we consider first momentum distribution function, which should give a complementary information about the interaction changes in the system. This is described in the next section.

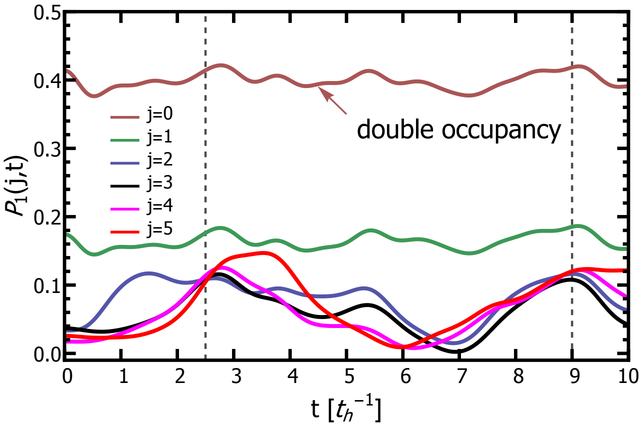

Figure 4.5: Temporal evolution of the singlet superconducting correlation function $P_1(j,t)$ calculated for an interaction quench as a function of lattice distance j. Here, we use same parameters, as in Fig. 4.4. The dynamics of double occupancy function is given by $P_1(j,t)$ at $j = 0$. The dashed lines indicate "snapshots" shown in Fig. 4.4(b).

4.2.2. Nonequilibrium correlation dynamics

In Fig. 4.6 we present the results of time–dependent calculations for the momentum distribution function n_k defined in Eq. (3.10). First, we plot n_k versus momentum k at different moments in time t (see Fig. 4.6 (a)). Due to the finite size of our lattice model the calculations of the momentum distribution function are restricted to discrete values of k. Nevertheless, the dynamical evolution of the system is still clearly visible. In fact, for the fixed value of k we find oscillating behavior of n_k with time. These oscillations manifest itself in the jump of the momentum distribution function Δn_k at the Fermi level. The temporal evolution of Δn_k is displayed in Fig. 4.6(b). Similar to the behavior of the previously discussed correlation functions (see section 4.2.1) the jump of the momentum distribution function Δn_k starts immediately to oscillate after the interaction quench. These observations implies that the electron system in nonequilibrium do not appear as a "pure" eigenstate neither of the initial CDW phase nor of the equilibrium superconducting phase described by Hamiltonian with final interaction parameters $U' = -4$, $V' = -0.25$.

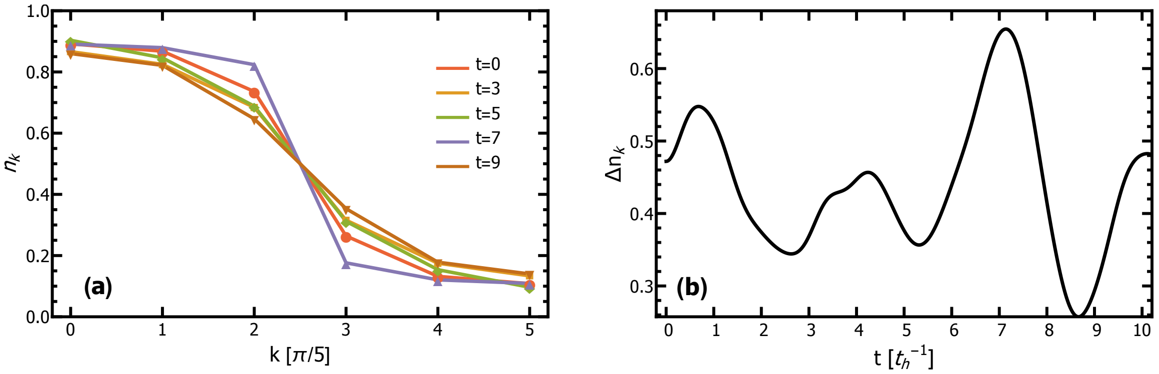

Figure 4.6: (a) Momentum distribution function n_k calculated after interaction quench for various moments in time t. Here, we use same parameters, as in Fig. 4.4. (b) Temporal evolution of the jump Δn_k at the Fermi level. Oscillating behavior is illustrated.

Further, we perform a Fourier transformation of the oscillations in Δn_k. The resulting spectrum is displayed in Fig. 4.7 by the black solid line and shows a few distinct low–energy peaks. In addition, we calculate the spectral representation of the stress tensor $\mathrm{Im}\chi_{\tau\tau}$ for low energies and for both phases with initial parameters of Hamiltonian $U = -4$, $V = 0.25$ describing CDW phase and for corresponding final equilibrium superconducting phase with parameters $U' = -4$, $V' = -0.25$. The resulting excitation spectra we plot together with Fourier transformation of $\Delta n_k(t)$ in Fig. 4.7 are indicate them by red and blue peaks, respectively. A comparison of all these spectra leads to some important conclusions. First of all, there are no peaks in the Fourier spectrum of $\Delta n_k(t)$, which can be assigned to the low energy excitation of the CDW phase. This observation together with the discussion from section 4.2.1 implies that the initial CDW correlations are strongly suppressed after the interaction quench. Moreover, the most intensive peaks in the Fourier spectrum can be identified as the low energy states for the singlet superconducting phase with parameters

$U' = -4$, $V' = -0.25$. Hence, we can conclude that the system driven out of equilibrium by interaction quench undergo a direct transition into a superconducting phase and shows oscillations between its different low–energy excited states.

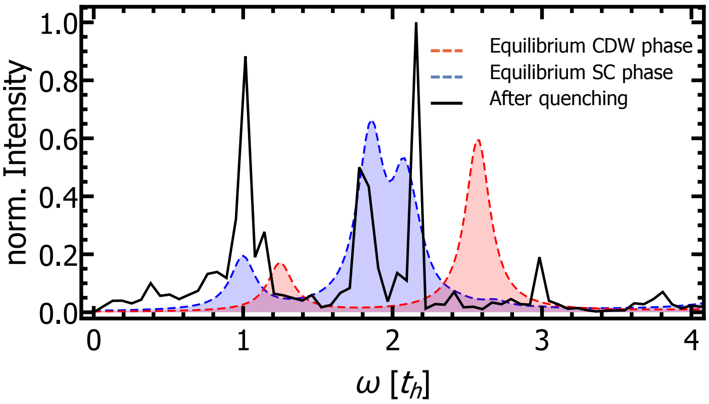

Figure 4.7: Fourier transformation of the jump $\Delta n_k(t)$ (black solid line) from Fig. 4.6(b). Blue peaks correspond to the excitation spectrum for the equilibrium SC state, whereas the read ones represent the excitation spectrum for the initial CDW state.

4.2.3. Time–dependent optical conductivity

The correlation functions discussed previously give an important information about the nonequilibrium dynamics of the electron system initiated by an interaction quench. However, these functions can not be measured directly in an experiment. Therefore, we include in our simulations an additional probing excitation of smaller intensity with the variable time delay Δt and calculate the time–dependent pump–probe optical conductivity. The strategy of calculations is described in section 3.4.2.

First, we present in Fig. 4.8 the real part of the optical conductivity $\sigma_1(\Delta t, \omega)$ obtained for different time delays Δt. The result of equilibrium calculation for the ground state of the initial CDW phase (performed at $\Delta t = 0$) is indicated by the red solid line. In this case the function $\sigma_1(\Delta t = 0, \omega)$ reveals an absorption peak at frequency $\omega \approx 1.9$. In addition, due to the finite–size effects and small interaction parameter values of the initial Hamiltonian we observe a second peak around $\omega \approx 0$ in conductivity spectrum[2]. After quenching the CDW absorption peak at $\omega \approx 1.9$ disappears completely and we observe strong enhancement of the peak magnitude at $\omega = 0$. Indeed, the calculations of $\sigma_1(\Delta t, \omega)$ at $\Delta t = 3$ and $\Delta t = 9$, which are respectively shown by orange and green lines in Fig. 4.8, reveal a shift of the spectral weight from absorption peak at $\omega \approx 1.9$ to peak at $\omega = 0$. Physically, this behavior indicates increase in the conductivity of the electron system. Further, a direct comparison of the results in nonequilibrium for $\sigma_1(\Delta t, \omega)$ with the optical conductivity calculated for the ground state of the equilibrium singlet superconducting phase with parameters $U' = -4$, $V' = -0.25$ (blue dashed line in Fig. 4.8) shows a good

---

[2] instead of an optical gap indicating the initial CDW phase

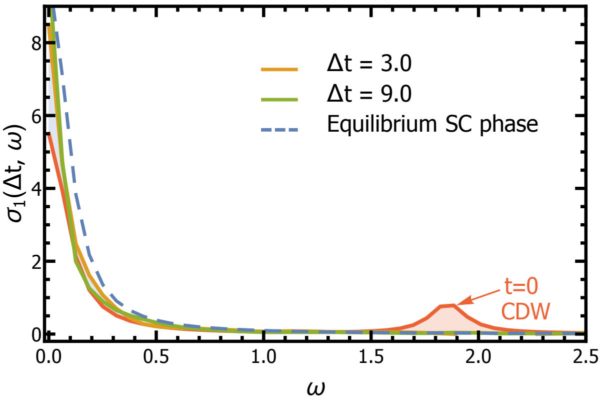

Figure 4.8: Real part of the optical conductivity $\sigma_1(\Delta t, \omega)$ calculated for an interaction quench at several time delays Δt. Here, we use same parameters, as in Fig. 4.4. Equilibrium result for singlet SC phase is shown for comparison by the blue dashed line.

agreement in their behaviors. It should be noted that the width of the peak at $\omega \approx 0$ in the equilibrium spectrum is caused by the finite–size effects of our lattice model.

Interestingly, the peak magnitude $\sigma_1(\Delta t, \omega = 0)$ at frequency $\omega \approx 0$ shows strong dependence on the time delay Δt between the pump–probe excitations, which is illustrated in Fig. 4.9. Here, we observe strong enhancement of $\sigma_1(\Delta t, \omega = 0)$ immediately after the interaction quench with the subsequent oscillations around its new average value. The frequencies of these oscillations reflects the dynamics of the correlation functions discussed in sections 4.2.2 and 4.2.1. For illustration, we perform Fourier transformation of these oscillations in $\sigma_1(\Delta t, \omega = 0)$ with respect to Δt. The resulting Fourier spectrum is pre-

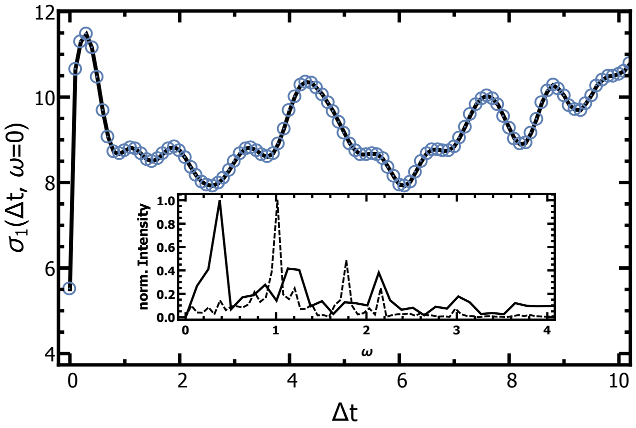

Figure 4.9: Magnitude of the low–energy peak ($\omega = 0$) in the $\sigma_1(\Delta t, \omega)$ spectrum as a function of time delay Δt obtained for an interaction quench. Here, we use same parameters, as in Fig. 4.4. The corresponding Fourier transformation of the oscillation is presented in the inset. The Fourier spectrum of the time–dependent correlation function from Fig. 4.7 is shown for comparison by the dashed line.

sented by a black solid line in the inset of Fig. 4.9 and shows a few distinct peaks. Due to the probing of the electron system with a short pulse of a small energy and fluency, we find that the most intensive peak in spectrum corresponds to the excitation at low energy. A comparison of the Fourier spectrum for $\sigma_1(\Delta t, \omega = 0)$ with corresponding spectrum for the correlation function[3], which is shown in the inset of Fig. 4.9 by the black dashed line, reveals that the position of the peaks in both cases shows a quite good match. However, the peaks differ in the intensity. This can be traced back to the differences in the energy and fluency of the pump and probe excitations.

Finally, let us discuss the corresponding imaginary part of the optical conductivity $\sigma_2(\Delta t, \omega)$. The results of the time–dependent computations for $\sigma_2(\Delta t, \omega)$ is presented in Fig. 4.10. Since the real and imaginary parts of the optical conductivity are connected through Kramers–Kronig relation, we observe in equilibrium $\sigma_2(\Delta t, \omega)$ at $\Delta t = 0$ (red solid line in Fig. 4.10) response at frequency $\omega \approx 1.9$ corresponding to absorption peak in CDW phase and a finite background, which is an artifact of the lattice model. After pumping we find that the signature of absorption at $\omega \approx 1.9$ disappears and the inductive response is enhanced with $1/\omega$–like behavior. This can be clearly seen for $\sigma_2(\Delta t, \omega)$ at $\Delta t = 3$ and $\Delta t = 9$, which are shown in Fig. 4.10 by orange and green line, respectively. Physically, this behavior corresponds to the enhancement of the superconducting correlations. Moreover, a comparison between these results for $\sigma_2(\Delta t, \omega)$ in nonequilibrium with its counterpart obtained for the ground state of the equilibrium singlet superconducting phase (blue dashed line in Fig. 4.10) reveals a quite good agreement in their behaviors.

All in all, in calculations of the time–dependent real $\sigma_1(\Delta t, \omega)$ and imaginary $\sigma_2(\Delta t, \omega)$ part of the optical conductivity we observe appearance of the transient Meissner effect, which is a fingerprint of the induced superconductivity [112]. This effect manifests itself in the increase of the spectral weight in $\sigma_1(\Delta t, \omega)$ at $\omega = 0$ and enhancement of the inductive response in $\sigma_2(\Delta t, \omega)$ with $1/\omega$–like behavior.

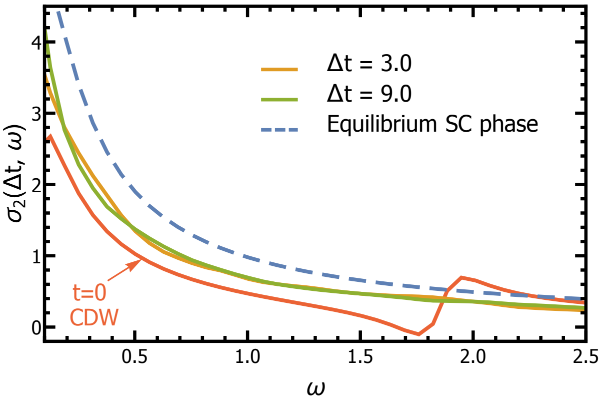

Figure 4.10: Imaginary part of the optical conductivity $\sigma_2(\Delta t, \omega)$ calculated for an interaction quench at several time delays Δt. Here, we use same parameters, as in Fig. 4.4. Equilibrium result for singlet SC phase is shown by the blue dashed line.

---

[3] see also Fig. 4.7

4.3. Induced singlet superconducting correlations resulting after quench by pulse

This section is devoted to the temporal evolution of the extended Hubbard model after a short pump pulse excitation (see path (3) in Fig. 4.1). Particular emphasis is on the superconducting phase transitions far from equilibrium. We prepare the system again in the ground state of the CDW phase and close to the transition boundary with the singlet superconducting phase. The initial interaction parameters of the Hamiltonian are $U = -3$, $V = 0.5$. Then, we apply the pump pulse of the Gaussian form, which reaches its maximum at $t = 0$. The central frequency of the pulse is chosen to match the lowest optical absorption peak energy of the unperturbed system to guarantee an effective transfer of the pulse energy to electrons and to avoid excessive pumping of the system. The duration time of the pump pulse we set to $\tau = 0.05$ in order to reach simultaneously different excited states of the system. Finally, the temporal evolution of the electron system together with its corresponding wave function is obtained by using the time–dependent Lanczos method.

4.3.1. Nonequilibrium dynamics after the pump pulse excitation

Based on the knowledge of the time–dependent wave function we calculate the relevant correlation functions. First, let us discuss the temporal evolution of the density–density correlation function $C(j, t)$. The results of computations are displayed in Fig. 4.11(a) and (b). Before pumping the electron system is prepared in the ground state of the CDW phase and $C(j, t)$ function shows characteristic for this phase "zigzag" structure (see red line in Fig. 4.11(b)). The excitation of the system with the pump pulse leads to the effective partial suppression of the charge density wave correlations with the subsequent

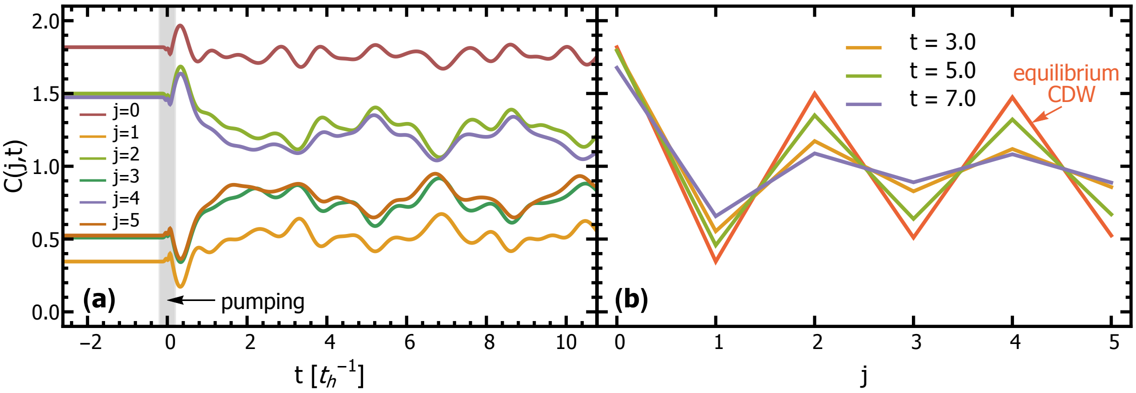

Figure 4.11: Results for the density–density correlation function $C(j, t)$ calculated after the pump pulse excitation of a Gaussian shape with parameters $\omega = 2.379$, $\tau = 0.05$, $A_0 = 5$. In (a) the temporal evolution of $C(j, t)$ for each lattice site j is presented, where the pulse is indicated by the gray region around $t = 0$. The "snapshots" of the correlation function at different moments in time are shown in (b).

oscillations. In fact, as shown in Fig. 4.11 (a) the density–density correlation function for a fixed lattice site value j starts to oscillate after pumping. In addition, we find that the frequency of these oscillations is independent of the lattice distance j (the Fourier analysis is given below). Thus, we can conclude that the pump pulse acts on the whole electron system and leads to its coherent excitation. Moreover, by plotting the correlation function $C(j,t)$ versus j at different moments in time (see Fig. 4.11 (b)) we observe an effective reduction in the magnitude of the CDW "zigzag" structure.

Now, we focus on the behavior of the singlet superconducting correlation function $P_1(j,t)$ after pumping. Since $P_1(j,t)$ at $j=0$ corresponds to the double occupancy function (see section 2.3.2) and $P_1(j,t)$ with $j>0$ gives information about the singlet superconducting correlations, it is convenient to discuss their temporal evolution separately. The results of the time–dependent computations for $P_1(j=0,t)$ and for $P_1(j>0,t)$ are presented in Fig. 4.12 (a) and (b), respectively. First of all, after pumping we find in the behavior of the double occupancy function $P_1(j=0,t)$ an effective decrease with strong oscillations around a new reduced value (see Fig. 4.12 (a)). Physically, it means that the excitation of the electron system by a pump pulse leads to a dynamical breaking and creation of electron pairs on a lattice. Moreover, at some moments in time (e.g. at $t\approx 3$, $t\approx 4$ etc.) one can observe a recovery of the double occupation function $P_1(j=0,t)$ to its initial value. Since the charge density wave correlations are partially suppressed after pumping, this behavior of $P_1(j=0,t)$ indicates a transient redistribution of the electron pairs on the lattice. Further, we find strong oscillations in the temporal evolution of singlet superconducting correlation function $P_1(j,t)$ for $j>0$, which are displayed in Fig. 4.12 (b). Importantly, after the pump pulse has gone the function $P_1(j>0,t)$ demonstrates a transient coherent increase for all $j>0$, which appears at around $t\approx 3$ in a quite narrow time frame and indicates the buildup of superconducting correlations. In order to get deeper understanding

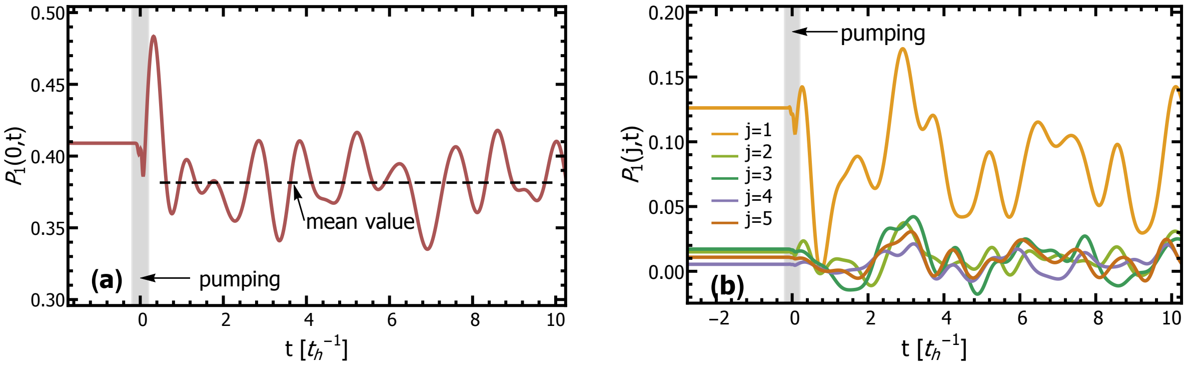

Figure 4.12: Results of the time–dependent computations for the singlet superconducting correlation function $P_1(j,t)$ after pump pulse. The pulse is indicated by the gray region around $t=0$ and has the same parameters as in Fig. 4.11. In (a) the dynamics of the double occupancy function represented by $P_1(j,t)$ at $j=0$ is shown. The results of calculations for $P_1(j,t)$ for each lattice site $j>0$ describing the singlet superconducting correlations are presented in (b).

of the nonequilibrium processes induced after pump pulse excitation we need to perform Fourier transformation of the obtained oscillations in the correlation functions.

The result of Fourier transformation for double occupancy function $P_1(j=0,t)$ [4] is displayed in Fig. 4.13 by the black solid line. As shown in this figure, the resulting Fourier spectrum contains several distinct peaks. In order to identify these peaks in the spectrum we calculate using Eq. (3.34) the low–energy spectral representation of the stress tensor operator $\mathrm{Im}\chi_{\tau\tau}$ for both initial CDW state with parameters $U=-3$, $V=0.5$ and equilibrium superconducting state with parameters $U=-3$, $V=-0.5$. The corresponding excitation spectrum for CDW with several distinct peaks and for superconducting phase characterized by two low–energy peaks (at $\omega<2$) are indicated in Fig. 4.13 by red and blue peaks, respectively. A direct comparison of all results reveals that the most intensive peaks in the Fourier spectrum correspond to the excited states of the initial CDW phase. In particular, low energy peaks at $\omega\approx1.5,\ 2.5,\ 3.5$ and 5.5 match perfectly with excitation spectrum for CDW phase. It is remarkable that a peak at $\omega\approx1.5$ might also represent an excited state of the superconducting phase, since one of the most intensive peaks in the optical spectrum of the superconducting state appears at the same frequency. In addition, a peak at $\omega\approx1$ in the Fourier spectrum can be assigned to the second intensive peak in the spectrum of the superconducting phase. At this point it is reasonable to ask a question whether these observations are an indication of a transient superconducting state. In order to give a clear answer to this question we need an additional information about the system in nonequilibrium, which can be extracted from the time–dependent optical conductivity spectrum. This is discussed in the next section.

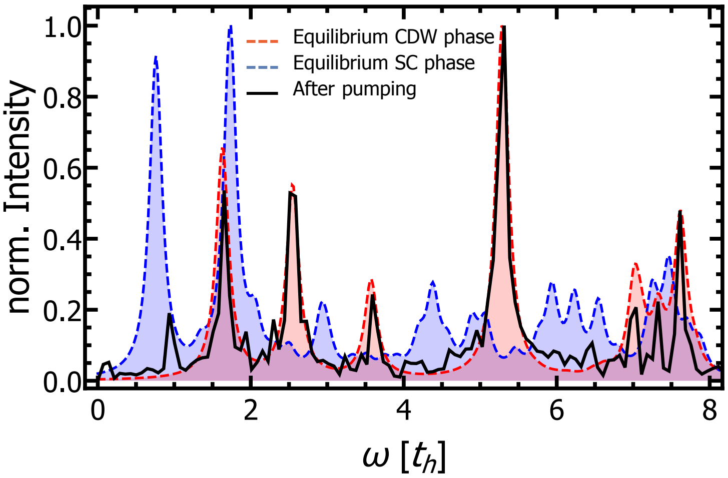

Figure 4.13: Fourier transformation of the oscillations in $P_1(0,t)$ from Fig. 4.12(a). The corresponding Fourier spectrum is shown by the black solid line. Blue peaks illustrate the excitations spectrum for the equilibrium SC state, whereas the red ones represent the excitation spectrum for the initial CDW state.

---

[4] It should be noted that similar Fourier spectra can be obtained from Fourier transformation for other correlation functions. The results differ slightly in intensity of peaks, but not in peak positions.

4.3.2. Time–dependent optical conductivity

Now, by using an additional probing pulse with a variable time delay Δt we simulate according to section 3.4.2 an important for the experiment time–dependent optical conductivity. The results of computations are displayed in Fig. 4.14.

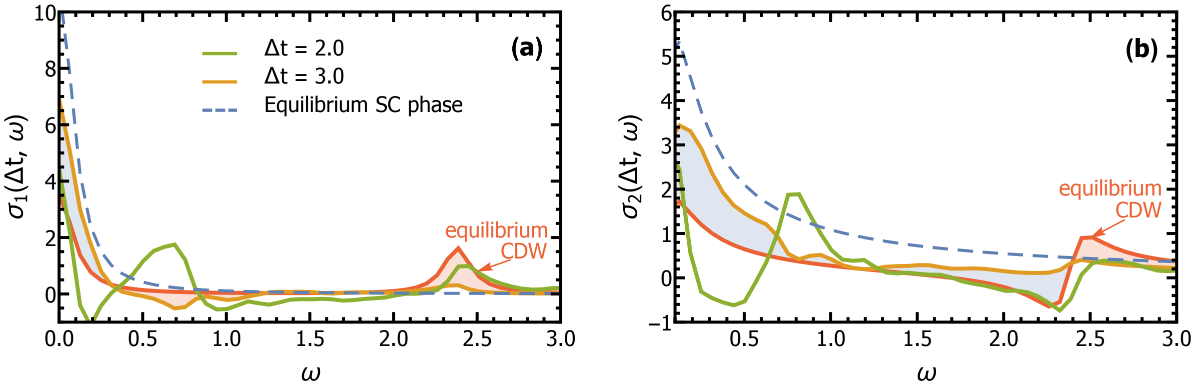

Figure 4.14: Time–dependent optical conductivity calculated after the pump pulse excitation for several time delays Δt. Here, we use same parameters as in Fig. 4.11. The real part of the spectrum is shown in (a), whereas the corresponding imaginary part is illustrated in (b). In addition, optical conductivity calculated for equilibrium singlet superconducting phase with parameters $U = -3$, $V = -0.5$ is shown in both figures by the blue dashed line for comparison.

Let us focus first on the real part of the optical conductivity $\sigma_1(\Delta t, \omega)$, which was computed for several time delays Δt and is presented in Fig. 4.14 (a). The result of calculation for the ground state of the CDW phase before pumping is indicated in the figure by the red solid line. In this case the function $\sigma_1(\Delta t, \omega)$ reveals an absorption peak at the frequency $\omega \approx 2.4$ and an additional peak at $\omega = 0$, which is an artifact of the lattice model as discussed previously in section 4.2.3. After pumping with time delay $\Delta t = 2$ (green solid line in Fig. 4.14 (a)) we find a partial decrease in the spectral weight of the CDW peak at $\omega \approx 2.4$. In addition, we observe appearance of a new low–energy peak at $\omega \approx 0.7$. The physical origin of this in–gap state can be explained as follows: Since the electron system is initially prepared in the ground state of the CDW phase, it reveals before pumping an alternating order of the double occupied and empty sites. A subsequent excitation of the system by an optical pump pulse leads to an initial breaking of the electron pairs[5] and to a corresponding creation of the photo–carriers. However, the photo–carriers remain localized on the lattice through the still existing alternating order with double occupied sites. As a result they are limited in movability. Further, we find from calculation of $\sigma_1(\Delta t, \omega)$ at $\Delta t = 3$ (shown by orange line in Fig. 4.14 (a)) disappearance of both peaks at $\omega \approx 2.4$ and at $\omega \approx 0.7$ and increase in the peak magnitude at $\omega = 0$. This behavior indicates a collective motion of the electrons on a lattice and consequently

---

[5] see also results of calculations of the correlation functions in Figs. 4.11 and 4.12

increase in the conductivity of the electron system. This is an important observation, since the CDW correlations are not fully suppressed by the pulse excitation according to our simulations of the correlations functions (see section 4.3.1) and might be interpreted as depinning of CDW. Moreover, the peak at $\omega = 0$ might also indicate superconducting state, since the finite size–effects of the lattice model lead to a finite width of this peak and, as a result, it is difficult to distinguish from our calculations between Drude and superconducting δ–peak.

Therefore, we consider now imaginary part of the optical conductivity $\sigma_2(\Delta t, \omega)$, which is displayed in Fig. 4.14 (b). From equilibrium calculations (red solid line in Fig. 4.14 (b)) we find response of the system at frequency $\omega \approx 2.4$ corresponding to the absorption peak in $\sigma_1(\Delta t, \omega)$ for the initial CDW phase with a finite background, which can be traced back to the size–effects of the lattice model. After pumping with time delay $\Delta t = 2$ (green solid line in Fig. 4.14 (b)) we observe an additional response at $\omega \approx 0.7$, which indicates the in–gap state discussed previously. Interestingly, both signatures of the optical absorption at $\omega \approx 0.7$ and $\omega \approx 2.5$ disappear completely at $\Delta t = 3$, as shown in Fig. 4.14 (b) by the orange line. Moreover, we observe increase in the inductive response with a $1/\omega$–like behavior, which corresponds to the buildup of the superconducting correlations. In addition, a direct comparison of the results for $\sigma_1(\Delta t, \omega)$ and $\sigma_2(\Delta t, \omega)$ in a nonequilibrium state at $\Delta t = 3$ with the corresponding counterpart calculated for the ground state of the equilibrium singlet superconducting phase with parameters $U = -3$, $V = -0.5$ (blue dashed line in Fig. 4.14 (a) and (b)) shows a quite good agreement in their behaviors.

Hence, we can conclude, that we find fingerprints of the induced superconductivity in the computations of the real part $\sigma_1(\Delta t, \omega)$ and the imaginary part $\sigma_2(\Delta t, \omega)$ of the optical conductivity for an electron system excited by a short optical pulse. These signatures emerges in the calculations in form of the transient Meissner effect. In other words, we observe in a quite narrow time frame a transient enhancement of the peak magnitude at $\omega = 0$ in $\sigma_1(\Delta t, \omega)$ and corresponding transient increase of the inductive response in $\sigma_2(\Delta t, \omega)$ with $1/\omega$–like behavior. Moreover, since the CDW order is not fully suppressed by the optical excitation, an additional observation of the superconducting fingerprints indicates the dynamical coexistence of the SC and CDW correlations far from equilibrium. This is in contrast to previously discussed situation with interaction quench (see section 4.2), where a full suppression of CDW and enhancement of superconductivity was observed.

4.4. Summary and discussion of results from optical control simulations

In this chapter we have numerically simulated ultrafast nonequilibrium dynamics for an one–dimensional Hubbard model with strongly correlated electrons on a lattice of 10 sites. For this system we have chosen periodic boundary conditions. In particular, we have investigated the possibility to induce singlet superconducting correlations far from equilibrium. For this purpose, the system was driven out of equilibrium in two different ways: (i) by in-

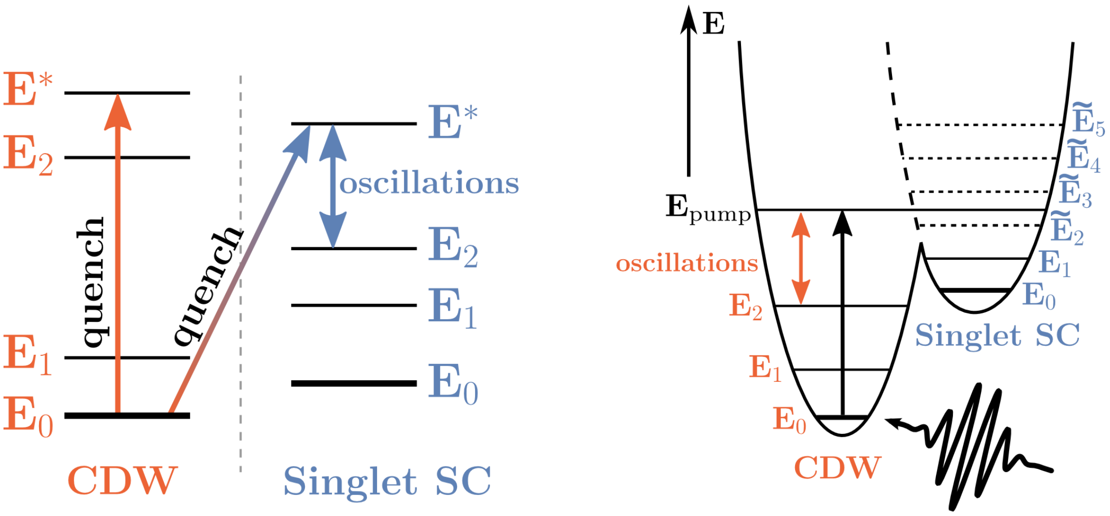

(a) Interaction quench **(b) Quench by pulse**

Figure 4.15: Schematic illustration of transient superconducting phase transitions in the extended Hubbard model induced by (a) interaction quench and (b) by quench by pulse. In both cases the system is initially prepared in the ground state of the charge density wave (CDW) phase. (a) An interaction quench leads to a direct transition into the superconducting phase (SC). Hereby, the system appears in a nonequilibrium state E*, which is not a "pure" eigenstate neither of equilibrium CDW nor of singlet SC phase. Oscillations between nonequliibrium E* and excited states of the superconducting phase occur. Quenching inside CDW phase leads to nonequilibrium excitation within the same phase. (b) In case of the quench by pulse the system can be excited to a joint quantum state of CDW phase with superconducting phase. As a result, fingerprints of the singlet SC phase can be observed after pumping. In addition, dominant oscillations between excited states in the CDW phase occur.

teraction quench and (ii) by quench by pulse. By using time–dependent Lanczos algorithm introduced in section 3.2 we were able to construct for both cases quite exactly[6] the time–dependent wave function describing the electron system in nonequilibrium. Based on its knowledge we have investigated the buildup of the superconducting correlations by means of several time–dependent correlation and response functions. A schematic illustration of transient superconducting phase transitions in the extended Hubbard model for the case of interaction quench and quench by pulse is presented in Fig. 4.15 (a) and (b), respectively.

First, we have focused on a situation with interaction quenches. Prepared the system in an equilibrium ground state of the CDW phase, we have switched interaction parameters of its Hamiltonian into the superconducting region. In this case a direct transition into the superconducting state was observed[7]. Indeed, the calculations of the density–density corre-

---

[6] within the framework of the exact diagonalization technique

[7] It should be noted that quenching inside CDW phase, also close to the transition boundary with superconducting phase, leads only to nonequilibrium excitation of the electron system within the same

lation function $C(j,t)$ reveal a strong suppression of the charge density wave correlations. Also, the behavior of the double occupancy function with small oscillations around the initial equilibrium value indicates a redistribution of the electron pairs on the lattice after quenching. Moreover, the singlet superconducting correlation function $P_1(j,t)$ shows an enhancement of the superconducting correlations in nonequilibrium. In addition, a direct comparison of the nonequilibrium results of $P_1(j,t)$ at several moments in time with its counterpart calculated for equilibrium superconducting ground state reveals quite perfect agreement. However, due to the fact that the interaction quench is a nonadiabatic process, the system does not follow the changes induced by the quench. In other words, the system do not appear in the ground state of the singlet superconducting phase after quenching, but in some nonequilibrium state (marked by E^* in Fig.4.15 (a)), which is not a "pure" eigenstate neither of equilibrium CDW nor of equilibrium singlet superconducting phase. As a result, oscillations between nonequlibrium state E^* and the low–energy eigenstates of the superconducting phase occur (see Fig. 4.15 (a)). This behavior manifests itself in the slow oscillations of the singlet superconducting correlation function $P_1(j,t)$ and of the jump of the momentum distribution function at the Fermi level Δn_k. More importantly, the results of Fourier transformation of these oscillations supports the interpretation of the nonequilibrium state E^* and reveal that the most intensive peaks of the Fourier spectra correspond to the low–energy eigenstates of the superconducting phase. There are no peaks in spectrum, which could correspond to the CDW phase. Finally, we have calculated the time–depended real $\sigma_1(\Delta t,\omega)$ and imaginary $\sigma_2(\Delta t,\omega)$ part of optical conductivity, which can be measured in an experiment, and observed appearance of a transient Meissner effect, which is a fingerprint of the induced superconductivity. In fact, the indications of the increased conductivity was found in the temporal evolution of $\sigma_1(\Delta t,\omega)$. In particular, the spectral weight of low energy peak corresponding to the equilibrium CDW state is shifted after quenching to a peak at frequency $\omega = 0$. As a result, the magnitude of this peak is immediately increased and showed some oscillations around a higher value. In addition, the Fourier transformation of these oscillations reveals a good agreement with the Fourier spectrum obtained from the correlation functions. Furthermore, the calculations of $\sigma_2(\Delta t,\omega)$ showed increase of the inductive response after pumping with $1/\omega$–like behavior, which indicates the enhancement of the superconducting correlations.

Second part of this chapter was devoted to the situation with a quench by a short optical pump pulse. The electron system was again prepared in an equilibrium ground state of the CDW phase, but close to the transition boundary with the singlet superconducting phase. By adjusting the amplitude of the pump pulse and tuning its frequency to the first low–energy absorption peak of the unperturbed CDW state a transient crossover from CDW phase into a singlet superconducting phase was observed (see Fig. 4.15 (b)). In fact, the computation of the time–dependent density–density correlation function $C(j,t)$ indicates after pumping an effective partial suppression of the charge density wave correlations with the subsequent oscillations. An additional calculation of the double occupancy function reveals similar behavior with oscillation of, however, quite large magnitude. Furthermore,

---

phase, as illustrated in Fig. 4.15 (a).

the oscillations are observed in the temporal evolution of the singlet superconducting correlation function $P_1(j,t)$. Importantly, after the pump pulse has gone the function $P_1(j,t)$ shows in a quite narrow time frame transient enhancement of the superconducting correlations. Hence, in contrast to the situation with the interaction quench, in case of the pump pulse quenching a dynamical coexistence of the CDW and singlet superconducting correlations is possible. Performing a Fourier transformation of the oscillations in the correlation functions we have found that most peaks in the Fourier spectrum correspond to the low–energy eigenstates of the CDW phase. However, some peaks can be identified with the eigenstates of the singlet superconducting phase. In other words, due to the low–energy excitation of the system with a short pump pulse its several eigenstates can be addressed simultaneously and oscillations between these states may occur. Also a joint quantum state of CDW phase with superconducting phase can be reached. It should be noted that in case of the pulses with higher excitation frequency the buildup of the superconducting correlations is suppressed due to the pumping of too much energy into the system. Finally, we have investigated the time–dependent real $\sigma_1(\Delta t,\omega)$ and imaginary $\sigma_2(\Delta t,\omega)$ part of the optical conductivity. From calculations of $\sigma_1(\Delta t,\omega)$ we have observed after pumping a transient shift of the spectral weight from low energy peak, corresponding to a CDW state, into peak at $\omega = 0$. As a result, the magnitude of this peak is enhanced, which in turn means increase in the conductivity. At the same time, the computations of $\sigma_2(\Delta t,\omega)$ reveals a transient increase in the inductive response with $1/\omega$–like behavior, which corresponds to enhancement of the superconducting correlations. Both properties indicate a transient Meissner effect.

To summarize the results of our simulation, we should go back to the question, which was raised in the introduction. Since the indications of the transient superconducting phase transitions were observed [78,80,88–91] in layered cuprates by addressing some vibrational mode with ultrashort optical pulses, most previous theoretical studies were focused on the interpretation of this phenomenon in application to these particular materials. Some models suggested increase in the interlayered coupling through non–linear interaction with the laser field [81,89] or by melting of the competing order [84,86], others explained enhancement of superconducting correlations by periodic modulation of a phonon mode [82–85,87]. However, the important question about the possibility to induced superconductivity in general for different types of materials was so far disregarded. With our studies we wished to fill up this gap in understanding of this transient phenomenon and demonstrated a buildup of the singlet superconducting correlations in nonequilibrium for a lattice model with strongly correlated electrons. Hereby, we have considered two nonequilibrum scenarios with interaction quench and quench by pulse. In the later case, the build up of the singlet superconducting correlations appear even when the pulse has gone.

Similar question was raised in an experimental work, which was published few weeks ago [92]. In this work optical response of a conventional s–wave superconductor K_3C_{60} was investigated in equilibrium and after photo–excitation. The results of measurements are shown in Fig. 4.16. Experimental data obtained in equilibrium above critical temperature T_c reveals a metallic state with a narrow Drude peak and a polaronic band at 55meV (see Fig. 4.16(a) and (b)). A cooling below T_c leads to appearance of an optical gap in the real part $\sigma_1(\omega)$ and divergent $1/\omega$–like behavior in imaginary part $\sigma_2(\omega)$ of the optical conductivity. The measurements of the transient optical response of K_3C_{60} after photo–excitation with time delay $\Delta t = 1$ps, which was initially prepared in the metallic state at temperatures up to 100K (see Fig. 4.16(c)-(e)), reveal changes in the optical conductivity similar to the equilibrium cooling below T_c. Thus, a transient Meissner effect was observed in nonequilibrium experiment on an s–wave superconductor, indicating a transient transition from a metallic state into a superconducting phase.

All in all, since our simulations predict qualitatively similar results to those observed in recent measurements, one can conclude that our studies may open new way to induce superconductivity out of equilibrium in an experiment.

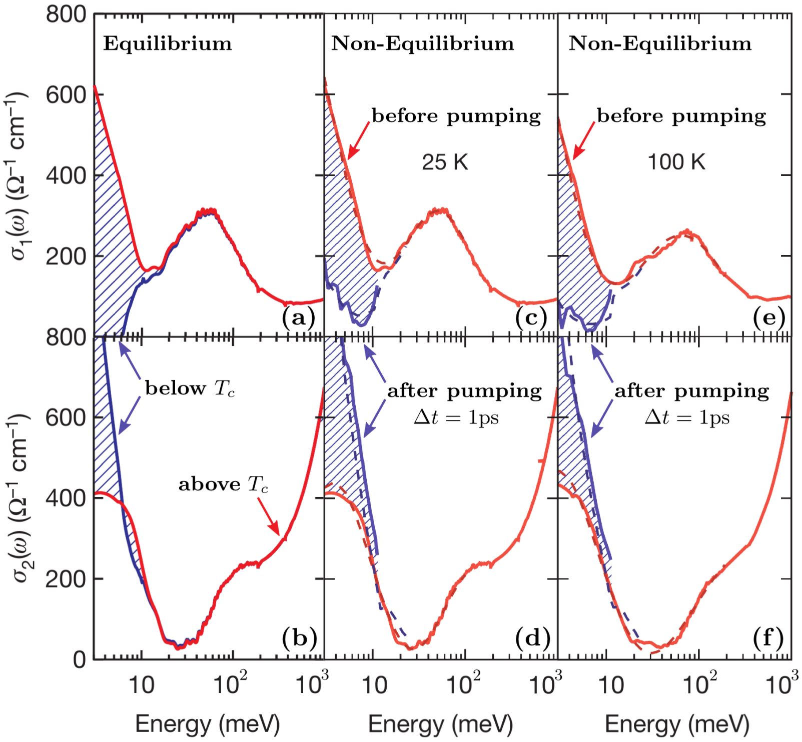

Figure 4.16: Equilibrium and transient optical response of K_3C_{60}. (a) and (b) display measuring results of real $\sigma_1(\omega)$ and imaginary $\sigma_2(\omega)$ part of the optical conductivity in equilibrium, respectively. Results above T_c are shown by the red line and indicate metallic state with a narrow Drude peak. Measured data below T_c is represented by the blue line, which shows appearance of an optical gap in $\sigma_1(\omega)$ and divergent behavior in $\sigma_2(\omega)$. In column (c), (d) the corresponding measured data at $T = 25\text{K} > T_c$ in equilibrium (red line) and after photo–excitation with time delay $\Delta t = 1$ps (blue line) are shown. Changes induced by photo–excitation are similar to the equilibrium cooling below T_c (column (a) and (b)). Similar results observed for equilibrium (red line) and transient (blue line) measurements at $T = 100$K, which are shown in column (e), (f). Fit to the data is shown by dashed lines. Figures are adapted from Ref. [92].

Part II

Non–Equilibrium Higgs spectroscopy

Chapter 5

Two–band superconductors in equilibrium

The recently discovered superconductivity in several multiband compounds [113–115] opens a completely new field for both theoretical and experimental studies. Due to the overlap of different bands in this type of superconductors, the Cooper pairs can be built not only within one band, but also the electron tunneling between the bands is allowed. This gives rise to different order parameters on different Fermi surfaces and also leads to the intrinsic Josephson effect. As a consequence, many new physical phenomena associated with different amplitudes and relative phases of the gaps are expected. For instance, it is well known [2, 3, 6] that the breaking of a continuous symmetry is associated with the appearance of a collective excitation. In a single–band superconductor with a two–component order parameter this leads to amplitude (Higgs mode) and phase (gauge mode) fluctuations of a superconducting gap. In contrast, for the two–band case an additional phase mode is expected [116], which corresponds to a relative phase oscillation of the superconducting condensates.

This part of the thesis is devoted to excitation of collective modes in superconductors out of equilibrium. Here, we consider two important classes of multiband superconductors. The first one describes the ordinary two–band superconductors with spin singlet pairing. The relevant examples are pnictides and MgB_2. The second one deals with the some exotic type of the superconducting systems, the crystal structure of which lacks an inversion center. In this case a lifting of the spin– and related to it band degeneracy is possible. More importantly, due to the spin–orbit coupling caused by the absence of the inversion center, for the first time in the history of superconductivity a superposition of both triplet and singlet contributions to the superconducting gaps can be observed. By using different theoretical approaches we investigate possibilities of excitation different collective modes in the described above classes of two–band superconductors. Especially, we will focus on the optical pump–probe excitations, where the light pulses are considered in the low intensity limit.

5.1. Two–band superconductivity with spin–singlet pairing

5.1.1. BCS–Leggett–Hamiltonian

Let us start with a description of a two–band superconducting system with spin–singlet pairing correlation in equilibrium. The reduced Hamiltonian of a two–band superconductor takes the following form in the mean–field approximation [117, 118]:

$$\hat{H}_{\mathrm{BCS}} = \hat{H}_0 + \sum_{l=1}^{2} \sum_{\mathbf{k}\in\mathcal{W}} \left[\Delta_{\mathbf{k}l}\hat{c}^{\dagger}_{\mathbf{k}\uparrow l}\hat{c}^{\dagger}_{-\mathbf{k}\downarrow l} + \Delta^{*}_{\mathbf{k}l}\hat{c}_{-\mathbf{k}\downarrow l}\hat{c}_{\mathbf{k}\uparrow l}\right] \tag{5.1}$$

with $\hat{c}^{\dagger}_{\mathbf{k}\sigma l}$ ($\hat{c}_{\mathbf{k}\sigma l}$) being creation (annihilation) of an electron on a band $l = \{1, 2\}$ with the momentum $\mathbf{k}$ and spin $\sigma =\uparrow, \downarrow$. The first part in Eq. (5.1)

$$\hat{H}_0 = \sum_{l=1}^{2} \sum_{\mathbf{k}\sigma} \xi_{\mathbf{k}\sigma l}\hat{c}^{\dagger}_{\mathbf{k}\sigma l}\hat{c}_{\mathbf{k}\sigma l} \tag{5.2}$$

denotes the normal state with the band energy $\xi_{\mathbf{k}\sigma l}$ measured from the chemical potential in the l–th band, whereas the Cooper pairing is described by the second part with the superconducting gaps $\Delta_{\mathbf{k}l}$:

$$\Delta_{\mathbf{k}l} = \sum_{j=1}^{2} \sum_{\mathbf{k}'\in\mathcal{W}} V^{lj}_{\mathbf{k}\mathbf{k}'} \left\langle \hat{c}_{-\mathbf{k}'\downarrow j}\hat{c}_{\mathbf{k}'\uparrow j} \right\rangle \tag{5.3}$$

The attractive electronic interaction $V^{lj}_{\mathbf{k}\mathbf{k}'}$ between the bands $l, j \in \{1, 2\}$ appears in the energy region $|\xi_{\mathbf{k}\sigma l}| \leq \hbar\omega_D$ with ω_D being the Debye cut–off frequency and with a corresponding set $\mathcal{W}$ of the momentum vectors $\mathbf{k}, \mathbf{k}'$. Here, $V^{lj}_{\mathbf{k}\mathbf{k}'}$ is considered in the weak coupling limit. Importantly, in contrast to the one–band superconductors, where the Cooper pairing is determined by the intraband coupling $l = j$, in two–band superconductors there exists an additional interband coupling between the different bands $l \neq j$. This leads to the occurrence of the intrinsic Josephson effect.

An additional side remark deserve the gap equation (5.3). For the case of s–wave superconductors with attractive momentum–independent pairing interactions $V^{l,j}_{\mathbf{k}\mathbf{k}'} \equiv V_{lj}$, $l, j = 1, 2$ and $\Delta_{\mathbf{k}l} \equiv \Delta_l$ this equation can be represented in matrix form [118]:

$$0 = \left\{ -\boldsymbol{\lambda}^{-1} + \begin{pmatrix} \Xi_1 & 0 \\ 0 & \Xi_2 \end{pmatrix} \right\} \cdot \begin{pmatrix} \Delta_1 \\ \Delta_2 \end{pmatrix} \tag{5.4}$$

with the band–selected function

$$\Xi_l = \langle \theta_{\mathbf{k}l} \rangle_{\mathrm{FS}} \quad ; \quad \theta_{\mathbf{k}l} = \frac{1}{2E_{\mathbf{k}l}} \tanh \frac{E_{\mathbf{k}l}}{2k_{\mathrm{B}}T} \tag{5.5}$$

and an interaction matrix $\boldsymbol{\lambda}$

$$\boldsymbol{\lambda} = \begin{pmatrix} \lambda_{11} & \lambda_{12} \\ \lambda_{12} & \lambda_{22} \end{pmatrix} \quad ; \quad \lambda_{lj} = V_{lj} N_{\mathrm{F}l} \ . \tag{5.6}$$

Here, $N_{\mathrm{F}l}$ is the density of states (DoS) at the Fermi level for each band l. The form of Eq. (5.4) will be important for the discussions in section 5.2.3.

Further, in order to simplify the description of a two–band system in a superconducting state we choose a convenient and well established way, which consists in introducing an energy matrix in a particle–hole space[1]. In this case we combine for each band l the creation and annihilation operators to spinors:

$$\underline{\hat{C}}_{\mathbf{k}l} = \begin{pmatrix} \hat{c}_{\mathbf{k}\uparrow l} \\ \hat{c}^{\dagger}_{-\mathbf{k}\downarrow l} \end{pmatrix} \quad ; \quad \underline{\hat{C}}^{\dagger}_{\mathbf{k}l} = \begin{pmatrix} \hat{c}^{\dagger}_{\mathbf{k}\uparrow l} & \hat{c}_{-\mathbf{k}\downarrow l} \end{pmatrix} \tag{5.7}$$

and energy contributions from Eq. (5.1) to the energy matrix

$$\underline{\xi}_{\mathbf{k}l} = \begin{pmatrix} \xi_{\mathbf{k}l} & \Delta_{\mathbf{k}l} \\ \Delta^{*}_{\mathbf{k}l} & -\xi_{-\mathbf{k}l} \end{pmatrix} \ . \tag{5.8}$$

Thus, the Hamiltonian (5.1) takes the following compact form

$$\hat{H}_{\mathrm{BCS}} \ = \ \sum_{l=1}^{2} \sum_{\mathbf{k}} \underline{\hat{C}}^{\dagger}_{\mathbf{k}l} \cdot \underline{\xi}_{\mathbf{k}l} \cdot \underline{\hat{C}}_{\mathbf{k}l} \ , \tag{5.9}$$

which reflects the structure of the normal state.

5.1.2. Bogoliubov–Valatin–Transformation

Now, it is convenient to separate the description of a two–band superconductor into the parts describing condensate and quasiparticles, respectively. This can be achieved by a straightforward diagonalization of the Hamiltonian (5.9). For this purpose we perform the Bogoliubov–Valatin transformation [4, 119], which is readily generalized to the two–band case [118]. This operation is equivalent to the rotation in the Nambu space for each band l. Physically, it represents a transformation from the electronic picture into the fermionic quasiparticle excitation basis $\underline{\hat{\alpha}}_{\mathbf{k}l}$:

$$\underline{\hat{\alpha}}_{\mathbf{k}l} \ = \ \underline{U}^{\dagger}_{\mathbf{k}l} \cdot \underline{\hat{C}}_{\mathbf{k}l} \quad ; \quad \underline{\hat{\alpha}}_{\mathbf{k}l} = \begin{pmatrix} \hat{\alpha}_{\mathbf{k}\uparrow l} \\ \hat{\alpha}^{\dagger}_{-\mathbf{k}\downarrow l} \end{pmatrix} \tag{5.10}$$

---

[1] which is also known, as the Nambu space [5]

The unitary Bogoliubov–Valatin transformation matrix $\underline{U}_{\mathbf{k}l}$ takes the following form

$$\underline{U}_{\mathbf{k}l} = \begin{pmatrix} u_{\mathbf{k}l} & -v_{\mathbf{k}l} \\ v^*_{\mathbf{k}l} & u_{\mathbf{k}l} \end{pmatrix} \quad ; \quad \underline{U}^\dagger_{\mathbf{k}l} = \begin{pmatrix} u_{\mathbf{k}l} & v_{\mathbf{k}l} \\ -v^*_{\mathbf{k}l} & u_{\mathbf{k}l} \end{pmatrix} . \tag{5.11}$$

with the BCS–coherence factors $u_{\mathbf{k}l}$ and $v_{\mathbf{k}l}$. Due to the free choice for the sign of $u_{\mathbf{k}l}$ and $v_{\mathbf{k}l}$, we use the following convention:

$$u_{\mathbf{k}l} = \sqrt{\frac{1}{2}\left(1 + \frac{\xi_{\mathbf{k}l}}{E_{\mathbf{k}l}}\right)} \quad ; \quad v_{\mathbf{k}l} = \sqrt{\frac{1}{2}\left(1 - \frac{\xi_{\mathbf{k}l}}{E_{\mathbf{k}l}}\right)} \tag{5.12}$$

with $E_{\mathbf{k}l} = \sqrt{\xi^2_{\mathbf{k}l} + |\Delta_{\mathbf{k}l}|^2}$. Thus, the BCS–Leggett–Hamiltonian (5.9) after this transformation takes the following form

$$\hat{H}_{\mathrm{BCS}} \;=\; \underbrace{U_{\mathrm{BCS}}(0)}_{T=0} + \underbrace{\sum_{l=1}^{2}\sum_{\mathbf{k}\sigma} E_{\mathbf{k}l}\hat{\alpha}^\dagger_{\mathbf{k}\sigma l}\hat{\alpha}_{\mathbf{k}\sigma l}}_{T>0} \tag{5.13}$$

As one can see, the Bogoliubov–Valatin transformation has a clear physical meaning: While the first term in the Hamiltonian (5.13) describes the ground state energy at $T = 0$ and corresponds to a superconducting condensate, the operators $\hat{\alpha}_{\mathbf{k}\sigma l}$ and $\alpha_{\mathbf{k}\sigma l}$ can be interpreted as ones to create and annihilate a fermionic quasiparticle in a quantum state $|\mathbf{k}, \sigma, l\rangle$ with the energy $E_{\mathbf{k}l}$. The statistical physics of the quasiparticle excitations can be described by the Fermi–Dirac distribution:

$$\nu_{\mathbf{k}l} = \left\langle \hat{\alpha}^\dagger_{\mathbf{k}\sigma l}\hat{\alpha}_{\mathbf{k}\sigma l} \right\rangle = \frac{1}{\exp\left(\frac{E_{\mathbf{k}l}}{k_{\mathrm{B}}T}\right) + 1} \tag{5.14}$$

Further, it is convenient to construct the energy density matrix, which in analogy to the energy matrix $\xi_{\mathbf{k}l}$ takes the following form:

$$\underline{n}_{\mathbf{k}l} = \begin{pmatrix} n_{\mathbf{k}l} & -\Delta_{\mathbf{k}l}\theta_{\mathbf{k}l} \\ -\Delta^*_{\mathbf{k}l}\theta_{\mathbf{k}l} & 1 - n_{-\mathbf{k}l} \end{pmatrix} \tag{5.15}$$

This density matrix can be also diagonalized by performing Bogoliubov–Valatin transformation. With the unitary matrix $\underline{U}_{\mathbf{k}l}$ one finds:

$$\underline{U}^\dagger_{\mathbf{k}l} \cdot \underline{n}_{\mathbf{k}l} \cdot \underline{U}_{\mathbf{k}l} = \begin{pmatrix} \nu_{\mathbf{k}l} & 0 \\ 0 & 1 - \nu_{-\mathbf{k}l} \end{pmatrix} \tag{5.16}$$

5.2. Noncentrosymmetric superconductors

Next, we discuss a new class of the superconducting system, the crystal structure of which lacks an inversion center. These superconductors without inversion symmetry are called noncentrosymmetric (NCS) and are characterized by the appearance of a strong Rashba type spin–orbit coupling (SOC). As a result, one observes in NCS (i) lifting of the band degeneracy associated with a splitting into a two–band structure and, more importantly, for the first time in the history of superconductivity (ii) the mixture of both singlet and triplet contributions to the superconducting gaps is possible [16–18, 120].

5.2.1. Strong Rashba–type SOC

Let us start with the properties of the antisymmetric spin–orbit coupling (ASOC) in a noncentrosymmetric crystal and discuss them in some details. First, the appearance of ASOC modifies the effective Hamiltonian for noninteracting electrons in the normal state in the following way [121]:

$$\hat{H}_0 = \sum_{\mathbf{k}\sigma\sigma'} \hat{c}^{\dagger}_{\mathbf{k}\sigma} \left[\xi_{\mathbf{k}}\delta_{\sigma\sigma'} + \boldsymbol{\gamma}_{\mathbf{k}} \cdot \boldsymbol{\tau}_{\sigma\sigma'}\right] \hat{c}_{\mathbf{k}\sigma'} \tag{5.17}$$

with $\xi_{\mathbf{k}}$ being the band energy measured from the Fermi level, $\sigma, \sigma' = \uparrow, \downarrow$ and $\boldsymbol{\tau}$ corresponding to the vector of the Pauli matrices $\boldsymbol{\tau} = \{\tau^x, \tau^y, \tau^z\}$. The new term in Hamiltonian[2] describes an antisymmetric spin–orbit coupling [120] through the vector $\boldsymbol{\gamma}_{\mathbf{k}}$ of the form:

$$\boldsymbol{\gamma}_{\mathbf{k}} = \frac{\hbar}{4mc^2}\frac{1}{\mathrm{V}}\int\limits_{\mathrm{V}} d^3r\, \boldsymbol{\nabla} U(\mathbf{r}) \times \mathbf{v}_{\mathbf{k}}(\mathbf{r}) \tag{5.18}$$

with $\mathbf{v}_{\mathbf{k}}(\mathbf{r})$ being the effective group velocity and $U(\mathbf{r})$ denoting the lattice potential. It should be noted that in cases of an inversion symmetry with $U(-\mathbf{r}) = U(\mathbf{r})$ the vector $\boldsymbol{\gamma}_{\mathbf{k}}$ vanishes, as expected, by performing a spatial integration over the volume V. Moreover, due to the dependence on the lattice potential, the antisymmetric spin–orbit coupling reflects the underlying symmetry of the crystal. In other words, the vector $\boldsymbol{\gamma}_{\mathbf{k}}$ has the property $g\boldsymbol{\gamma}_{g^{-1}\mathbf{k}} = \boldsymbol{\gamma}_{\mathbf{k}}$ with g being the symmetry operation of the crystallographic point group $\mathcal{G}$. Furthermore, the antisymmetric spin–orbit coupling can be associated with an effective internal ($\mathbf{k}$–dependent) magnetic field $\mathbf{b}_{\mathbf{k}}$

$$\boldsymbol{\gamma}_{\mathbf{k}} = -\boldsymbol{\gamma}_{-\mathbf{k}} = -\frac{\gamma\hbar}{2}\mathbf{b}_{\mathbf{k}}\ , \tag{5.19}$$

which, as we will show in the next section 5.2.2, lifts the band degeneracy. Here, the quantity $\gamma = 2g\mu_B/\hbar$ represents the gyromagnetic ratio. In order to have two distinct bands we assume a strong coupling limit for the antisymmetric spin–orbit coupling $\boldsymbol{\gamma}_{\mathbf{k}}$ and use a parametrization $\boldsymbol{\gamma}_{\mathbf{k}} = \alpha_{\mathrm{so}}\mathbf{f}_{\mathbf{k}}$ with α_{so} being the strength of the coupling and $\mathbf{f}_{\mathbf{k}}$ representing

---

[2] which marked with red color in Eq. (5.17)

the normalized vector function, which describes the anisotropy of the interaction:

$$\mathbf{f_k} = \frac{\boldsymbol{\gamma}_\mathbf{k}}{\sqrt{\langle \|\boldsymbol{\gamma}_\mathbf{k}\|^2 \rangle_{\mathrm{FS}}}} \tag{5.20}$$

with the norm $f_\mathbf{k} = \|\boldsymbol{\gamma}_\mathbf{k}\| / \sqrt{\langle \|\boldsymbol{\gamma}_\mathbf{k}\|^2 \rangle_{\mathrm{FS}}}$. Here, we introduce the Fermi surface (FS) average $\langle \ldots \rangle_{\mathrm{FS}}$, which for a given **k**–dependent function $z(\mathbf{k})$ is defined:

$$\langle z(\mathbf{k}) \rangle_{\mathrm{FS}} = \int\limits_0^{2\pi} d\phi \int\limits_0^{\pi} d\theta \sin\theta z(\mathbf{k}) \tag{5.21}$$

with azimuthal ϕ and polar θ angles.

In order to illustrate the **k**–dependence of antisymmetric spin–orbit coupling let us consider two important examples. For the tetragonal point group symmetry $\mathcal{G} = C_{4v}$, which is applicable for $\mathrm{CePt_3Si}$ [15], the ASOC reads:

$$\boldsymbol{\gamma}_\mathbf{k} = \gamma_\perp (\hat{\mathbf{k}} \times \hat{\mathbf{e}}_z) + \gamma_\| \hat{k}_x \hat{k}_y \hat{k}_z (\hat{k}_x^2 - \hat{k}_y^2) \hat{\mathbf{e}}_z \tag{5.22}$$

It should be mentioned that for $\gamma_\| = 0$ one can recognize the case of the Rashba interaction in two–dimensional systems [122, 123]. An illustration of the ASOC for C_{4v} point group[3] in the leading order is shown in Fig. 5.1. In this case one finds anysotropic interaction along the z–axes. For the cubic point group $\mathcal{G} = O(432)$, which is relevant for $\mathrm{Li_2Pd_xPt_{3-x}B}$ [124], $\boldsymbol{\gamma}_\mathbf{k}$ takes the following form:

$$\boldsymbol{\gamma}_\mathbf{k} = \gamma_1 \hat{\mathbf{k}} - \gamma_3 [\hat{k}_x (\hat{k}_y^2 + \hat{k}_z^2) \hat{\mathbf{e}}_x + \hat{k}_y (\hat{k}_z^2 + \hat{k}_x^2) \hat{\mathbf{e}}_y + \hat{k}_z (\hat{k}_x^2 + \hat{k}_y^2) \hat{\mathbf{e}}_z] \tag{5.23}$$

Here, the first term with γ_1 describes the isotropic spin–orbit coupling, whereas the anisotropy of interaction is given by the term with γ_3. Thus, the case with the isotropic two–band splitting can be realized by considering only the term with γ_1.

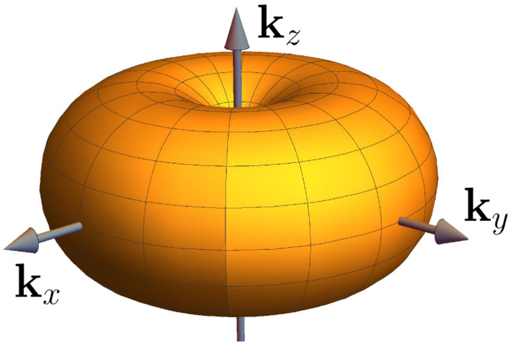

Figure 5.1: Representation of the ASOC $\gamma_\mathbf{k}$ for C_{4v} point group described by Eq. (5.22) in momentum space. Strong anisotropy along the k_z–axis is illustrated.

---

[3] will be important for discussions in Chap. 6

5.2.2. Superconducting state

What are the consequences of the ASOC for the superconducting state? In order to answer this question we construct, first, in analogy to the two–band case (see sec. 5.1), an energy matrix $\underline{\xi}^0_{\mathbf{k}}$ of a noncentrosymmetric superconductor, which takes in the spin representation the following form:

$$\underline{\xi}^0_{\mathbf{k}} = \begin{pmatrix} \xi_{\mathbf{k}}\mathbb{1} + \boldsymbol{\gamma}_{\mathbf{k}} \cdot \boldsymbol{\tau} & \boldsymbol{\Delta}_{\mathbf{k}} \\ \boldsymbol{\Delta}^{\dagger}_{\mathbf{k}} & -[\xi_{-\mathbf{k}}\mathbb{1} + \boldsymbol{\gamma}_{-\mathbf{k}} \cdot \boldsymbol{\tau}]^T \end{pmatrix} \tag{5.24}$$

This 4×4 matrix represents an extension of the Hamiltonian from Eq. (5.17) by terms characterizing the off–diagonal long range order and described by the energy gap matrix $\boldsymbol{\Delta}_{\mathbf{k}}$. Now, due to the presence of the ASOC the classification of the superconducting order parameter with respect to spin singlet (even parity) and spin triplet (odd parity) is no longer valid. Thus, the mixture of both is possible. Sigrist and co-workers have demonstrated [17, 18] that the ASOC is not destructive for the triplet pairing, if one assumes $\mathbf{d}_{\mathbf{k}} \parallel \boldsymbol{\gamma}_{\mathbf{k}}$. This implies that we can make the following ansatz for the energy gap matrix:

$$\boldsymbol{\Delta}_{\mathbf{k}} = \left(\Delta_s(T)\mathbb{1} + \mathbf{d}_{\mathbf{k}}(T) \cdot \boldsymbol{\tau}\right) i\tau^y \; , \tag{5.25}$$

with $\Delta_s(T)$ and $\mathbf{d}_{\mathbf{k}}(T)$ reflecting the singlet and triplet part of the pair potential, respectively. Also quantity $\boldsymbol{\tau}$ represents here the vector of Pauli spin matrices. The energy matrix $\underline{\xi}^0_{\mathbf{k}}$ can be block–diagonalized by performing an unitary transformation, which is described by the matrix $\mathbf{U}_{\mathbf{k}}$ in the form of a SU(2) rotation:

$$\mathbf{U}_{\mathbf{k}} = \mathrm{e}^{-i\frac{\theta_\gamma}{2}\hat{\mathbf{n}}_\gamma \cdot \boldsymbol{\tau}} \; ; \; \cos\theta_\gamma = \hat{\boldsymbol{\gamma}}_{\mathbf{k}} \cdot \hat{\mathbf{z}} \; ; \; \mathbf{n}_\gamma = \frac{\boldsymbol{\gamma}_{\mathbf{k}} \times \hat{\mathbf{z}}}{\|\boldsymbol{\gamma}_{\mathbf{k}} \times \hat{\mathbf{z}}\|} \tag{5.26}$$

This transformation [4] corresponds to a rotation in a spin space into the $\hat{\mathbf{z}}$–direction about the polar angle θ_γ between $\boldsymbol{\gamma}_{\mathbf{k}}$ and $\hat{\mathbf{z}}$. Physically, this describes a switch from the spin into the *helicity–band basis* or simply *band basis*, which is convenient in the limit of large spin–orbit coupling. In this case one can use the two–band description for NCS. A straightforward extension of this unitary transformation into Nambu space reads [125]:

$$\underline{\xi}^{(band)}_{\mathbf{k}} \equiv \underline{U}^{\dagger}_{\mathbf{k}} \underline{\xi}^0_{\mathbf{k}} \underline{U}_{\mathbf{k}} = \begin{pmatrix} \xi_{\mathbf{k}+} & 0 & 0 & \Delta_{\mathbf{k}+} \\ 0 & \xi_{\mathbf{k}-} & -\Delta_{\mathbf{k}-} & 0 \\ 0 & -\Delta^*_{\mathbf{k}-} & -\xi_{\mathbf{k}-} & 0 \\ \Delta^*_{\mathbf{k}+} & 0 & 0 & -\xi_{\mathbf{k}+} \end{pmatrix} \; ; \; \underline{U}_{\mathbf{k}} = \begin{pmatrix} \mathbf{U}_{\mathbf{k}} & 0 \\ 0 & \mathbf{U}^*_{\mathbf{k}} \end{pmatrix} \tag{5.27}$$

with the energy values $\xi_{\mathbf{k}\mu} = \xi_{\mathbf{k}} + \mu\|\boldsymbol{\gamma}_{\mathbf{k}}\|$ and the gap functions $\Delta_{\mathbf{k}\mu} = \Delta_s(T) + \mu\Delta_{tr}(T)f_{\mathbf{k}}$. Here, the quantities $\Delta_s(T)$ and $\Delta_{tr}(T)$ describe the singlet and triplet contribution to

---

[4] similar to the Bogoliubov–Valatin transformation for the two–band superconductors (see section 5.1.2)

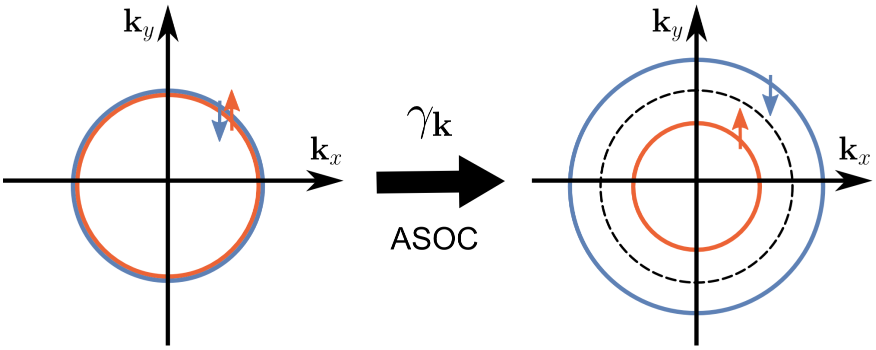

Figure 5.2: Illustration of the band splitting in the momentum space due to an ASOC $\gamma_\mathbf{k}$. On the left the cross–section of the Fermi surface in the k_x–k_y plane for a free electron gas is presented. Owing to the ASOC the Fermi surface is then splitted into two bands with corresponding spin polarized (↑ or ↓) electrons, as shown on the right.

the pair potential, respectively. Introducing a band–index $\mu = \pm 1$, one may write the equilibrium energy matrix in the band basis in the compact form:

$$\underline{\xi}^0_{\mathbf{k}\mu} = \begin{pmatrix} \xi_{\mathbf{k}\mu} & \mu\Delta_{\mathbf{k}\mu} \\ \mu\Delta^*_{\mathbf{k}\mu} & -\xi_{-\mathbf{k}\mu} \end{pmatrix} \tag{5.28}$$

In analogy, one can find for the equilibrium density matrix:

$$\underline{n}^0_{\mathbf{k}\mu} = \begin{pmatrix} \frac{1}{2} - \xi_{\mathbf{k}\mu}\theta_{\mathbf{k}\mu} & -\mu\Delta_{\mathbf{k}\mu}\theta_{\mathbf{k}\mu} \\ -\mu\Delta^*_{\mathbf{k}\mu}\theta_{\mathbf{k}\mu} & \frac{1}{2} + \xi_{\mathbf{k}\mu}\theta_{\mathbf{k}\mu} \end{pmatrix} \tag{5.29}$$

with the band–selected function

$$\theta_{\mathbf{k}\mu} = \frac{1}{2E_{\mathbf{k}\mu}} \tanh \frac{E_{\mathbf{k}\mu}}{2k_\mathrm{B}T}$$

and $E_{\mathbf{k}\mu} = [\xi^2_{\mathbf{k}\mu} + \Delta^2_{\mathbf{k}\mu}]^{1/2}$.

It is worth mentioning that this type of the spin–orbit coupling (SOC) leads to two important properties of the noncentrosymmetric superconductors: First, one observes lifting of the spin and band degeneracy (see Fig. 5.2) associated with the splitting into a two–band structure [5]. Second, for the first time in a history of a superconductivity the mixture of the superconducting order parameter with respect to spin singlet (even parity) and spin triplet (odd parity) is possible. In other words, the parity for noncentrosymmetric superconductors is no longer a good quantum number.

---

[5] compare the form of the energy $\underline{\xi}^0_{\mathbf{k}\mu}$ and density $\underline{n}^0_{\mathbf{k}\mu}$ matrices for NCS with their counterparts for a two–band superconductor from Eqs. (5.8) and (5.15), respectively

5.2.3. Energy gap equation

Now, let us focus on the energy gap equation for a noncentrosymmetric superconductor in the helicity band basis (with $\mu = \pm 1$). Its self–consistent form is given by [6]:

$$\Delta_{\mathbf{k}\mu} = -\sum_{\nu=\pm 1}\sum_{\mathbf{p}} V_{\mathbf{kp}}^{\mu\nu}\theta_{\mathbf{p}\nu}\Delta_{\mathbf{p}\nu} \tag{5.30}$$

with $V_{\mathbf{kp}}^{\mu\nu}$ being the phenomenological pairing interaction and the function $\theta_{\mathbf{p}\nu}$ defined in previous section. In accordance to Refs. [126, 127] we choose for $V_{\mathbf{kp}}^{\mu\nu}$ the generalized two–gap weak–coupling ansatz of the following form:

$$V_{\mathbf{kp}}^{\mu\nu} = -\left[V_s + \mu\nu V_{tr} f_{\mathbf{k}} f_{\mathbf{p}} + V_m\left(\mu f_{\mathbf{k}} + \nu f_{\mathbf{p}}\right)\right]\Theta\left(\epsilon_0 - |\xi_{\mathbf{k}\mu}|\right)\Theta\left(\epsilon_0 - |\xi_{\mathbf{p}\nu}|\right) \tag{5.31}$$

with $\mu, \nu = \pm 1$. Here, we assume that the pairing interaction appears in the small region $2\epsilon_0$ around the Fermi energy of both bands. Furthermore, due to the different behaviors under parity one can distinguish between three different contributions to the pairing interaction. First, there is singlet pairing channel (V_s), which has the even parity with respect to $\mathbf{k} \to -\mathbf{k}$. Then, we take into account the term with the odd parity $\mathbf{k} \to -\mathbf{k}$, which corresponds to triplet pairing channel (V_{tr}). Finally, there is a contribution with a mixed parity (V_m), which originates from the Dzyaloshinskii–Moriya (DM) interaction [127–129].

Now, let us define the dimensionless pairing interaction constants

$$\lambda_\alpha = N(0)V_\alpha \quad \text{with} \ \alpha = s, tr, m \tag{5.32}$$

with $N(0)$ being the density of states (DoS) on the Fermi surface for one spin projection. As a result, by using the definitions (5.31) and (5.32) we can rewrite the energy gap equation (5.30) into the matrix form:

$$\left\{-\boldsymbol{\lambda}^{-1} + \begin{pmatrix} \Xi_0 & \Xi_1 \\ \Xi_1 & \Xi_2 \end{pmatrix}\right\} \cdot \begin{pmatrix} \Delta_s \\ \Delta_{tr} \end{pmatrix} = \begin{pmatrix} 0 \\ 0 \end{pmatrix} \tag{5.33}$$

with the interaction matrix $\boldsymbol{\lambda}$

$$\boldsymbol{\lambda} = \begin{pmatrix} \lambda_s & \lambda_m \\ \lambda_m & \lambda_{tr} \end{pmatrix} \ ; \ \boldsymbol{\lambda}^{-1} = \frac{1}{|\boldsymbol{\lambda}|}\begin{pmatrix} \lambda_{tr} & -\lambda_m \\ -\lambda_m & \lambda_s \end{pmatrix} , \tag{5.34}$$

where $|\boldsymbol{\lambda}| \equiv \lambda_s\lambda_{tr} - \lambda_m^2$ is the determinant of the matrix $\boldsymbol{\lambda}$, and with the quantity

$$\Xi_n = \textstyle\sum_\mu \langle(\mu f_{\mathbf{k}})^n \theta_{\mathbf{k}\mu}\rangle \ , \quad n = 0, 1, 2. \tag{5.35}$$

It should be noted that the form of energy gap equation (5.33) for noncentrosymmetric

---

[6] the description is similar to that for the ordinary two–band superconductors (see Eq: (5.3))

superconductor is reminiscent of gap equation (5.4) formulated for s–wave two–band superconducting system. However, in case of NCS one deals with more general situation due to the complex structure of the pairing interactions.

The energy gap equation (5.33) can be solved analytically for different temperature regimes (see Appendix A). However, for this thesis the low temperature limit is important. In this limit ($T \to 0$) the integrals Ξ_n defined in Eq. (5.35) take the following form:

$$\Xi_n = \sum_\mu \left\langle (\mu f_{\mathbf{k}})^n \ln\left(\frac{2\epsilon_0}{\Delta_{\mathbf{k}\mu}}\right)\right\rangle = \sum_\mu \left\langle (\mu f_{\mathbf{k}})^n \ln\left(\frac{2\epsilon_0}{\Delta_s\left(1+\mu f_{\mathbf{k}} t\right)}\right)\right\rangle \;, \tag{5.36}$$

where we have defined a triplet-to-singlet ratio $t = \Delta_{tr}/\Delta_s$. For the small values of t we can perform a Taylor expansion for the integrals Ξ_n, which leads to:

$$\Xi_n = \ln\left(\frac{2\epsilon_0}{\Delta_s}\right)\sum_\mu \langle(\mu f_{\mathbf{k}})^n\rangle - \sum_\mu \left\langle (\mu f_{\mathbf{k}})^n \sum_{m=1}^{\infty} (-1)^{m+1}\frac{(\mu f_{\mathbf{k}} t)^m}{m}\right\rangle \tag{5.37}$$

This result can now be used for solving the energy gap equation (5.33). Substituting Eq. (5.37) into Eq. (5.33) yields:

$$\begin{aligned} 2\ln\left(\frac{2\epsilon_0}{\Delta_s}\right) &= \frac{\lambda_{tr}}{\lambda_s\lambda_{tr}-\lambda_m^2} + \left[2t - \frac{\lambda_m}{\lambda_s\lambda_{tr}-\lambda_m^2}\right] t \\ 2\ln\left(\frac{2\epsilon_0}{\Delta_s}\right) &= \frac{\lambda_s}{\lambda_s\lambda_{tr}-\lambda_m^2} + \left[2t - \frac{\lambda_m}{\lambda_s\lambda_{tr}-\lambda_m^2}\right] \frac{1}{t} \end{aligned} \tag{5.38}$$

From these equations one can obtain the triplet to singlet ratio t:

$$t = \frac{\lambda_m}{\lambda_s - \lambda_{tr} + 2|\boldsymbol{\lambda}|} \tag{5.39}$$

with the determinant of matrix $\boldsymbol{\lambda}$ from Eq. (5.34).

5.3. Collective excitations

A fundamental property of all types of superconductors is the appearance of a collective excitation, which is a result of breaking the continuous $U(1)$ symmetry. This is the statement of the general Goldstone theorem, which was formulated in 1962 [2]. For instance, in neutral superfluids with a two–component order parameter one can excite a so–called Anderson–Bogoliubov or gauge mode [4–6], which corresponds to the angular excitation in the Mexican hat potential of the free energy $\mathcal{F}$ (see Fig. 1.1). The existence of this phase mode is necessary to restore the particle conservation law. On the other hand, in charged systems, like single band superconductors, this collective excitation is shifted to the plasma mode according to the Anderson–Higgs mechanism [6, 8] and appears in most cases in the quasiparticle continuum. This is the result of the long–range Coulomb interaction. Moreover, one–band superconductors exhibit, in addition, amplitude fluctuations of the order parameter. Due to the approximate particle–hole symmetry of the superconducting excitations and similarities to the Lorentz invariant theory [130], these radial excitation in the Mexican hat potential of the free energy $\mathcal{F}$ (see Fig. 1.1) corresponds to the Higgs mode from the high energy physics.

The s–wave two–band superconductors exhibit beside the amplitude (Higgs) and the phase (gauge) mode also a new collective excitation [116], which occurs due to the Josephson coupling between the bands and corresponds to the fluctuations in the relative phase of the two coupled order parameters. In other words, this mode represents out–of–phase oscillations of the superconducting condensates. In close to equilibrium case, where the linearized response can be expected, the phase (Leggett) and the amplitude (Higgs) modes are decoupled and correspond to mutually orthogonal fluctuation. An illustration for both modes in two–band superconductors is shown in Fig. 5.3.

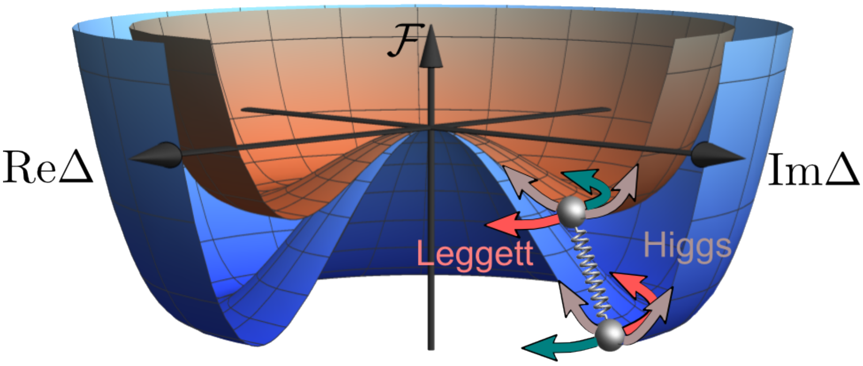

Figure 5.3: Illustration of the effective free–energy landscape $\mathcal{F}$ for a two–band superconductor with the red and the blue Mexican hat potential, representing the upper and the lower band, respectively. The amplitude (Higgs) mode and the phase (Leggett) mode are shown with the gray and the red/green arrows, respectively.

What can we learn from the collective modes? First of all, these are the characteristic features for all types of superconductors and reflects the properties of the superconducting condensates. In fact, the frequency of the Higgs oscillation in a superconductor corresponds to the twice of the value of the order parameter amplitude [50, 53]. Further, from the phase (Leggett) mode one can get the information about the interband coupling between the bands. Indeed, in the long wavelength limit ($|\mathbf{q}| \to 0$) the frequency of the Leggett mode takes for s–wave two–band superconductors the following form:

$$\omega_{\mathrm{L}}^2(\mathbf{q} \to 0) = 4V_{12}\Delta_1\Delta_2 \frac{1}{V_{11}V_{22} - V_{12}^2} \left(\frac{1}{N_{\mathrm{F}1}} + \frac{1}{N_{\mathrm{F}2}} \right) \tag{5.40}$$

with $N_{\mathrm{F}l}$ being the density of states at the Fermi level for each band l. This can be important for studying the novel type of the superconducting systems without inversion symmetry, where a complex mixing of singlet and triplet superconductivity occurs. For these superconductors it is not *a priori* clear, whether there is a coupling between the condensates and, as a result, if the Leggett mode may appear. Finally, from the theoretical point of view the collective modes are necessary to restore the particle conservation law, which is broken together with the $U(1)$ symmetry.

In general, to excite collective modes in a superconducting system, one needs to apply external perturbation, which shakes the superconducting condensate. This is, however, a quite challenging task, since both Higgs and Leggett modes have neither charge nor momentum. While the Leggett mode is though infrared active [131] and was so far observed in Raman experiment on an s–wave two–band superconductor MgB_2 [132], Higgs mode has negligibly small coupling to the possible response functions due to the approximate particle–hole symmetry and is not directly detectable (see discussion in the introduction). The theoretical investigations of the possibility to direct excite these collective modes in different types of two–band superconductors is the subject of our further considerations.

Chapter 6

Dynamical response of noncentrosymmetric superconductors

One way to study the dynamical properties of a superconductor consists in using the framework of the matrix kinetic theory (MKT). Here, the central role is playing the matrix kinetic equation, which corresponds to the Landau–Boltzmann equation [133, 134] for the normal Fermi liquids. Its first formulation was done in 1969 for the single band superconductors [49]. Since that time the theory was extended to the two–band case [118] and used to discus the Raman response properties of the noncentrosymmetric superconductors [120]. However, the matrix kinetic approach is limited to the quasiklassical regime with the transferred momentum $|\mathbf{q}| \ll k_{\mathrm{F}}$ and the energy $\hbar\omega \ll E_{\mathrm{F}}$. While the amplitude fluctuations of the order parameter show in this case only negligible small coupling to the response functions, the phase fluctuations can be still observable.

In this chapter we recapitulate the most important principles of the kinetic theory and extend it to the case of the noncentrosymmetric superconductors. In particular, we calculate all collective excitations corresponding to the condensate phase dynamics of NCS and investigate their properties.

6.1. Matrix Kinetic Theory

The external perturbation $\delta\zeta$ of a superconducting system leads to the modification of its equilibrium density matrix $\underline{n}^0_{\mathbf{k}\mu}$. Within the framework of the matrix kinetic theory we focus on the linear response of the noncentrosymmetric superconductors to a scalar electromagnetic potential $\phi(\mathbf{q}, \omega)$. The external field is assumed to vary with the frequency ω and momentum $\mathbf{q}$, so that it takes the form $\propto \exp(i\mathbf{q}\cdot\mathbf{r} - i\omega t)$. In addition, there also exist molecular potentials, which consist of the short–range Fermi–liquid interactions. However, these potentials lead to a renormalization of the electron mass and, therefore, will not be taken into further discussions. Moreover, due to the long–range Coulomb interaction $V_{\mathbf{q}} = 4\pi e^2/\mathbf{q}^2$ in a charged system, one also needs to take into account a charge fluctuation term, which can be incorporated into the considerations by means of the random phase approximation (RPA), i.e.

$$\chi = \frac{\chi^{(0)}}{[1 - V_{\mathbf{q}}\chi^{(0)}]} \ , \tag{6.1}$$

where χ is a generalized response function and $\chi^{(0)}$ its unrenormalized counterpart.

Now, the response to the effective perturbation $\delta\zeta \equiv e\phi(\mathbf{q},\omega) + V_{\mathbf{q}}\delta n(\mathbf{q},\omega)$, with δn being the total density response of the system, is described by a modified density matrix for each band μ [49, 120]

$$\underline{n}^{\mu}_{\mathbf{p}\mathbf{p}'} = \begin{pmatrix} \left\langle \hat{c}^{\dagger}_{\mathbf{p}}\hat{c}_{\mathbf{p}'} \right\rangle_{\mu} & \left\langle \hat{c}^{\dagger}_{\mathbf{p}}\hat{c}^{\dagger}_{-\mathbf{p}'} \right\rangle_{\mu} \\ \left\langle \hat{c}_{-\mathbf{p}}\hat{c}_{\mathbf{p}'} \right\rangle_{\mu} & \left\langle \hat{c}_{-\mathbf{p}}\hat{c}^{\dagger}_{-\mathbf{p}'} \right\rangle_{\mu} \end{pmatrix} \ , \tag{6.2}$$

which is a 2×2–matrix in Nambu–space with $\mathbf{p} = \hbar(\mathbf{k} + \mathbf{q}/2)$, $\mathbf{p}' = \hbar(\mathbf{k} - \mathbf{q}/2)$. The Fourier transformation of $\underline{n}^{\mu}_{\mathbf{p}\mathbf{p}'}$ describes the evolution of the system in space and time after perturbation $\delta\zeta$. More importantly, the perturbation $\delta\zeta$ induces fluctuations of the pairing amplitude $g_{\mathbf{k}\mu} = -\theta_{\mathbf{k}\mu}\Delta_{\mathbf{k}\mu}$ and, in addition, phase fluctuations of the superconducting order parameter, which are associated with the collective phase modes in NCS.

The evolution of the density matrix $\underline{n}^{\mu}_{\mathbf{p}\mathbf{p}'}$ in momentum space is given by the von Neumann equation

$$\hbar\omega\, \underline{n}^{\mu}_{\mathbf{p}\mathbf{p}'} + \sum_{\mathbf{p}''} [\underline{n}^{\mu}_{\mathbf{p}\mathbf{p}''}, \underline{\xi}^{\mu}_{\mathbf{p}''\mathbf{p}'}] = 0 \ , \tag{6.3}$$

which describes the quantum dynamic of the system in the clean limit. The 2×2 energy matrix $\underline{\xi}^{\mu}_{\mathbf{p}''\mathbf{p}'}$ plays here the role of the Hamiltonian of the system. This Eq (6.3) is valid for the whole quasiklassical regime ($|\mathbf{q}| \ll k_{\mathrm{F}}$, $\hbar\omega \ll E_{\mathrm{F}}$) and can be solved by linearization density matrix $\underline{n}^{\mu}_{\mathbf{p}\mathbf{p}'}$, as well as, energy matrix $\underline{\xi}^{\mu}_{\mathbf{p}\mathbf{p}'}$. Therefore, we make the following ansatz:

$$\begin{array}{lclclcl} \underline{n}^{\mu}_{\mathbf{p}\mathbf{p}'} & \equiv & \underline{n}_{\mathbf{k}\mu}(\mathbf{q},\omega) & = & \underline{n}^{0}_{\mathbf{k}\mu}\delta_{\mathbf{q},0} & + & \delta\underline{n}_{\mathbf{k}\mu}(\mathbf{q},\omega) \\ \underline{\xi}^{\mu}_{\mathbf{p}\mathbf{p}'} & \equiv & \underline{\xi}_{\mathbf{k}\mu}(\mathbf{q},\omega) & = & \underline{\xi}^{0}_{\mathbf{k}\mu}\delta_{\mathbf{q},0} & + & \delta\underline{\xi}_{\mathbf{k}\mu}(\mathbf{q},\omega) \end{array} \tag{6.4}$$

with the equilibrium quasiparticle energy $\underline{\xi}^{0}_{\mathbf{k}\mu}$ and the distribution function $\underline{n}^{0}_{\mathbf{k}\mu}$ defined in Eqs. (5.28) and (5.29), respectively. The momentum and frequency–dependent deviation from equilibrium can be defined in the appropriate way as 2×2 matrices in the Nambu space:

$$\delta\underline{n}_{\mathbf{k}\mu} = \begin{pmatrix} \delta n_{\mathbf{k}\mu} & \mu\delta g_{\mathbf{k}\mu} \\ \mu\delta g^{*}_{\mathbf{k}\mu} & -\delta n_{-\mathbf{k}\mu} \end{pmatrix} \quad \text{and} \quad \delta\underline{\xi}_{\mathbf{k}\mu} = \begin{pmatrix} \delta\xi_{\mathbf{k}\mu} & \mu\delta\Delta_{\mathbf{k}\mu} \\ \mu\delta\Delta^{*}_{\mathbf{k}\mu} & -\delta\xi_{-\mathbf{k}\mu} \end{pmatrix} \tag{6.5}$$

with $\delta\xi_{\mathbf{k}\mu} = \delta\xi_{-\mathbf{k}\mu} = \delta\zeta$. Thus, for each band $\mu = \pm 1$ the matrix equation (6.3) takes the following linear form:

$$\hbar\omega\delta\underline{n}_{\mathbf{k}\mu} + \delta\underline{n}_{\mathbf{k}\mu}\underline{\xi}^{0}_{\mathbf{k}-\frac{\mathbf{q}}{2}\mu} - \underline{\xi}^{0}_{\mathbf{k}+\frac{\mathbf{q}}{2}\mu}\delta\underline{n}_{\mathbf{k}\mu} = \delta\underline{\xi}_{\mathbf{k}\mu}\underline{n}^{0}_{\mathbf{k}-\frac{\mathbf{q}}{2}\mu} - \underline{n}^{0}_{\mathbf{k}+\frac{\mathbf{q}}{2}\mu}\delta\underline{\xi}_{\mathbf{k}\mu} \tag{6.6}$$

Therefore, we have to solve in total a set of eight equations. Further, it is convenient to decompose the diagonal elements of the energy and density deviation matrices according to their parity with respect to $\mathbf{k} \to -\mathbf{k}$:

$$\begin{aligned} \delta n^{(s)}_{\mathbf{k}\mu} &= \frac{1}{2}\left(\delta n_{\mathbf{k}\mu} + s\delta n_{-\mathbf{k}\mu}\right) \\ \delta \xi^{(s)}_{\mathbf{k}\mu} &= \frac{1}{2}\left(\delta \xi_{\mathbf{k}\mu} + s\delta \xi_{-\mathbf{k}\mu}\right) \end{aligned} \tag{6.7}$$

with the labeling $s = \pm 1$. On the same way, we separate the off–diagonal components into their real and imaginary parts:

$$\begin{aligned} \delta g^{(s)}_{\mathbf{k}\mu} &= \frac{1}{2}\left(\delta g_{\mathbf{k}\mu}\frac{\Delta^*_{\mathbf{k}\mu}}{|\Delta_{\mathbf{k}\mu}|} + s\frac{\Delta_{\mathbf{k}\mu}}{|\Delta_{\mathbf{k}\mu}|}\delta g^*_{-\mathbf{k}\mu}\right) \\ \delta \Delta^{(s)}_{\mathbf{k}\mu} &= \frac{1}{2}\left(\delta \Delta_{\mathbf{k}\mu}\frac{\Delta^*_{\mathbf{k}\mu}}{|\Delta_{\mathbf{k}\mu}|} + s\frac{\Delta_{\mathbf{k}\mu}}{|\Delta_{\mathbf{k}\mu}|}\delta \Delta^*_{-\mathbf{k}\mu}\right) \end{aligned} \tag{6.8}$$

This decomposition has an advantage that the real part $\delta\Delta^{(+)}_{\mathbf{k}\mu}$ describes exclusively the amplitude fluctuations and the imaginary part $\Delta^{(-)}_{\mathbf{k}\mu}$ represents the "pure" phase fluctuations of the superconducting order parameter. By using the matrix inversion method described in details in Ref. [118,135] together with the defined in Eqs. (6.7) and (6.8) specifications, we obtain from the off–diagonal components of Eq. (6.3) the important relation between fluctuations of the pairing amplitude $g_{\mathbf{k}\mu}$ and phase fluctuations of the order parameter:

$$2\Delta_{\mathbf{k}\mu}[\delta g^{(-)}_{\mathbf{k}\mu} + \theta_{\mathbf{k}\mu}\delta\Delta^{(-)}_{\mathbf{k}\mu}] = \omega\lambda_{\mathbf{k}\mu}\delta\zeta - [\omega^2 - (\mathbf{q}\cdot\mathbf{v}_{\mathbf{k}\mu})^2]\lambda_{\mathbf{k}\mu}\frac{\delta\Delta^{(-)}_{\mathbf{k}\mu}}{2\Delta_{\mathbf{k}\mu}} \tag{6.9}$$

Here, we have identified the condensate response or the generalized Tsuneto function [136], which in the NCS case takes the following form:

$$\lambda_{\mathbf{k}\mu} = 4\Delta^2_{\mathbf{k}\mu}\frac{\theta_{\mathbf{k}\mu}[\omega^2 - (\mathbf{q}\cdot\mathbf{v}_{\mathbf{k}\mu})^2] + \Phi_{\mathbf{k}\mu}(\mathbf{q}\cdot\mathbf{v}_{\mathbf{k}\mu})^2}{(\mathbf{q}\cdot\mathbf{v}_{\mathbf{k}\mu})^2[\omega^2 - 4\xi^2_{\mathbf{k}\mu}] - \omega^2[\omega^2 - 4E^2_{\mathbf{k}\mu}]} \tag{6.10}$$

where $\mathbf{v}_{\mathbf{k}\mu} = \partial\xi_{\mathbf{k}\mu}/\partial\hbar\mathbf{k}$ and $\Phi_{\mathbf{k}\mu} = -\partial n_{\mathbf{k}\mu}/\partial\xi_{\mathbf{k}\mu}$ with momentum distribution function $n_{\mathbf{k}\mu}$. Importantly, this function generates the condensate density through the sum rule $\sum_{\mathbf{p}\mu}\lambda_{\mathbf{p}\mu} = N(0)\sum_\mu\langle\lambda_{\hat{\mathbf{p}}\mu}\rangle_{\mathrm{FS}} \equiv N(0)\lambda$, where $N(0)$ is the DoS at the Fermi level for one spin projection.

Further, from the diagonal components of Eq. (6.3) we find a relation, which describes the coupling between the phase fluctuations of the order parameter and the density response function for noncentrosymmetric superconductors:

$$\delta n_{\mathbf{k}\mu} = \left(\frac{(\mathbf{q}\cdot\mathbf{v}_{\mathbf{k}\mu})^2\,\varphi_{\mathbf{k}\mu}}{\omega^2 - (\mathbf{q}\cdot\mathbf{v}_{\mathbf{k}\mu})^2} - \lambda_{\mathbf{k}\mu}\right)\delta\zeta + \omega\lambda_{\mathbf{k}\mu}\frac{\delta\Delta^{(-)}_{\mathbf{k}\mu}}{2\Delta_{\mathbf{k}\mu}} \tag{6.11}$$

with $\varphi_{\mathbf{k}\mu} = \Phi_{\mathbf{k}\mu} - \lambda_{\mathbf{k}\mu}$ being the quasiparticle response. Since we are only interested in the condensate response of a superconductor, we may safely ignore these quasiparticle contributions $\propto \varphi_{\mathbf{k}\mu}$ in Eq. (6.11). Thus, we find for the density response function $\delta n_{\mathbf{k}\mu}$ the simplified expression:

$$\delta n_{\mathbf{k}\mu} = -\lambda_{\mathbf{k}\mu}\delta\zeta + \omega\lambda_{\mathbf{k}\mu}\delta\Delta^{(-)}_{\mathbf{k}\mu}/2\Delta_{\mathbf{k}\mu} \tag{6.12}$$

Here, it is also important to mention that due to the particle–hole symmetry the amplitude fluctuations of the order parameter show in the linear response approximation negligible small coupling to the response functions. Therefore, they can be neglected.

Finally, we can calculate the condensate density response, as follows:

$$\delta n_{\mathrm{s}} = \sum_{\mathbf{k}\mu} \delta n_{\mathbf{k}\mu} \ , \tag{6.13}$$

which is exclusively determined by the condensate response $\lambda_{\mathbf{k}\mu}$ and contains according to Eq. (6.12) the whole information on the relevant order parameter collective phase modes in NCS. Now, combining Eq. (6.9) for each band $\mu = \pm 1$ with both the superconducting gap equation (5.30) and its straightforward variation

$$\delta\Delta^{(-)}_{\mathbf{k}\mu} = \sum_{\mathbf{p}\nu} V^{\mu\nu}_{\mathbf{kp}} \delta g^{(-)}_{\mathbf{p}\nu} \tag{6.14}$$

where $\delta g^{(-)}_{\mathbf{p}\nu} = -\theta_{\mathbf{p}\mu}\delta\Delta^{(-)}_{\mathbf{p}\mu}$ and $V^{\mu\nu}_{\mathbf{kp}}$ is the pairing interaction defined in Eq. (5.31), we obtain the main result of our analysis:

$$\delta n_{\mathrm{s}}(\mathbf{q},\omega) = \frac{\omega^2_{\mathrm{G}}(\mathbf{q})[\omega^2 - \omega'^2_{\mathrm{L}}(\mathbf{q})]N(0)\lambda}{\omega^4 - [\omega^2_{\mathrm{P}}(\hat{\mathbf{q}}) + \omega^2_{\mathrm{G}}(\mathbf{q}) + \omega^2_{\mathrm{L}}(\mathbf{q})]\,\omega^2 + [\omega^2_{\mathrm{P}}(\hat{\mathbf{q}}) + \omega^2_{\mathrm{G}}(\mathbf{q})]\,\omega'^2_{\mathrm{L}}(\mathbf{q})} e\phi(\mathbf{q},\omega) \tag{6.15}$$

This will be discussed in details in the next sections.

6.2. New collective modes

Let us now take a closer look on the denominator of Eq. (6.15). Its zeros correspond to the strong fluctuations of the condensate density response and, consequently, represent the collective excitations in a noncentrosymmetric system. Thus, in order to obtain the collective modes in NCS we need to solve the quadratic equation with respect to ω^2:

$$\omega^4 - \left[\omega^2_{\mathrm{P}}(\hat{\mathbf{q}}) + \omega^2_{\mathrm{G}}(\mathbf{q}) + \omega^2_{\mathrm{L}}(\mathbf{q})\right]\omega^2 + \left[\omega^2_{\mathrm{P}}(\hat{\mathbf{q}}) + \omega^2_{\mathrm{G}}(\mathbf{q})\right]\omega'^2_{\mathrm{L}}(\mathbf{q}) = 0 \tag{6.16}$$

with $\hat{\mathbf{q}} = \mathbf{q}/|\mathbf{q}|$. Here, we identify the characteristic *gauge* mode frequency $\omega_{\mathrm{G}}(\mathbf{q})$ with $\omega^2_{\mathrm{G}}(\mathbf{q}) = \sum_\mu \langle\lambda_{\hat{\mathbf{p}}\mu}(\mathbf{q}\cdot\mathbf{v}_{\mathbf{p}\mu})^2\rangle_{\mathrm{FS}}/\lambda$ together with the *condensate plasma* mode frequency $\omega_{\mathrm{P}}(\hat{\mathbf{q}})$ with $\omega^2_{\mathrm{P}}(\hat{\mathbf{q}}) = 4\pi n e^2 \sum_\mu 3\,\langle\lambda_{\hat{\mathbf{p}}\mu}(\hat{\mathbf{q}}\cdot\hat{\mathbf{p}})^2\rangle_{\mathrm{FS}}/m$ of NCS. Also, as we will show later, the frequencies $\omega'_{\mathrm{L}}(\mathbf{q})$ and $\omega_{\mathrm{L}}(\mathbf{q})$ correspond to the new *Leggett* mode frequencies in noncentrosymmetric superconductors. A straightforward solution of Eq. (6.16) leads to the following results:

$$\omega_{1,2}^2 = \frac{1}{2}\Big(\omega_{\mathrm{P}}^2(\hat{\mathbf{q}}) + \omega_{\mathrm{G}}^2(\mathbf{q}) + \omega_{\mathrm{L}}^2(\mathbf{q})\Big)\left[1 \pm \sqrt{1 - 4\frac{[\omega_{\mathrm{P}}^2(\hat{\mathbf{q}}) + \omega_{\mathrm{G}}^2(\mathbf{q})]\,\omega_{\mathrm{L}}'^2(\mathbf{q})}{\left(\omega_{\mathrm{P}}^2(\hat{\mathbf{q}}) + \omega_{\mathrm{G}}^2(\mathbf{q}) + \omega_{\mathrm{L}}^2(\mathbf{q})\right)^2}}\,\right] \tag{6.17}$$

This expression can be further simplified by using a Taylor expansion of the square root, where by considering terms up to second order in $|\mathbf{q}|$ one gets

$$\omega_{1,2}^2 = \Big(\omega_{\mathrm{P}}^2(\hat{\mathbf{q}}) + \omega_{\mathrm{G}}^2(\mathbf{q}) + \omega_{\mathrm{L}}^2(\mathbf{q})\Big)\frac{[1 \pm 1]}{2} \mp \frac{[\omega_{\mathrm{P}}^2(\hat{\mathbf{q}}) + \omega_{\mathrm{G}}^2(\mathbf{q})]\,\omega_{\mathrm{L}}'^2(\mathbf{q})}{\omega_{\mathrm{P}}^2(\hat{\mathbf{q}}) + \omega_{\mathrm{G}}^2(\mathbf{q}) + \omega_{\mathrm{L}}^2(\mathbf{q})}\,. \tag{6.18}$$

Now, let us first discuss the case of the neutral system, where in the absence of the long–range Coulomb interaction the plasma frequency disappears $\omega_{\mathrm{P}}^2(\hat{\mathbf{q}}) = 0$. Thus, one finds from Eq. (6.18) two collective modes with the frequencies:

$$\begin{aligned}
\omega_1^2 &= \omega_{\mathrm{G}}^2(\mathbf{q}) + \mathcal{O}\left(\frac{\omega_{\mathrm{G}}^4(\mathbf{q})}{\omega_{\mathrm{L}}^2(\mathbf{q})}\right) && \text{Gauge mode}\\
\omega_2^2 &= \omega_{\mathrm{L}}^2(\mathbf{q}) + \mathcal{O}\left(\frac{\omega_{\mathrm{G}}^4(\mathbf{q})}{\omega_{\mathrm{L}}^2(\mathbf{q})}\right) && \text{Leggett mode}
\end{aligned} \tag{6.19}$$

The first solution ω_1 corresponds to the characteristic *gauge* mode of NCS, which is seen in the first order to emerge as sum of the band–selected gauge modes. Moreover, in the low temperature limit one finds that the gauge mode is independent on the point group symmetry and takes similar form to the two–band superconductors [116, 137]:

$$\omega_{\mathrm{G}}^2(\mathbf{q}) = \frac{\sum_\mu \langle \lambda_{\hat{\mathbf{p}}\mu}(\mathbf{q}\cdot\mathbf{v}_{\mathbf{p}\mu})^2\rangle_{\mathrm{FS}}}{\lambda} \rightarrow \frac{1}{6}\sum_\mu v_{\mathrm{F}\mu}^2|\mathbf{q}|^2 \tag{6.20}$$

with $v_{\mathrm{F}\mu}$ being the Fermi velocity on the band $\mu = \pm 1$. The second excitation can be identified as a *new Leggett's collective* mode in NCS, which corresponds to the out–of–phase oscillations in the relative phase of the superconducting condensates. The properties of this mode will be discussed in details in the following sections.

Next, we discover the Anderson–Higgs mechanism in NCS. By including the Coulomb interaction [1] with the correspondingly nonzero plasma mode frequency $\omega_{\mathrm{P}}(\hat{\mathbf{q}})$ we obtain from Eq. (6.18) the following result:

$$\begin{aligned}
\omega_1^2 &= \omega_{\mathrm{P}}^2(\hat{\mathbf{q}}) + \omega_{\mathrm{G}}^2(\mathbf{q}) + \omega_{\mathrm{L}}^2(\mathbf{q}) - \omega_{\mathrm{L}}'^2(\mathbf{q}) + \mathcal{O}\left(\frac{\omega_{\mathrm{L}}^2(\mathbf{q})}{\omega_{\mathrm{P}}^2(\hat{\mathbf{q}})}\right) && \text{Plasma mode}\\
\omega_2^2 &= \omega_{\mathrm{L}}'^2(\mathbf{q}) + \mathcal{O}\left(\frac{\omega_{\mathrm{L}}^2(\mathbf{q})}{\omega_{\mathrm{P}}^2(\hat{\mathbf{q}})}\right) && \text{Leggett mode}
\end{aligned} \tag{6.21}$$

Here, we can draw an important conclusion that the gauge mode is now shifted to the

---

[1] Here, we use the Coulomb renormalization within RPA according to Eq. (6.1)

plasma mode, i.e. $\omega_{\mathrm{P}}^2(\mathbf{q}) = \omega_{\mathrm{P}}^2(\hat{\mathbf{q}}) + \omega_{\mathrm{G}}^2(\mathbf{q})$. In other words, this means that this collective excitation becomes a mass. The Leggett mode frequency is also changed to $\omega'_{\mathrm{L}}(\mathbf{q})$.

Finally, it is important to note that the full condensate density response δn_{s} as described by Eq. (6.15) is also manifested in the condensate dielectric function $\epsilon \equiv 1 - V_{\mathbf{q}}\delta n_{\mathrm{s}}^{(0)}/e\phi$, with $\delta n_{\mathrm{s}}^{(0)} \equiv \delta n_{\mathrm{s}}(\omega_{\mathrm{P}}(\hat{\mathbf{q}}) \to 0)$.

6.2.1. Conservation law

An important advantage of the matrix kinetic theory is the straightforward physical interpretation of its results. Especially, the gauge invariance of the whole theory can be demonstrated easily by taking into account *all* phase fluctuation modes of the order parameter. Let us illustrate this issue in the details. As one can see from Eq. (6.12) the density response functions $\delta n_{\mathbf{k}\mu}$ are directly connected with the phase fluctuations of the order parameter $\delta\Delta^{(-)}_{\mathbf{k}\mu}$. The integration of this result over the momentum space $\mathbf{k}$ yields together with the density current response $\mathbf{j} = \sum_{\mathbf{k}\mu} \mathbf{v}_{\mathbf{k}\mu}\delta n_{\mathbf{k}\mu}$ to the continuity equation

$$\omega\delta n - \mathbf{q}\cdot\mathbf{j} = \sum_{\mathbf{k}\mu} \lambda_{\mathbf{k}\mu} \left\{ \left[\omega^2 - (\mathbf{q}\cdot\mathbf{v}_{\mathbf{k}\mu})^2\right] \frac{\delta\Delta^{(-)}_{\mathbf{k}\mu}}{2\Delta_{\mathbf{k}\mu}} - \omega\delta\zeta \right\} \ , \tag{6.22}$$

which at first glance displays a non–vanishing right-hand side. However, by using Eq. (6.9) and the variation of the energy gap equation (6.14) one finds after a straightforward, but lengthy calculation:

$$\omega\delta n - \mathbf{q}\cdot\mathbf{j} = 0 \tag{6.23}$$

As a result, within the framework of the matrix kinetic theory one is able to satisfy the particle conservation law and, associated with it, the gauge invariance of the theory.

6.3. Leggett mode

This section is devoted to the properties of the Leggett mode in noncentrosymmetric superconductors. This mode was first predicted for ordinary two–band superconductors [116] and corresponds to the out–of–phase oscillations in the relative phase of the superconducting condensates. Therefore, its frequency scales with the interband coupling and has, consequently, finite mass in the long wavelength limit ($|\mathbf{q}| \to 0$) [118].

For the neutral noncentrosymmetric system we find in Eq (6.19) the following result:

$$\omega_{\mathrm{L}}^2(\mathbf{q}) = \Lambda_0^2 + \frac{\alpha_0\alpha_2\left(\omega_{\mathbf{q}0}^2 + \omega_{\mathbf{q}2}^2\right) - 2\alpha_1^2\omega_{\mathbf{q}1}^2}{(\alpha_0\alpha_2 - \alpha_1^2)} - \omega_{\mathrm{G}}^2(\mathbf{q}) \tag{6.24}$$

where we define the quantities α_n

$$\alpha_n = \Delta_s\Delta_{tr} \sum_{\mu} \left\langle \frac{\lambda_{\hat{\mathbf{k}}\mu}}{\Delta^2_{\mathbf{k}\mu}} (\mu f_{\mathbf{k}})^n \right\rangle_{\mathrm{FS}} \tag{6.25}$$

together with the abbreviation

$$\omega_{\mathbf{q}n}^2 = \frac{\Delta_s \Delta_{tr}}{\alpha_n} \sum_{\mu} \left\langle \frac{\lambda_{\hat{\mathbf{k}}\mu}}{\Delta_{\mathbf{k}\mu}^2} \left(\mathbf{q} \cdot \mathbf{v}_{\mathbf{k}\mu}\right)^2 \left(\mu f_{\mathbf{k}}\right)^n \right\rangle_{\mathrm{FS}} . \tag{6.26}$$

The long wavelength part ($\Lambda_0 \equiv \omega_{\mathrm{L}}(\mathbf{q} \to 0)$) in Eq. (6.24) represents the mass of the Leggett mode in NCS and the rest describes its dispersion. Let us discuss them one by one.

6.3.1. Long wavelength limit

From Eq. (6.24) in the long wavelength limit ($\mathbf{q} \to 0$), we find the mass of the Leggett mode

$$\Lambda_0^2 \equiv \omega_{\mathrm{L}}^2(\mathbf{q} \to 0) = 4\gamma_{\mathrm{ncs}} \Delta_s \Delta_{tr} \frac{\lambda}{\alpha_0 \alpha_2 - \alpha_1^2} , \tag{6.27}$$

the form of which is reminiscent of the Leggett mode frequency predicted for the two–band superconductors with the spin–singlet pairing and given in Eq. (5.40). In NCS, however, the mass of the Leggett mode is proportional to the singlet Δ_s and triplet Δ_{tr} contributions to the superconducting gaps and scales with the coupling strength γ_{ncs}, which depends on the mixing term, as follows:

$$\gamma_{\mathrm{ncs}} = \frac{\lambda_m}{|\boldsymbol{\lambda}|} + \Xi_1 \tag{6.28}$$

with the integral $\Xi_1 = \sum_\mu \langle (\mu f_{\mathbf{k}}) \theta_{\mathbf{k}\mu} \rangle$ and $|\boldsymbol{\lambda}| = \lambda_s \lambda_{tr} - \lambda_m^2$ being the determinant of the interaction matrix in Eq. (5.34). Importantly, this Leggett mode in noncentrosymmetric superconductors shows a clear dependence [2] on the symmetry of the antisymmetric spin–orbit coupling $f_{\mathbf{k}}$ and on the point group symmetry of the crystal structure under consideration associated with it. In the limit of small triplet to singlet ratio t the definition (6.27) can be further simplified. In this case one can perform Taylor expansion of $1/\Delta_{\mathbf{k}\mu}^2$ in the integrals α_n. Thus, one obtains in the second order of t the following result:

$$\alpha_n / t = \sum_\mu \left\langle (\mu f_{\mathbf{k}})^n \left(1 - 2t(\mu f_{\mathbf{k}}) + 3t^2 (\mu f_{\mathbf{k}})^2\right) \right\rangle + \mathcal{O}\left(t^3\right) \tag{6.29}$$

Further, the coupling strength of the Leggett mode γ_{ncs} from Eq. (6.28) takes in the same limit according to Eq. (5.39) and together with the integral

$$\Xi_1 = -2t = -\frac{2\lambda_m}{\lambda_s - \lambda_{tr} + 2|\boldsymbol{\lambda}|} \tag{6.30}$$

the following form:

$$\gamma_{\mathrm{ncs}} = \frac{\lambda_s - \lambda_{tr}}{|\boldsymbol{\lambda}|} t \tag{6.31}$$

---

[2] the ASOC $f_{\mathbf{k}}$ appears in the definition (6.25) of quantities α_n, as well as, in integral Ξ_1. Therefore, it manifests itself in the Leggett mode frequency defined in Eq. (6.27)

Finally, inserting this result together with the calculated integrals α_n from Eq. (6.29) into the definition (6.27) of the Leggett mode, we obtain:

$$\Lambda_0^2 = 2\Delta_s^2 \frac{\lambda_s - \lambda_{tr}}{|\boldsymbol{\lambda}|} \left[1 - \left(3\left\langle f_{\mathbf{k}}^4 \right\rangle_{\mathrm{FS}} - 1\right) t^2\right] \tag{6.32}$$

In general, for given set of coupling parameters λ_s, λ_{tr}, λ_m, and for a particular point group symmetry $\mathcal{G}$ the mass of Leggett mode Λ_0 can be determined from Eq. (6.27). For illustration we plot in Fig. 6.1 the numerically calculated Leggett mode mass Λ_0 for the important C_{4v} point group symmetry with fixed $\lambda_s = 0.1$ as a function of λ_m. The values of λ_{tr} are treated as parameters in our calculations. Interestingly, one observes different behaviors for Λ_0 depending on the relation of the pairing constants λ_s, λ_{tr}, and λ_m. For a small triplet contribution, which is indicated in Fig. 6.1 by the blue upper solid line, we find a monotonic increase of Λ_0. Further, this behavior is changed at around $\lambda_{tr} = 1/2\lambda_s$ to a nonmonotonic one, which is shown with the red middle solid line. Finally, for $\lambda_s \approx \lambda_{tr}$ we obtain the important case that Λ_0 can become zero in contrast to the ordinary two–band situation. Corresponding situation is displayed in Fig. 6.1 by the black lower solid line. This can be explained by zeros in the gap functions $\Delta_{\mathbf{k}\mu} = \Delta_s + \mu\Delta_{tr} f_{\mathbf{k}}$. The analytical solution for small triplet to singlet ratio t, which is given in Eq. (6.32), is displayed in Fig. 6.1 by the dashed lines.

In summary, we can conclude that the mass of the Leggett mode in noncentrosymmetric superconductors can appear undamped below the quasiparticle continuum for particular parameters of the pairing interactions. Hence, it might help experimentalists to estimate in which materials the new Leggett modes are most easiest observable.

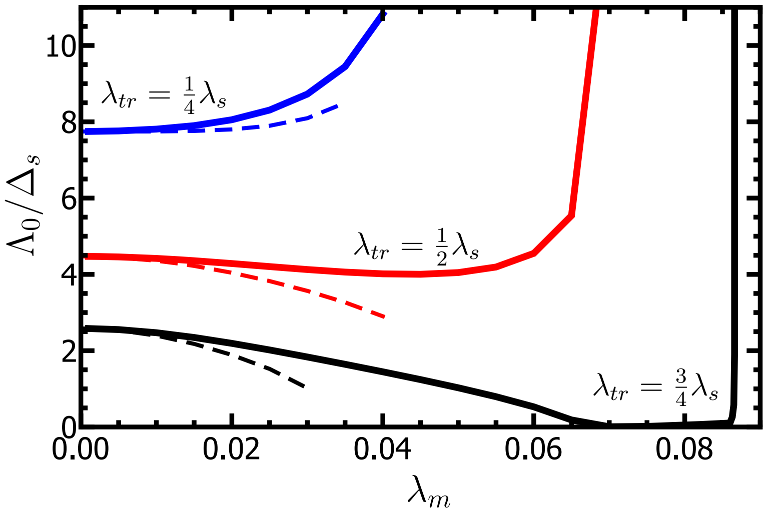

Figure 6.1: Normalized mass of the Leggett mode for NCS systems with C_{4v} point group symmetry for fixed $\lambda_s = 0.1$ as a function of the mixing term and various λ_{tr}: $\lambda_{tr} = 0.025$ (upper solid line), $\lambda_{tr} = 0.05$ (middle solid line) and $\lambda_{tr} = 0.075$ (lower solid line). The dashed lines correspond to Eq. (6.32) which is an analytical solution in the limit of small t.

6.3.2. Dispersion

Now, let us discuss the dispersion of the Leggett mode $(\omega_{\mathrm{L}}^2(\mathbf{q}) - \Lambda_0^2)$ given in Eq. (6.24). First, we find, as expected, for all considered point groups the quadratic behavior of the dispersion with $|\mathbf{q}|$, i.e.$(\omega_{\mathrm{L}}^2(\mathbf{q}) - \Lambda_0^2) \propto |\mathbf{q}|^2$. Next, in analogy to the mass Λ_0, the slope of the Leggett mode shows clearly the dependence on both the triplet to singlet ratio $t = \Delta_{tr}/\Delta_s$ and the point group symmetry $f_{\mathbf{k}}$. For illustration we show in Fig. 6.2 the numerically calculated slope of the Leggett mode for the tetragonal point group C_{4v}. In Fig. 6.2(a) the slope is plotted along the $\hat{\mathbf{q}}_x$– and $\hat{\mathbf{q}}_y$–direction. The calculated upward parabola corresponds to $t = 0.5$, while the downward parabola represents the case with $t = 1.5$. In addition, we find in case of the identical contributions from singlet and triplet $t = 1$ a constant slope of $1/3$, which is independent of $\hat{\mathbf{q}}_x$ and $\hat{\mathbf{q}}_y$.

In Fig. 6.2(b) the slope is now plotted along the $\hat{\mathbf{q}}_z$–direction for various triplet to singlet ratios t, which reveals a non–monotonic behavior for fixed $\hat{\mathbf{q}}_z$. In contrast, for the cubic point group $O(432)$ we find in all directions $\omega_{\mathrm{L}}^2(\mathbf{q}) - \Lambda_0^2 = \frac{1}{3}\mathbf{v}_{\mathrm{F}}^2|\mathbf{q}|^2$ independent of t, since the underlying ASOC is isotropic to leading order. It should be mentioned that this situation with $f_{\mathbf{k}} = 1$ corresponds to the ordinary two–band case with the isotropic gaps.

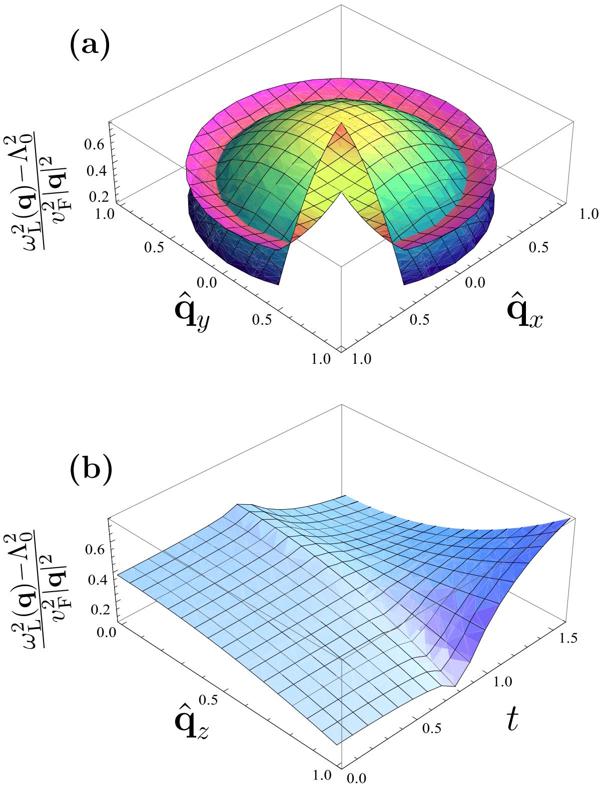

Figure 6.2: Slope of the dispersion of the Leggett mode for NCS systems with C_{4v} point group symmetry as a function of the unit vectors $\hat{\mathbf{q}}_x, \hat{\mathbf{q}}_y, \hat{\mathbf{q}}_z$. (a) Comparison of the slope for $t = 0.5$ (upward parabola) and $t = 1.5$ (downward parabola), (b) slope along the $\hat{\mathbf{q}}_z$–direction for various $t = \Delta_{tr}/\Delta_s$.

6.3.3. Anderson–Higgs mechanism

Now, we turn to the discussion of the role of the Anderson–Higgs mechanism for the new Leggett modes in noncentrosymmetric superconductors. From Eq. (6.21) we find a Coulomb renormalized Leggett mode of the following form:

$$\omega_{\mathrm{L}}'^{2}(\mathbf{q}) = \Lambda_0^2 + \frac{\alpha_0\alpha_2\omega_{\mathbf{q}0}^2\omega_{\mathbf{q}2}^2 - \alpha_1^2\omega_{\mathbf{q}1}^4}{\left(\alpha_0\alpha_2 - \alpha_1^2\right)\omega_{\mathrm{G}}^2(\mathbf{q})} \tag{6.33}$$

Here, we can draw some important conclusions: First, the Leggett mass Λ_0 remains unchanged, since the r.h.s. of Eq. (6.27) does not depend on ω_{G}. Physically, this corresponds to the fact that the Meissner effect in the presence of a new Leggett mode is unchanged. Second, the dispersion of the Leggett mode is only slightly changed. Since $\omega_{\mathrm{G}}(\mathbf{q}\to 0)\to 0$ and $\omega_{\mathrm{P}} \gg \omega_{\mathrm{L}}$, the higher order corrections nearly vanish. Thus, we need to consider only the difference between the Coulomb–renormalized Leggett mode ω_{L}' defined in Eq. (6.33) and its unrenormalized counterpart ω_{L} defined in Eq. (6.24):

$$\omega_{\mathrm{L}}^2(\mathbf{q}) - \omega_{\mathrm{L}}'^{2}(\mathbf{q}) = \frac{\alpha_0\alpha_2\left(\omega_{\mathbf{q}0}^2 + \omega_{\mathbf{q}2}^2\right) - 2\alpha_1^2\omega_{\mathbf{q}1}^2}{\left(\alpha_0\alpha_2 - \alpha_1^2\right)} - \omega_{\mathrm{G}}^2(\mathbf{q}) - \frac{\alpha_0\alpha_2\omega_{\mathbf{q}0}^2\omega_{\mathbf{q}2}^2 - \alpha_1^2\omega_{\mathbf{q}1}^4}{\left(\alpha_0\alpha_2 - \alpha_1^2\right)\omega_{\mathrm{G}}^2(\mathbf{q})} \tag{6.34}$$

For simplicity we study isotropic spin–orbit coupling $f_{\mathbf{k}} = 1$, which corresponds to the leading order of $f_{\mathbf{k}}$ for the cubic point group $O(432)$. Thus, Eq. (6.34) can be simplified to

$$\omega_{\mathrm{L}}^2(\mathbf{q}) - \omega_{\mathrm{L}}'^{2}(\mathbf{q}) = \frac{2\alpha_0^2\omega_{\mathbf{q}0}^2 - 2\alpha_1^2\omega_{\mathbf{q}1}^2}{\left(\alpha_0^2 - \alpha_1^2\right)} - \omega_{\mathrm{G}}^2(\mathbf{q}) - \frac{\alpha_0^2\omega_{\mathbf{q}0}^4 - \alpha_1^2\omega_{\mathbf{q}1}^4}{\left(\alpha_0^2 - \alpha_1^2\right)\omega_{\mathrm{G}}^2(\mathbf{q})} \tag{6.35}$$

with $\omega_{\mathrm{G}}^2 = \frac{1}{6}\sum_\mu v_{\mathrm{F}\mu}^2|\mathbf{q}|^2$ and $v_{\mathrm{F}\mu}$ being the Fermi velocity on the band $\mu = \pm 1$. Further, by using definitions (6.25) and (6.26) we find a more compact form:

$$\omega_{\mathrm{L}}^2(\mathbf{q}) - \omega_{\mathrm{L}}'^{2}(\mathbf{q}) = \omega_{\mathrm{G}}^2(\mathbf{q}) - \frac{\left\langle(\mathbf{q}\cdot\mathbf{v}_{\mathbf{k}+})^2\right\rangle_{\mathrm{FS}}\left\langle(\mathbf{q}\cdot\mathbf{v}_{\mathbf{k}-})^2\right\rangle_{\mathrm{FS}}}{\omega_{\mathrm{G}}^2(\mathbf{q})} \tag{6.36}$$

Finally, assuming the same DoS on both bands, i.e. $N_\mu(0) = N(0)$, and almost similar Fermi velocities, i.e. $(v_{\mathrm{F}+} - v_{\mathrm{F}-}) \ll v_{\mathrm{F}}$ with $v_{\mathrm{F}} = \max_\mu v_{\mathrm{F}\mu}$, one obtains after performing the integration:

$$\frac{\omega_{\mathrm{L}}^2(\mathbf{q}) - \omega_{\mathrm{L}}'^{2}(\mathbf{q})}{v_{\mathrm{F}}^2|\mathbf{q}|^2} \approx \frac{1}{6}\frac{\left(v_{\mathrm{F}+}^2 - v_{\mathrm{F}-}^2\right)}{v_{\mathrm{F}+}^2 + v_{\mathrm{F}-}^2}\frac{\left(v_{\mathrm{F}+}^2 - v_{\mathrm{F}-}^2\right)}{v_{\mathrm{F}}^2} \ll 1 \tag{6.37}$$

Therefore, we can conclude that the dispersion of the Leggett mode and the results shown in Fig. 6.2 are nearly unchanged due to the Anderson–Higgs mechanism [3].

---

[3] A similar result has been found for the case of ordinary two–band superconductors [116, 118, 137].

6.4. Conclusion

Within the framework of the (Nambu) matrix kinetic theory in the clean limit we have demonstrated the existence of two phase collective modes in noncentrosymmetric superconductors, the dispersion of which is illustrated in Fig. 6.3. The first mode $\omega_{\mathrm{G}}^2(\mathbf{q})$ corresponds to the characteristic gauge mode in NCS and is common for all superconducting systems. We have found that this mode is shifted to the plasma mode $\omega_{\mathrm{P}}^2(\mathbf{q})$ according to the Anderson–Higgs mechanism, i.e. $\omega_{\mathrm{P}}^2(\mathbf{q}) = \omega_{\mathrm{P}}^2(\hat{\mathbf{q}}) + \omega_{\mathrm{G}}^2(\mathbf{q})$. The second collective phase excitation, which beside the gauge mode is necessary to guarantee the charge conservation law, represents the new Leggett modes in NCS. For both modes we have derived an analytical expression describing their characteristic mass and dispersion for various crystal symmetries. These properties reflect the underlying spin–orbit coupling and depend strongly on the triplet to singlet ratio $t = \Delta_{tr}/\Delta_s$. Moreover, we have found from the numerical calculations performed exemplary for C_{4v} point group that (i) in contrast to the ordinary two-band superconductors, where the Leggett mode always appears as a massive collective excitation, its counterpart in NCS systems can be massless under certain conditions, (ii) it survives in the limit of vanishing triplet to singlet ratio $t = \Delta_{tr}/\Delta_s$, and (iii) its slope depends strongly on the ratio $t = \Delta_{tr}/\Delta_s$. Finally, we showed that the mass of the Leggett mode remains unaffected by the Anderson–Higgs mechanism, but its dispersion is changed. In the limiting case of small $\mathbf{q}$ the dispersion modification is however negligible.

All in all, our new results for the collective modes generalize the known solutions for ordinary two–band superconductors which can be obtained in the limit $f_{\mathbf{k}} \equiv 1$ [118, 137].

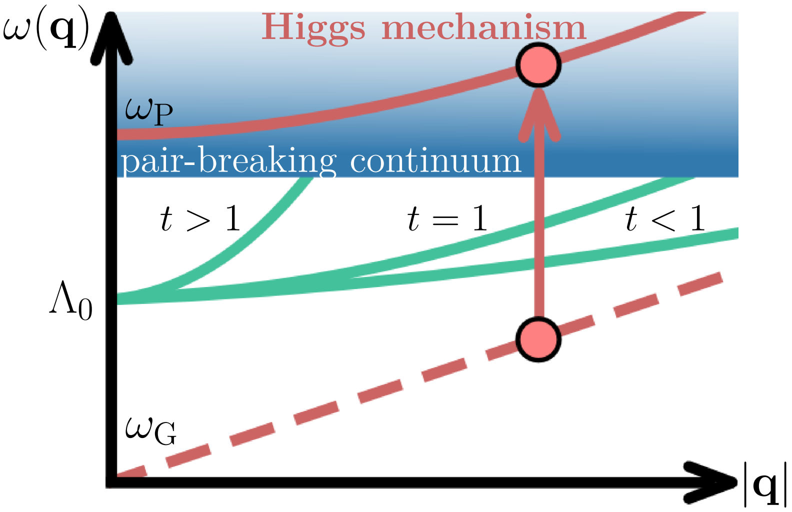

Figure 6.3: Illustration of various calculated collective modes (T=0) common to all NCS. The Anderson–Higgs mechanism shifts the gauge mode ω_{G} (dashed line) to the plasma mode ω_{P} usually lying in the pair–breaking continuum. The new Leggett modes (solid green lines) unique to NCS are only slightly changed by this process (not visible) and the mass Λ_0 remains unchanged. Importantly, in some cases $\Lambda_0 \to 0$ is possible. The slope of the Leggett modes depends strongly on the ratio $t = \Delta_{tr}/\Delta_s$.

Chapter 7

Results of calculations of ultrafast dynamics in singlet superconductors

Now let us investigate the possibility to excite collective modes out of equilibrium in the sense of a pump–probe experiment. This type of measurements is based on the idea of applying two ultrafast pulses. The first relative strong one (*pump pulse*) drives the superconducting system out of equilibrium without destroying completely the superconducting correlations. Then, the second weaker one (*probe pulse*), which appears with some tunable time delay after the pump pulse, makes a "snapshot" of the superconducting state in nonequilibrium.

In this chapter we present a semi–numerical method to simulate the pump–probe experiment in application for two–band superconductors with the singlet pairing correlations. The theoretical description is based on the two–band BCS theory discussed in section 5.1. In order to study the temporal evolution of the superconducting system we go beyond the linear response theory (MKT) presented in previous chapter and use instead the framework of the density matrix formalism. The time dependence of the single–particle density matrices is then calculated from the Heisenberg's differential equation of motion.

7.1. Pump pulse excitation

7.1.1. Non–linear interaction with an electromagnetic field

Let us start the discussion by considering the first optical pulse, which is called pump pulse, and its effect on the dynamics in a two–band superconductor with singlet pairing correlations. For this purpose we prepare the superconducting system in equilibrium in some initial state, which is described by Hamiltonian $\hat{H}_{\text{BCS}}$ from Eq. (5.1). Then, the superconductor gets exposed to the action of a short Gaussian–like pulse (see an illustration in Fig. 7.1). In this case, the electromagnetic field excites Bogoliubov quisiparticles above the superconducting gaps, which leads to corresponding changes in the superconducting order parameters. Thus, the superconducting system in nonequilibrium is described by a time–dependent BCS–Hamiltonian $\hat{H}_{\mathrm{BCS}}(t)$, which corresponding nonequilibrium energy matrix $\underline{\xi}_{\mathbf{k}l}(t)$ takes the following form:

$$\underline{\xi}_{\mathbf{k}l}(t) = \begin{pmatrix} \xi_{\mathbf{k}l} & \Delta_{\mathbf{k}l}(t) \\ \Delta^*_{\mathbf{k}l}(t) & -\xi_{-\mathbf{k}l} \end{pmatrix} \tag{7.1}$$

It is important to note that the superconducting gaps $\Delta_{\mathbf{k}l}(t)$ are time–dependent in nonequilibrium and obey the following relation:

$$\Delta_{\mathbf{k}l}(t) = \sum_{j=1}^{2} \sum_{\mathbf{k}'\in\mathcal{W}} V^{lj}_{\mathbf{k}\mathbf{k}'} \left\langle \hat{c}_{-\mathbf{k}'\downarrow j} \hat{c}_{\mathbf{k}'\uparrow j} \right\rangle (t) \tag{7.2}$$

with the time–dependent expectation value $\left\langle \hat{c}_{-\mathbf{k}'\downarrow j} \hat{c}_{\mathbf{k}'\uparrow j} \right\rangle (t)$ and pairing interaction strength $V^{lj}_{\mathbf{k}\mathbf{k}'}$, which are assumed to remain constant during the whole nonequilibrium process.

Now, in order to simulate collective excitation of the superconducting system, we need to go beyond the linear response approximation and take into account nonlinear coupling of the superconducting condensates to the electromagnetic field. In addition, we assume that the pump pulse acts quite gently in order to break some Cooper pairs in the superconducting condensates without suppressing superconductivity in the system completely. In other words, we model pulses in a so–called low–fluency regime (in contrast to optical control experiments with very intense pulses, as discussed in the first part of this thesis). The coupling of the pump pulse to a two–band superconductor is then given by:

$$\hat{H}_{\mathrm{em}}(t) = \hat{H}^{(1)}_{\mathrm{em}}(t) + \hat{H}^{(2)}_{\mathrm{em}}(t) \tag{7.3}$$

with the terms $\hat{H}^{(1)}_{\mathrm{em}}(t)$ and $\hat{H}^{(2)}_{\mathrm{em}}(t)$

$$\begin{aligned} \hat{H}^{(1)}_{\mathrm{em}}(t) &= e\hbar \sum_{\mathbf{k}\mathbf{q}\sigma l} \frac{(2\mathbf{k}+\mathbf{q})\cdot \mathbf{A}_{\mathbf{q}}(t)}{2m_l} \hat{c}^{\dagger}_{\mathbf{k}+\mathbf{q}\sigma l} \hat{c}_{\mathbf{k}\sigma l} \\ \hat{H}^{(2)}_{\mathrm{em}}(t) &= e^2 \sum_{\mathbf{k}\mathbf{q}\sigma l} \frac{\left(\sum_{\mathbf{q}'} \mathbf{A}_{\mathbf{q}-\mathbf{q}'}(t)\cdot \mathbf{A}_{\mathbf{q}'}(t)\right)}{2m_l} \hat{c}^{\dagger}_{\mathbf{k}+\mathbf{q}\sigma l} \hat{c}_{\mathbf{k}\sigma l} \ , \end{aligned} \tag{7.4}$$

which describe one- and two–photon absorption, respectively. Here, we introduced the effective electron mass m_l for each band l and a transverse vector potential $\mathbf{A}_{\mathbf{q}}(t)$ with the momentum $\mathbf{q}$ dependence. The vector potential $\mathbf{A}_{\mathbf{q}}(t)$ is considered in the Coulomb gauge and assumed to take the following form:

$$\mathbf{A}_{\mathbf{q}}(t) = \mathbf{A}_0 \exp\left(-\left(2t\sqrt{\ln 2}/\tau\right)^2 \right) \left[\delta_{\mathbf{q},\mathbf{q}_0} e^{-i\omega_0 t} + \delta_{\mathbf{q},-\mathbf{q}_0} e^{+i\omega_0 t} \right] \tag{7.5}$$

with the following parameters: $\mathbf{A}_0 = A_0 \hat{\mathbf{e}}_y$ denotes the pulse amplitude, which is polarized along the y axis, $\mathbf{q}_0 = q_0\hat{\mathbf{e}}_x$ represents the wave vector in the propagation direction along the x axis, ω_0 is a central frequency of the pulse, and τ is the full width at half maximum ($FWHM$) of the pulse. In all our calculations we adjust the pulse in a way that it reaches its maximum at $t = 0$ps. In addition, at a thousandth of its maximum we make a cut off for the pulse. An illustration of a single pump pulse is shown in Fig. 7.1.

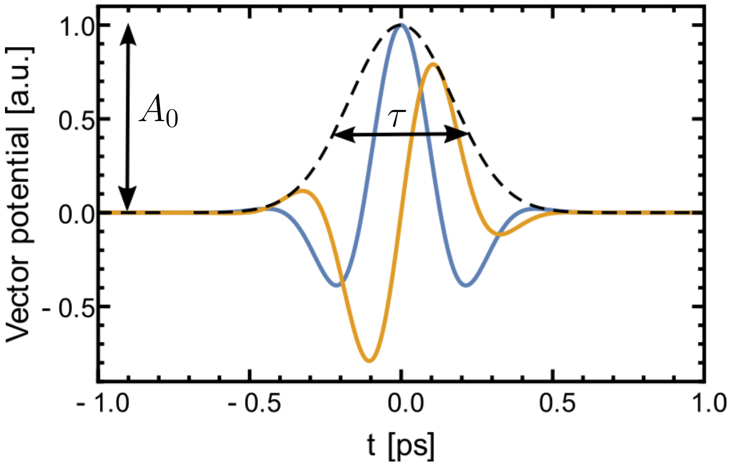

Figure 7.1: Illustration of a single pump pulse. The corresponding vector potential $\mathbf{A}_\mathbf{q}(t)$ has parameters: $A_0 = 1$a.u., $\tau = 0.4$ps, $\hbar\omega_0 = 8$meV. Its imaginary and real parts are shown by yellow and blue solid lines, respectively. The envelope of the pulse is illustrated by the black dashed line.

Finally, the total Hamiltonian of the superconducting system with the coupling to the electromagnetic field is modeled by $\hat{H}_{\text{tot}}(t) = \hat{H}_{\text{BCS}}(t) + \hat{H}_{\text{em}}(t)$. In analogy to the equilibrium case (see section 5.1) it is convenient to describe superconducting condensate and quasiparticles separately. Therefore, we perform a transformation of the Hamiltonian $\hat{H}_{\text{tot}}(t)$ by using the Bogoliubov–Valatin transformation at each time t.

7.1.2. Bogoliubov–Valatin transformation for nonequilibrium

There are two equivalent ways of performing Bogoliubov–Valatin transformation in order to modify the time–dependent Hamiltonian. The first method consists in diagonalizing of $\hat{H}_{\text{tot}}(t)$ in each moments in time t by using the time–dependent quisiparticle basis, which leads to some additional terms in the equation of motion [23,47]. Here, we will use, however, another approach and take the time–independent unitary matrix $\underline{U}_{\mathbf{k}l}$ defined in Eq. (5.11) with the BCS–coherence factors $u_{\mathbf{k}l}$ and $v_{\mathbf{k}l}$:

$$u_{\mathbf{k}l} = \sqrt{\frac{1}{2}\left(1 + \frac{\xi_{\mathbf{k}l}}{E_{\mathbf{k}l}}\right)} \quad ; \quad v_{\mathbf{k}l} = \sqrt{\frac{1}{2}\left(1 - \frac{\xi_{\mathbf{k}l}}{E_{\mathbf{k}l}}\right)} \tag{7.6}$$

where $E_{\mathbf{k}l} = \sqrt{\epsilon_{\mathbf{k}l}^2 + |\Delta_{\mathbf{k}l}|^2}$ is excitation energy of the quasiparticles in equilibrium for each band l. In this case the fermionic quasiparticle operators $\hat{\alpha}_{\mathbf{k}\sigma l}$ remain time–independent.

In order to make our description more compact, we introduced the following notation:

$$\hat{\alpha}_{\mathbf{k}l} \equiv \hat{\alpha}_{\mathbf{k}\uparrow l} \quad ; \quad \hat{\beta}_{\mathbf{k}l} \equiv \hat{\alpha}_{-\mathbf{k}\downarrow l} \tag{7.7}$$

After this type of Bogoliubov–Valatin transformation the time–dependent Hamiltonian $\hat{H}_{\text{BCS}}$ is no more diagonal. Its corresponding energy matrix takes the following form:

$$\underline{\xi}_{\mathbf{k}l}(t) = \begin{pmatrix} R_{\mathbf{k}l}(t) & C_{\mathbf{k}l}(t) \\ C^*_{\mathbf{k}l}(t) & -R_{-\mathbf{k}l}(t) \end{pmatrix} \tag{7.8}$$

with

$$\begin{aligned} R_{\mathbf{k}l}(t) &= u^2_{\mathbf{k}l}\xi_{\mathbf{k}l} - |v_{\mathbf{k}l}|^2\,\xi_{-\mathbf{k}l} + u_{\mathbf{k}l}v_{\mathbf{k}l}\Delta^*_{\mathbf{k}l}(t) + u_{\mathbf{k}l}v^*_{\mathbf{k}l}\Delta_{\mathbf{k}l}(t) \\ C_{\mathbf{k}l}(t) &= u^2_{\mathbf{k}l}\Delta_{\mathbf{k}l}(t) - v^2_{\mathbf{k}l}\Delta^*_{\mathbf{k}l}(t) - v_{\mathbf{k}l}u_{\mathbf{k}l}\xi_{\mathbf{k}l} - v_{\mathbf{k}l}u_{\mathbf{k}l}\xi_{-\mathbf{k}l} \end{aligned} \tag{7.9}$$

Thus, we find for the Hamiltonian $\hat{H}_{\text{BCS}}$[1] the following result:

$$\hat{H}_{\text{BCS}}(t) = \sum_{l=1}^{2}\sum_{\mathbf{k}} \left\{ R_{\mathbf{k}l}(t)\hat{\alpha}^\dagger_{\mathbf{k}l}\hat{\alpha}_{\mathbf{k}l} + R_{-\mathbf{k}l}(t)\hat{\beta}^\dagger_{\mathbf{k}l}\hat{\beta}_{\mathbf{k}l} + C^*_{\mathbf{k}l}(t)\hat{\beta}_{\mathbf{k}l}\hat{\alpha}_{\mathbf{k}l} + C_{\mathbf{k}l}(t)\hat{\alpha}^\dagger_{\mathbf{k}l}\hat{\beta}^\dagger_{\mathbf{k}l} \right\} \tag{7.10}$$

In addition, the time–dependent energy gap equation (7.2) can be rewritten in terms of the quasiparticle densities:

$$\Delta_{\mathbf{k}l}(t) = \sum_{\mathbf{k}',j} V^{lj}_{\mathbf{k},\mathbf{k}'} \left(v_{\mathbf{k}'j}u_{\mathbf{k}'j}\left[-\alpha^\dagger_{\mathbf{k}'j}\alpha_{\mathbf{k}'j} - \beta^\dagger_{\mathbf{k}'j}\beta_{\mathbf{k}'j} + 1 \right] + u^2_{\mathbf{k}'j}\beta_{\mathbf{k}'j}\alpha_{\mathbf{k}'j} - v^2_{\mathbf{k}'j}\alpha^\dagger_{\mathbf{k}'j}\beta^\dagger_{\mathbf{k}'j} \right) \tag{7.11}$$

Here, we have used the definitions $\left\langle \hat{\alpha}^\dagger_{\mathbf{k}l}\hat{\alpha}_{\mathbf{k}l} \right\rangle(t) = \alpha^\dagger_{\mathbf{k}l}\alpha_{\mathbf{k}l}$, etc. in order to keep our notation compact. In analogy, the part of the Hamiltonian $\hat{H}_{\text{tot}}(t)$, which describes coupling of the condensate to the electromagnetic field, is found to take the following form:

$$\begin{aligned} \hat{H}^{(1)}_{\text{em}} &= e\hbar \sum_{\mathbf{k},\mathbf{q},l} \frac{1}{2m_l}(2\mathbf{k}+\mathbf{q})\cdot\mathbf{A}_{\mathbf{q}} & & \Big\{ L^{(+)}_{\mathbf{k},\mathbf{q},l}\hat{\alpha}^\dagger_{\mathbf{k}+\mathbf{q}l}\hat{\alpha}_{\mathbf{k}l} - M^{(-)*}_{\mathbf{k},\mathbf{q},l}\hat{\alpha}^\dagger_{\mathbf{k}+\mathbf{q}l}\hat{\beta}^\dagger_{\mathbf{k}l} \\ & & & +M^{(-)}_{\mathbf{k},\mathbf{q},l}\hat{\beta}_{\mathbf{k}+\mathbf{q}l}\hat{\alpha}_{\mathbf{k}l} - L^{(+)*}_{\mathbf{k},\mathbf{q},l}\hat{\beta}^\dagger_{\mathbf{k}l}\hat{\beta}_{\mathbf{k}+\mathbf{q}l} \Big\} \\ \hat{H}^{(2)}_{\text{em}} &= \sum_{\mathbf{k},\mathbf{q},l} \frac{e^2}{2m_l}\left(\sum_{\mathbf{q}'} \mathbf{A}_{\mathbf{q}-\mathbf{q}'}\cdot\mathbf{A}_{\mathbf{q}'} \right) & & \Big\{ L^{(-)}_{\mathbf{k},\mathbf{q},l}\hat{\alpha}^\dagger_{\mathbf{k}+\mathbf{q}l}\hat{\alpha}_{\mathbf{k}l} + L^{(-)*}_{\mathbf{k},\mathbf{q},l}\hat{\beta}^\dagger_{\mathbf{k}l}\hat{\beta}_{\mathbf{k}+\mathbf{q}l} \\ & & & -M^{(+)*}_{\mathbf{k},\mathbf{q},l}\hat{\alpha}_{\mathbf{k}+\mathbf{q}l}\hat{\beta}_{\mathbf{k}l} - M^{(+)}_{\mathbf{k},\mathbf{q},l}\hat{\beta}_{\mathbf{k}+\mathbf{q}l}\hat{\alpha}_{\mathbf{k}l} \Big\} \end{aligned} \tag{7.12}$$

with the new BCS–coherence factors:

$$\begin{aligned} L^{(s)}_{\mathbf{k},\mathbf{q},l} &= u_{\mathbf{k}l}u_{\mathbf{k}+\mathbf{q}l} + s v^*_{\mathbf{k}l}v_{\mathbf{k}+\mathbf{q}l} & \quad M^{(s)}_{\mathbf{k},\mathbf{q},l} &= v^*_{\mathbf{k}l}u_{\mathbf{k}+\mathbf{q}l} + s u_{\mathbf{k}l}v^*_{\mathbf{k}+\mathbf{q}l} \\ L^{(s)*}_{\mathbf{k},\mathbf{q},l} &= u_{\mathbf{k}l}u_{\mathbf{k}+\mathbf{q}l} + s v_{\mathbf{k}l}v^*_{\mathbf{k}+\mathbf{q}l} & \quad M^{(s)*}_{\mathbf{k},\mathbf{q},l} &= v_{\mathbf{k}l}u_{\mathbf{k}+\mathbf{q}l} + s u_{\mathbf{k}l}v_{\mathbf{k}+\mathbf{q}l} \end{aligned}$$

---

[1] It is easy to prove, that this BCS–Leggett–Hamiltonian in equilibrium assumes the diagonal form.

7.1.3. Equations of motion

Now, since all necessary preparations are done, we can formulate the equations of motion based on the density matrix formalism, which describe the nonequilibrium dynamics in a superconducting system. In this sense, we focus on the following time–dependent expectation values for each band $l = 1, 2$:

$$\alpha^\dagger_{\mathbf{k}l}\alpha_{\mathbf{p}l} \quad , \quad \beta^\dagger_{\mathbf{k}l}\beta_{\mathbf{p}l} \quad , \quad \alpha^\dagger_{\mathbf{k}l}\beta^\dagger_{\mathbf{p}l} \quad , \quad \alpha_{\mathbf{p}l}\beta_{\mathbf{k}l} \; , \tag{7.13}$$

which determines all quantities of particular interest (e.g., energy gaps from Eq. (7.11)). Here, the terms $\alpha^\dagger_{\mathbf{k}l}\alpha_{\mathbf{p}l}$, $\beta^\dagger_{\mathbf{k}l}\beta_{\mathbf{p}l}$ correspond to the quasiparticle excitations and anomalous expectation values $\alpha^\dagger_{\mathbf{k}l}\beta^\dagger_{\mathbf{p}l}$, $\alpha_{\mathbf{p}l}\beta_{\mathbf{k}l}$ can be viewed as contribution from the superconducting condensate. The time evolution of each quasiparticle expectation value can be generally obtained from the Heisenberg's equation of motion:

$$\frac{d}{dt}\alpha^\dagger_{\mathbf{k}l}\alpha^\dagger_{\mathbf{p}l} = \frac{i}{\hbar}\left\langle\left[\hat{H}_{\text{tot}}(t), \hat{\alpha}^\dagger_{\mathbf{k}l}\hat{\alpha}^\dagger_{\mathbf{p}l}\right]\right\rangle \quad ; \quad \text{etc.} \tag{7.14}$$

with the time–dependent Hamiltonian given in section 7.1.2

$$\hat{H}_{\text{tot}}(t) = \hat{H}_{\text{BCS}}(t) + \hat{H}^{(1)}_{\text{em}}(t) + \hat{H}^{(2)}_{\text{em}}(t) \tag{7.15}$$

So, in order to get a differential equation for a quasiparticle expectation value, we need to calculate a commutator of the underlying operator and the Hamiltonian. It is important to note that since the laser field couples indices $\mathbf{k}$, $\mathbf{k}+n\mathbf{q}$ with an integer n (see Eq. (7.12)), the equations of motion for the expectation values with only these indices should be obtained. Also considering only the small values of $\mathbf{A}_\mathbf{q}$ we may ignore contributions with $n > 4$. The calculations of commutator relations are quite lengthy, but straightforward. Thus, we show here only the result for the quasiparticle expectation value $\alpha^\dagger_{\mathbf{k}l}\alpha_{\mathbf{k}+\mathbf{q}l}$:

$$i\hbar\frac{d}{dt}\alpha^\dagger_{\mathbf{k}l}\alpha_{\mathbf{k}+\mathbf{q}l} = \left\langle\left[\hat{\alpha}^\dagger_{\mathbf{k}l}\hat{\alpha}_{\mathbf{k}+\mathbf{q}l}, \hat{H}_{\text{BCS}} + \hat{H}^{(1)}_{\text{em}} + \hat{H}^{(2)}_{\text{em}}\right]\right\rangle \tag{7.16}$$

where the right hand side of this equation takes the following form:

$$\begin{aligned}
\left\langle\left[\hat{\alpha}^\dagger_{\mathbf{k}l}\hat{\alpha}_{\mathbf{k}+\mathbf{q}l}, \hat{H}_{\text{BCS}}\right]\right\rangle =& \left(R_{\mathbf{k}+\mathbf{q}l} - R_{\mathbf{k}l}\right)\alpha^\dagger_{\mathbf{k}l}\alpha_{\mathbf{k}+\mathbf{q}l} + C_{\mathbf{k}+\mathbf{q}l}\alpha^\dagger_{\mathbf{k}l}\beta^\dagger_{\mathbf{k}+\mathbf{q}l} + C^*_{\mathbf{k}l}\alpha_{\mathbf{k}+\mathbf{q}l}\beta_{\mathbf{k}l} \\
\left\langle\left[\hat{\alpha}^\dagger_{\mathbf{k}l}\hat{\alpha}_{\mathbf{k}+\mathbf{q}l}, \hat{H}^{(1)}_{\text{em}}\right]\right\rangle =& \frac{e\hbar}{2m_l}\sum_{\mathbf{q}'=\pm\mathbf{q}}\mathbf{A}_{\mathbf{q}'}\cdot\Big\{(2\mathbf{k}+\mathbf{q}')\left(M^{(-)}_{\mathbf{k},\mathbf{q}',l}\alpha_{\mathbf{k}+\mathbf{q}l}\beta_{\mathbf{k}+\mathbf{q}'l} - L^{(+)}_{\mathbf{k},\mathbf{q}',l}\alpha^\dagger_{\mathbf{k}+\mathbf{q}'l}\alpha_{\mathbf{k}+\mathbf{q}l}\right) \\
&+ (2\mathbf{k}+2\mathbf{q}-\mathbf{q}')\left(L^{(+)*}_{\mathbf{k}+\mathbf{q},-\mathbf{q}',l}\alpha^\dagger_{\mathbf{k}l}\alpha_{\mathbf{k}+\mathbf{q}-\mathbf{q}'l} + M^{(-)*}_{\mathbf{k}+\mathbf{q},-\mathbf{q}',l}\alpha^\dagger_{\mathbf{k}l}\beta^\dagger_{\mathbf{k}+\mathbf{q}-\mathbf{q}'l}\right)\Big\} \\
\left\langle\left[\hat{\alpha}^\dagger_{\mathbf{k}l}\hat{\alpha}_{\mathbf{k}+\mathbf{q}l}, \hat{H}^{(2)}_{\text{em}}\right]\right\rangle =& \frac{e^2}{2m_l}\sum_{\mathbf{q}'=0,\pm2\mathbf{q}}\left(\sum_{\mathbf{q}_i=\pm\mathbf{q}}\mathbf{A}_{\mathbf{q}'-\mathbf{q}_i}\cdot\mathbf{A}_{\mathbf{q}_i}\right)\Big\{-L^{(-)}_{\mathbf{k},\mathbf{q}',l}\alpha^\dagger_{\mathbf{k}+\mathbf{q}'l}\alpha_{\mathbf{k}+\mathbf{q}l} \\
&+L^{(-)*}_{\mathbf{k}+\mathbf{q},-\mathbf{q}',l}\alpha^\dagger_{\mathbf{k}l}\alpha_{\mathbf{k}+\mathbf{q}-\mathbf{q}'l} - M^{(+)*}_{\mathbf{k}+\mathbf{q},-\mathbf{q}',l}\alpha^\dagger_{\mathbf{k}l}\beta^\dagger_{\mathbf{k}+\mathbf{q}-\mathbf{q}'l} - M^{(+)}_{\mathbf{k},\mathbf{q}',l}\alpha_{\mathbf{k}+\mathbf{q}l}\beta_{\mathbf{k}+\mathbf{q}'l}\Big\}
\end{aligned} \tag{7.17}$$

Importantly, since we start from the equilibrium BCS ground state with the confined set of possible momenta $\mathbf{k} \in \mathcal{W}$ for each band l (see Fig. 7.2), the interactions with the electromagnetic field is considered to take place only in this region. Therefore, we should restrict our calculation to $\mathbf{k}, \mathbf{k}+\mathbf{q} \in \mathcal{W}$. Equations of motion for other expectation values are presented in Appendix B.1. It is worth mentioning that all the expectation values with different momenta $\mathbf{k}$ and $\mathbf{p}$ can be combined into a form of the density matrix. This is useful for the numerical implementation.

7.1.4. Numerical implementation

In order to solve the differential equations of motion (7.14) numerically we perform a standard 4-th order Runge–Kutta algorithm [138]. This is implemented in C++ by using the *boost* library with the subsequent parallelization of the program code with *OpenMP*.

To model the two–band superconducting system we use two simple parabolic bands, which are illustrated in Fig. 7.2 (a). As discussed in the previous section, we are interested in the regions with $\mathbf{k} \in \mathcal{W}$ for both bands $l = 1, 2$, where the attractive electronic interaction takes place. Since the calculations of quasiparticle expectation values require integration over two bands, the numerical computations are quite time consuming. In order to reduce numerical effort we perform our calculations only along one $\mathbf{k}$–direction in a two–dimensional momentum space (see Fig. 7.2(b)). This simplification does not lead to any significant physical differences in the results, as it was also indicated in the previous studies for a one–band superconductor [47]. Hence, we choose a line in momentum space at fixed value of k_y and parallel to k_x. This choice is justified due to the definition (7.5) of the vector potential $\mathbf{A_q}(t)$. Finally, according to discussion in the previous section we perform a discretisation of possible $\mathbf{k}$ values by dividing the set $\mathcal{W}$ on $q = |\mathbf{q}|$ for each band l (indicated by red rectangles in Fig. 7.2 (b)).

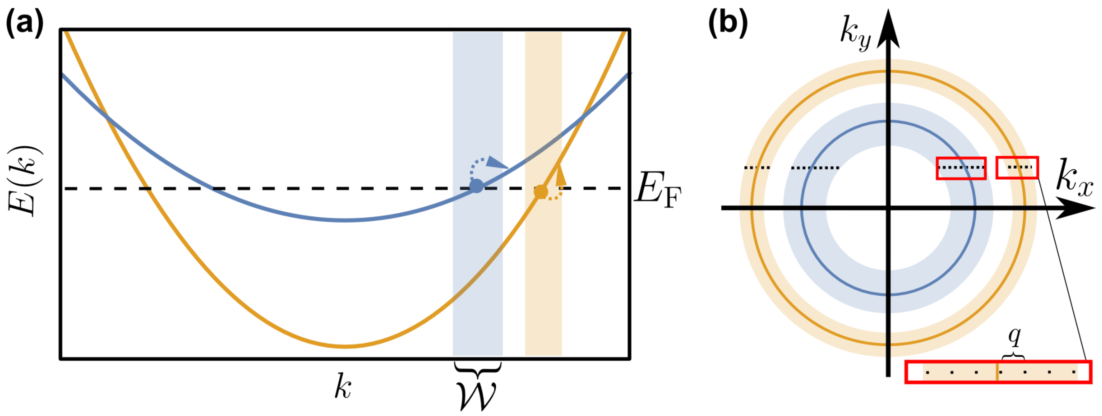

Figure 7.2: (a) Illustration of the energy dispersion in 1D for a two–band superconductor with electron–like excitations (full dots). (b) Two–dimensional momentum space with a cut at the Fermi level ($E(\mathbf{k}) = E_\mathrm{F}$ in (a)). Discretisation mesh for numerical calculation is shown by the red rectangles. The solid lines represent $\mathbf{k} = \mathbf{k}_{\mathrm{F}i}, i = \{1, 2\}$. The integration is performed at the fixed k_y level.

7.2. Response to the probe pulse

Now, let us discuss the second pulse, which is used to probe the system. The laser field is described again by the vector potential of the Gaussian–like form, which is given by Eq. (7.5). For the parameters of the probe pulse we use the amplitude A_0^{pr}, width τ_{pr} and frequency ω_0^{pr}. In accordance with the experimental setup [33–35, 38] we choose the probe pulse to be very short in time. Thus we are able to analyze the dynamics of the superconducting system in a very broad frequency range. Also, since the probe pulse should not additionally destroy the superconducting condensates, we assume its energy to be below the excitation energy of the smallest gap, i.e. $\hbar\omega_0^{\text{pr}} < 2|\Delta_2|$. In addition, we assume that the probe pulse intensity is weaker than the intensity of the pump pulse. In this case, we can neglect nonlinear therms of the second order in $\mathbf{A}$ (see Eq. (7.3)) and consider only the linear coupling of the probe pulse to the superconducting system. It is important to mention that we apply the probe pulse after the pump pulse with a variable time delay Δt. Moreover, we assume that there is no overlap between both pulses. This is possible due to the cut–off in the vector potential $\mathbf{A}$ and for $\Delta t > \tau + \tau_{\text{pr}}$. This way, we probe the properties of the superconducting system at different moments in time. In order to illustrate the pump–probe process we plot in Fig. 7.3 both pulses with a time delay Δt.

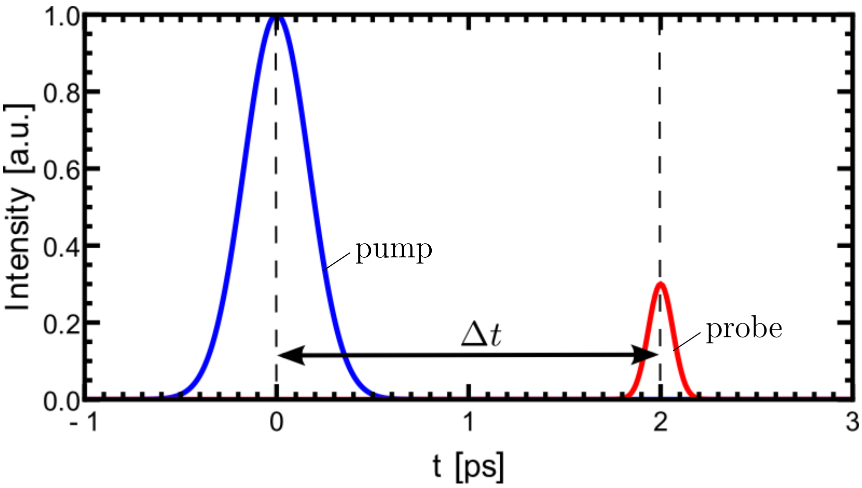

Figure 7.3: Illustration of the temporal evolution for the pump (blue solid line) and probe (red solid line) pulses. The time interval between the pulses is $\Delta t = 2$ps. The parameters of the pump vector potential are: $A_0 = 1$ a.u, $\tau = 0.4$ps, $\hbar\omega_0 = 8$meV and of the probe vector potential: $A_0^{\text{pr}} = 0.3$ a.u, $\tau_{\text{pr}} = 0.15$ps, $\hbar\omega_0^{\text{pr}} = 5.5$meV.

Now, let us focus on the calculation of the optical pump–probe conductivity $\sigma(\Delta t, \omega)$. Here, we choose the same strategy, as discussed previously in section 3.4.2 with optical control simulations. For a numerical implementation we need to perform, however, some additional preparing calculations. First, we should calculate the time–dependent current density $\mathbf{j}_{\mathbf{q}_{\text{pr}}}(\Delta t, t)$ induced by a probing excitation, which depends on the time delay Δt

between the pump and probe pulses. According to Ref. [47] the current density is given by

$$\mathbf{j}_{\mathbf{q}_\mathrm{pr}}(\Delta t, t) = \mathbf{j}^{(1)}_{\mathbf{q}_\mathrm{pr}}(\Delta t, t) + \mathbf{j}^{(2)}_{\mathbf{q}_\mathrm{pr}}(\Delta t, t) \tag{7.18}$$

with

$$\begin{aligned} \mathbf{j}^{(1)}_{\mathbf{q}_\mathrm{pr}}(\Delta t, t) &= -\sum_{l=1}^{2}\sum_{\mathbf{k},\sigma} \frac{e\hbar}{2m_l V}\left(2\mathbf{k} + \mathbf{q}_\mathrm{pr}\right)\left\langle \hat{c}^\dagger_{\mathbf{k},\sigma,l}\hat{c}_{\mathbf{k}+\mathbf{q}_\mathrm{pr},\sigma,l}\right\rangle(\Delta t, t) \\ \mathbf{j}^{(2)}_{\mathbf{q}_\mathrm{pr}}(\Delta t, t) &= -\sum_{l=1}^{2}\sum_{\mathbf{k},\mathbf{q},\sigma} \frac{e^2}{m_l V}\mathbf{A}_{\mathbf{q}_\mathrm{pr}-\mathbf{q}}\left\langle \hat{c}^\dagger_{\mathbf{k},\sigma,l}\hat{c}_{\mathbf{k}+\mathbf{q},\sigma,l}\right\rangle(\Delta t, t) \end{aligned} \tag{7.19}$$

and $\mathbf{q}_\mathrm{pr}$ being the wave vector of the probe pulse. Due to the fact that $\mathbf{j}^{(2)}_{\mathbf{q}_\mathrm{pr}}(\Delta t, t)$ induces only constant offset in the imaginary part of the spectrum, we neglect its contributions in our calculations. A straightforward Bogoliubov–Valatin transformation of the remaining term leads to the result:

$$\begin{aligned} \mathbf{j}^{(1)}_{\mathbf{q}_\mathrm{pr}}(\Delta t, t) = -\sum_{l=1}^{2}\frac{e\hbar}{2m_l V}\sum_{\mathbf{k}}\left(2\mathbf{k} + \mathbf{q}_\mathrm{pr}\right)\Big[&L^{(+)}_{\mathbf{k},\mathbf{q}_\mathrm{pr},l}\left(\alpha^\dagger_{\mathbf{k}l}\alpha_{\mathbf{k}+\mathbf{q}_\mathrm{pr},l} - \beta^\dagger_{\mathbf{k}+\mathbf{q}_\mathrm{pr},l}\beta_{\mathbf{k}l}\right) \\ &+M^{(-)}_{\mathbf{k},\mathbf{q}_\mathrm{pr},l}\left(\alpha^\dagger_{\mathbf{k}l}\beta^\dagger_{\mathbf{k}+\mathbf{q}_\mathrm{pr},l} + \alpha_{\mathbf{k}+\mathbf{q}_\mathrm{pr},l}\beta_{\mathbf{k}l}\right)\Big] \end{aligned} \tag{7.20}$$

Here, we used the same notation [2] , as in section 7.1.2. Now, the time evolution of the current density $\mathbf{j}_{\mathbf{q}_\mathrm{pr}}(\Delta t, t) = \mathbf{j}^{(1)}_{\mathbf{q}_\mathrm{pr}}(\Delta t, t)$ is fully determined by the quasiparticle densities, which can be numerically obtained again by using the density matrix formalism (see section 7.1.3). However, some additional numerical approximations should be done. Due to the different wave vectors $\mathbf{q} \neq \mathbf{q}_\mathrm{pr}$ of the pump and probe pulses one should introduce a new momentum grid for the quasiparticle densities of the probe pulse. However, the difference of $\mathbf{q} - \mathbf{q}_\mathrm{pr}$ is quite small in comparison with the momentum $\mathbf{k}$ so that one can still use the same discretization mesh. In addition, we make an approximation for the diagonal elements:

$$\alpha^\dagger_{\mathbf{k}+\mathbf{q}_\mathrm{pr},l}\beta^\dagger_{\mathbf{k}+\mathbf{q}_\mathrm{pr},l} \approx \alpha^\dagger_{\mathbf{k}+\mathbf{q}_\mathrm{p},l}\beta^\dagger_{\mathbf{k}+\mathbf{q}_\mathrm{p},l} \quad , \quad \text{etc.} \tag{7.21}$$

For the off–diagonal terms, i.e. $\alpha^\dagger_{\mathbf{k}+m\mathbf{q}_\mathrm{pr},l}\beta^\dagger_{\mathbf{k}+n\mathbf{q}_\mathrm{pr},l}$ etc., we choose the matrix element to be zero whenever $|m-n| > 1$. Due to the linear coupling of the probe we need to perform our calculations only in the first order of $\mathbf{A}_{\mathbf{q}_\mathrm{pr}}$. Therefore, in the linear response approximation the differential equations for each band l for the probe pulse are given by:

$$\begin{aligned} i\hbar\frac{d}{dt}\alpha^\dagger_{\mathbf{k},l}\alpha_{\mathbf{k}+\mathbf{q}_\mathrm{pr},l} = &\left(R_{\mathbf{k}+\mathbf{q}_\mathrm{pr},l} - R_{\mathbf{k},l}\right)\alpha^\dagger_{\mathbf{k},l}\alpha_{\mathbf{k}+\mathbf{q}_\mathrm{pr},l} + C_{\mathbf{k}+\mathbf{q}_\mathrm{pr},l}\alpha^\dagger_{\mathbf{k},l}\beta^\dagger_{\mathbf{k}+\mathbf{q}_\mathrm{pr},l} + C^*_{\mathbf{k},l}\alpha_{\mathbf{k}+\mathbf{q}_\mathrm{pr},l}\beta_{\mathbf{k},l} \\ &+\frac{e\hbar}{2m}2\mathbf{k}\cdot\mathbf{A}_{\mathbf{q}_\mathrm{pr}}\left\{L^{(+)}_{\mathbf{k},\mathbf{q}_\mathrm{pr},l}\left(\alpha^\dagger_{\mathbf{k},l}\alpha_{\mathbf{k},l} - \alpha^\dagger_{\mathbf{p}_\mathrm{p},l}\alpha_{\mathbf{p}_\mathrm{p},l}\right) + M^{(-)}_{\mathbf{k},\mathbf{q}_\mathrm{pr},l}\left(\alpha_{\mathbf{p}_\mathrm{p},l}\beta_{\mathbf{p}_\mathrm{p},l} - \alpha^\dagger_{\mathbf{k},l}\beta^\dagger_{\mathbf{k},l}\right)\right\} \end{aligned} \tag{7.22}$$

---

[2] i.e. $\left\langle \hat{\alpha}^\dagger_{\mathbf{k}l}\hat{\alpha}_{\mathbf{k}+\mathbf{q}_\mathrm{pr},l}\right\rangle(\Delta t, t) = \alpha^\dagger_{\mathbf{k}l}\alpha_{\mathbf{k}+\mathbf{q}_\mathrm{pr},l}$, etc.

with shortcut $\mathbf{p}_{\mathrm{p}} = \mathbf{k} + \mathbf{q}_{\mathrm{p}}$. The differential equations for the remaining quasiparticle densities are shown in Appendix B.2. Finally, the conductivity can be calculated from:

$$\sigma(\Delta t, \omega) = \frac{j(\Delta t, \omega)}{i\omega A(\Delta t, \omega)} \tag{7.23}$$

with the Fourier transformed component of the vector potential along the y–axis with respect to time t:

$$A(\Delta t, \omega) = \int\limits_{-\infty}^{\infty} dt \hat{\mathbf{e}}_y \cdot \mathbf{A}_{\mathbf{q}_{\mathrm{pr}}}(\Delta t, t) e^{i\omega t} \tag{7.24}$$

and of the current density:

$$j(\Delta t, \omega) = \int\limits_{-\infty}^{\infty} dt \hat{\mathbf{e}}_y \cdot \mathbf{j}_{\mathbf{q}_{\mathrm{pr}}}(\Delta t, t) e^{i\omega t} \ , \tag{7.25}$$

respectively.

Chapter 8

Results of simulations of Higgs modes in superconductors in nonequilibrium

Based on the framework of the density–matrix theory, which is introduced in chapter 7, we present here the results of our time–resolved simulations for a two–band superconductor. We start with the discussion of two decoupled bands, where the interband coupling V_{12} is set to zero. In this case both superconducting gaps Δ_l, $l = 1, 2$ evolves independently with time. Therefore, the qualitative comparison of the results with the previous theoretical studies for a one–band superconductor is possible [47, 56].

The second part of this chapter is devoted to the role of the final interband coupling in two–band superconductors with the singlet pairing correlations, which are driven out of equilibrium. In particular, we study the effects of the laser pulse excitation on the dynamics of the coupled superconducting gaps by variation of the pump pulse width and intensity.

8.1. Numerical parameters

Let us introduce the parameters, which we use for our numerical simulations. First, we prepare our two–band system in the BCS ground state at zero temperature. In order to keep things on the simplest nontrivial level, we consider attractive momentum–independent pairing interactions with $V^{lj}_{\mathbf{k}\mathbf{k}'} = V_{lj}$, $l, j = 1, 2$. Moreover, the interband coupling V_{11} in the first band ($l = 1$) is assumed to be larger, than in the second band with V_{22}. Hence, according to Eq. (7.2) it leads to two s–wave order parameters with the distinct superconducting gaps $\Delta_{\mathbf{k}l} \equiv \Delta_l$. These assumptions are suitable, for example, for MgB_2 superconductor, where the strong electron coupling appears in the σ–bonding boron orbital and the weaker pairing formation occurs in the π–bonding state [139]. The material parameters of this superconducting system are well–known from the various experimental and theoretical studies [140], and will be used for our numerical calculations. The numbers are presented in Table 8.1. For simplicity, we consider a tetragonal crystal structure with the lattice constant $a = 3.5 \cdot 10^{-10}$m. Moreover, the electron's dispersion in momentum space is described within the tight bounding approximation by two parabolic bands [1]. Here, the Fermi momentum is given by $k_{\mathrm{F}l} = \sqrt{2m_l E_{\mathrm{F}l}}/\hbar$ with the Fermi energy $E_{\mathrm{F}l}$. The curvature of the bands is described by the effective electron mass m_l, which is measured in units of the free electron mass m_0. The electron pairing formation is assumed to take place within the energy window of $2\hbar\omega_{\mathrm{Debye}}$ and the initial superconducting gaps are given by $|\Delta_l|$.

	$\lvert\Delta_l\rvert$ [meV]	m_l/m_0	$\mathrm{E}_{\mathrm{F}l}$ [meV]	$\mathrm{k}_{\mathrm{F}l} \cdot a$	$\hbar\omega_{\mathrm{Debye}}$ [meV]
σ band ($l = 1$)	7.0	2.74	700.996	2.4850	50.0
π band ($l = 2$)	3.0	1.01	2863.222	3.0450	50.0

Table 8.1: Material parameter values describing the two–band superconducting system. The numbers were taken from the experimental and theoretical studies of MgB_2 superconductor [140].

Now, in order to excite both gaps in nonequilibrium, we adjust the central energy of the pump pulse in a way, that it lies in between $2|\Delta_1|$ and $2|\Delta_2|$. Thereby, due to the Gaussian shape of the laser field, which is given in Eq. (7.5), one is able to break Cooper–pairs in both superconducting condensates and excite quasiparticles above the gaps. For our numerical calculations it turned out that the pump pulse with the energy $\hbar\omega = 8$meV gives sufficiently good results. The pulse width τ and its amplitude A_0 are variable parameters in our simulations.

For probing the superconducting system we use a weaker laser pulse of the similar form. Its energy $\hbar\omega_0^{\mathrm{pr}} = 5.5$meV is chosen to be smaller, than the excitation energy of the smallest energy gap, i.e. $\hbar\omega_0^{\mathrm{pr}} < 2 \min\limits_{l=1,2} |\Delta_l|$. In this case the probe pulse does not additionally destroy the superconducting condensates. Further, we take the width of the pulse $\tau_{\mathrm{pr}} = 0.15$ps to be very short in time, in order to probe over a very broad energy region. Finally, for the amplitude of the probe pulse we choose the value $A_0^{\mathrm{pr}} = 10 \cdot 10^{-8}$Js/(Cm). The parameters of both pulses are summarized in Table 8.2.

	energy [meV]	duration [ps]	intensity [Js/(Cm)]
pump pulse	$\hbar\omega_0 = 8.0$	τ, variable	A_0, variable
probe pulse	$\hbar\omega_0^{\mathrm{pr}} = 5.5$	$\tau_{\mathrm{pr}} = 0.15$	$A_0^{\mathrm{pr}} = 10 \cdot 10^{-8}$

Table 8.2: Parameter values of the pump and probe laser fields in numerical simulations.

---

[1] an illustration of the electron band configuration is shown in Fig. 7.2

8.2. Two independent bands

8.2.1. Response on the pump pulse

Let us first discuss the case of two decoupled bands with the interband coupling $V_{12} = 0$ and accordingly two distinct gaps. An action of the strong ultrafast pump laser pulse leads to the breaking of Cooper pairs in both superconducting condensates and to the excitation of Bogoliubov quasiparticles above the gaps Δ_l, $l \in \{1, 2\}$. Consequently, the amplitudes of the order parameters $|\Delta_l|$ are reduced. In the language of the free energy this correspond to the shrinking of the Mexican–hat potential with the reduction of its minimum value. However, depending on the laser pulse width τ one can distinguish between two nonequilibrium scenarios, which are schematically illustrated in Fig. 8.1.

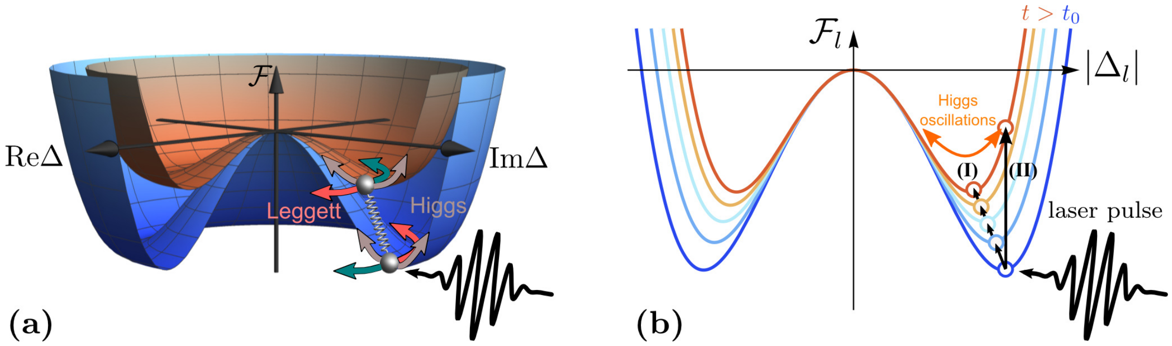

Figure 8.1: Illustration of the excitation process for a two–band superconductor. (a) Effective free–energy landscape $\mathcal{F}$ for a two–band superconductor with blue and red Mexican hat potentials, representing the lower and upper band, respectively. The pump pulse excitation leads to the modification of the free energy landscape $\mathcal{F}$. (b) Temporal evolution of the Mexican hat potential from (a) for each band l shown in cross–section. After an action of the pump laser pulse the free energy $\mathcal{F}_l$, $l = \{1, 2\}$ is modified and a superconductor can be excited on two different ways: (I) the system changes adiabatically with $\mathcal{F}_l$ due to the broad pulse; (II) a short pulse leads to the non–adiabatic excitation of a superconducting system resulting in oscillations of $|\Delta_l|$ around the new minimum of $\mathcal{F}_l$.

The first situation (path (I) in Fig. 8.1(b)) appears, when the superconducting system reacts on a faster time scale $\tau_{\Delta_l} \simeq h/(2|\Delta|_l) \ll \tau$ than the pump pulse. In this case the superconductor can adiabatically follow the changes of the free energy $\mathcal{F}_l$ and one observes a monotonic reduction of the order parameter amplitudes $|\Delta_l|$. This occurs independently of the pulse fluency $A_0^2\tau$. An illustration of this behavior is shown exemplary in Fig. 8.2, where we plot $|\Delta_l|$ as a function of time for a pump pulse with the width $\tau = 5$ps and different amplitudes. Since we do not consider any relaxation channels in our model, the superconducting system does not return to the initial equilibrium state after the light pulse has gone and the reduced value of the order parameter $|\Delta_l|$ remains approximately constant. By increasing the pulse intensity we are able to break more Cooper pairs in the superconducting system. As a result, we observe a stronger decrease of the superconducting amplitudes $|\Delta_l|$ with the pulse fluency.

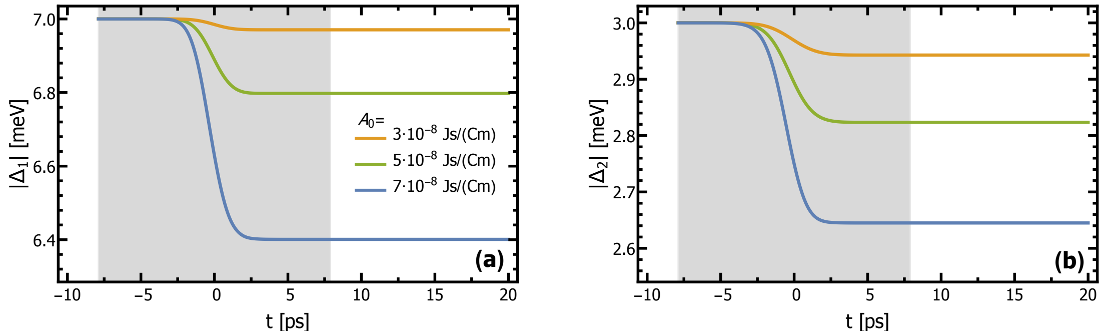

Figure 8.2: Temporal evolution of order parameters (a) $|\Delta_1|(t)$ and (b) $|\Delta_2|(t)$ after a broad pump pulse with $\hbar\omega_0$=8meV, τ = 5.0ps and different amplitudes A_0. The pump pulse is indicated in both figures by the gray region around $t = 0$.

A more interesting case represents an excitation of a two–band superconductor with the short laser pulse, which now acts on a faster time scale than the superconducting system can response, i.e. $\tau_{\Delta_l} \gg \tau$. This non–adiabatic situation corresponds to the rapid changes in the free energy $\mathcal{F}_l$, which is marked in Fig. 8.1(b) by path (II), and, consequently, to the non–thermal excitation of the Bogoliubov quasiparticles. The calculated temporal evolution of the order parameter amplitudes $|\Delta_l|$ for pump pulse with τ = 0.4ps and energy $\hbar\omega_0$ = 8meV is presented in Fig. 8.3. In contrast to the adiabatic case (I) we observe oscillations of the order parameters after their monotonic decrease. This oscillations do not disappear even when the pulse has gone and occurs around the asymptotic gap values $|\Delta_l^\infty|$ for $t \to \infty$ with the characteristic single frequencies for each band l. The later fact can be clearly seen after performing the Fourier analysis of the superconducting oscillations (see Fig. 8.3 (b) and (d)). We obtain one peak for each band in Fourier spectrum at the energy values $\hbar\omega_{\mathrm{H}l} = 2|\Delta_l^\infty|$. This leads to the important conclusion that the superconducting order parameters oscillate at frequencies, which reflect the asymptotic gap values $|\Delta_l^\infty|$. However, these oscillations are not simple harmonic and show damping with the decay factor of $1/\sqrt{t}$. As already mentioned in the adiabatic case, we study our superconducting model in the collisionless limit without any relaxation channels. Therefore, these damped oscillations can only come from the decoherence effects between the quasiparticle densities with different momenta. Similar results were observed for the one–band superconductors [47, 48, 50, 53, 65]. In case of simple interaction quench [53, 65] one derived an analytical expression for the SC gap oscillations using the Anderson pseudospin representation:

$$|\Delta| = |\Delta^\infty| \left[1 + \Gamma \frac{\cos\left(2|\Delta^\infty|t/\hbar + \Phi\right)}{\sqrt{t|\Delta^\infty|}}\right] \tag{8.1}$$

with Γ and Φ denoting amplitude and phase of the oscillations, respectively. A comparison of this analytical result for each band l (red lines in Fig. 8.3) with our numerical data shows,

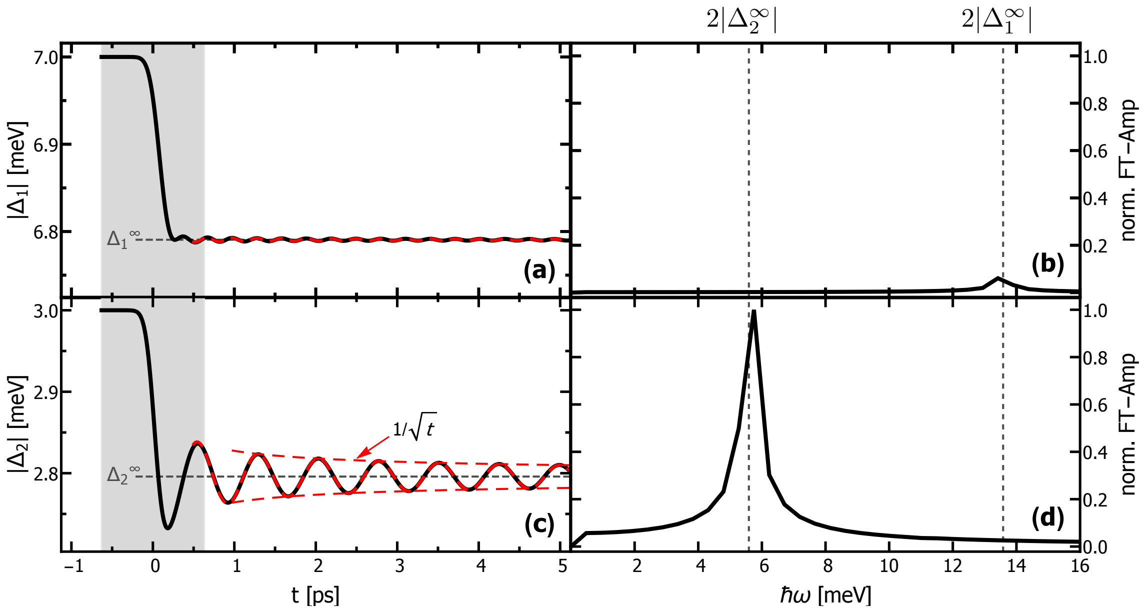

Figure 8.3: Excitation of a superconductor by a short pump pulse with $\hbar\omega_0$=8meV, $\tau = 0.4$ps and $A_0 = 10 \cdot 10^{-8}$Js/(Cm). (a),(c) Temporal evolution of $|\Delta_l|$ (black line) together with the analytical fit curve and $1/\sqrt{t}$ envelope (red dashed lines). Here, the pulse is indicated by the gray region around $t = 0$. (b),(d) Fourier transformation for $\Delta_1(t)$ and $\Delta_2(t)$, respectively. The dashed lines at $2\Delta_l^\infty$ serve as guides to the eye.

however, a very good agreement. Finally, we observe that the intensity of oscillations and, in turn, the intensity of the peaks in the Fourier spectra are different for different bands. This can be explained by the fact that the pump pulse with the excitation energy $\hbar\omega = 8$meV, lying in between $2\Delta_1$ and $2\Delta_2$, breaks more Cooper pairs in the smaller gap than in the larger one.

What is the physical origin of these oscillations? Due to the Heisenberg's uncertainty principle a short pulse in the time domain and, in turn, broad pulse in the energy domain induces a shaking of the whole superconducting condensates. This collective excitation of a superconductor leads to the radial oscillations in the Mexican–hat potential of the free energy $\mathcal{F}_l$ (see Fig. 8.1) and, accordingly, to excitation of the amplitude modes. Due to the approximate particle–hole symmetry of the superconducting excitations and therefore similar description to the Lorentz invariant theory [130], these amplitude modes correspond to the Higgs mode from the high energy physics.

The asymptotic gap value of the order parameters $|\Delta_l^\infty|$ and therefore the frequency of the Higgs mode in a superconductor are affected by the integrated pump pulse intensity $|A_0|^2\tau$. In order to illustrate this statement, we plot $|\Delta_l^\infty|$ as a function of fluency for each band l. The result is shown in Fig. 8.4. Here, we find that the increase of the pump pulse intensity leads to decrease of the asymptotic gap value $|\Delta_l^\infty|$ of the order parameter in each band l. This can be explained by the fact that the intense pulses can break more Cooper pairs in the superconducting condensates. This is an important observation, because other collective excitations in a superconductor, like phonons, magnons or similar, are almost independent from the intensity of the pump pulse. Therefore, the Higgs modes can be clearly identified in an experiment. A first experimental observation of the Higgs mode was done in the group of R. Shimano [35] by studying the thin NbN films with the THz–pump and THz–probe spectroscopy. The resulting time evolution of the transmitted electrical laser field showed pronounced oscillation for different pump fluency, which are in a good agreement with Eq. (8.1).

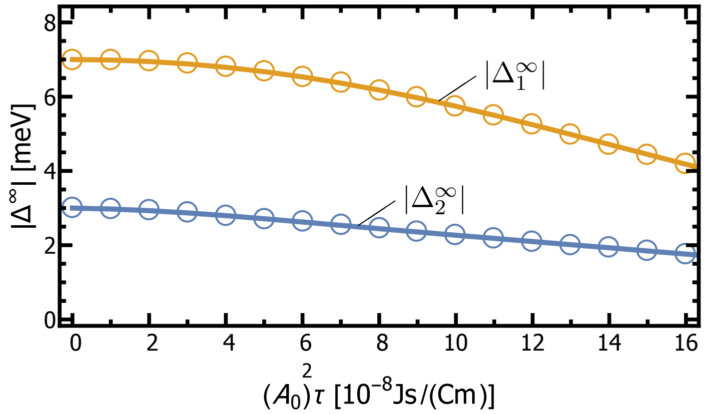

Figure 8.4: Asymptotic gap values $|\Delta_l^\infty|$, $l = 1, 2$ as functions of the integrated pump pulse intensity $A_0^2\tau$. The pump pulse has parameters: $\hbar\omega = 8\mathrm{meV}$, $\tau = 0.4\mathrm{ps}$.

8.2.2. Pump–probe response

Now, let us examine the possibility to excite Higgs oscillations in the pump–probe experiment. For this purpose we consider a pump pulse excitation in a nonadiabatic regime with pulse parameters: $\hbar\omega_0 = 8\mathrm{meV}$, $\tau = 0.4\mathrm{ps}$, and $A_0 = 10 \cdot 10^{-8}\mathrm{Js/(Cm)}$. For probing the system at different time delays Δt we apply an additional weak pulse with a short duration time, which parameters are given in Table 8.2. The strategy of the pump–probe response calculations is described in section 7.2.

In Figs. 8.5 (a) and (b) we first show the results of computations for real $\sigma_1(\Delta t, \omega)$ and imaginary $\sigma_2(\Delta t, \omega)$ parts of the optical conductivity versus frequency ω, respectively. The calculations were performed at time delay $\Delta t = 5.5\mathrm{ps}$. As can be clearly seen in Figs. 8.5 (a) and (b), both $\sigma_1(\Delta t, \omega)$ and $\sigma_2(\Delta t, \omega)$ exhibit only a single sharp edge, which appears at the Higgs mode frequency $\omega_{\mathrm{H2}} = 2\Delta_2^\infty/\hbar$ corresponding to the superconducting gap oscillations in the lower band $l = 2$. Interestingly, the Higgs mode at higher frequency, which results in superconducting order parameter oscillations in the upper band $l = 1$, do not appear (or more precisely, can not be clearly identified) in the conductivity spectrum. The reason is that it is mostly overdamped by the quasiparticle continuum. Therefore, we will skip discussion of this mode in the following. It should be also mentioned that a dip at low frequencies in the result of calculation for $\sigma_1(\Delta t, \omega)$ (see Fig. 8.5 (a)) is an artifact of numerical calculations and caused by numerical discretization discussed in section 7.1.4 and by finite size–effects of the model.

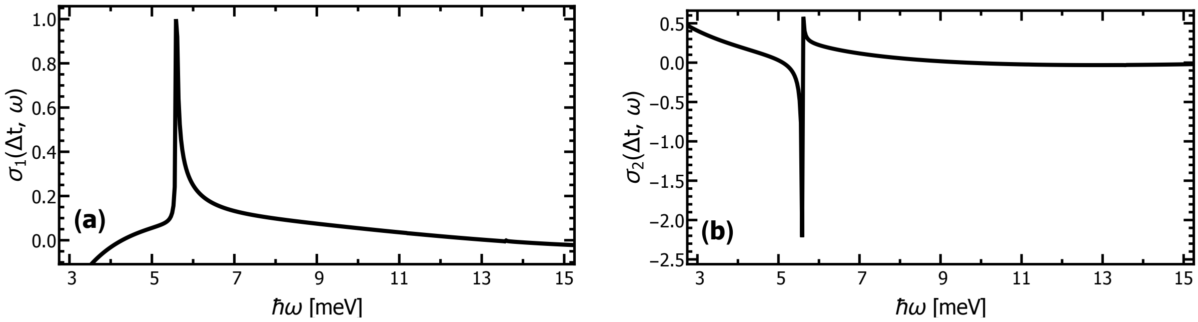

Figure 8.5: (a) Real $\sigma_1(\Delta t, \omega)$ and (b) imaginary $\sigma_2(\Delta t, \omega)$ parts of the pump–probe response as a function of frequency calculated at time delay $\Delta t = 5.5$ps. The system is excited by a pump pulse with parameters $\hbar\omega_0 = 8$meV, $\tau = 0.4$ps, and $A_0 = 10 \cdot 10^{-8}$Js/(Cm).

Next we plot the real part of the optical conductivity $\sigma_1(\Delta t, \omega)$ as a function of delay time Δt. The result is illustrated in Fig. 8.6. Here, we can observe that the position of the sharp edge for Higgs mode ω_{H2} remains independent with regard to time. However, we find that the important dynamics of the superconducting gap manifests itself in the intensity oscillations of the pump–probe signal as a function of Δt. In addition, it should be noted that similar behavior can be found in the imaginary part of the optical conductivity, since $\sigma_1(\Delta t, \omega)$ and $\sigma_2(\Delta t, \omega)$ provide same information about the dynamics in the system through Krammers–Kronig relation. The changes in the intensity of the pump–probe response can be clearly observed at the Higgs frequency ω_{H2}, where the conductivity shows the sharp edge (see Fig. 8.6). Let us discuss this behavior in more detail. For that reason we plot in Fig. 8.7 (a) the intensity of the pump–probe signal at ω_{H2} as a function of time delay Δt. First, we find here fast decaying oscillations with regard to time. Further, a comparison with the temporal evolution of the superconducting gap $\Delta_2(t)$ (see Fig. 8.3) reveals a quite good agreement in their behaviors. Finally, Fourier transforming with respect to Δt shows two distinct peaks in spectrum (see Fig. 8.7 (b)). The position of the peaks correspond to

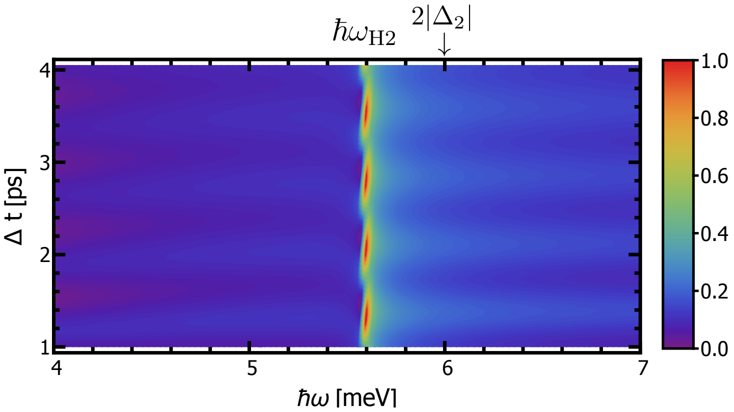

Figure 8.6: Real part of the pump–probe response $\sigma_1(\Delta t, \omega)$ plotted for various time delays Δt with the color–coded intensity of the signal. The parameters of the laser pulses are the same as in Fig. 8.5. The oscillations are clearly seen at $\hbar\omega_{\mathrm{H2}} = 2|\Delta_2^\infty|$.

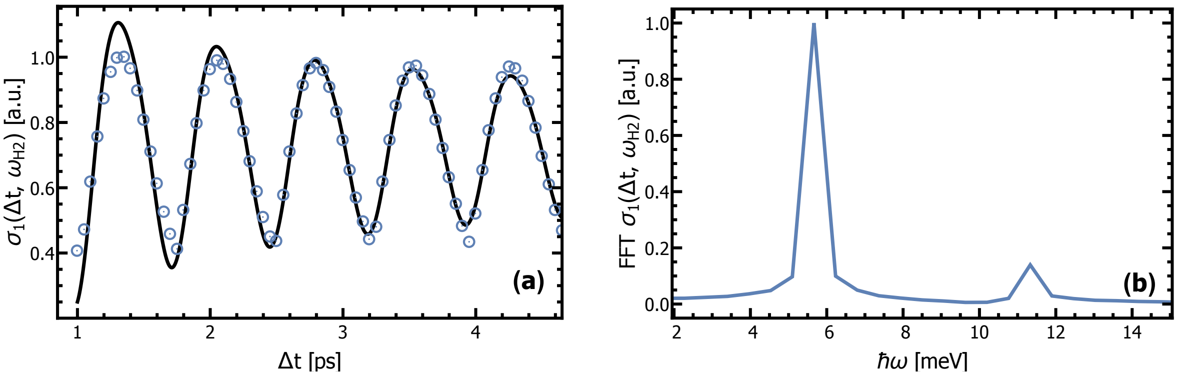

Figure 8.7: (a) Time dependent magnitude of a peak in $\sigma_1(\Delta t, \omega)$ at frequency $\omega_{\mathrm{H2}} = 2\Delta_2^\infty/\hbar$ (see also Fig. 8.6). Oscillating behavior is illustrated. Black line represents the data fit by using Eq. (8.1). (b) The Fourier spectrum of the oscillations from (a).

the Higgs mode ω_{H2} and to its higher harmonics. This observation supports the results of the previous theoretical studies for the case of single band superconductors [47, 56].

8.3. Two bands with finite interband coupling

8.3.1. Nonequilibrium scenarios after the pump pulse excitation

Now, let us study the nonequilibrium excitation of a two–band superconducting system with an additional nonzero interband coupling V_{12}. In analogy to the discussion in section 8.2.1, we distinguish here between two dynamical regimes. First, we focus on the adiabatic excitations of a superconductor with a broad pump pulse. For the parameter values of the pulse we choose: $\hbar\omega_0 = 8\mathrm{meV}$, $\tau = 5\mathrm{ps}$, $A_0 = 5 \cdot 10^{-8}\mathrm{Js/(Cm)}$. The results of time–dependent calculations for superconducting gaps $|\Delta_l(t)|$, $l = \{1, 2\}$ with different relative interband coupling $v = V_{12}/V_{11}$ are shown in Fig. 8.8. Here, we observe independently of v a monotonic reduction of the superconducting gaps $|\Delta_l|$ resulted after pumping. However, since both order parameters are connected via Eq. (7.2), the reduced gap values depend strongly on coupling between the bands v. This effect seems to be stronger in the gap $|\Delta_2|$ with lower energy. This can be explained by different values of the intraband couplings V_{11} and V_{22} in bands $l = 1$ and $l = 2$, respectively. Similar behavior was also observed in the previous theoretical studies on two–band superconductors [59].

By pumping with a short pump pulse $\tau \ll \tau_{\Delta_l}$ we has to deal with non–adiabatic situation. In this case the excitation of the collective modes in a two–band superconducting system is possible (see discussion in section 8.2.1). Thus, we adjust the duration of the pump pulse to $\tau = 0.4\mathrm{ps}$ and perform the time–dependent simulations. In Fig. 8.9 (a)-(c) we present the result of calculations of the order parameter amplitudes $|\Delta_l|$, $l = \{1, 2\}$ together with the relative phase $\Phi_2 - \Phi_1$ of the superconducting gaps for three different relative interband couplings v. First of all, we find in the dynamics of both order parameter

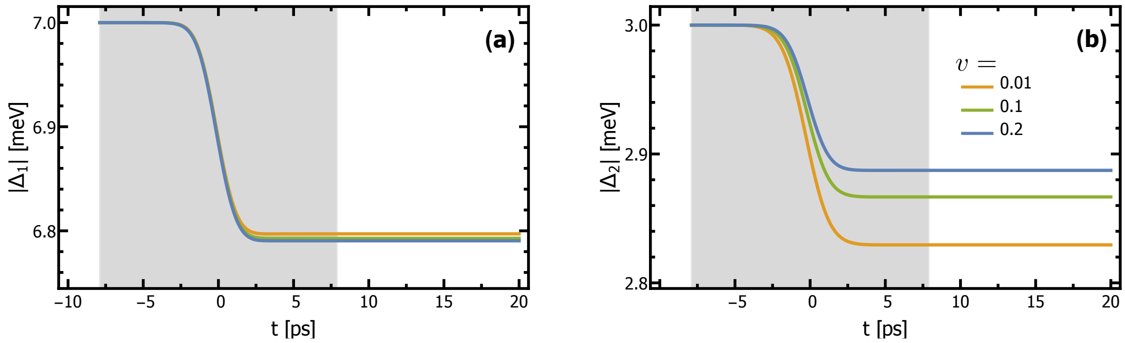

Figure 8.8: Temporal evolution of the order parameters (a) $|\Delta_1|(t)$ and (b) $|\Delta_2|(t)$ for different values of the relative interband coupling $v = V_{12}/V_{11}$ after a broad pump pulse excitation with $\hbar\omega_0 = 8\text{meV}$, $\tau = 5.0\text{ps}$, $A_0 = 5 \cdot 10^{-8}\text{Js/(Cm)}$. The pulse is indicated in both figures by the gray region around $t = 0$.

amplitudes $|\Delta_l|$ their monotonic reduction due to the excitation of the quasiparticles above the superconducting gaps with the subsequent oscillations. Further, the magnitude of the oscillations seems to have no damping in contrast to the situation with two decoupled bands (see section 8.2.1). This can be explained by appearance of an additional competing oscillation, which manifests itself also in the dynamics of the relative phase between the superconducting gaps (see Fig. 8.9 (c)). Finally, the Fourier analysis of all these oscillations, shown in Fig. 8.9 (d)-(e), reveals occurrence of three different modes at frequencies ω_{H1}, ω_{H2}, and ω_{L}. Also the higher harmonics of ω_{L} are observable. Let us discuss all modes one by one. The collective excitations with $\omega_{\mathrm{H}l} = 2|\Delta_l^\infty|/\hbar$ appear only in the amplitude channel of the order parameter and correspond to the Higgs amplitude modes, which were discussed in previous section 8.2.1. This frequency dependence of the modes on the approximate gap value Δ_l holds independently of the relative interband coupling v and also for all laser intensities A_0. Due to the interband Cooper pair tunneling, both Higgs modes are clearly visible in the dynamics of each gap. However, the intensity of the higher Higgs mode ω_{H1} in both order parameter oscillations Δ_l is damped stronger due to the location within the Bogoliubov quasiparticle continuum, which is bounded by Δ_2^∞.

Besides two Higgs modes we observe appearance of a new collective excitation in the nonequilibrium spectrum, which is located below the quasiparticle continuum. This third mode in two–band superconductors shows pronounced oscillations with the single frequency ω_{L} in the temporal evolution of the relative phases between both gaps (see Fig. 8.9 (c),(f)). This mode reveals a strong dependance on the relative interband coupling v. While the frequency ω_{L} increases with the increasing value of v, the intensity of the mode gets reduced. Hence, these out of phase oscillations of the superconducting condensates can be identified as the Leggett phase mode. It should be noted that according to the discussion in section 6.3 the two–band superconductors exhibit two possible characteristic phase oscillations of the order parameter. However, the second phase mode in superconductors should appear at plasma frequency far above the quasiparticle continuum and is therefore strongly overdamped. Therefore, we will skip discussion of this mode in the following.

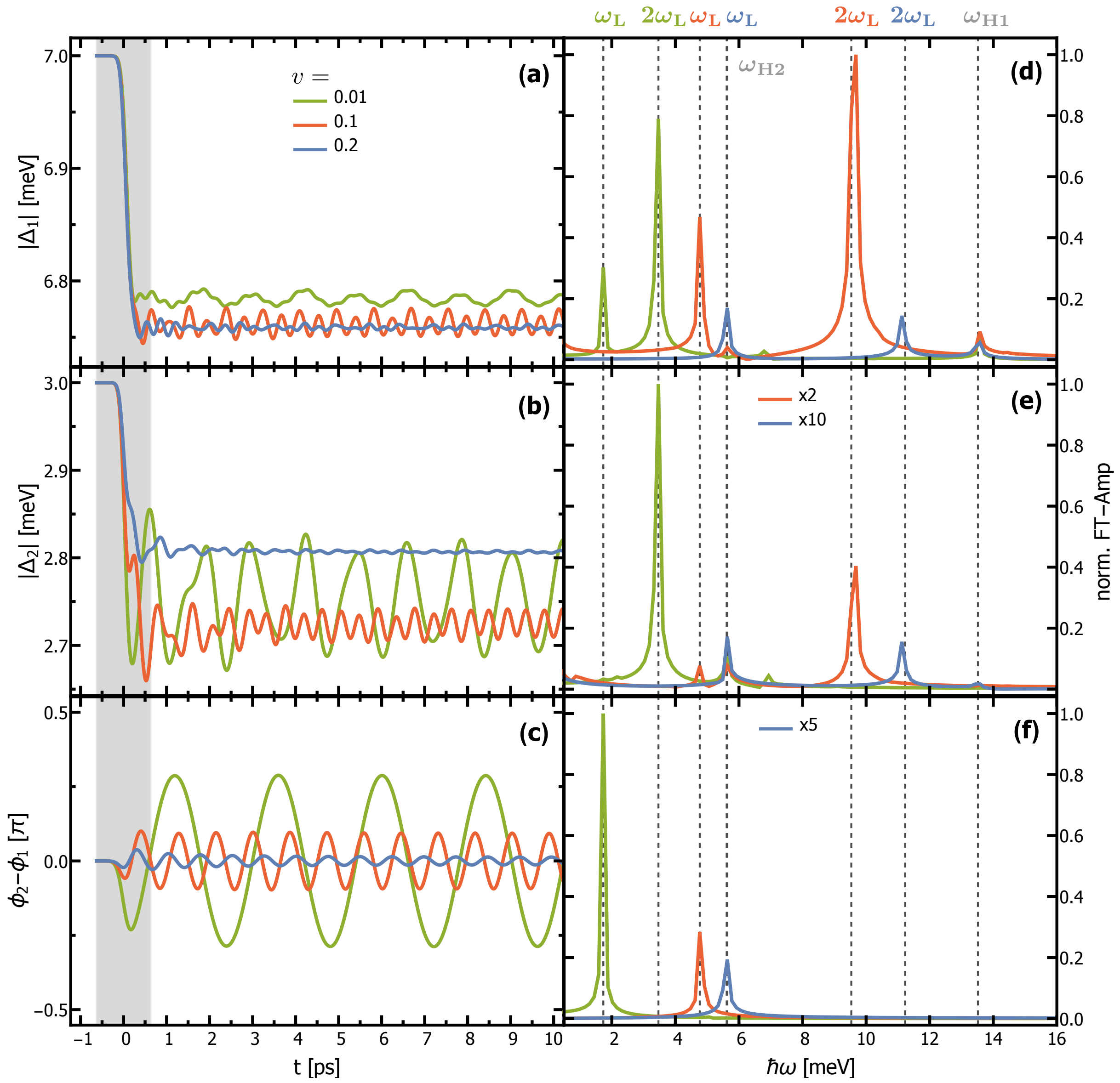

Figure 8.9: Excitation of a two–band superconductor with different values of the relative interband coupling v by a short pump pulse. The pulse is indicated by the gray region around $t = 0$ and has parameters $\hbar\omega_0$=8meV, $\tau = 0.4$ps and $A_0 = 10 \cdot 10^{-8}$Js/(Cm). (a), (b) Temporal evolution of order parameter amplitudes $|\Delta_l|$, $l = \{1, 2\}$. (d), (e) Fourier spectrum of the amplitude oscillations in panels (a) and (b). (c) Time dependence of the relative phase $\phi_2 - \phi_1$ between the gaps. (f) Fourier spectrum of the oscillations in panel (c). The dashed lines in all Fourier spectra serve as a guide to the eye.

8.3.2. Amplitude–phase mode coupling

In this section we would like to address the question whether there are further consequences of the interband coupling for the dynamics of the superconducting gaps in nonequilibrium. In this sense we consider a perturbation of a two–band superconducting system by a short pump pulse and for different relative interband couplings v. Here, we choose for the pump pulse following parameter values: $\hbar\omega_0 = 8\text{meV}$, $\tau = 0.4\text{ps}$ and $A_0 = 10{\cdot}10^{-8}\text{Js}/(\text{Cm})$.

Now, let us consider the oscillations in the relative phase of the superconducting condensates $\phi_2 - \phi_1$ as a function of v. In Fig. 8.10 we plot the energies of the phase mode oscillations obtained by performing Fourier transformation versus relative interband coupling v. Here, we find that for small values of v the Leggett mode frequency ω_L (shown in Fig. 8.10 by blue open circles) reveals a square root increase. This behavior is in a good agreement with the modified Leggett expression (see Eq. (5.40)) for the nonequilibrium case:

$$\omega_\text{L}^{(eq)} = 2\sqrt{|\Delta_1^\infty||\Delta_2^\infty|\frac{v}{V_{22} - V_{11}v^2}\left(\frac{1}{N_{\text{F}1}} + \frac{1}{N_{\text{F}2}}\right)} \tag{8.2}$$

with $N_{\text{F}l}$ being the density of states on different bands l. Here, we use asymptotic superconducting gap values $|\Delta_l^\infty|$ instead of their equilibrium counterparts $|\Delta_l|$. Moreover, the analytic expression in Eq. (8.2) represents a a good parameter–free fit to the numerically obtained data at low v, as indicated in Fig. 8.10. Here, the analytical fit is shown by the blue solid line. Most important is, however, the region with larger v, where the Leggett mode ω_L shows deviation from square root behavior of Eq. (8.2). The reason is that as soon

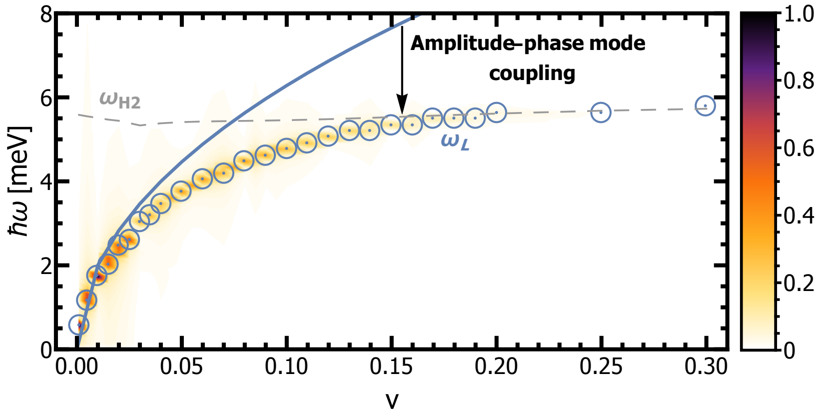

Figure 8.10: Fourier spectrum of the phase oscillations in $\phi_2 - \phi_1$ as a function of the relative interband coupling v for a two–band superconductor. Here, the system is perturbed by a short pulse with parameters $\hbar\omega_0 = 8\text{meV}$, $\tau = 0.4\text{ps}$ and $A_0 = 10 \cdot 10^{-8}\text{Js}/(\text{Cm})$. The intensity of the Fourier signal is given by the color code. The blue open circles represent the frequency of the calculated Leggett mode ω_L in nonequilibrium. In addition, the blue line indicates the frequency of the equilibrium Leggett mode obtained from Eq. (8.2) and is shown for comparison. The gray dashed line corresponds to the Higgs mode at frequency $\omega_{\text{H}2} = 2|\Delta_2^\infty|/\hbar$.

as the Leggett mode approaches the lowest Higgs mode frequency (shown by gray dashed line in Fig. 8.10), the strong interaction between both modes occurs in nonequlibrium. As a result of this amplitude–phase mode coupling, the Leggett mode is repelled below the quasiparticle continuum and remains undamped for a wide parameter range of v. Thus, it can be expected that the Leggett mode observed in MgB_2 [132] with $v \approx 0.2$ under close to equilibrium conditions should be shifted below $2\Delta_2$ in nonequilbrium.

The dynamical amplitude–phase mode coupling in nonequilibrium has a far–reaching consequences. Indeed, the Leggett mode, as a relative phase oscillation of the superconducting condensates, manifests itself in the dynamics of the gap amplitudes $|\Delta_l(t)|$. This can be seen in Figs. 8.11 (a) and (b), where we plot the energy of gap oscillations obtained by performing Fourier transformation for $|\Delta_1(t)|$ and $|\Delta_2(t)|$ versus v, respectively. Here, the Leggett mode together with the analytical fit from Eq (8.2) are shown by blue open circles and a solid line respectively. In addition we can identify two Higgs modes corresponding to amplitude oscillations of order parameters, which are shown by gray open squares and triangles. As discussed in previous section both amplitude modes show no dependence on the relative interband coupling v. It is remarkable that we observe a strong higher harmonic of the Leggett mode $2\omega_\mathrm{L}$ (green open circles), which can even appear in the energy region between the gaps. Moreover, as $2\omega_\mathrm{L}$ approaches the quasiparticle continuum a resonance with the Higgs mode ω_{H2} occurs, which is indicated by strong intensity increase in the Fourier spectrum (see Figs. 8.11 (a) and (b)).

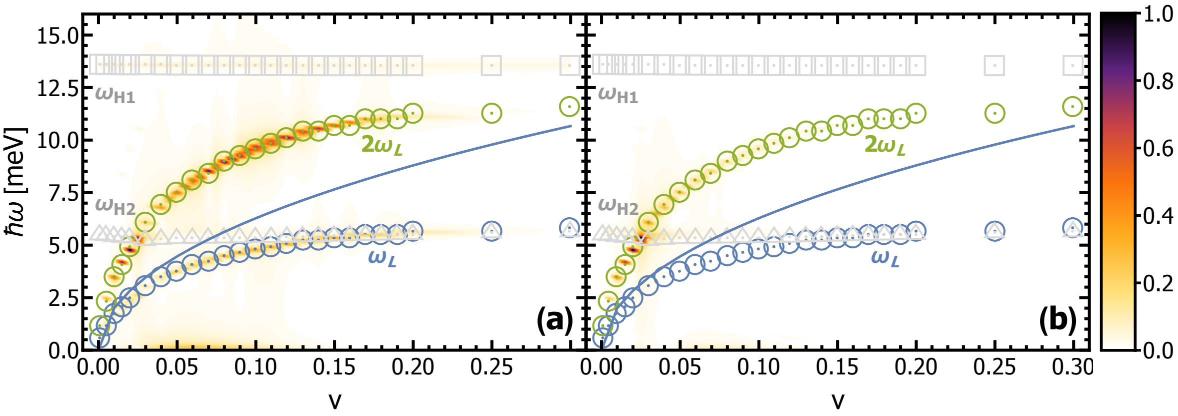

Figure 8.11: Fourier spectrum of the amplitude oscillations in superconducting gaps (a) $|\Delta_1|$ in the first band and (b) $|\Delta_2|$ in the second band as functions of the relative interband coupling v for a two–band superconductor. The parameters of the laser pulse are the same as in Fig. 8.10. The intensity of the Fourier signal is given by the color code. The open circles correspond to the Leggett mode frequency ω_L (blue) and to its higher harmonic $2\omega_\mathrm{L}$ (green). The frequencies of the Higgs modes in first and second band, ω_{H1} and ω_{H2}, are shown by open squares and triangles, respectively. In addition, the blue line indicates the frequency of the equilibrium Leggett mode obtained from Eq. (8.2)and is shown for comparison.

8.3.3. Fluency dependence

Now, let us consider the fluency dependence of the collective excitations in a two–band superconductor with the finite relative interband coupling v. For our simulations we chose the pump pulse with $\hbar\omega_0 = 8\text{meV}$, $\tau = 0.4\text{ps}$ and variable intensity A_0. The calculated temporal evolution of the superconducting gaps $|\Delta_1|(t)$ and $|\Delta_2|(t)$ for a two–band superconductor with the relative interband coupling $v = 0.12$ is presented in Fig. 8.12 (a) and (b), respectively. Here, we demonstrate the results for three different integrated pump pulse intensities $|A_0|^2\tau$.

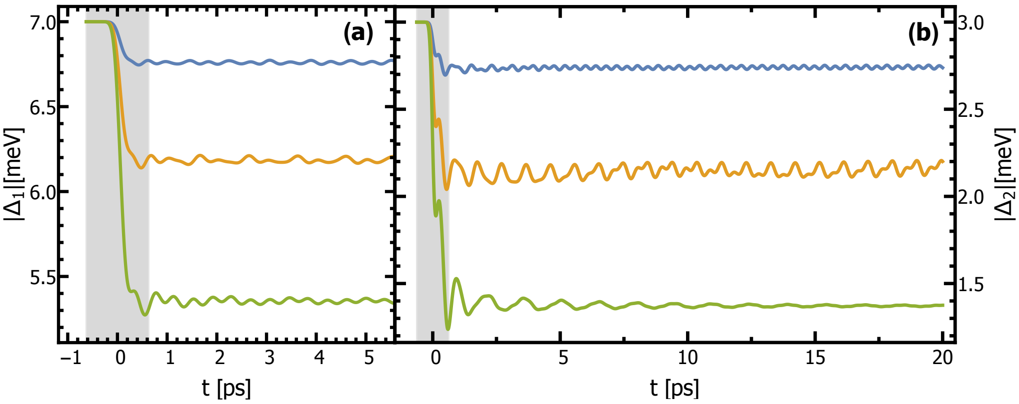

Figure 8.12: Fluency dependence of the gap dynamics in (a) $|\Delta_1|$ and (b) $|\Delta_2|$ for a two–band superconductor with the relative interband coupling $v = 0.12$. The simulations were done for integrated pump pulse intensities $|A_0|^2\tau = 4.0$ (blue solid line), 7.5 (orange solid line) and $11.0 \cdot 10^{-8}\text{Js}/(\text{Cm})$ (green solid line). The pulse is indicated by the gray region around $t = 0$.

From our simulations we find a similarity to the results discussed in section 8.2.1 for the case $v = 0$. More precisely, we observe that the frequencies of the amplitude Higgs modes $\omega_{\text{H}l}$ for each band l can be manipulated by the pump pulse. In fact, with increasing the fluency of pulse one breaks more and more Cooper pairs in a two–band superconductor. This leads to the partial suppression of the superconductivity and effectively to the reduction of the superconducting gap amplitudes. Hence, the connected with it frequencies of the Higgs modes are also decreased. In addition, we find for strong pump pulse intensity harmonic oscillations with an algebraic decay in the dynamics of the superconducting gaps, which are shown in Fig. 8.12 by the green solid lines. This behavior is reminiscent to the time evolution of the uncoupled superconducting gaps from section 8.2.1

For deeper understanding of the gaps dynamics we calculate the time dependence of the relative phase $\phi_2 - \phi_1$ between the gaps as a function of the pump pulse fluency and perform subsequently the Fourier transformation of the results. In Fig. 8.13(a) we plot the corresponding Fourier spectrum versus the integrated pump pulse intensity $|A_0|^2\tau$. In addition, we show in the same figure the frequency of the Higgs mode $\omega_{\text{H}2}$ by the gray dashed line. The temporal evolution of $\phi_2 - \phi_1$ is exemplary shown for several values of $|A_0|^2\tau$ in Figs. 8.13(b), (c) and (d). While for a small pulse intensity the Leggett and

Higgs mode appear almost far apart, we find that both modes can be brought into the resonance by increasing $|A_0|^2\tau$. This can be also clearly seen in the time dependence of the relative phase $\phi_2 - \phi_1$, which for weak pulses exhibit undamped harmonic oscillations (presented in Fig. 8.13(b)) and reveals beating effect for stronger pulse intensities (displayed in Fig. 8.13(c)). Further, we observe a strong enhancement in the intensity of the Fourier signal in the resonance condition. Importantly, this behavior manifests itself in the time dependent oscillations of the superconducting gaps shown in Fig. 8.12. Finally, an additional increasing of the pump fluency $|A_0|^2\tau$ leads to the strong reduction of the Leggett mode intensity. In this case the Leggett oscillation is strongly suppressed by the pump pulse and one observes its overdamped behavior, which is illustrated in Fig. 8.13(d). As a result, the Leggett mode does not drive the dynamics of the superconducting gaps anymore. This explains the algebraic decay in the time evolution of Δ_1 and Δ_2 shown in Fig. 8.12 by the green lines.

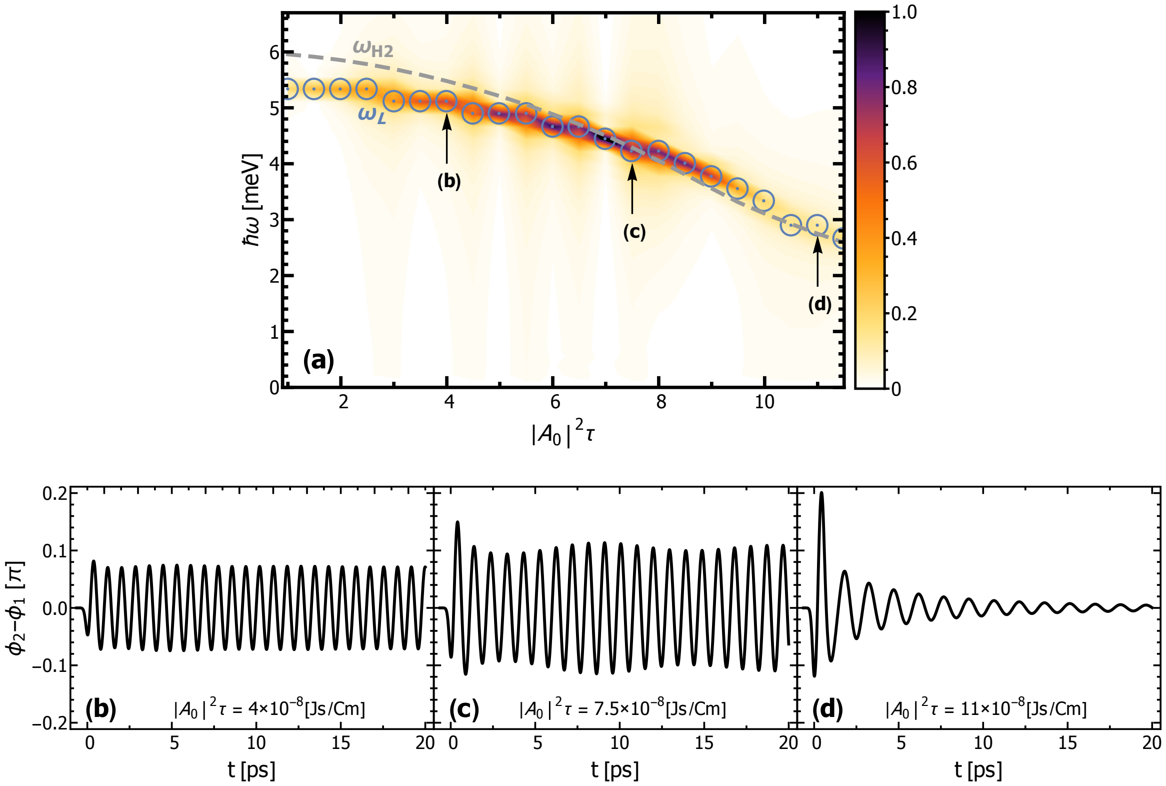

Figure 8.13: Fluency dependence of the phase dynamics in a two–band superconductor with the relative interband coupling $v = 0.12$. (a) Fourier spectrum of the relative phase $\phi_2 - \phi_1$ versus integrated pump pulse intensity $|A_0|^2\tau$. The intensity of the Fourier signal is given by the color code. The open circles display the Leggett mode frequency ω_L in nonequilibrium, whereas the gray dashed line corresponds to the frequency of the Higgs mode ω_{H2}. (b), (c) and (d) present the temporal evolution of $\phi_2 - \phi_1$ for $|A_0|^2\tau = 4.0$, 7.5 and $11.0 \cdot 10^{-8}$Js/(Cm), respectively.

The Higgs mode can even be tuned into resonance with twice the frequency of the Leggett mode $2\omega_\mathrm{L}$. For demonstration we consider a two–band superconductor with the relative interband coupling $v = 0.0225$. In Fig. 8.14 we plot the corresponding Fourier transformed phase oscillations $\phi_2 - \phi_1$ as a function of different integrated pump pulse intensities $|A_0|^2\tau$.

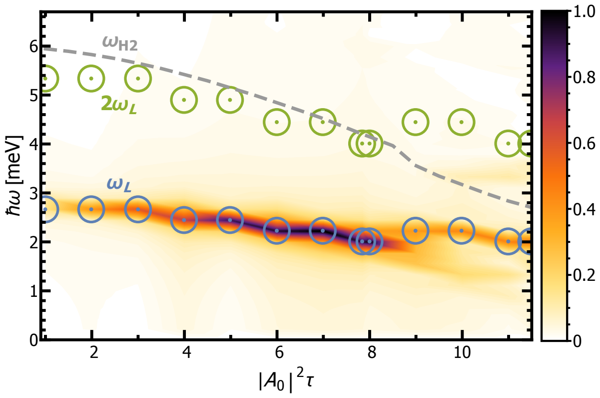

Figure 8.14: Fourier spectrum of the relative phase $\phi_2 - \phi_1$ as a function of the pump pulse fluency $|A_0|^2\tau$ for a two–band superconductor with $v = 0.0225$. The intensity of the Fourier signal is given by the color code. The open circles represent the Leggett mode frequency ω_L (blue) and its higher harmonic $2\omega_\mathrm{L}$ (green) in nonequilibrium, whereas the gray dashed line displays the Higgs mode frequency $\omega_{\mathrm{H}2}$.

The results show an enhancement in the magnitude of the relative phase oscillations $\phi_2 - \phi_1$ with increasing pulse fluency. Especially, the strongest effect appears in the resonance condition between Higgs and the twice Leggett mode frequency $2\omega_\mathrm{L}$. This is also reflected in the dynamics of the superconducting gaps $|\Delta_1|$ and $|\Delta_2|$, which we show in in Fig. 8.15 exemplary for $|A_0|^2\tau = 4.0$ and $7.84 \cdot 10^{-8}$Js/(Cm). Finally, for strong pulse intensities the Leggett mode is slightly shifted to higher frequencies and occurs, however, overdamped.

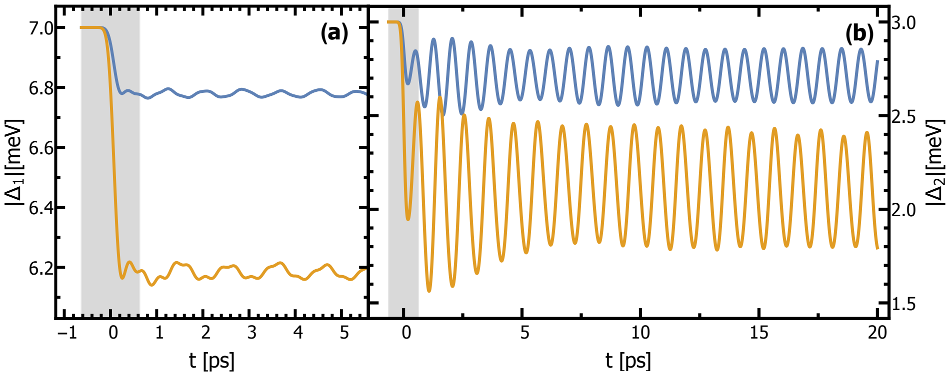

Figure 8.15: Fluency dependence of the gap dynamics in (a) $|\Delta_1|$ and (b) $|\Delta_2|$ for a two–band superconductor with $v = 0.0225$. The results are shown for integrated pump pulse intensities $|A_0|^2\tau = 4.0$ (blue solid line) and $7.84 \cdot 10^{-8}$Js/(Cm) (orange solid line). The pump pulse is indicated by the gray region around $t = 0$.

8.3.4. Optical conductivity

Finally, we include an additional probing pulse of smaller intensity with variable time delay Δt in our calculation, in order to simulate pump–probe experiment. The strategy of the calculations is described in section 7.2. Here, we choose the following parameters for the pump pulse: $\hbar\omega_0 = 8\text{meV}$, $\tau = 0.4\text{ps}$ and $A_0 = 10 \cdot 10^{-8}\text{Js}/(\text{Cm})$. In order to probe the system we take a weaker pulse with a short duration time and, in turn, wide spectral bandwidth. Parameters of the probe pulse are given in Table 8.2. For simplicity, we consider a two–band superconducting system with the relative interband coupling $v = 0.01$. The calculations with other coupling strength reveal qualitatively similar behavior.

In Fig. 8.16 (a) and (b) we present the results of calculations for real $\sigma_1(\Delta t, \omega)$ and imaginary $\sigma_2(\Delta t, \omega)$ part of the optical conductivity versus frequency ω, respectively. The computations were done at time delay $\Delta t = 2.5\text{ps}$. First, we find in both $\sigma_1(\Delta t, \omega)$ and $\sigma_2(\Delta t, \omega)$ a clear sharp edge at the Higgs mode frequency $\omega_{\text{H2}} = 2\Delta_2^\infty/\hbar$ corresponding to superconducting gap oscillations in the lower band $l = 2$. Similar signatures were observed in case of two uncoupled bands as discussed in section 8.2.2. Further, beside a sharp edge at frequency ω_{H2} we can identify an additional peak with a smaller intensity at frequency ω_{L} of the Leggett mode. Our calculations reveal also a few small spikes in the low frequency range ($\omega \ll \omega_{\text{L}}$), which are artifacts of the numerical calculations. In fact, in this region the numerical discretization discussed in section 7.1.4 together with finite size–effects of the model have a stronger influence on the simulations. In addition, it should be also mentioned that Higgs mode from upper band $l = 1$ with frequency $\omega_{\text{H1}} = 2\Delta_1^\infty/\hbar$ is not visible in the conductivity spectra in Figs. 8.16 (a) and (b), due to the overdamping in quasiparticle continuum.

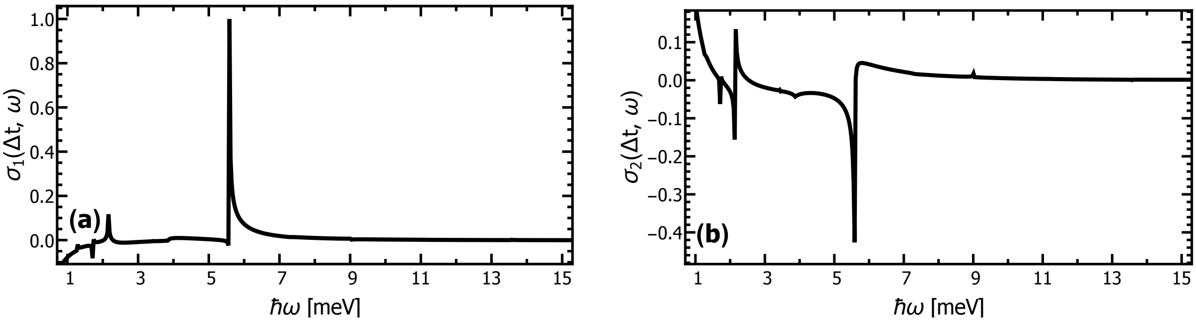

Figure 8.16: (a) Real and (b) imaginary part of the pump–probe response $\sigma(\Delta t, \omega)$ as a function of frequency ω calculated for the time delay $\Delta t = 2.5\text{ps}$. The dynamics in the system is induced by a pump pulse with parameters: $\hbar\omega_0 = 8\text{meV}$, $\tau = 0.4\text{ps}$ and $A_0 = 10 \cdot 10^{-8}\text{Js}/(\text{Cm})$.

Now, by plotting the real part of the optical conductivity $\sigma_1(\Delta t, \omega)$ versus time delay Δt, as shown in Fig. 8.17, we find that the position of the sharp edges for Higgs and Leggett modes remain unchanged as function of time. However, the important oscillations, which reflect the dynamics of these collective excitations, can be found in the temporal

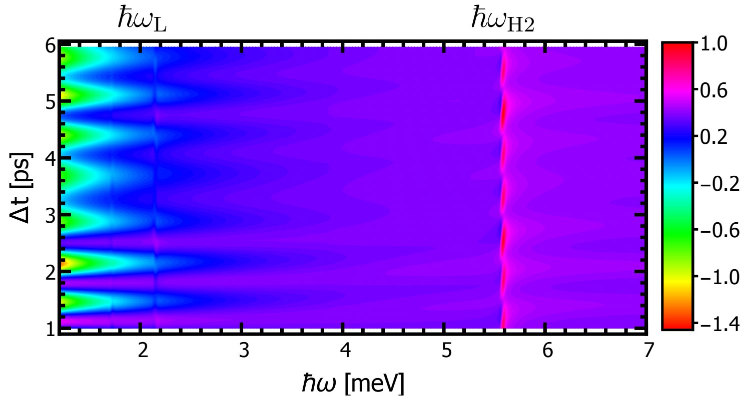

Figure 8.17: Real part of the pump–probe optical conductivity $\sigma_1(\Delta t, \omega)$ plotted as a function of time delay Δt for a two–band superconducting system with the relative interband coupling $v = 0.01$. Intensity of the signal is given by the color code. The parameters of the laser pulses are the same as in Fig. 8.16. Oscillations are clearly seen at $\hbar\omega_L$ and $\hbar\omega_{H2}$.

changes of intensity in the pump–probe response. These oscillations are most prominent at the frequencies, where the conductivity reveals sharp edges. It should be noted that similar behavior can be found in the temporal evolution of the imaginary part of the optical conductivity $\sigma_2(\Delta t, \omega)$, since both quantities $\sigma_1(\Delta t, \omega)$ and $\sigma_2(\Delta t, \omega)$ are connected through Kramers–Kronig relation.

Finally, let us consider the oscillation in the intensity of the pump–probe response $\sigma_1(\Delta t, \omega)$ shown in Fig. 8.17 in some more detail. For this purpose we plot in Fig. 8.18 (a) the pump–probe signal at the sharp edge with ω_{H2} corresponding to the lower Higgs mode [2]

---

[2] qualitatively similar result can be found at other frequencies.

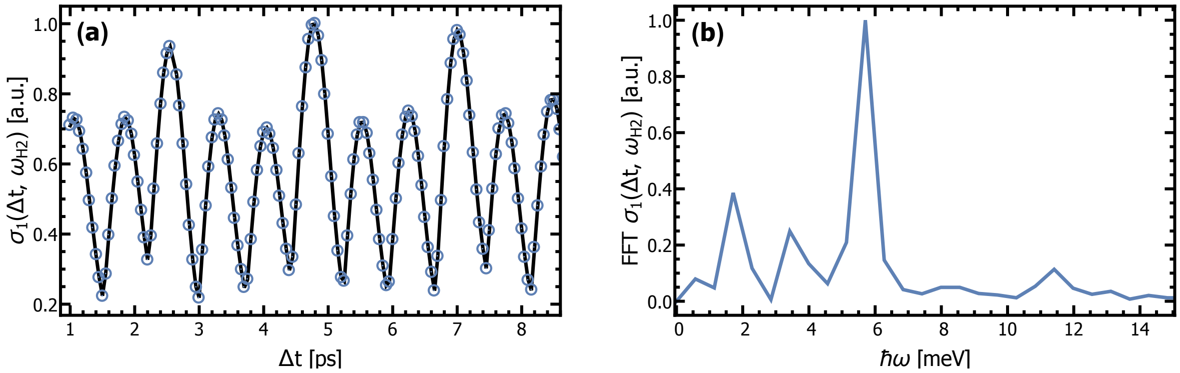

Figure 8.18: (a) Time dependent pump–probe signal $\sigma_1(\Delta t, \omega)$ at the lower Higgs mode frequency $\omega_{H2} = 2\Delta_2^\infty/\hbar$ (see also Fig. 8.17 and sharp edge in Fig. 8.16(a)). The oscillations in the intensity of the pump–probe response are clearly visible. (b) Corresponding Fourier spectrum of the oscillations from (a).

versus time delay Δt. Here, we find fast oscillations accompanied with the slow ones. Importantly, the oscillations show no decay in contrast to the case of uncoupled bands (see section 8.2.2). Physically it means that due to the coupling between amplitude and phase modes in nonequlibrium the Higgs oscillations are additionally driven by the Leggett mode. Next, we perform Fourier transformation of the oscillations in $\sigma_1(\Delta t, \omega)$ with respect to Δt. The resulting spectrum is shown in Fig. 8.18 (b). Here, we find as expected a few distinct peaks, which correspond to the lower Higgs mode ω_{H2} and to the Leggett mode ω_{L} together with their higher harmonics. Thus, we can conclude that by using time–dependent optical pump–probe spectroscopy one is able to access collective excitations in a superconductor, which are associated with oscillations of the order parameter.

8.4. Conclusion

Employing the density–matrix theory we have numerically investigated the nonequlibrium dynamics of the superconducting gaps in a two–band superconductor after its former excitation with an ultrafast pump pulse. We have found that depending on the pulse duration τ one can distinguish between two different nonequilibrium scenarios. In case of adiabatic regime with broad pulses $\tau \gg \tau_{\Delta_l}$ we have observed a monotonic reduction of the superconducting gap amplitudes of the order parameters, which is caused by the partial suppression of the superconductivity due to the action of the light pulse. On the other hand, short pulses $\tau \ll \tau_{\Delta_l}$ (nonadiabatic regime) lead to excitation of the collective modes in two–band superconductors. Here, we have identified for the first time two Higgs amplitude modes, which are independent of the interband coupling strength between the bands. However, they can be manipulated by the intensity of the pump pulse. Then, besides the Higgs modes we have detected the Leggett phase mode in nonequilibrium, which manifests itself in the relative phase oscillations of the superconducting condensates. This mode depends strongly on the finite interband coupling between the bands. Further, we have found that this type of nonequilibrium excitation of a two–band superconducting system leads to a strong coupling between amplitude and phase modes. This is in contrast to the equilibrium situation, where the Higgs and Leggett mode appear as independent collective excitations. Moreover, the amplitude–phase mode coupling results in the shift of the Leggett mode frequency below the Bogoliubov quasiparticle continuum. Therefore, the Leggett mode remains undamped for a very broad interband coupling region. Furthermore, by adjusting the pump pulse intensity we were able to bring the Higgs and Leggett mode into the resonance and on this way maximize the oscillatory signal in the dynamics of the superconducting gaps. Finally, we have found that both Higgs amplitude and Leggett phase mode can be observed in the time–resolved pump–probe experiments. Both modes appears as clear oscillations in the signal of optical conductivity.

Chapter 9

Summary

The recent progress in nonequilibrium pump–probe time–domain spectroscopy opened new perspectives in studying dynamical properties of a superconductor. In fact, the unique combination of a high time resolution governed by optical laser pulses on the femtosecond timescale together with the spectral selectivity made it possible to access intrinsic processes of this material on a fundamental level. Based on the measuring conditions the known pump–probe experimental techniques presented in the introduction can be divided into several different categories, which are schematically illustrated in Fig. 9.1. In the past, the optical nonequilibrium experiments were performed at almost exclusively near–infrared or visible frequency range, which enables to study relaxation of hot incoherent quasiparticles back into the superconducting condensate and Cooper pair formation dynamics or to disentangle the electronic and phononic contributions to the superconducting glue by their ultrafast response. This type of measurements can be generally classified as non–equilibrium spectroscopy (see Fig. 9.1). With the development of pulsed technique to terahertz (THz) frequency range, where photon energy is almost of the order of the superconducting gap, it became possible to investigate qualitatively new properties of a superconductor. In particular, by using optical excitation of high intensity at THz frequency one was able to perform controlled transient transitions into a superconducting–like state. These optical control measurements (see Fig. 9.1) have already built a novel research frontier of the modern solid state physics.

Inspired by the potential of the pump–probe time–resolved measuring technique at THz frequency range, we have modeled two corresponding nonequilibrium scenarios in: (i) high– and (ii) low–fluency regime by combining several analytical and numerical methods. In particular, we have investigated transient superconducting phase transitions which are relevant for optical control measurements, and collective excitations of a superconducting condensate far from equilibrium. In the light of our results we proposed in the latter case a new type of the nonequilibrium pump–probe studies, which we called Higgs spectroscopy.

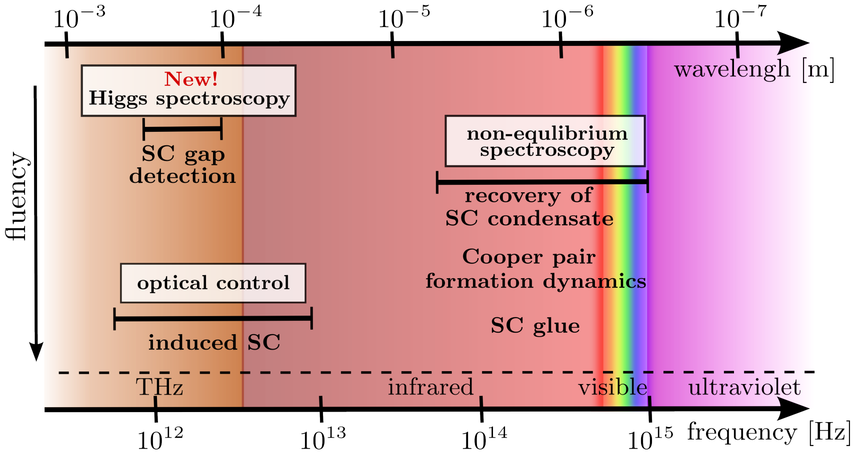

Figure 9.1: Schematic classification of pump–probe measurements based on the spectral selectivity and intensity of the pulses: (i) non–equilibrium spectroscopy, which deals with the recovery of a superconducting condensate; (ii) optical control technique, which was recently used to induce superconductivity; and (iii) Higgs spectroscopy, with which we propose to investigate the properties of a superconducting gap. The last two classes were theoretically studied in this thesis. The horizontal bars indicate the frequency region of the applied technique where the main effects can be observed. The abbreviation **SC** stands for superconducting.

Optical control of matter

In the first part of this thesis we simulated a pump–probe experiment in high–fluency regime and explored in this case the possibility of inducing singlet superconducting correlations far from equilibrium. For this purpose we have chosen a one–dimensional extended Hubbard model, which was assumed to describe strongly correlated electrons on a 10–site lattice at half–filing with periodic boundary conditions and at zero temperature. The nonequilibrium dynamics in the electron system was induced in two different ways: (i) by interaction quench and (ii) by quench by pulse. Within the framework of the time–dependent exact diagonalization technique we constructed in both cases an accurate time–dependent wave function reflecting the properties of the electron system in nonequilibrium. Based on its knowledge we investigated the buildup of the superconducting correlations by means of several time–dependent correlation and response functions.

First, we considered nonequilibrium dynamics of the electron system after interaction quench. In this case we prepared the system initially in an equilibrium ground state of the charge density wave (CDW) phase and switched afterwards the interaction parameters of its Hamiltonian into the superconducting region. The time–dependent calculations of the density–density correlation function $C(j,t)$ revealed a strong suppression of CDW correlations. At the same time, we obtained slow oscillations in the computed singlet superconducting correlation function $P_1(j,t)$, where a strong transient enhancement of the superconducting correlations in nonequilibrium was observed. Moreover, a direct comparison of the nonequilibrium results of $P_1(j,t)$ at several moments in time with its counterpart calculated for equilibrium superconducting ground state revealed quite good agreement and indicated a transition into the superconducting phase. From the Fourier transformation of $P_1(j,t)$ we found that almost all peaks of the Fourier spectra correspond to the low–energy eigenstates of the superconducting phase, whereas there were no peaks, which could be identified with the CDW phase. Hence we can conclude that after quenching the system undergoes a direct transition into a superconducting phase and appears in some nonequilibrium state, which is not a "pure" eigenstate of the equilibrium CDW or the equilibrium singlet SC phase. As a result, oscillations between this nonequilibrium state and the low–energy eigenstates of the SC phase occurred. Finally, we calculated the important for experiments time–dependent optical conductivity $\sigma(\Delta t, \omega)$, where the superconducting fingerprints emerged as the transient Meissner effect. In other words, we found an enhancement of the peak amplitude at $\omega = 0$ in the real part of the optical conductivity and an increase of the inductive response with $1/\omega$–like behavior in its imaginary part.

Second, we studied the situation with a quench by a short optical pump pulse. We prepared the system again initially in an equilibrium ground state of the CDW phase, but close to the transition boundary with the singlet superconducting phase. By adjusting the amplitude of the pump pulse and tuning its frequency to the first low–energy absorption peak of the unperturbed CDW state we demonstrated a transient transition from the CDW phase into a singlet superconducting phase. In fact, from computations of the time–dependent density–density correlation function $C(j,t)$ after pumping we found an effective partial suppression of the CDW correlations with subsequent oscillations. Concurrently, we observed oscillations in the temporal evolution of the singlet superconducting correlation function $P_1(j,t)$ indicating a temporal enhancement of the superconducting correlations after pumping. Further, we performed a Fourier transformation of these oscillations and found that most peaks in the Fourier spectrum correspond to the low–energy eigenstates of the CDW phase. However, some peaks can be assigned to the eigenstates of the singlet superconducting phase. Finally, we observed that the fingerprint of the singlet superconducting correlations appeared as a transient Meissner effect in calculations of the time–dependent optical conductivity $\sigma(\Delta t, \omega)$. Hence, we can conclude that, in contrast to the situation with interaction quench, in case of the optical pumping a temporal dynamical coexistence of the CDW and singlet superconducting correlations is possible.

Coming back to the question raised in the introduction, with our simulations we could successfully demonstrate a transient phase transition into a singlet superconducting state far from equilibrium. The fingerprints of the induced superconductivity emerge in (i) calculations of correlation functions, (ii) analysis of the Fourier spectra, and (iii) computation of the time–dependent optical conductivity. These observations generalize the previous theoretical studies [81–87], where investigations of the induced superconductivity in nonequilibrium were restricted exclusively to the layered cuprate materials. In this sense, our studies give a proof of the concept for a buildup of the singlet superconducting correlations and might open a new way to induce superconductivity far from equilibrium in an experiment. In fact, a possible light–induced s–wave superconductivity observed experimentally in the bulk of K_3C_{60} at high temperatures was reported in Ref. [92] a few weeks ago. In this experiment the measurements of the transient optical response of K_3C_{60} after photo–excitation with time delay $\Delta t = 1\text{ps}$ revealed changes in the optical conductivity similar to the equilibrium cooling below the critical temperature T_{c}. In particular, one observed transient Meissner effect in a way qualitatively similar to the prediction of our calculations, which is reflected in the temporal enhancement of the delta peak in the real part of the optical conductivity $\sigma_1(\Delta t, \omega)$ and corresponding increase of the inductive response in its imaginary part $\sigma_2(\Delta t, \omega)$. Further improvements of our method might concern the inclusion of the electron–phonon interactions into the Hamiltonian and corresponding extensions to the Hubbard–Holzstein model in nonequilibrium.

Non–Equilibrium Higgs spectroscopy

The second part of this thesis is devoted to simulations of a pump–probe experiment in low–fluency regime. In this case, we investigated collective mode excitations in a two–band superconductor out of equilibrium. First of all, we studied the properties of the collective modes under the close to equilibrium conditions, where a linearized response can be expected. Employing (Nambu-) matrix kinetic theory in the clean limit and at zero temperature we analytically formulated a comprehensive, gauge–invariant description of the collective modes associated with the phase fluctuations of the superconducting order parameter for the general case of two–band superconducting systems. In particular, we applied this approach to the case of recently discovered noncentrosymmetric superconductors (NCS). As a result, we demonstrated for the first time the existence of two collective modes in NCS systems: the gauge mode (or Nambu-Goldstone Boson), common to all superconductors, and the new Leggett mode, which usually occurs in the context of collective fluctuations of the interband phase difference in ordinary two-band superconductors. Moreover, we provided a detailed analysis of their mass and dispersion together with the general role of these collective excitations in NCS systems. In particular, we found that these collective excitations depend strongly on the point group symmetry of the crystal structure under consideration and consequently reflect the underlying spin orbit coupling. Also, we showed that both modes are necessary to guarantee charge conservation law. In addition, numerical calculations for the most interesting class of NCS systems with C_{4v} point group symmetry reveal that the Leggett mode may appear, under certain conditions, as a massless collective excitation in contrast to ordinary two–band superconductors. Furthermore, its slope showed a strong dependence on the triplet–to–singlet ratio $t = \Delta_{tr}/\Delta_s$. This might help experimentalists to estimate in which materials is the Leggett mode most easily observable. Finally, we demonstrated that the gauge mode is shifted to the plasma mode of higher energy according to the Anderson-Higgs mechanism. The mass of the new Leggett mode remained, however, unaffected by this process, but its dispersion is changed.

Next, we focused on the nonequilibrium dynamics of superconducting gaps in an s–wave two–band superconductor induced by an ultrafast pump pulse excitation. For this purpose we formulated a Hamiltonian which describes a nonlinear coupling of the superconducting condensates to an optical pulse. Here, the laser field was assumed to depend on the momentum $\mathbf{q}$ and to have a Gaussian envelope. In order to simulate the nonequilibrium dynamics in this model, we elaborated a semi–numerical method based on the density–matrix formalism (DMF), which goes beyond the common studies of relaxation processes [40–46]. By adjusting a central energy of the pump pulse in the midpoint between both superconducting gaps and by varying its duration time τ we investigated two nonequilibrium scenarios. In case of broad pulses, whose duration time was larger than the reaction time of the superconducting system ($\tau \gg \tau_{\Delta_l}$), we found a monotonic reduction of the superconducting gap amplitudes. This is a direct result of the partial suppression of superconductivity due to the action of the light pulse. On the other hand, by applying short pulses in the so–called nonadiabatic regime, i.e. pulses with $\tau \ll \tau_{\Delta_l}$, we obtained oscillations in the nonequilibrium dynamics of the superconducting gap. Here, we first identified two Higgs modes at frequencies $\omega_{\mathrm{H}l} = 2|\Delta_l^{\infty}|/\hbar$ with $|\Delta_l^{\infty}|$ being the asymptotic gap values. These modes represent amplitude oscillations of the corresponding superconducting gaps and show no dependence on the interband coupling strength between the bands. Importantly, by varying the intensity of the pump pulse excitation we found that the frequency of the Higgs modes can be manipulated. It should be noted that in the limiting case of vanishing interband coupling our simulations also reflect results of previous theoretical studies of the amplitude modes, which were restricted to a single band s–wave superconductor [47, 48, 50–58, 65]. In addition to the amplitude Higgs modes we identified the Leggett phase mode in the response of the superconducting gaps, which manifests itself in the relative phase oscillations of the superconducting condensates and depends strongly on the finite interband coupling between the bands. In contrast to the situation under the close to equilibrium conditions, where the amplitude and phase fluctuations of the order parameter appeared as independent collective excitations, we found a strong coupling between Higgs and Leggett modes in nonequilibrium. As a result, we observed that in nonequilibrium the Leggett mode is pushed below the Bogoliubov quasiparticle continuum and remains undamped for a wide parameter range of the interband coupling. Furthermore, by adjusting the pump pulse intensity we were able to bring the Higgs and Leggett modes into resonance and in this way maximize the oscillatory signal in the dynamics of the superconducting gaps. Finally, based on the computation of the time–dependent optical conductivity, we predicted the appearance of both Higgs amplitude and Leggett phase mode in the time–resolved pump–probe experiments. In other words, both modes should appear as clear oscillations in the optical conductivity signal.

All in all, by using a semi–numerical method based on DMF we demonstrated that the Higgs modes can be excited not only in one-, but also in general two–band superconducting systems. Here, the following nonadiabatic conditions should be fulfilled:

(i) the duration time of the pump pulse is shorter than the reaction time of the superconducting system;

(ii) the photon energy is of the order of the superconducting gap (at terahertz frequency range) to guarantee coherent excitation of the quasiparticles across the gap without high–energy phononic modes;

(iii) and the intensity of the pump pulse is in low–fluency regime to ensure that the superconductivity is only partially destroyed.

Since Higgs mode was observed in experiments so far in certain materials under close to equilibrium conditions (see in the introduction), our simulations should open a new class of pump–probe studies, where the Higgs modes can be detected directly in all types of superconductors. As a result, this nonequilibrium Higgs spectroscopy (see Fig. 9.1) should open a direct access to the properties of a superconducting order parameter. Recent report [35] on the Higgs mode observation in ultrafast response of the BCS superconductor ($\mathrm{Nb}_{1-x}\mathrm{Ti}_x\mathrm{N}$) using THz pump pulses in a nonadiabatic regime supports our predictions. Moreover, we predicted excitation of the phase Leggett mode beside amplitude Higgs modes in two–band superconductors, which also manifests itself in the time–resolved pump–probe conductivity signal. Also, we found the unusual strong coupling of amplitude (Higgs) and phase (Leggett) modes in nonequilibrium. Thus, it would be interesting to explore the behavior of the Higgs mode and other collective excitations in more exotic superconductors, like noncentrosymmetric superconductors or cuprates. In particular, in case of d–wave superconductors where several Higgs modes reflecting the symmetry of the superconducting gap can be expected [14], we await interactions between these modes after nonadiabatic excitation. Here, the pump pulse direction and consequently the dependence on the momentum $\mathbf{q}$ should play an important role. Finally, the observation of Higgs mode in the time–dependent spectral function and prediction for the tr–ARPES is worth additional research.

In conclusion, in this thesis we gave a comprehensive study of nonequilibrium dynamics in a superconductor induced by an ultrafast pulse excitation at terahertz (THz) frequency range. Using time–dependent exact diagonalization technique we successfully demonstrated in case of strong THz laser fields a possibility of light controlled transitions into a transient singlet superconducting state. Our results do not only generalize previous theoretical studies [81–87], but give a completely new insight into the phenomenon of the induced superconductivity. Moreover, the signatures for a buildup of the singlet superconducting correlation, which we predicted from calculations of the time–dependent optical conductivity, were recently observed in an optical pump–probe experiment [92]. More importantly, we formulated a microscopic theory for excitations of collective modes in a superconductor out of equilibrium by ultrashort THz laser pulses in low–fluency regime. Here, we specified conditions, under which the amplitude (Higgs) mode can be directly detected. In this sense we proposed a new type of the nonequilibrium pump–probe studies to determine properties of the superconducting gap. In addition, for the case of two–band superconductors we predicted beside the Higgs mode appearance of the phase (Leggett) mode in the dynamics of the superconducting order parameters. Furthermore, we found their strong coupling in nonequilibrium and, as a result, a new unusual interplay between Higgs and Leggett modes. Finally, we made predictions that both modes can be experimentally observed with the current pump–probe technique.

Appendix

Appendix A

Analytical solution of the energy gap equation in case of NCS

The energy gap equations for the noncentrosymmetric superconductors given in Eq. (5.33) can be solved analytically at different temperature (T) limits. To begin with, let us consider the quantity from section 5.2.3:

$$\Xi_n = \sum_\mu \langle (\mu f_{\mathbf{k}})^n \, \theta_{\mathbf{k}\mu} \rangle \quad ; \quad n = \{0, 1, 2\} \tag{A.1}$$

where the integral kernel is determined by the band–selected function $\theta_{\mathbf{k}\mu}$ of the following form:

$$\theta_{\mathbf{k}\mu} = \frac{1}{2E_{\mathbf{k}\mu}} \tanh \frac{E_{\mathbf{k}\mu}}{2k_{\mathrm{B}}T} \tag{A.2}$$

with $E_{\mathbf{k}\mu} = \left[\xi^2_{\mathbf{k}\mu} + \Delta^2_{\mathbf{k}\mu}\right]^{1/2}$. Now, it is useful to rewrite the function $\theta_{\mathbf{k}\mu}$ in Eq (A.2) in form of the Matsubara sum by using integration in the complex plain [107, 118]. Thus, after some algebra we get:

$$\frac{1}{2E_{\mathbf{k}\mu}} \tanh \frac{E_{\mathbf{k}\mu}}{2k_{\mathrm{B}}T} = k_{\mathrm{B}}T \sum_n \frac{1}{\hbar^2\omega_n^2 + E^2_{\mathbf{k}\mu}} \tag{A.3}$$

with $\omega_n = (2n+1)\pi k_{\mathrm{B}}T/\hbar$ being the Matsubara frequency. Also, it is convenient to introduce the function:

$$\theta^0_{\mathbf{k}\mu} = \frac{1}{2\xi_{\mathbf{k}\mu}} \tanh \frac{\xi_{\mathbf{k}\mu}}{2k_{\mathrm{B}}T} \ , \tag{A.4}$$

which corresponds to the case of vanishing gaps ($\Delta_{\mathbf{k}\mu} \equiv 0$) in Eq. (A.2). Further, by using definitions (A.2) and (A.4) we represent the quantity Ξ_n from Eq. (A.1) in the following form:

$$\Xi_n = \sum_\mu \left\langle (\mu f_{\mathbf{k}})^n \, \theta^0_{\mathbf{k}\mu} \right\rangle - \sum_\mu \left\langle (\mu f_{\mathbf{k}})^n \underbrace{\left[\theta^0_{\mathbf{k}\mu} - \theta_{\mathbf{k}\mu}\right]}_{\equiv \mathcal{P}_{\mathbf{k}\mu}(x)} \right\rangle \tag{A.5}$$

Here, we have defined the function

$$\mathcal{P}_{\mathbf{k}\mu}(x) = \theta^{0}_{\mathbf{k}\mu} - \theta_{\mathbf{k}\mu} \ , \tag{A.6}$$

which depends on $x = \Delta_s/k_{\mathrm{B}}T$ and triplet to singlet ratio $t = \Delta_{tr}/\Delta_s$. In order to demonstrate this statement, we put the Matsubara sum representation from Eq. (A.3) into a definition (A.6) of the $\mathcal{P}_{\mathbf{k}\mu}(x)$ function. After some lengthy but straightforward calculations we obtain:

$$\mathcal{P}_{\mathbf{k}\mu}(x) = 2\sum_{n=0}^{\infty} \frac{\sqrt{(2n+1)^2 + \left(\frac{x}{\pi}\right)^2 (1+\mu f_{\mathbf{k}} t)^2} - (2n+1)}{(2n+1)\sqrt{(2n+1)^2 + \left(\frac{x}{\pi}\right)^2 (1+\mu f_{\mathbf{k}} t)^2}} \tag{A.7}$$

In order to simplify the notation let us introduce:

$$r_{n\mu} \equiv \sqrt{(2n+1)^2 + \left(\frac{x}{\pi}\right)^2 (1+\mu f_{\mathbf{k}} t)^2} \tag{A.8}$$

Now, since we are interested in the form of the function Ξ_n from Eq. (A.5) let us calculate the sum and difference of the same function $\mathcal{P}_{\mathbf{k}\mu}(x)$ for two bands $\mu = \pm 1$:

$$\begin{aligned} \mathcal{P}_{\mathbf{k}+}(x) + \mathcal{P}_{\mathbf{k}-}(x) &= 2\sum_{n=0}^{\infty}\left[\frac{2}{2n+1} - \frac{r_{n+} + r_{n-}}{r_{n+} r_{n-}}\right] \\ \mathcal{P}_{\mathbf{k}+}(x) - \mathcal{P}_{\mathbf{k}-}(x) &= 2\sum_{n=0}^{\infty}\left[\frac{r_{n+} - r_{n-}}{r_{n+} r_{n-}}\right] \end{aligned} \tag{A.9}$$

Importantly, in the limit of small triplet-to-singlet ratio $t = \Delta_{tr}/\Delta_s$ the results in Eq. (A.9) take an especially simple form:

$$\begin{aligned} \mathcal{P}_{\mathbf{k}+}(x) + \mathcal{P}_{\mathbf{k}-}(x) &= 4\sum_{n=0}^{\infty} \frac{\sqrt{(2n+1)^2 + \left(\frac{x}{\pi}\right)^2} - (2n+1)}{(2n+1)\sqrt{(2n+1)^2 + \left(\frac{x}{\pi}\right)^2}} \equiv 2\mathcal{P}(x) \\ \mathcal{P}_{\mathbf{k}+}(x) - \mathcal{P}_{\mathbf{k}-}(x) &= 4 f_{\mathbf{k}} t \sum_{n=0}^{\infty} \frac{\left(\frac{x}{\pi}\right)^2}{\left[(2n+1)^2 + \left(\frac{x}{\pi}\right)^2\right]^{3/2}} \equiv 2 f_{\mathbf{k}} t \lambda(x) \end{aligned} \tag{A.10}$$

where one can identify the Tsuneto function [136]:

$$\lambda(x) = \pi k_{\mathrm{B}} T \sum_{n} \frac{\Delta_s^2}{[(\hbar\omega_n)^2 + \Delta_s^2]^{3/2}} \ , \tag{A.11}$$

It should be noted that the Tsuneto function $\lambda(x)$ describes the response of a superconducting condensate. Its temperature dependence is presented in Figs. A.1 (a) and (b), where we use a representation of $\lambda(x)$ as a function of $x = \Delta_s(T)/k_\mathrm{B}T$ and of T/T_c, respectively. As can be seen from the figures, the Tsuneto function takes in low temperature limit the value of 1, whereas in Ginzburg–Landau (GL) regime with $T \to T_\mathrm{c}$ this function vanishes.

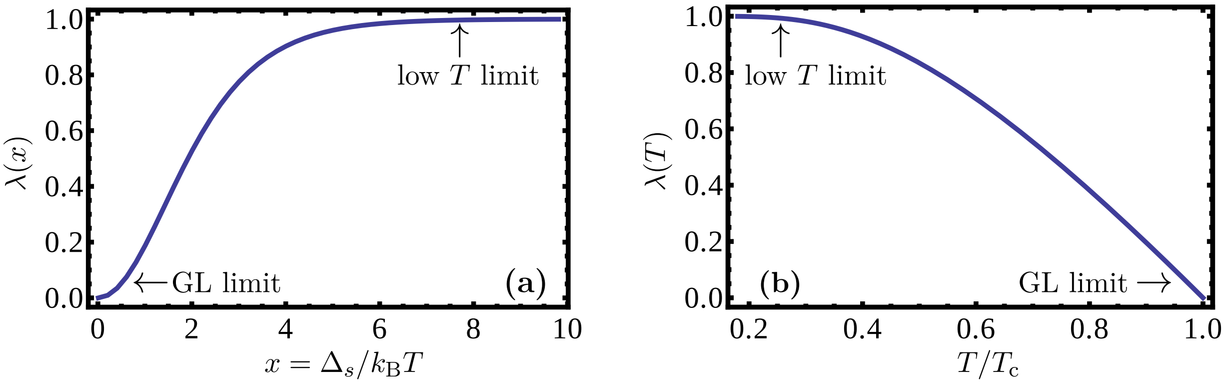

Figure A.1: Tsuneto function versus (a) $x = \Delta_s(T)/k_\mathrm{B}T$ and (b) T/T_c. In low temperature (T) limit the Tsuneto function takes the value of 1. On the other hand, in case of Ginzburg–Landau (GL) regime this function vanishes.

Now, in the limit of small triplet–to–singlet ratio t, where Eq. (A.10) can be used, we obtain for the function Ξ_n from Eq. (A.5) following results:

$$\begin{aligned}
\Xi_0 &= 2\ln\left(\frac{2\gamma\epsilon_0}{\pi k_\mathrm{B}T}\right) - 2\mathcal{P}(x) + \mathcal{O}(t^2) \\
\Xi_1 &= -2t\lambda(x) + \mathcal{O}(t^3) \\
\Xi_2 &= 2\ln\left(\frac{2\gamma\epsilon_0}{\pi k_\mathrm{B}T}\right) - 2\mathcal{P}(x) + \mathcal{O}(t^2)
\end{aligned} \tag{A.12}$$

Finally, inserting these results for Ξ_n into the energy gap equations (5.33) from section 5.2.3 we find:

$$\begin{aligned}
2\mathcal{P}(x) + 2t^2\lambda(x) &= 2\ln\frac{T_\mathrm{c}}{T} - \frac{\lambda_m}{\lambda_s\lambda_{tr} - \lambda_m^2}\left(t - t_c\right) \\
2\mathcal{P}(x) + 2\lambda(x) &= 2\ln\frac{T_\mathrm{c}}{T} - \frac{\lambda_m}{\lambda_s\lambda_{tr} - \lambda_m^2}\left(\frac{1}{t} - \frac{1}{t_c}\right) ,
\end{aligned} \tag{A.13}$$

Here, we used a notation $t_c = -\lambda_m/\left(\lambda_s - \lambda_{tr}\right)$. Now, we solve Eq. (A.13) with respect to the triplet to singlet ratio t. Thus, after some algebra we get:

$$t = -\frac{\lambda_m}{\lambda_s - \lambda_{tr} + 2\lambda(x)\left(\lambda_s\lambda_{tr} - \lambda_m^2\right)} \tag{A.14}$$

It should be noted that the temperature dependence for the triplet–to–singlet ratio is determined by the Tsuneto function discussed above. Since in this work we are interested in the low temperature calculations, we take in the last step (see Eq. (A.14)) $T \to 0$ limit and use $\lambda(x) = 1$. Hence, in this limit we obtain for the triplet–to–singlet ratio the following result:

$$t(T=0) = -\frac{\lambda_m}{\lambda_s - \lambda_{tr} + 2|\boldsymbol{\lambda}|} \tag{A.15}$$

with

$$|\boldsymbol{\lambda}| \equiv \lambda_s \lambda_{tr} - \lambda_m^2 \tag{A.16}$$

It is important to mention that the result in Eq. (A.15) can be further used to obtain the coupling strength of the Leggett mode γ_{NCS} from (6.28) in the case of small triplet to singlet ratio

$$\gamma_{\mathrm{NCS}} = \frac{\lambda_m}{|\boldsymbol{\lambda}|} + \Xi_1 \tag{A.17}$$

with

$$\Xi_1 = -2t = \frac{2\lambda_m}{\lambda_s - \lambda_{tr} + 2|\boldsymbol{\lambda}|} \tag{A.18}$$

Appendix B

Equations of motion

B.1. Pump pulse excitation

Here, we present the equations of motion for all quasiparticles expectation values, which were discussed in section 7.1.3. In this case we used a fact that with $H^{(1)}_{\mathrm{em}}$ only excitations with $\mathbf{q}' = \pm\mathbf{q}$ arises, whereas with $H^{(2)}_{\mathrm{em}}$ the excitations with $\mathbf{q}' = 0, \pm 2\mathbf{q}$ are possible.

(I). Differential equation for $\alpha^\dagger_{\mathbf{k}l}\beta^\dagger_{\mathbf{k+q}l}$

The first differential equation is given by

$$i\hbar\frac{d}{dt}\alpha^\dagger_{\mathbf{k}l}\beta^\dagger_{\mathbf{k+q}l} = -\left\langle\left[\hat{H}_{\mathrm{BCS}} + \hat{H}^{(1)}_{\mathrm{em}} + \hat{H}^{(2)}_{\mathrm{em}}, \hat{\alpha}^\dagger_{\mathbf{k}l}\hat{\beta}^\dagger_{\mathbf{k+q}l}\right]\right\rangle \tag{B.1}$$

The calculation of the commutator on the r.h.s. leads to the results:

$$\begin{aligned}
-\left\langle\left[\hat{H}_{\mathrm{BCS}}, \hat{\alpha}^\dagger_{\mathbf{kl}}\hat{\beta}^\dagger_{\mathbf{k+q}l}\right]\right\rangle =& -(R_{\mathbf{k}l} + R_{\mathbf{k+q}l})\alpha^\dagger_{\mathbf{k}l}\beta^\dagger_{\mathbf{k+q}l} + C^*_{\mathbf{k+q}l}\alpha^\dagger_{\mathbf{k}l}\alpha_{\mathbf{k+q}l} + C^*_{\mathbf{k}l}\left(\beta^\dagger_{\mathbf{k+q}l}\beta_{\mathbf{k}l} - \delta_{\mathbf{q},0}\right)\\
-\left\langle\left[\hat{H}^{(1)}_{\mathrm{em}}, \hat{\alpha}^\dagger_{\mathbf{k}l}\hat{\beta}^\dagger_{\mathbf{k+q}l}\right]\right\rangle =& \frac{e\hbar}{2m}\sum_{\mathbf{q}'=\pm\mathbf{q}}\mathbf{A}_{\mathbf{q}'}\times\\
&\times\Big\{(2\mathbf{k}+\mathbf{q}')\left(-L^{(+)}_{\mathbf{k},\mathbf{q}'l}\alpha^\dagger_{\mathbf{k+q}'l}\beta^\dagger_{\mathbf{k+q}l} + M^{(-)}_{\mathbf{k},\mathbf{q}'l}\left(\beta^\dagger_{\mathbf{k+q}l}\beta_{\mathbf{k+q}'l} - \delta_{\mathbf{q},\mathbf{q}'}\right)\right)\\
&\quad + (2\mathbf{k}+2\mathbf{q}-\mathbf{q}')\left(L^{(+)}_{\mathbf{k+q},-\mathbf{q}'l}\alpha_{\mathbf{kl}}\beta_{\mathbf{k+q-q}'l} - M^{(-)}_{\mathbf{k+q},-\mathbf{q}'l}\alpha^\dagger_{\mathbf{kl}}\alpha_{\mathbf{k+q-q}'l}\right)\Big\}\\
-\left\langle\left[\hat{H}^{(2)}_{\mathrm{em}}, \hat{\alpha}^\dagger_{\mathbf{k}l}\hat{\beta}^\dagger_{\mathbf{k+q}l}\right]\right\rangle =& \frac{e^2}{2m}\sum_{\mathbf{q}'=0,\pm2\mathbf{q}}\left(\sum_{\mathbf{q}_i=\pm\mathbf{q}}\mathbf{A}_{\mathbf{q}'-\mathbf{q}_i}\cdot\mathbf{A}_{\mathbf{q}_i}\right)\times\\
&\times\Big\{-L^{(-)}_{\mathbf{k},\mathbf{q}'l}\alpha^\dagger_{\mathbf{k+q}'l}\beta^\dagger_{\mathbf{k+q}l} - L^{(-)}_{\mathbf{k+q},-\mathbf{q}'l}\alpha^\dagger_{\mathbf{kl}}\beta^\dagger_{\mathbf{k+q-q}'l}\\
&\quad -M^{(+)}_{\mathbf{k+q},-\mathbf{q}'l}\alpha^\dagger_{\mathbf{k}l}\alpha_{\mathbf{k+q-q}'l} - M^{(+)}_{\mathbf{k},\mathbf{q}'l}\left(\beta^\dagger_{\mathbf{k+q}l}\beta_{\mathbf{k+q}'l} - \delta_{\mathbf{q},\mathbf{q}'}\right)\Big\}
\end{aligned} \tag{B.2}$$

(II). Differential equation for $\beta_{\mathbf{k}+\mathbf{q}l}\alpha_{\mathbf{k}l}$

The second differential equation is given by

$$i\hbar\frac{d}{dt}\beta_{\mathbf{k}+\mathbf{q}l}\alpha_{\mathbf{k}l} = -\left\langle\left[\hat{H}_{\rm BCS} + \hat{H}^{(1)}_{\rm em} + \hat{H}^{(2)}_{\rm em}, \hat{\beta}_{\mathbf{k}+\mathbf{q}l}\hat{\alpha}_{\mathbf{k}l}\right]\right\rangle \tag{B.3}$$

The calculation of the commutator on the r.h.s. leads to the results:

$$\begin{aligned}
-\left\langle\left[\hat{H}_{\rm BCS}, \hat{\beta}_{\mathbf{k}+\mathbf{q}l}\hat{\alpha}_{\mathbf{k}l}\right]\right\rangle =& -(R_{\mathbf{k}l} + R_{\mathbf{k}+\mathbf{q}l})\alpha_{\mathbf{k}l}\beta_{\mathbf{k}+\mathbf{q}l} - C_{\mathbf{k}+\mathbf{q}l}\alpha^{\dagger}_{\mathbf{k}+\mathbf{q}l}\alpha_{\mathbf{k}l} - C_{\mathbf{k}l}\left(\beta^{\dagger}_{\mathbf{k}l}\beta_{\mathbf{k}+\mathbf{q}l} - \delta_{\mathbf{q},0}\right)\\
-\left\langle\left[\hat{H}^{(1)}_{\rm em}, \hat{\beta}_{\mathbf{k}+\mathbf{q}l}\hat{\alpha}_{\mathbf{k}l}\right]\right\rangle =& \frac{e\hbar}{2m}\sum_{\mathbf{q}'=\pm\mathbf{q}}\mathbf{A}_{-\mathbf{q}'}\cdot(2\mathbf{k}+\mathbf{q}')\left\{L^{(+)*}_{\mathbf{k},\mathbf{q}'l}\alpha_{\mathbf{k}+\mathbf{q}'l}\beta_{\mathbf{k}+\mathbf{q}l} - L^{(+)*}_{\mathbf{k}+\mathbf{q},-\mathbf{q}'l}\alpha_{\mathbf{k}l}\beta_{\mathbf{k}+\mathbf{q}-\mathbf{q}'l}\right.\\
&\left. -M^{(-)*}_{\mathbf{k}+\mathbf{q},-\mathbf{q}'l}\alpha^{\dagger}_{\mathbf{k}+\mathbf{q}-\mathbf{q}'l}\alpha_{\mathbf{k}l} + M^{(-)*}_{\mathbf{k},\mathbf{q}'l}\left(\beta_{\mathbf{k}+\mathbf{q}'l}\beta_{\mathbf{k}'l} - \delta_{\mathbf{q},\mathbf{q}'}\right)\right\}\\
-\left\langle\left[\hat{H}^{(2)}_{\rm em}, \hat{\beta}_{\mathbf{k}+\mathbf{q}l}\hat{\alpha}_{\mathbf{k}l}\right]\right\rangle =& \frac{e^2}{2m}\sum_{\mathbf{q}'=0,\pm2\mathbf{q}}\left(\sum_{\mathbf{q}_i=\pm\mathbf{q}}\mathbf{A}_{\mathbf{q}_i-\mathbf{q}'}\mathbf{A}_{-\mathbf{q}_i}\right)\times\\
&\times\left\{L^{(-)*}_{\mathbf{k},\mathbf{q}'l}\alpha_{\mathbf{k}+\mathbf{q}'l}\beta_{\mathbf{k}+\mathbf{q}l} + L^{(-)*}_{\mathbf{k}+\mathbf{q},-\mathbf{q}'l}\alpha_{\mathbf{k}l}\beta_{\mathbf{k}+\mathbf{q}-\mathbf{q}'l}\right.\\
&\left. -M^{(+)*}_{\mathbf{k}+\mathbf{q},-\mathbf{q}'l}\alpha^{\dagger}_{\mathbf{k}+\mathbf{q}-\mathbf{q}'l}\alpha_{\mathbf{k}l} + M^{(+)*}_{\mathbf{k},\mathbf{q}'l}\left(\delta_{\mathbf{q},\mathbf{q}'} - \beta_{\mathbf{k}+\mathbf{q}'l}\beta_{\mathbf{k}+\mathbf{q}l}\right)\right\}
\end{aligned} \tag{B.4}$$

(III). Differential equation for $\alpha^{\dagger}_{\mathbf{k}l}\alpha_{\mathbf{k}+\mathbf{q}l}$

The third differential equation is given by

$$i\hbar\frac{d}{dt}\alpha^{\dagger}_{\mathbf{k}l}\alpha_{\mathbf{k}+\mathbf{q}l} = -\left\langle\left[\hat{H}_{\rm BCS} + \hat{H}^{(1)}_{\rm em} + \hat{H}^{(2)}_{\rm em}, \hat{\alpha}^{\dagger}_{\mathbf{k}l}\hat{\alpha}_{\mathbf{k}+\mathbf{q}l}\right]\right\rangle \tag{B.5}$$

The r.h.s. of this equation takes the following form:

$$\begin{aligned}
\left\langle\left[\hat{H}_{\rm BCS}, \hat{\alpha}^{\dagger}_{\mathbf{k}l}\hat{\alpha}^{\dagger}_{\mathbf{k}+\mathbf{q}l}\right]\right\rangle =& -\left\{\left(R_{\mathbf{k}+\mathbf{q}l} - R_{\mathbf{k}l}\right)\alpha^{\dagger}_{\mathbf{k}l}\alpha_{\mathbf{k}+\mathbf{q}l} + C_{\mathbf{k}+\mathbf{q}l}\alpha^{\dagger}_{\mathbf{k}l}\beta^{\dagger}_{\mathbf{k}+\mathbf{q}l} + C^{*}_{\mathbf{k}l}\alpha_{\mathbf{k}+\mathbf{q}l}\beta_{\mathbf{k}l}\right\}\\
\left\langle\left[\hat{H}^{(1)}_{\rm em}, \hat{\alpha}^{\dagger}_{\mathbf{k}l}\hat{\alpha}^{\dagger}_{\mathbf{k}+\mathbf{q}l}\right]\right\rangle =& -\frac{e\hbar}{2m_l}\sum_{\mathbf{q}'=\pm\mathbf{q}}\mathbf{A}_{\mathbf{q}'}\cdot\left\{(2\mathbf{k}+\mathbf{q}')\left(M^{(-)}_{\mathbf{k},\mathbf{q}',l}\alpha_{\mathbf{k}+\mathbf{q}l}\beta_{\mathbf{k}+\mathbf{q}'l} - L^{(+)}_{\mathbf{k},\mathbf{q}',l}\alpha^{\dagger}_{\mathbf{k}+\mathbf{q}'l}\hat{\alpha}_{\mathbf{k}+\mathbf{q}l}\right)\right.\\
&\left. +(2\mathbf{k}+2\mathbf{q}-\mathbf{q}')\left(L^{(+)*}_{\mathbf{k}+\mathbf{q},-\mathbf{q}',l}\alpha^{\dagger}_{\mathbf{k}l}\alpha_{\mathbf{k}+\mathbf{q}-\mathbf{q}'l} + M^{(-)*}_{\mathbf{k}+\mathbf{q},-\mathbf{q}',l}\alpha^{\dagger}_{\mathbf{k}l}\beta^{\dagger}_{\mathbf{k}+\mathbf{q}-\mathbf{q}'l}\right)\right\}\\
\left\langle\left[\hat{H}^{(2)}_{\rm em}, \hat{\alpha}^{\dagger}_{\mathbf{k}l}\hat{\alpha}^{\dagger}_{\mathbf{k}+\mathbf{q}l}\right]\right\rangle =& -\frac{e^2}{2m_l}\sum_{\mathbf{q}'=0,\pm2\mathbf{q}}\left(\sum_{\mathbf{q}_i=\pm\mathbf{q}}\mathbf{A}_{\mathbf{q}'-\mathbf{q}_i}\cdot\mathbf{A}_{\mathbf{q}_i}\right)\left\{-L^{(-)}_{\mathbf{k},\mathbf{q}',l}\alpha^{\dagger}_{\mathbf{k}+\mathbf{q}'l}\alpha_{\mathbf{k}+\mathbf{q}l}\right.\\
&\left. +L^{(-)*}_{\mathbf{k}+\mathbf{q},-\mathbf{q}',l}\alpha^{\dagger}_{\mathbf{k}l}\alpha_{\mathbf{k}+\mathbf{q}-\mathbf{q}'l} - M^{(+)*}_{\mathbf{k}+\mathbf{q},-\mathbf{q}',l}\alpha^{\dagger}_{\mathbf{k}l}\beta^{\dagger}_{\mathbf{k}+\mathbf{q}-\mathbf{q}'l} - M^{(+)}_{\mathbf{k},\mathbf{q}',l}\alpha_{\mathbf{k}+\mathbf{q}l}\beta_{\mathbf{k}+\mathbf{q}'l}\right\}
\end{aligned} \tag{B.6}$$

(IV). Differential equation for $\beta^\dagger_{\mathbf{k}l}\beta_{\mathbf{k+q}l}$

The fourth differential equation is given by

$$i\hbar\frac{d}{dt}\beta^\dagger_{\mathbf{k}l}\beta_{\mathbf{k+q}l} = -\left\langle\left[\hat{H}_{\mathrm{BCS}} + \hat{H}^{(1)}_{\mathrm{em}} + \hat{H}^{(2)}_{\mathrm{em}}, \hat{\beta}^\dagger_{\mathbf{k}l}\hat{\beta}_{\mathbf{k+q}l}\right]\right\rangle \tag{B.7}$$

The r.h.s. of this equation takes the following form:

$$\begin{aligned}
-\left\langle\left[\hat{H}_{\mathrm{BCS}}, \hat{\beta}^\dagger_{\mathbf{k}l}\hat{\beta}^\dagger_{\mathbf{k+q}l}\right]\right\rangle =& \left(R_{\mathbf{k+q}l} - R_{\mathbf{k}l}\right)\beta^\dagger_{\mathbf{k}l}\beta_{\mathbf{k+q}l} + C_{\mathbf{k+q}l}\alpha^\dagger_{\mathbf{k+q}l}\beta^\dagger_{\mathbf{k}l} + C^*_{\mathbf{k}l}\alpha_{\mathbf{k}l}\beta_{\mathbf{k+q}l} \\
-\left\langle\left[\hat{H}^{(1)}_{\mathrm{em}}, \hat{\beta}^\dagger_{\mathbf{k}l}\hat{\beta}^\dagger_{\mathbf{k+q}l}\right]\right\rangle =& \frac{e\hbar}{2m}\sum_{\mathbf{q}'=\pm\mathbf{q}}\mathbf{A}_{\mathbf{q}'}\times \\
&\times\Big\{(2\mathbf{k}-\mathbf{q}')\left(-M^{(-)}_{\mathbf{k-q}',\mathbf{q}'l}\alpha_{\mathbf{k-q}'l}\beta_{\mathbf{k+q}l} + L^{(+)*}_{\mathbf{k-q}',\mathbf{q}'l}\beta^\dagger_{\mathbf{k-q}'l}\beta_{\mathbf{k+q}l}\right) \\
&\quad -(2\mathbf{k}+2\mathbf{q}+\mathbf{q}')\left(M^{(-)*}_{\mathbf{k+q},\mathbf{q}'l}\alpha^\dagger_{\mathbf{k+q+q}'l}\beta^\dagger_{\mathbf{k}l} + L^{(+)*}_{\mathbf{k+q},\mathbf{q}'l}\beta^\dagger_{\mathbf{k}l}\beta^\dagger_{\mathbf{k+q+q}'l}\right)\Big\} \\
-\left\langle\left[\hat{H}^{(2)}_{\mathrm{em}}, \hat{\beta}^\dagger_{\mathbf{k}l}\hat{\beta}^\dagger_{\mathbf{k+q}l}\right]\right\rangle =& \frac{e^2}{2m}\sum_{\mathbf{q}'=0,\pm2\mathbf{q}}\left(\sum_{\mathbf{q}_i=\pm\mathbf{q}}\mathbf{A}_{\mathbf{q}'-\mathbf{q}_i}\cdot\mathbf{A}_{\mathbf{q}_i}\right)\times \\
&\times\Big\{-M^{(+)}_{\mathbf{k-q}',\mathbf{q}'l}\alpha_{\mathbf{k-q}'l}\beta_{\mathbf{k+q}l} - L^{(-)*}_{\mathbf{k-q}',\mathbf{q}'l}\beta^\dagger_{\mathbf{k-q}'l}\beta_{\mathbf{k+q}l} \\
&\quad -M^{(+)*}_{\mathbf{k+q},\mathbf{q}'l}\alpha^\dagger_{\mathbf{k+q+q}'l}\beta^\dagger_{\mathbf{k}l} + L^{(-)*}_{\mathbf{k+q},\mathbf{q}'l}\beta_{\mathbf{k}l}\beta_{\mathbf{k+q+q}'l}\Big\}
\end{aligned} \tag{B.8}$$

B.2. Probe pulse excitation

Finally, we show equations of motion for all quasiparticles expectation values, which were discussed in section 7.2.

$$\begin{aligned}
i\hbar\frac{d}{dt}\alpha^\dagger_{\mathbf{k}l}\beta^\dagger_{\mathbf{k+q}_{\mathrm{pr}}l} =& -(R_{\mathbf{k}l} + R_{\mathbf{k+q}_{\mathrm{pr}}l})\alpha^\dagger_{\mathbf{k}l}\beta^\dagger_{\mathbf{k+q}_{\mathrm{pr}}l} + C^*_{\mathbf{k+q}_{\mathrm{pr}}l}\alpha^\dagger_{\mathbf{k}l}\alpha_{\mathbf{k+q}_{\mathrm{pr}}l} + C^*_{\mathbf{k}l}\beta^\dagger_{\mathbf{k+q}_{\mathrm{pr}}l}\beta_{\mathbf{k}l} \\
&+\frac{e\hbar}{2m}2\mathbf{k}\cdot\mathbf{A}_{\mathbf{q}_{\mathrm{pr}}}\left\{L^{(+)}_{\mathbf{k},\mathbf{q}_{\mathrm{pr}}l}\left(\alpha^\dagger_{\mathbf{k}l}\beta^\dagger_{\mathbf{k}l} - \alpha^\dagger_{\mathbf{p}_pl}\beta^\dagger_{\mathbf{p}_pl}\right) + M^{(-)}_{\mathbf{k},\mathbf{q}_{\mathrm{pr}}l}\left(\alpha^\dagger_{\mathbf{k}l}\alpha_{\mathbf{k}l} + \left[\beta^\dagger_{\mathbf{p}_pl}\beta_{\mathbf{p}_pl} - 1\right]\right)\right\} \\
i\hbar\frac{d}{dt}\alpha_{\mathbf{k+q}_{\mathrm{pr}}l}\beta_{\mathbf{k}l} =& (R_{\mathbf{k}l} + R_{\mathbf{k+q}_{\mathrm{pr}}l})\alpha_{\mathbf{k+q}_{\mathrm{pr}}l}\beta_{\mathbf{k}l} + C_{\mathbf{k}l}\alpha^\dagger_{\mathbf{k}l}\alpha_{\mathbf{k+q}_{\mathrm{pr}}l} + C_{\mathbf{k+q}_{\mathrm{pr}}l}\beta^\dagger_{\mathbf{k+q}_{\mathrm{pr}}l}\beta_{\mathbf{k}l} \\
&+\frac{e\hbar}{2m}2\mathbf{k}\cdot\mathbf{A}_{\mathbf{q}_{\mathrm{pr}}}\left\{L^{(+)}_{\mathbf{k},\mathbf{q}_{\mathrm{pr}}l}\left(\alpha_{\mathbf{k}l}\beta_{\mathbf{k}l} - \alpha_{\mathbf{p}_pl}\beta_{\mathbf{p}_pl}\right) - M^{(-)}_{\mathbf{k},\mathbf{q}_{\mathrm{pr}}l}\left(\alpha^\dagger_{\mathbf{p}_pl}\alpha_{\mathbf{p}_pl} + [\beta_{\mathbf{k}l}\beta_{\mathbf{k}l} - 1]\right)\right\} \\
i\hbar\frac{d}{dt}\alpha^\dagger_{\mathbf{k}l}\alpha_{\mathbf{k+q}_{\mathrm{pr}}l} =& \left(R_{\mathbf{k+q}_{\mathrm{pr}}l} - R_{\mathbf{k}l}\right)\alpha^\dagger_{\mathbf{k}l}\alpha_{\mathbf{k+q}_{\mathrm{pr}}l} + C_{\mathbf{k+q}_{\mathrm{pr}}l}\alpha^\dagger_{\mathbf{k}l}\beta^\dagger_{\mathbf{k+q}_{\mathrm{pr}}l} + C^*_{\mathbf{k}l}\alpha_{\mathbf{k+q}_{\mathrm{pr}}l}\beta_{\mathbf{k}l} \\
&+\frac{e\hbar}{2m}2\mathbf{k}\cdot\mathbf{A}_{\mathbf{q}_{\mathrm{pr}}}\left\{L^{(+)}_{\mathbf{k},\mathbf{q}_{\mathrm{pr}}l}\left(\alpha^\dagger_{\mathbf{k}l}\alpha_{\mathbf{k}l} - \alpha^\dagger_{\mathbf{p}_pl}\alpha_{\mathbf{p}_pl}\right) + M^{(-)}_{\mathbf{k},\mathbf{q}_{\mathrm{pr}}l}\left(\alpha_{\mathbf{p}_pl}\beta_{\mathbf{p}_pl} - \alpha^\dagger_{\mathbf{k}l}\beta^\dagger_{\mathbf{k}l}\right)\right\} \\
i\hbar\frac{d}{dt}\beta^\dagger_{\mathbf{k+q}_{\mathrm{pr}}l}\beta_{\mathbf{k}l} =& \left(R_{\mathbf{k}l} - R_{\mathbf{k+q}_{\mathrm{pr}}l}\right)\beta^\dagger_{\mathbf{k+q}_{\mathrm{pr}}l}\beta_{\mathbf{k}l} + C_{\mathbf{k}l}\alpha^\dagger_{\mathbf{k}l}\beta^\dagger_{\mathbf{k+q}_{\mathrm{pr}}l} + C^*_{\mathbf{k+q}_{\mathrm{pr}}l}\alpha_{\mathbf{k+q}_{\mathrm{pr}}l}\beta_{\mathbf{k}l} \\
&+\frac{e\hbar}{2m}2\mathbf{k}\cdot\mathbf{A}_{\mathbf{q}_{\mathrm{pr}}}\left\{L^{(+)}_{\mathbf{k},\mathbf{q}_{\mathrm{pr}}l}\left(\beta^\dagger_{\mathbf{k}l}\beta_{\mathbf{k}l} - \beta^\dagger_{\mathbf{p}_pl}\beta_{\mathbf{p}_pl}\right) + M^{(-)}_{\mathbf{k},\mathbf{q}_{\mathrm{pr}}l}\left(\alpha_{\mathbf{k}l}\beta_{\mathbf{k}l} - \alpha^\dagger_{\mathbf{p}_pl}\beta^\dagger_{\mathbf{p}_pl}\right)\right\}
\end{aligned} \tag{B.9}$$

Bibliography

[1] J. Bardeen, L. N. Cooper & J. R. Schrieffer. **Theory of superconductivity**. *Phys. Rev.* **108**, 1175 (1957).

[2] J. Goldstone, S. Weinberg & A. Salam. **Broken symmetries**. *Phys. Rev.* **127**, 965 (1962).

[3] Y. Nambu. **Nobel Lecture: Spontaneous symmetry breaking in particle physics: A case of cross fertilization**. *Rev. Mod. Phys.* **81**, 1015 (2009).

[4] N. N. Bogoliubov. **A new method in the theory of superconductivity**. *Soviet Physics JETP-USSR* **7**, 41–46, 51–55 (1958).

[5] Y. Nambu. **Quasi–particles and gauge invariance in the theory of superconductivity**. *Phys. Rev.* **117**, 648 (1960).

[6] P. W. Anderson. **Plasmons, gauge invariance, and mass**. *Phys. Rev.* **130**, 439 (1963).

[7] P. W. Anderson. **New Method in the Theory of Superconductivity**. *Phys. Rev.* **110**, 985 (1958).

[8] P. W. Higgs. **Broken symmetries and the masses of gauge bosons**. *Phys. Rev. Lett.* **13**, 508 (1964).

[9] R. Sooryakumar & M. V. Klein. **Raman Scattering by Superconducting-Gap Excitations and Their Coupling to Charge-Density Waves**. *Phys. Rev. Lett.* **45**, 660 (1980).

[10] M.-A. Méasson, Y. Gallais, M. Cazayous, B. Clair, P. Rodière, L. Cario & A. Sacuto. **Amplitude Higgs mode in the $2H$ – NbSe$_2$ superconductor**. *Phys. Rev. B* **89**, 060503 (2014).

[11] D. Sherman, U. S. Pracht, B. Gorshunov, S. Poran, J. Jesudasan, M. Chand, P. Raychaudhuri, M. Swanson, N. Trivedi, A. Auerbach, M. Scheffler, A. Frydman

& M. Dressel. **The Higgs mode in disordered superconductors close to a quantum phase transition**. *Nat. Phys.* **11**, 188 (2015).

[12] P. Littlewood & C. Varma. **Gauge–invariant theory of the dynamical interaction of charge–density waves and superconductivity**. *Phys. Rev. Lett.* **47**, 811 (1981).

[13] P. B. Littlewood & C. M. Varma. **Amplitude collective modes in superconductors and their coupling to charge–density waves**. *Phys. Rev. B* **26**, 4883 (1982).

[14] Y. Barlas & C. M. Varma. **Amplitude or Higgs modes in d-wave superconductors**. *Phys. Rev. B* **87**, 054503 (2013).

[15] E. Bauer, G. Hilscher, H. Michor, C. Paul, E. W. Scheidt, A. Gribanov, Y. Seropegin, H. Noël, M. Sigrist & P. Rogl. **Heavy fermion superconductivity and magnetic order in noncentrosymmetric $CePt_3Si$**. *Phys. Rev. Lett.* **92**, 027003 (2004).

[16] P. A. Frigeri, D. F. Agterberg & M. Sigrist. **Spin susceptibility in superconductors without inversion symmetry**. *New J. Phys.* **6**, 115 (2004).

[17] P. A. Frigeri, D. F. Agterberg, A. Koga & M. Sigrist. **Superconductivity without inverions symmetry: MnSi versus $CePt_3Si$**. *Phys. Rev. Lett.* **92**, 097001 (2004).

[18] P. A. Frigeri, D. F. Agterberg, A. Koga & M. Sigrist. **Erratum: Superconductivity without inverions symmetry: MnSi versus $CePt_3Si$ [Phys. Rev. Lett. 92, 097001 (2004)]**. *Phys. Rev. Lett.* **93**, 099903 (2004).

[19] A. H. Zewail. **Femtochemistry: Atomic–Scale Dynamics of the Chemical Bond**. *J. Phys. Chem. A* **104**, 5660 (2000).

[20] A. L. Cavalieri, N. Muller, T. Uphues, V. S. Yakovlev, A. Baltuska, B. Horvath, B. Schmidt, L. Blumel, R. Holzwarth, S. Hendel, M. Drescher, U. Kleineberg, P. M. Echenique, R. Kienberger, F. Krausz & U. Heinzmann. **Attosecond spectroscopy in condensed matter**. *Nature* **449**, 1029 (2007).

[21] T. Pfeifer, C. Spielmann & G. Gerber. **Femtosecond x–ray science**. *Rep. Prog. Phys.* **69**, 443 (2006).

[22] L. Rettig, R. Cortés, S. Thirupathaiah, P. Gegenwart, H. S. Jeevan, M. Wolf, J. Fink & U. Bovensiepen. **Ultrafast Momentum–Dependent Response of Electrons in Antiferromagnetic $EuFe_2As_2$ Driven by Optical Excitation**. *Phys. Rev. Lett.* **108**, 097002 (2012).

[23] F. Rossi & T. Kuhn. **Theory of ultrafast phenomena in photoexcited semiconductors**. *Rev. Mod. Phys.* **74**, 895 (2002).

[24] D. N. Basov, R. D. Averitt, D. van der Marel, M. Dressel & K. Haule. **Electrodynamics of correlated electron materials**. *Rev. Mod. Phys.* **83**, 471 (2011).

[25] R. D. Averitt, A. I. Lobad, C. Kwon, S. A. Trugman, V. K. Thorsmølle & A. J. Taylor. **Ultrafast Conductivity Dynamics in Colossal Magnetoresistance Manganites**. *Phys. Rev. Lett.* **87**, 017401 (2001).

[26] S. Hellmann, T. Rohwer, M. Kallaene, K. Hanff, C. Sohrt, A. Stange, A. Carr, M. M. Murnane, H. C. Kapteyn, L. Kipp, M. Bauer & K. Rossnagel. **Time–domain classification of charge–density–wave insulators**. *Nat. Commun.* **3**, 1069 (2012).

[27] A. Kimel, A. Kirilyuk, A. Tsvetkov, R. Pisarev & T. Rasing. **Laser–induced ultrafast spin reorientation in the antiferromagnet $TmFeO_3$**. *Nature* **429**, 850 (2004).

[28] R. Kaindl, M. Carnahan, D. Chemla, S. Oh & J. Eckstein. **Dynamics of cooper pair formation in $Bi_2Sr_2CaCu_2O_{8+\delta}$**. *Phys. Rev. B* **72**, 060510 (2005).

[29] L. Perfetti, P. A. Loukakos, M. Lisowski, U. Bovensiepen, H. Eisaki & M. Wolf. **Ultrafast electron relaxation in superconducting $Bi_2Sr_2CaCu_2O_{8+\delta}$ by time-resolved photoelectron spectroscopy**. *Phys. Rev. Lett.* **99**, 197001 (2007).

[30] R. P. Saichu, I. Mahns, A. Goos, S. Binder, P. May, S. G. Singer, B. Schulz, A. Rusydi, J. Unterhinninghofen, D. Manske, P. Guptasarma, M. S. Williamsen & M. Rübhausen. **Two-Component Dynamics of the Order Parameter of High Temperature $Bi_2Sr_2CaCu_2O_{8+\delta}$ Superconductors Revealed by Time-Resolved Raman Scattering**. *Phys. Rev. Lett.* **102**, 177004 (2009).

[31] A. Pashkin, M. Porer, M. Beyer, K. W. Kim, A. Dubroka, C. Bernhard, X. Yao, Y. Dagan, R. Hackl, A. Erb, J. Demsar, R. Huber & A. Leitenstorfer. **Femtosecond Response of Quasiparticles and Phonons in Superconducting $YBa_2Cu_3O_{7-\delta}$ Studied by Wideband Terahertz Spectroscopy**. *Phys. Rev. Lett.* **105**, 067001 (2010).

[32] M. Beck, M. Klammer, S. Lang, P. Leiderer, V. V. Kabanov, G. N. Gol'tsman & J. Demsar. **Energy–Gap Dynamics of Superconducting NbN Thin Films Studied by Time–Resolved Terahertz Spectroscopy**. *Phys. Rev. Lett.* **107**, 177007 (2011).

[33] S. Dal Conte, C. Giannetti, G. Coslovich, F. Cilento, D. Bossini, T. Abebaw, F. Banfi, G. Ferrini, H. Eisaki, M. Greven, A. Damascelli, D. van der Marel & F. Parmigiani. **Disentangling the Electronic and Phononic Glue in a High-T_c Superconductor**. *Science* **335**, 1600 (2012).

[34] R. Matsunaga & R. Shimano. **Nonequilibrium BCS State Dynamics Induced by Intense Terahertz Pulses in a Superconducting NbN Film**. *Phys. Rev. Lett.* **109**, 187002 (2012).

[35] R. Matsunaga, Y. I. Hamada, K. Makise, Y. Uzawa, H. Terai, Z. Wang & R. Shimano. Higgs Amplitude Mode in the BCS Superconductors $Nb_{1-x}Ti_xN$ Induced by Terahertz Pulse Excitation. *Phys. Rev. Lett.* **111**, 057002 (2013).

[36] M. Beck, I. Rousseau, M. Klammer, P. Leiderer, M. Mittendorff, S. Winnerl, M. Helm, G. N. Gol'tsman & J. Demsar. Transient Increase of the Energy Gap of Superconducting NbN Thin Films Excited by Resonant Narrow–Band Terahertz Pulses. *Phys. Rev. Lett.* **110**, 267003 (2013).

[37] B. Mansart, J. Lorenzana, A. Mann, A. Odeh, M. Scarongella, M. Chergui & F. Carbone. Coupling of a high–energy excitation to superconducting quasiparticles in a cuprate from coherent charge fluctuation spectroscopy. *Proc. Natl. Acad. Sci. U.S.A.* **110**, 4539 (2013).

[38] R. Matsunaga, N. Tsuji, H. Fujita, A. Sugioka, K. Makise, Y. Uzawa, H. Terai, Z. Wang, H. Aoki & R. Shimano. Light–induced collective pseudospin precession resonating with Higgs mode in a superconductor. *Science* **345**, 1145 (2014).

[39] A. Pashkin & A. Leitenstorfer. Particle physics in a superconductor. *Science* **345**, 1121 (2014).

[40] E. Abrahams & T. Tsuneto. Time variation of Ginzburg–Landau order parameter. *Phys. Rev* **152**, 416 (1966).

[41] N. B. Kopnin. *Theory of Nonequlibrium Suerconductivity* (Clarenton, Oxford, 2001).

[42] A. G. Aronov, Y. M. Galperin, V. L. Gurevich & V. I. Kozub. The Boltzmann–Equation Description of Transport in Superconductors. *Adv. Phys.* **30**, 539 (1981).

[43] V. V. Kabanov, J. Demsar & D. Mihailovic. Kinetics of a Superconductor Excited with a Femtosecond Optical Pulse. *Phys. Rev. Lett.* **95**, 147002 (2005).

[44] W. H. Parker. Modified heating theory of nonequilibrium superconductors. *Phys. Rev. B* **12**, 3667 (1975).

[45] E. J. Nicol & J. P. Carbotte. Comparison of s - and d -wave gap symmetry in nonequilibrium superconductivity. *Phys. Rev. B* **67**, 214506 (2003).

[46] C. S. Owen & D. J. Scalapino. Superconducting State under the Influence of External Dynamic Pair Breaking. *Phys. Rev. Lett.* **28**, 1559 (1972).

[47] T. Papenkort, V. M. Axt & T. Kuhn. Coherent dynamics and pump-probe spectra of BCS superconductors. *Phys. Rev. B* **76**, 224522 (2007).

[48] T. Papenkort, T. Kuhn & V. M. Axt. Coherent control of the gap dynamics of BCS superconductors in the nonadiabatic regime. *Phys. Rev. B* **78**, 132505 (2008).

[49] O. Betbeder-Matibet & P. Nozieres. Transport equations in clean superconductors. *Annals of Physics* **51**, 392 (1969).

[50] A. F. Volkov & S. M. Kogan. Collisionless relaxation of energy–gap in superconductors. *Soviet Physics JETP-USSR* **65**, 2038 (1973).

[51] R. A. Barankov, L. S. Levitov & B. Z. Spivak. Collective Rabi Oscillations and Solitons in a Time-Dependent BCS Pairing Problem. *Phys. Rev. Lett.* **93**, 160401 (2004).

[52] E. A. Yuzbashyan, B. L. Altshuler, V. B. Kuznetsov & V. Z. Enolskii. Nonequilibrium cooper pairing in the nonadiabatic regime. *Phys. Rev. B* **72**, 220503 (2005).

[53] E. A. Yuzbashyan, O. Tsyplyatyev & B. L. Altshuler. Relaxation and persistent oscillations of the order parameter in fermionic condensates. *Phys. Rev. Lett.* **96**, 097005 (2006).

[54] M. Dzero, A. A. Kirmani & E. A. Yuzbashyan. Nonadiabatic dynamics of superfluid spin–orbit–coupled degenerate Fermi gas. *Phys. Rev. A* **92**, 053626 (2015).

[55] A. P. Schnyder, D. Manske & A. Avella. Resonant generation of coherent phonons in a superconductor by ultrafast optical pump pulses. *Phys. Rev. B* **84**, 214513 (2011).

[56] H. Krull, D. Manske, G. S. Uhrig & A. P. Schnyder. Signatures of nonadiabatic BCS state dynamics in pump–probe conductivity. *Phys. Rev. B* **90**, 014515 (2014).

[57] H. Krull. *Conductivity of strongly pupump superconductors: An electron–phonon system far from equilibrium.* Ph.D. thesis, Technische Universität Dortmund (2014).

[58] J. Unterhinninghofen, D. Manske & A. Knorr. Theory of ultrafast nonequilibrium dynamics in d-wave superconductors. *Phys. Rev. B* **77**, 180509 (2008).

[59] A. Akbari, A. P. Schnyder, D. Manske & I. Eremin. Theory of nonequilibrium dynamics of multiband superconductors. *EPL* **101**, 17002 (2013).

[60] S. R. White & A. E. Feiguin. Real–time evolution using the density matrix renormalization group. *Phys. Rev. Lett.* **93**, 076401 (2004).

[61] F. B. Anders & A. Schiller. Real–time dynamics in quantum–impurity systems: A time–dependent numerical renormalization–group approach. *Phys. Rev. Lett.* **95**, 196801 (2005).

[62] J. K. Freericks, V. M. Turkowski & V. Zlatić. Nonequilibrium Dynamical Mean-Field Theory. *Phys. Rev. Lett.* **97**, 266408 (2006).

[63] M. Sentef, A. F. Kemper, B. Moritz, J. K. Freericks, Z.-X. Shen & T. P. Devereaux. Examining Electron-Boson Coupling Using Time-Resolved Spectroscopy. *Phys. Rev. X* **3**, 041033 (2013).

[64] H. Aoki, N. Tsuji, M. Eckstein, M. Kollar, T. Oka & P. Werner. Nonequilibrium dynamical mean–field theory and its applications. *Rev. Mod. Phys.* **86**, 779 (2014).

[65] N. Tsuji & H. Aoki. Theory of Anderson pseudospin resonance with Higgs mode in superconductors. *Phys. Rev. B* **92**, 064508 (2015).

[66] A. F. Kemper, M. A. Sentef, B. Moritz, J. K. Freericks & T. P. Devereaux. Direct observation of Higgs mode oscillations in the pump-probe photoemission spectra of electron-phonon mediated superconductors. *Phys. Rev. B* **92**, 224517 (2015).

[67] S. Kaiser, S. R. Clark, D. Nicoletti, G. Cotugno, R. I. Tobey, N. Dean, S. Lupi, H. Okamoto, T. Hasegawa, D. Jaksch & A. Cavalleri. Optical Properties of a Vibrationally Modulated Solid State Mott Insulator. *Sci. Rep.* **4** (2014).

[68] K. Ikegami, K. Ono, J. Togo, T. Wakabayashi, Y. Ishige, H. Matsuzaki, H. Kishida & H. Okamoto. Ultrafast photoinduced melting of spin-Peierls phase in the organic charge-transfer compounds alkali-tetracyanoquinodimethane. *Phys. Rev. B* **76**, 085106 (2007).

[69] T. Ogasawara, M. Ashida, N. Motoyama, H. Eisaki, S. Uchida, Y. Tokura, H. Ghosh, A. Shukla, S. Mazumdar & M. Kuwata-Gonokami. Ultrafast Optical Nonlinearity in the Quasi–One–Dimensional Mott Insulator Sr_2CuO_3. *Phys. Rev. Lett.* **85**, 2204 (2000).

[70] S. Iwai, M. Ono, A. Maeda, H. Matsuzaki, H. Kishida, H. Okamoto & Y. Tokura. Ultrafast Optical Switching to a Metallic State by Photoinduced Mott Transition in a Halogen-Bridged Nickel-Chain Compound. *Phys. Rev. Lett.* **91**, 057401 (2003).

[71] H. Okamoto, H. Matsuzaki, T. Wakabayashi, Y. Takahashi & T. Hasegawa. Photoinduced Metallic State Mediated by Spin-Charge Separation in a One-Dimensional Organic Mott Insulator. *Phys. Rev. Lett.* **98**, 037401 (2007).

[72] S. Wall, D. Brida, S. R. Clark, H. P. Ehrke, D. Jaksch, A. Ardavan, S. Bonora, H. Uemura, Y. Takahashi, T. Hasegawa, H. Okamoto, G. Cerullo & A. Cavalleri. Quantum interference between charge excitation paths in a solid-state Mott insulator. *Nat Phys* **7**, 114 (2011).

[73] R. Fukaya, Y. Okimoto, M. Kunitomo, K. Onda, T. Ishikawa, S. Koshihara, H. Hashimoto, S. Ishihara, A. Isayama, H. Yui & T. Sasagawa. **Ultrafast electronic state conversion at room temperature utilizing hidden state in cuprate ladder system**. *Nat. Commun.* **6**, 8519 (2015).

[74] H. Lu, S. Sota, H. Matsueda, J. Bonča & T. Tohyama. **Enhanced Charge Order in a Photoexcited One-Dimensional Strongly Correlated System**. *Phys. Rev. Lett.* **109**, 197401 (2012).

[75] H. Matsuzaki, M. Iwata, T. Miyamoto, T. Terashige, K. Iwano, S. Takaishi, M. Takamura, S. Kumagai, M. Yamashita, R. Takahashi, Y. Wakabayashi & H. Okamoto. **Excitation-Photon-Energy Selectivity of Photoconversions in Halogen-Bridged Pd-Chain Compounds: Mott Insulator to Metal or Charge-Density-Wave State**. *Phys. Rev. Lett.* **113**, 096403 (2014).

[76] H. Lu, C. Shao, J. Bonča, D. Manske & T. Tohyama. **Photoinduced in-gap excitations in the one-dimensional extended Hubbard model**. *Phys. Rev. B* **91**, 245117 (2015).

[77] M. Rini, R. Tobey, N. Dean, J. Itatani, Y. Tomioka, Y. Tokura, R. W. Schoenlein & A. Cavalleri. **Control of the electronic phase of a manganite by mode-selective vibrational excitation**. *Nature* **449**, 72 (2007).

[78] D. Fausti, R. I. Tobey, N. Dean, S. Kaiser, A. Dienst, M. C. Hoffmann, S. Pyon, T. Takayama, H. Takagi & A. Cavalleri. **Light–Induced Superconductivity in a Stripe–Ordered Cuprate**. *Science* **331**, 189 (2011).

[79] A. D. Caviglia, R. Scherwitzl, P. Popovich, W. Hu, H. Bromberger, R. Singla, M. Mitrano, M. C. Hoffmann, S. Kaiser, P. Zubko, S. Gariglio, J.-M. Triscone, M. Först & A. Cavalleri. **Ultrafast Strain Engineering in Complex Oxide Heterostructures**. *Phys. Rev. Lett.* **108**, 136801 (2012).

[80] S. Kaiser, C. R. Hunt, D. Nicoletti, W. Hu, I. Gierz, H. Y. Liu, M. Le Tacon, T. Loew, D. Haug, B. Keimer & A. Cavalleri. **Optically induced coherent transport far above T_c in underdoped $YBa_2Cu_3O_{6+\delta}$**. *Phys. Rev. B* **89**, 184516 (2014).

[81] A. Subedi, A. Cavalleri & A. Georges. **Theory of nonlinear phononics for coherent light control of solids**. *Phys. Rev. B* **89**, 220301 (2014).

[82] R. Höppner, B. Zhu, T. Rexin, A. Cavalleri & L. Mathey. **Redistribution of phase fluctuations in a periodically driven cuprate superconductor**. *Phys. Rev. B* **91**, 104507 (2015).

[83] S. J. Denny, S. R. Clark, Y. Laplace, A. Cavalleri & D. Jaksch. **Proposed Parametric Cooling of Bilayer Cuprate Superconductors by Terahertz Excitation**. *Phys. Rev. Lett.* **114**, 137001 (2015).

[84] M. Knap, M. Babadi, G. Refael, I. Martin & E. Demler. Dynamical Cooper pairing in nonequilibrium electron-phonon systems. *Phys. Rev. B* **94**, 214504 (2016).

[85] Z. M. Raines, V. Stanev & V. M. Galitski. Enhancement of superconductivity via periodic modulation in a three-dimensional model of cuprates. *Phys. Rev. B* **91**, 184506 (2015).

[86] A. A. Patel & A. Eberlein. Light-induced enhancement of superconductivity via melting of competing bond-density wave order in underdoped cuprates. *Phys. Rev. B* **93**, 195139 (2016).

[87] M. A. Sentef, A. F. Kemper, A. Georges & C. Kollath. Theory of light-enhanced phonon-mediated superconductivity. *Phys. Rev. B* **93**, 144506 (2016).

[88] W. Hu, S. Kaiser, D. Nicoletti, C. R. Hunt, I. Gierz, M. C. Hoffmann, M. Le Tacon, T. Loew, B. Keimer & A. Cavalleri. Optically enhanced coherent transport in $YBa_2Cu_3O_{6.5}$ by ultrafast redistribution of interlayer coupling. *Nat. Mater.* **13**, 705 (2014).

[89] R. Mankowsky, A. Subedi, M. Forst, S. O. Mariager, M. Chollet, H. T. Lemke, J. S. Robinson, J. M. Glownia, M. P. Minitti, A. Frano, M. Fechner, N. A. Spaldin, T. Loew, B. Keimer, A. Georges & A. Cavalleri. Nonlinear lattice dynamics as a basis for enhanced superconductivity in $YBa_2Cu_3O_{6.5}$. *Nature* **516**, 71 (2014).

[90] R. Mankowsky, M. Först, T. Loew, J. Porras, B. Keimer & A. Cavalleri. Coherent modulation of the $YBa_2Cu_3O_{6+x}$ atomic structure by displacive stimulated ionic Raman scattering. *Phys. Rev. B* **91**, 094308 (2015).

[91] E. Casandruc, D. Nicoletti, S. Rajasekaran, Y. Laplace, V. Khanna, G. D. Gu, J. P. Hill & A. Cavalleri. Wavelength-dependent optical enhancement of superconducting interlayer coupling in $La_{1.885}Ba_{0.115}CuO_4$. *Phys. Rev. B* **91**, 174502 (2015).

[92] M. Mitrano, A. Cantaluppi, D. Nicoletti, S. Kaiser, A. Perucchi, S. Lupi, P. Di Pietro, D. Pontiroli, M. Riccò, S. R. Clark, D. Jaksch & A. Cavalleri. Possible light-induced superconductivity in K_3C_{60} at high temperature. *Nature* **530**, 461 (2016).

[93] C. R. Hunt, D. Nicoletti, S. Kaiser, T. Takayama, H. Takagi & A. Cavalleri. Two distinct kinetic regimes for the relaxation of light-induced superconductivity in $La_{1.675}Eu_{0.2}Sr_{0.125}CuO_4$. *Phys. Rev. B* **91**, 020505 (2015).

[94] D. Nicoletti, E. Casandruc, Y. Laplace, V. Khanna, C. R. Hunt, S. Kaiser, S. S. Dhesi, G. D. Gu, J. P. Hill & A. Cavalleri. Optically induced superconductivity in striped $La_{2-x}Ba_xCuO_4$ by polarization-selective excitation in the near infrared. *Phys. Rev. B* **90**, 100503 (2014).

[95] J. Orenstein & J. S. Dodge. **Terahertz time-domain spectroscopy of transient metallic and superconducting states**. *Phys. Rev. B* **92**, 134507 (2015).

[96] D. Nicoletti, M. Mitrano, A. Cantaluppi & A. Cavalleri. **Comment on "Terahertz time-domain spectroscopy of transient metallic and superconducting states" (arXiv:1506.06758)**. *ArXiv e-prints* 1506.07846 (2015).

[97] J. Hubbard. **Electron Correlations in Narrow Energy Bands**. *Proc. R. Soc. A* **276**, 238 (1963).

[98] J. Solyom. **The Fermi gas model of one-dimensional conductors**. *Adv. Phys.* **28**, 201 (1979).

[99] J. Voit. **Phase diagram and correlation functions of the half–filled extended Hubbard model in one dimension**. *Phys. Rev. B* **45**, 4027 (1992).

[100] J. Voit. **One–dimensional Fermi liquids**. *Rep. Prog. Phys.* **58**, 977 (1995).

[101] H. Q. Lin & J. E. Hirsch. **Condensation transition in the one-dimensional extended Hubbard model**. *Phys. Rev. B* **33**, 8155 (1986).

[102] C. Lanczos. **An Iteration Method for the Solution of the Eigenvalue Problem of Linear Differential and Integral Operators**. *J. Res. Nat. Bur. Stand.* **45**, 255 (1950).

[103] S. Maekawa, T. Tohyama, S. E. Barnes, S. Ishihara, W. Koshibae & G. Khaliullin. *Physics of Transition Metal Oxides* (Springer-Verlag Berlin Heidelberg, 2004).

[104] R. Clay, A. Sandvik & D. Campbell. **Possible exotic phases in the one–dimensional extended Hubbard model**. *Phys. Rev. B* **59**, 4665 (1999).

[105] M. Eckstein, M. Kollar & P. Werner. **Interaction quench in the Hubbard model: Relaxation of the spectral function and the optical conductivity**. *Phys. Rev. B* **81**, 115131 (2010).

[106] S. A. Hamerla. *Dynamics of Fermionic Hubbard Models after Interaction Quenches in One and Two Dimensions*. Ph.D. thesis, Technische Universität Dortmund (2013).

[107] A. Altland & B. Simons. *Condensed Matter Field Theory* (Cambridge University Press, 2010).

[108] R. Kubo. **Statistical–Mechanical Theory of Irreversible Processes. 1. General Theory and Simple Applications to Magnetic and Conduction Problems**. *J. Phys. Soc. Jpn.* **12**, 570 (1957).

[109] G. Mahan. *Many–particle Physics* (Springer, New York, 1981).

[110] Z. Lenarčič, D. Golež, J. Bonča & P. Prelovšek. **Optical response of highly excited particles in a strongly correlated system**. *Phys. Rev. B* **89**, 125123 (2014).

[111] C. Shao, T. Tohyama, H.-G. Luo & H. Lu. **A numerical method to compute optical conductivity based on the pump-probe simulations**. *ArXiv e-prints* 1507.01200 (2015).

[112] D. N. Basov & T. Timusk. **Electrodynamics of high-T_c superconductors**. *Rev. Mod. Phys.* **77**, 721 (2005).

[113] W.-H. Jiao, Z.-T. Tang, Y.-L. Sun, Y. Liu, Q. Tao, C.-M. Feng, Y.-W. Zeng, Z.-A. Xu & G.-H. Cao. **Superconductivity in a Layered $Ta_4Pd_3Te_{16}$ with $PdTe_2$ Chains**. *J. Am. Chem. Soc.* **136**, 1284 (2014).

[114] Y. Kamihara, T. Watanabe, M. Hirano & H. Hosono. **Iron-based layered superconductor La[$O_{1-x}F_x$]FeAs (x=0.05-0.12) with T_c=26 K**. *J. Am. Chem. Soc.* **130**, 3296 (2008).

[115] J. Nagamatsu, N. Nakagawa, T. Muranaka, Y. Zenitani & J. Akimitsu. **Superconductivity at 39 K in magnesium diboride**. *Nature* **410**, 63 (2001).

[116] A. J. Leggett. **Number–phase fluctuations in two–band superconductors**. *Prog. Theor. Phys.* **36**, 901 (1966).

[117] H. Suhl, B. T. Matthias & L. R. Walker. **Bardeen–Cooper–Schrieffer theory of superconductivity in the case of overlapping bands**. *Phys. Rev. Lett.* **3**, 552 (1959).

[118] N. Bittner. *Response und kollektive Anregungen in Zweiband–Supraleitern*. Master's thesis, Technische Universität München (2012). Unpublished.

[119] J. G. Valatin. **Comments on the theory of superconductivity**. *Nuovo Cimento* **7**, 843 (1958).

[120] E. Bauer & M. Sigrist (eds.) *Non–centrosymmetric superconductors* (Springer, Heidelberg, 2012).

[121] K. V. Samokhin. **Spin susceptibility of noncentrosymmetric superconductors**. *Phys. Rev. B* **76**, 094516 (2007).

[122] L. Gor'kov & E. Rashba. **Superconducting 2D system with lifted spin degeneracy: Mixed single–triplet state**. *Phys. Rev. Lett.* **87**, 037004 (2001).

[123] G. Dresselhaus. **Spin–Orbit Coupling Effects in Zinc Blende Structures**. *Phys. Rev.* **100**, 580 (1955).

[124] K. Togano, P. Badica, Y. Nakamori, S. Orimo, H. Takeya & K. Hirata. **Superconductivity in the Metal Rich Li-Pd-B Ternary Boride**. *Phys. Rev. Lett.* **93**, 247004 (2004).

[125] A. Vorontsov, I. Vekhter & M. Eschrig. **Andreev bound states in non-centrosymmetric superconductors**. *Physica B: Condensed Matter* **403**, 1095 (2008).

[126] K. V. Samokhin & V. P. Mineev. **Gap structure in noncentrosymmetric superconductors**. *Phys. Rev. B* **77**, 104520 (2008).

[127] P. A. Frigeri, D. F. Agterberg, I. Milat & M. Sigrist. **Phenomenological theory of the s-wave state in superconductors without an inversion center**. *EPJ B* **54**, 435 (2006).

[128] I. E. Dzyaloshinskii. **A thermodynamic theory of weak ferromagnetism of antiferromagnetics**. *J. Phys. Chem. Solids* **4**, 241 (1958).

[129] T. Moriya. **Anisotropic Superexchange Interaction and Weak Ferromagnetism**. *Phys. Rev.* **120**, 91 (1960).

[130] C. M. Varma. **Higgs boson in superconductors**. *J. Low Temp. Phys.* **126**, 901 (2002).

[131] M. V. Klein. **Theory of Raman scattering from Leggett's collective mode in a multiband superconductor: Application to MgB_2**. *Phys. Rev. B* **82**, 014507 (2010).

[132] G. Blumberg, A. Mialitsin, B. S. Dennis, M. V. Klein, N. D. Zhigadlo & J. Karpinski. **Observation of Leggett's Collective Mode in a Multiband Superconductor**. *Phys. Rev. Lett.* **99**, 227002 (2007).

[133] P. Wölfle. **Kinetic theory of anisotropic Fermi superfluids**. *J. Low Temp. Phys.* **22**, 157 (1976).

[134] L. D. Landau. **Theory of Fermi liquids**. *Zhurnal Eksperimental'noi i Teoreticheskoi Fiziki* **30**, 1058 (1956).

[135] L. Klam. *Unconventional properties of non–centrosymmetric superconductors*. Ph.D. thesis, Universität Stuttgart (2010).

[136] T. Tsuneto. **Transverse collective excitations in superconductors and electromagnetic absorption**. *Phys. Rev.* **118**, 1029 (1960).

[137] S. C. Sharapov, V. P. Gusynin & H. Beck. **Effective action approach to the Leggett's mode in two–band superconductors**. *Eur. Phys. J. B* **30**, 45 (2002).

[138] W. H. Press, B. P. Flannery, S. A. Teukolsky & W. T. Vetterling. *Numerical Recipes in C: The Art of Scientific Computing* (Cambridge University Press, New York, NY, USA, 1988).

[139] H. Choi, D. Roundy, H. Sun, M. Cohen & S. Louie. The origin of the anomalous superconducting properties of MgB_2. *Nature* **418**, 758 (2002).

[140] X. X. Xi. Two–band superconductor magnesium diboride. *Rep. Prog. Phys.* **71**, 116501 (2008).

List of publications

Coupling of Higgs and Leggett modes in nonequilibrium superconductors H. Krull, N. Bittner, G. S. Uhrig, D. Manske, and A. P. Schnyder. *Nat. Commun.* **7**, 11921 (2016)

Leggett Modes and the Anderson–Higgs Mechanism in Superconductors without Inversion Symmetry N. Bittner, D. Einzel, L. Klam, and D. Manske. *Phys. Rev. Lett.* **115**, 227002 (2015)

Two–fluid Description of Two–band Superconductors N. Bittner, and D. Einzel. *J. Low. Temp. Phys.* **174**, 184 (2014)

List of additional publications

Correlation between Fermi surface transformations and superconductivity in the electron-doped high-Tc superconductor $\mathbf{Nd_{2-x}Ce_xCuO_4}$ T. Helm, M. V. Kart–sovnik, C. Proust, B. Vignolle, C. Putzke, E. Kampert, I. Sheikin, E.-S. Choi, J. S. Brooks, N. Bittner, W. Biberacher, A. Erb, J. Wosnitza, and R. Gross. *Phys. Rev. B*, **92**, 094501 (2015)

Fermi Surface of the Electron-Doped Cuprate Superconductor $\mathbf{Nd_{2-x}Ce_xCuO_4}$ Probed by High-Field Magnetotransport M. V. Kartsovnik, T. Helm, C. Putzke, F. Wolff-Fabris, I. Sheikin, S. Lepault, C. Proust, D. Vignolles, N. Bittner, W. Biberacher, A. Erb, J. Wosnitza, and R. Gross. *New J. Phys.* **13**, 015001 (2011)

Magnetic Breakdown in the Electron-Doped Cuprate Superconductor $\mathbf{Nd_{2-x}Ce_xCuO_4}$: The Reconstructed Fermi Surface Survives in the Strongly Overdoped Regime T. Helm, M. V. Kartsovnik, I. Sheikin, M. Bartkowiak, F. Wolff-Fabris, N. Bittner, W. Biberacher, M. Lambacher, A. Erb, J. Wosnitza, and R. Gross *Phys. Rev. Lett.* **105**, 247002 (2010)

Evolution of the Fermi Surface of the Electron-Doped High-Temperature Superconductor $\mathbf{Nd_{2-x}Ce_xCuO_4}$ Revealed by Shubnikov de Haas Oscillations T. Helm, M. V. Kartsovnik, M. Bartkowiak, N. Bittner, M. Lambacher, A. Erb, J. Wosnitza, and R. Gross. *Phys. Rev. Lett.* **103**, 157002 (2009)

Acknowledgment

At the end of this thesis I would like to express my deepest gratitude to all people, whose support and encouragement made this work possible:

First of all, I am deeply grateful to Prof. Walter Metzner for giving me the opportunity to become a member of his group at Max–Planck–Institute (MPI) for Solid State Research in Stuttgart. I highly appreciate many helpful discussions and his valuable suggestions. Also, I would like to thank him for the possibility to attend a lot of different workshops and conferences, and for the freedom to participate in different research projects. I am highly indebted to my supervisor Prof. Dirk Manske for introducing me to interesting problems of modern solid state physics and for sharing his experience and knowledge with me. His enthusiasm and novel ideas has been inspiring to me. Moreover, I would like to thank him for always being there when I needed his help and advice. Also, I wish to thank Prof. Felix von Oppen for showing interest to my work and for agreeing to be a co–referee of this thesis. I highly appreciated the opportunity to give seminar talks to his group at Freie Universität Berlin and to have enlightening discussions afterwards.

Further, I would like to express my sincerest thanks and appreciation to all my collaborators. In particular, I am extremely grateful to Prof. Dietrich Einzel from Walther–Meissner–Institute (WMI) in Garching by Munich not only for his support and valuable advices, but also for explaining to me complicated aspects of superconductivity in very educational way. I highly appreciated many helpful discussions and also his proofreading of this thesis. Also, I would like to thank Prof. Tohyama from Tokio University of Science for inviting me to Japan and for sharing his knowledge and experience in numerical implementation of the Lanczos algorithm. Under his guidance I was able to develop and extend my own code in C++, which was also used in a part of this thesis. Moreover, I am thankful for introducing me to the history and culture of Japan. Also, I would like to thank Yukawa Institute of Theoretical Physics in Japan for its hospitality. Many thanks goes to Andreas Schnyder, who was responsible for providing me with technical support and shared with me his profound scientific knowledge. Also, I would like to thank Ludwig Klam for enlightening discussions and for finding time to come to MPI after his work. I wish to thank Holger Krull for his technical support and helpful discussions during his stay at MPI in Stuttgart. Many thanks go to Mark Kartsovnik from WMI for being always welcome in his lab and for interesting discussions during his famous tea–time. Also I would like to thank Toni Helm for giving me an opportunity to take a part in his experimental work and for being so enthusiastic and positive. Finally, I am extremely grateful to Stefan Kaiser from experimental group at MPI for sharing his thoughts and ideas with me. I highly appreciated many valuable discussions and also his proofreading of this thesis.

Furthermore, I would like to take the opportunity and to thank all people at MPI in Stuttgart, who provided me a very nice working environment. In particular, a special thanks go to the computer service group for the technical support. Especially, I am highly indebted to Armin Burkhardt and Armin Schuhmacher for solving all the problems, which I had with Linux system, and for explaining to me, how the programming on clusters works. I wish to thank Jeanette Schüller-Knapp for her help with all bureaucratic matter and all members in our theory group at MPI for the great atmosphere. In particular, for this I need to thank: Jachym Sykora, Andreas Eberlein, Benjamin Obert, Raquel Queiroz, Eslam Khalaf, Tobias Holder, Moritz Hirschmann, Henri Menke, Demetrio Vilardi, Ciro Taranto, Wei Chen, Chia–Wei Huang and Pavel Ioselevich. In addition, a special thanks go to: Pavel Ostrovsky, Andrzej Oles, Adolfo Avella, Nils Hasselmann, Peter Horsch, and Roland Zeyher.

This thesis I would like to dedicate to the most important people in my life, who provided me with unconditional support and encouragement, and believed strong in me: my supportive and very enthusiastic brother Artur; my parents Andreas and Natalia, who gave me a chance to study and to find myself in Germany; my wife Ksenia, who shared with me all ups and downs, supported and encouraged me, and always enriched my daily life.